Johanna Schirmer

Effects of Two-Photon Oxidation for the Development of Graphene-Bio Interfaces

UNIVERSITY OF JYVÄSKYLÄ

FACULTY OF MATHEMATICS
AND SCIENCE

Johanna Schirmer

Effects of Two-Photon Oxidation for the Development of Graphene-Bio Interfaces

Esitetään Jyväskylän yliopiston matemaattis-luonnontieteellisen tiedekunnan suostumuksella
julkisesti tarkastettavaksi Ylistönrinteen auditoriossa FYS1
joulukuun 4. päivänä 2023 kello 12.

Academic dissertation to be publicly discussed, by permission of
the Faculty of Mathematics and Science of the University of Jyväskylä,
in Ylistönrinne, auditorium FYS1, on December 4, 2023, at 12 o'clock.

JYVÄSKYLÄN YLIOPISTO
UNIVERSITY OF JYVÄSKYLÄ

JYVÄSKYLÄ 2023

Editors
Mika Pettersson
Department of Chemistry, University of Jyväskylä
Päivi Vuorio
Open Science Centre, University of Jyväskylä

ABSTRACT

The discovery of graphene's excellent electronic properties established a research field towards creating graphene-based neural interfaces. Indeed, graphene can record neuronal activity, which is itself based on electrical signals. An active neuronal network is crucial for building a graphene-neuron interface, and is heavily dependent on the environment of the neuron, which consists of a gel-like matrix. Several factors, such as matrix stiffness and protein layers have been shown to affect the formation of the network. In the past decade, two-photon oxidation (2PO) of graphene was established as an all-optical, nanoscale method that introduces hydroxyl and epoxide groups on the graphene surface, while preserving the carbon network and the adjacent pristine graphene. In this thesis, the effects of 2PO of graphene on attached proteins and a supramolecular hydrogel were studied. Two well-known model proteins, horseradish peroxidase (HRP) and bovine serum albumin, were investigated regarding their noncovalent immobilization on pristine and 2PO graphene surfaces. Additionally, the enzymatic function of HRP immobilized on graphene was studied. The supramolecular hydrogel was analyzed regarding its stiffness, the incorporation of graphene oxide flakes into the gel and the surface-mediated self-assembly on pristine and 2PO graphene surfaces. The results present 2PO as a tool to tune protein immobilization and function, and its effect on the supramolecular self-assembly of an amino acid based amphiphile. Overall, this thesis contributes to the knowledge about surface-related effects towards graphene-bio interfaces.

Keywords: graphene, two-photon oxidation, graphene-bio interface, protein, supramolecular hydrogel

TIIVISTELMÄ (ABSTRACT IN FINNISH)

Grafeenin erinomaisten elektronisten ominaisuuksien löytäminen loi tutkimusalan grafeeniin perustuvien hermorajapintojen luomiseksi. Grafeeni voi todellakin mitata hermosolujen aktiivisuutta, joka itse perustuu sähköisiin signaaleihin. Aktiivinen hermosoluverkko on ratkaisevan tärkeä grafeeni-neuronirajapinnan rakentamiselle, ja se on voimakkaasti riippuvainen hermosolujen ympäristöstä, joka koostuu geelinkaltaisesta matriisista. Useiden tekijöiden, kuten ympäröivän matriisin jäykkyyden ja proteiinikerrosten, on osoitettu vaikuttavan verkoston muodostumiseen. Viimeisen vuosikymmenen aikana grafeenin kaksifotonihapetus (2PO) on kehittynyt täysin optiseksi, nanomittakaavan menetelmäksi, jonka avulla voidaan funktionalisoida hydroksyyli- ja epoksidiryhmiä grafeenin pinnalle säilyttäen yhtenäinen hiiliverkosto hapetetulla alueella samalla kun hapettamattoman grafeenin rakenne säilyy täysin muuttumattomana. Tässä opinnäytetyössä tutkittiin grafeenin kaksifotonihapetuksen vaikutuksia siihen kiinnitettyihin proteiineihin ja supramolekulaariseen hydrogeeliin. Kahta hyvin tunnettua malliproteiinia tutkittiin liittyen niiden ei-kovalenttiseen immobilisaatioon muokkaamattomille ja kaksifotonihapetetuille grafeenipinnoille. Lisäksi tutkittiin grafeeniin immobilisoidun piparjuuriperoksidaasin entsymaattista toimintaa. Supramolekulaarista hydrogeeliä analysoitiin sen jäykkyyden, grafeenioksidihiutaleiden sisällyttämisen geeliin ja pintavälitteisen itsejärjestäytymisen suhteen muokkaamattomilla ja kaksifotonihapetetuilla grafeenipinnoilla. Tulosten mukaan kaksifotonihapetus toimii työkaluna, jonka avulla voidaan säätää proteiinien immobilisaatiota ja toimintaa sekä aminohappopohjaisen amfifiilin supramolekulaarista itsejärjestäytymistä. Kaiken kaikkiaan tämä opinnäytetyö lisää tietoa pintailmiöistä liittyen grafeeni-biorajapintojen kehittämiseen.

Avainsanat: grafeeni, kaksifotoninen hapetus, grafeeni-biorajapinta, proteiini, supramolekulaarinen hydrogeeli

Author   Johanna Schirmer
                          Department of Chemistry
                          Nanoscience Center
                          University of Jyväskylä
                          Jyväskylä, Finland
                          johanna.j.schirmer@jyu.fi
                          ORCID: 0000-0001-9010-3131

Supervisors   Professor Mika Pettersson
                          Department of Chemistry
                          Nanoscience Center
                          University of Jyväskylä
                          Jyväskylä, Finland
                          mika.j.pettersson@jyu.fi

                          Professor Maija Nissinen
                          Department of Chemistry
                          Nanoscience Center
                          University of Jyväskylä
                          Jyväskylä, Finland
                          maija.nissinen@jyu.fi

Reviewers   Professor Carita Kvarnström
                          Department of Chemistry
                          University of Turku
                          Turku, Finland

                          Dr. Inês Gonçalves
                          Institute of Biomedical Engineering
                          University of Porto
                          Porto, Portugal

Opponent   Professor Chiara Zanardi
                          Department of Molecular Sciences and Nanosystems
                          University of Venice
                          Venice, Italy

PREFACE

The journey to this thesis started in 2018, during my exchange semester at the University of Jyväskylä. From the first discussion in my supervisor's office, I was excited about the research project that aims to connect graphene to nerve cells. Over the past five years, I have been able to expand my knowledge in interdisciplinary nanoscience and discuss research with excellent chemists, biologists, and physicists. This interdisciplinary approach and the international environment at the Nanoscience Center have broadened my horizons.

The result is a thesis that combines chemistry, biology, and materials science at the nanoscale. It includes three peer-reviewed articles and one manuscript. None of this would have been possible without the support of many people, whom I would like to thank in this section.

First, I would like to express my sincere gratitude to my supervisor, Professor Mika Pettersson: for giving me the opportunity to work on this interdisciplinary research project, for his scientific expertise, for being open to my ideas, and for the positive attitude and support at the right time. I am also very grateful for the support and expertise I received from my co-supervisor, Professor Maija Nissinen. Mika and Maija created an environment where I could grow as a young researcher.

This work could not have been done without the support and collaboration in our interdisciplinary research team. I would like to thank all current and former graphene team members for the thought-provoking discussions in our group meetings and helping me with my experiments. I would especially like to thank Olli Rissanen and Dr. Vesa-Matti Hiltunen for preparing the graphene samples, Dr. Kamila Mentel and Dr. Aleksei Emelianov for graphene oxidation, Dr. Eero Hulkko and Dr. Pasi Myllyperkiö for help and guidance in the laser lab, Dr. Andreas Johansson for many hours of imaging and Dr. Efstratios Sitsanidis, Romain Chevigny and Aku Lampinen for all the hours we spent together in the lab. It was a privilege to work with all of you. Also, I would like to thank the technical staff of our faculty for their assistance with all kinds of practical issues. For proofreading this thesis, my gratitude goes to Dr. Annabelle Mattern, Dr. Erich See and Romain Chevigny.

I would like to thank all my colleagues at the NSC, especially in the synthesis, hybrid, AFM, and laser labs, for creating such a great and supportive working environment. The numerous corridor and lab chats, sauna evenings, lunch and coffee break discussions and interesting seminars made me feel part of an international scientific community.

I would like to thank my friends from near and far for the welcome distraction from work, whether during lunch breaks, weekends, or vacations. You helped me clear my head and recharge my batteries. To my Finland friends, I thank you for creating so many wonderful memories over the past five years. It was a blast!

LIST OF INCLUDED ARTICLES

I   Efstratios D. Sitsanidis, Johanna Schirmer, Aku Lampinen, Kamila K. Mentel, Vesa-Matti Hiltunen, Visa Ruokolainen, Andreas Johansson, Pasi Myllyperkiö, Maija Nissinen and Mika Pettersson, Tuning protein adsorption on graphene surfaces *via* laser-induced oxidation, *Nanoscale Advances*, **2021**, 3, 2065-2074.

II   Johanna Schirmer, Ester Iatta, Aleksei Emelianov, Maija Nissinen and Mika Pettersson, Catalytic Activity of Horseradish Peroxidase Immobilized on Pristine and Two-Photon Oxidized Graphene, *Advanced Materials Interfaces, accepted manuscript.*

III   Efstratios D. Sitsanidis, Lara A. L. Dutra, Johanna Schirmer, Romain Chevigny, Manu Lahtinen, Andreas Johansson, Carmen C. Piras, David K. Smith, Marja Tiirola, Mika Pettersson and Maija Nissinen, Probing the Gelation Synergies and Anti-*Escherichia coli* Activity of Fmoc-Phenylalanine/Graphene Oxide Hybrid Hydrogel, *ACS Omega*, **2023**, 8, 10225-10234.

IV   Johanna Schirmer, Romain Chevigny, Aleksei Emelianov, Eero Hulkko, Andreas Johansson, Pasi Myllyperkiö, Efstratios D. Sitsanidis, Maija Nissinen and Mika Pettersson, Diversity at the nanoscale: laser-oxidation of single-layer graphene affects Fmoc-phenylalanine surface-mediated self-assembly, *Physical Chemistry Chemical Physics*, **2023**, 25, 8725-8733.

Author's contribution

In article **I**, the author of this thesis functionalized the graphene samples and performed Raman spectroscopy, atomic force microscopy (AFM) and data analysis. The author designed the experiments of article **II** and performed AFM and UV-Vis spectroscopy studies and data analysis. The preparation of the hydrogels, transition phase temperature, AFM and infrared and Raman spectroscopy characterization of the gels and corresponding data analysis were performed by the author for article **III**. In article **IV**, the author prepared the hydrogel samples, performed AFM and scattering-type scanning near-field optical microscopy experiments and density functional theory calculations, and analyzed all data. The author was involved in the preparation of the manuscripts for articles **I** and **III** and wrote the first drafts and final manuscripts of articles **II** and **IV**.

List of other articles to which the author has contributed

i Romain Chevigny, Johanna Schirmer, Carmen C. Piras, Andreas Johansson, Elina Kalenius, David K. Smith, Mika Pettersson, Efstratios D. Sitsanidis and Maija Nissinen, Triggering a transient organo-gelation system in a chemically active solvent, *Chemical Communications*, **2021**, 57, 10375-10378.

ii Romain Chevigny, Efstratios D. Sitsanidis, Johanna Schirmer, Eero Hulkko, Pasi Myllyperkiö, Maija Nissinen and Mika Pettersson, Nanoscale Probing of the Supramolecular Assembly in a Two-Component Gel by Near-Field Infrared Spectroscopy, *Chemistry – A European Journal*, **2023**, e202300155.

ABBREVIATIONS

2PO	Two-photon oxidation
AFM	Atomic force microscopy
b-BSA	Biotinylated bovine serum albumin
CNS	Central nervous system
CTC	Charge transfer complex
DFT	Density functional theory
Fmoc	*N*-Fluorenylmethyloxycarbonyl
FTIR	Fourier transform infrared
GBM	Graphene-based material
GFET	Graphene field-effect transistor
GO	Graphene oxide
HIM	Helium ion microscopy
HRP	Horseradish peroxidase
IR	Infrared
LMWG	Low-molecular-weight gelator
MIR	Mid-infrared
Phe	*L*-phenylalanine
PNS	Peripheral nervous system
PXRD	Powder X-ray diffraction
s-SNOM	Scattering-type scanning nearfield optical microscopy
SEM	Scanning electron microscopy
TEM	Transmission electron microscopy
TMB	3,3′,5,5′-Tetramethylbenzidine
UV	Ultraviolet
Vis	Visible

CONTENTS

ABSTRACT
TIIVISTELMÄ
PREFACE
LIST OF INCLUDED ARTICLES
ABBREVIATIONS
CONTENTS

1 INTRODUCTION

The human body is a complex organism, in the center of which is the brain.[1] Together with the spinal cord and billions of nerves, it forms the nervous system and coordinates all the actions of the body. From vital functions like breathing and temperature control to all our movements, memories and feelings, everything is controlled by the nervous system. It creates our reality. Accordingly, the tissue of the nervous system – the neural tissue – is very complex, and injuries or malfunction can have a huge impact on the life of a human. For this reason, research towards neural interfaces for implants and neuroprosthetics has long been a research field of enormous interest.[2] In fact, the first neuroprosthetic device was developed in 1972: the cochlear implant, which improves the hearing ability of the patient. Since then, neuroprosthetics have been developed further until this year (2023), when a man was able to naturally walk after a spinal cord injury that left him with tetraplegia, thanks to brain and spine neural interfaces.[3]

Existing neural interface systems usually communicate with the nerve cells (neurons) through microelectrode arrays containing many small electrodes that receive and transmit signals.[4] The devices commonly consist of materials that are much stiffer than the brain tissue. This causes tissue damage during the implantation, and poor cell adhesion and proliferation are observed. In recent years, research towards less stiff, flexible implants has expanded.[4,5]

In 2004, the exceptional electronic properties of the "miracle material" graphene were discovered.[6] Among the various proposed applications of this two-dimensional honeycomb carbon film was the improvement of the electronic performance of neural implants using graphene field-effect transistors (GFETs) instead of the many metal electrodes in an array.[7] However, the interactions between the graphene surface and the natural or artificial biomaterial need to be understood to develop functional and safe devices.

This thesis is part of a bigger project, which aims to create graphene-based interfaces for neuro applications. The included studies were performed to understand the effect of the graphene functionalization on surface interactions at the molecular level. However, the goal of creating an interface between a working graphene device and functional neurons was omnipresent in each step.

At the beginning of this introductory chapter, the biological background of the neural tissue in humans and the possibilities and requirements for neural interfaces are explained to show the broader context of this work. Secondly, low-molecular-weight supramolecular hydrogels as a possible artificial extracellular matrix are introduced, including surface-related effects on the gel network. Then, structure, properties and biological applications of graphene are introduced. Especially protein immobilization and the effects of graphene on self-assembly events are reviewed. Finally, the aims of this project are presented.

1.1 Biological background of the project

1.1.1 Neurons in their natural environment

Neurons are the main component of the nervous system in vertebrates. They forward sensory and actional signals through the whole body; thus, their functioning is crucial for the living organism.[1] The nervous system is further divided into the central nervous system (CNS), which involves the brain and the spinal cord, and the peripheral nervous system (PNS), which mainly consists of nerves.[8] An enormous network of neurons exists in the neural tissue: In the human brain, there are more than 10^{11} neurons, each connected to a thousand other neurons on average. To build up this huge network, neurons have a specific shape (FIGURE 1a): The cell body, which includes the nucleus, has many thin extensions, the dendrites, that radiate into the neural tissue. One-to-few long axons grow from the cell body and cause the elongated shape of the neuron. The length of an axon in an adult human can vary from below one millimeter to above one meter. The nerves in the PNS are bundles of these long axons that connect the CNS with every sensing part of the body. At the end of the axon, the cell branches again into many thin extensions. Due to all these thin extensions in the cell body and at the axon terminal, neurons can build their unique network and communicate through the whole body.

Neuronal signals are transmitted intracellularly by membrane potential changes and intercellularly by neurotransmitter molecules.[8] The signal transmission happens at the synapses, where an axon terminal extension of the presynaptic neuron is close to a dendrite of the postsynaptic neuron (FIGURE 1b). The membrane potential change arrives at the axon terminal of the presynaptic neuron and causes calcium channels to open, which leads to an influx of Ca^{2+} ions from the extracellular space. This in turn causes vesicles containing neurotransmitter molecules to release their cargo into the synaptic cleft *via* exocytosis, i.e., the fusion of the vesicle and cell membrane. The neurotransmitter molecules move the relatively short distance (≈ 20 nm[1]) between the two cells and bind to transmitter-gated ion channels, which open only upon binding of specific molecules. Next, sodium, calcium or potassium ions enter the postsynaptic neuron, causing another change in the membrane potential. If this process happens at many synapses, the overall change in the membrane potential leads

to the formation of an action potential, which is further transmitted through the axon by voltage-gated Na^+ channels.
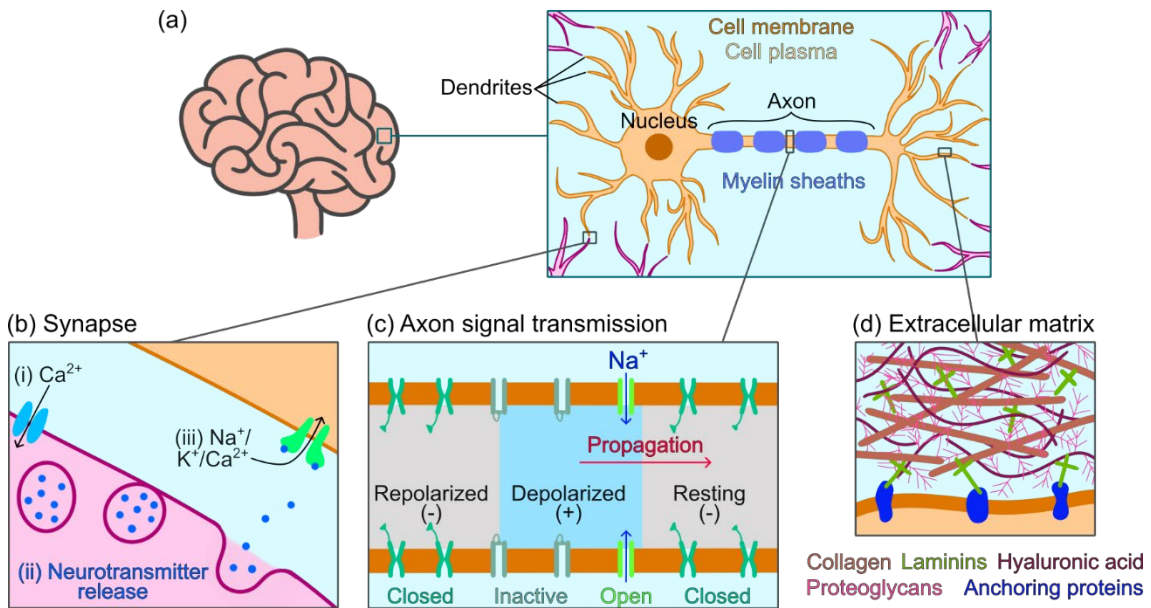

FIGURE 1   Schemes of a neuron and the neuronal signal transmission: (a) A neuron inside the brain, including cell compartment definitions. (b) Signal transmission from the presynaptic neuron (pink) to the postsynaptic neuron (orange) *via* neurotransmitters (blue). (c) Intracellular action potential propagation through the axon. (d) The extracellular matrix as a gel-like network of various components. The colored font indicates the described components.

In the axon, the abovementioned membrane potential change upon the influx of cations causes the opening of voltage-gated Na^+ channels (FIGURE 1c).[8] The resulting Na+ influx leads to a further change of the membrane potential and the opening of more voltage-gated Na^+ channels. The open channels will be inactivated automatically after a short period of time and stay inactive until the membrane potential has returned to its initial value. Thus, the signal transmission can only proceed in one direction by opening further closed – but not inactive – channels. The so-called myelin sheaths (FIGURE 1a) cover and insulate parts of the axon, which allows the action potential to jump from one myelin-free membrane node to another. Once the action potential reaches the axon terminal, it will again induce Ca^{2+} influx and neurotransmitter release. In this way, a signal is transmitted through the network of nerve cells in the whole human body to the desired destination, for example a muscle cell, with an intracellular speed of 100 meters per second or more.

A viable and functional neuronal network, however, requires more than the neurons themselves and other cell types. In any tissue of the human body, the cells are surrounded by a network of mainly proteins and sugars, the extracellular matrix (ECM, FIGURE 1d).[8] The components of the ECM are produced and secreted by the cells themselves. In the extracellular space, the molecules self-assemble and form a matrix with tissue-specific viscoelastic properties. For example, the ECM of teeth and bones is very stiff compared to the

soft ECM of neurons in the brain, which consists of collagen, laminins, and hyaluronic acid, among others. The ECM conducts several functions: It holds a tissue together, guides cells during the growth of the body and is a place of intercellular communication, as described above for the synapses.

Overall, the nervous system is a complex composite material crucial for any sensing and action mechanism in the human body. A vast number of cells, proteins and ions contribute to its function and thus the living of humans.

1.1.2 Neural interfaces

The processes and tissue composition of the neural tissue are very complex and specific, as explained above. However, from a chemist's perspective, they can be broken down into reaction steps and material properties.

The signal transmission can be divided into three steps: At the dendrite, the neuron acts like a sensor specific to certain small organic molecules (neurotransmitters). The intracellular transmission of the signal is induced by a change of potential, i.e., an electric stimulus, that is transmitted to the other end of the neuron. At the axon terminal, the neuron increases the concentration of neurotransmitters in the synaptic cleft. To mimic these processes and to communicate with neurons, electronic devices and artificial neurotransmitter sensors can be used.

The ECM components in the brain are secreted by the cells themselves if they are viable and functional. An artificial ECM could support neuronal growth and regeneration after injuries, but it must meet tissue-specific requirements for the viscoelastic properties, as neuronal growth was shown to depend on the matrix stiffness in cell cultures.[9-11] In fact, Georges *et al.*[9] found that if the matrix stiffness is comparable to the brain tissue (Young's modulus 0.1 kPa to 1 kPa[12]), the growth of neurons in a cell culture is preferred compared to the growth of glial cells, which are part of the neural tissue as well but cannot transmit signals. Kayal *et al.*[10] showed that neurons change their orientation and branching behavior upon changing matrix stiffness. These results highlight the importance of the viscoelastic material properties with regard to therapeutics for brain injuries. Once the neuronal network is functional, it will produce its own ECM. In this stage, it would be beneficial if the artificial ECM degrades by automatic or enzymatic degradation. Thus, the requirements for an artificial ECM are biocompatibility, biodegradability and matching viscoelastic properties with the target tissue.

In conclusion, the artificial surface and environment must be able to support the growth of a functional neuronal network close to the surface, detect signals from the neurons (neurotransmitter concentration changes), induce electric stimuli to the neurons and stay intact as long as it is in contact with the neural tissue.

1.2 Low-molecular-weight supramolecular hydrogels

Gels have sparked research interest in chemistry, physics, biology and materials science due to their versatile applications and tunable properties. They are omnipresent in the daily life in the form of, for example, food products like jelly, cosmetic products like hair gel and the gel-filling in bicycle saddles. An important part of the human body, the ECM of soft tissues (see section 1.1), is a gel as well. For this reason, gels are studied for biomedical applications. In this chapter, the concept, structure and possible biomedical applications of low-molecular-weight supramolecular hydrogels will be reviewed, followed by an introduction to surface-mediated self-assembly.

1.2.1 Structure and potential applications

By definition, a gel consists of at least two components: a liquid that is present in a substantial amount and a crosslinked substance.[13] Additionally, it has to be a soft, solid or solid-like material with certain viscoelastic properties. Depending on the nature of the solvent, gels can be divided into hydrogels and organogels. In the case of hydrogels, the solvent is water or other aqueous liquids such as buffer solutions. The crosslinking can be chemical (covalent) or physical (noncovalent), and each has its advantages, depending on the intended application of the gel.[14] Chemically crosslinked gels are more stable due to the formation of permanent covalent bonds and robust to chemical modification and dissolution. A physically linked gel, on the other hand, provides reversibility (degradability), mild gelation conditions and easy incorporation of biomolecules. The physical interactions underlying the gel formation can include hydrogen bonding and π-π stacking, among others, depending on the chemical structure of the gelator molecules.

A physical gel formed by noncovalent interactions between amphiphilic low-molecular-weight gelator (LMWG) molecules is a supramolecular gel.[15] LMWGs hierarchically self-assemble in solution upon certain stimuli, mostly into fibers (FIGURE 2). The stimuli include pH and temperature changes and sonication. Initially, the LMWG molecules self-assemble in one or two dimensions (primary structure).[16] Subsequently, aggregates such as fibers or ribbons are formed (secondary structure). The interactions between these aggregates further describe the tertiary structure of the gel. The solvent is entrapped in between the aggregates, which makes the resulting material a gel. The properties of this gel depend on several parameters, such as the LMWG chemical structure, its concentration, the solvent, and the stimulus.
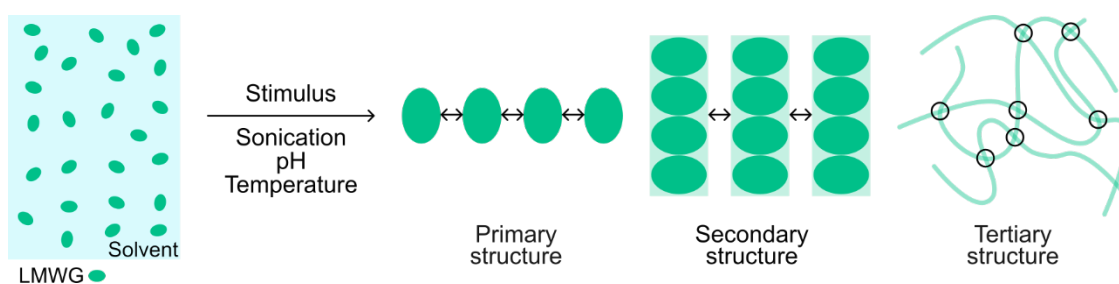
FIGURE 2   The gelation process and structural levels in a LMW supramolecular hydrogel. The double-sided black arrows and black circles indicate the interactions at each organizational level.

A biologically interesting group of LMWGs is the peptide amphiphiles. They consist of one to a few biocompatible amino acids linked *via* peptide bonds and modified with hydrophobic moieties, such as lipid tails or the fluorenylmethyloxycarbonyl (Fmoc) group.[17,18] The large number of possibly biocompatible amino acid based LMWGs and biocompatible solvents, such as buffer solutions, have led to a variety of possible biological applications for the resulting hydrogels. These include tissue engineering,[19] cell culturing[20] and therapeutics[21,22]. As mentioned above, the intended application of the gel defines the desired mechanical and chemical properties. For example, for tissue engineering, the hydrogel must be sufficiently strong to support cells and chemically resistant to *in vivo* stress, for instance, through enzymatic degradation and pH changes. When used in therapeutics or as ECM mimic for neural interfaces, on the other hand, the gel might be intended to degrade in the body after a successful therapy or neuronal network formation, respectively. The tuneability of the self-assembly and the gel's properties opens the possibility for application-specific material engineering. The existing results involving LMW supramolecular hydrogels in biological applications are promising. However, the research field is relatively young, with the first peptide amphiphile self-assembly reported in 2001,[23] which is why some gelation-affecting parameters are not yet fully understood. These need to be elucidated to develop safe and reliable biomaterials.

1.2.2   Surface-mediated self-assembly

The gelation process of supramolecular hydrogels is sensitive to several factors, like the parameters mentioned above, but also the size and volume of the gelation container and the surface on which the gelation event takes place.[24,25] In fact, surface-mediated self-assembly has become a research field of its own in recent years. It explores self-assembly processes that are affected by certain surface properties.

Studies usually describe the effects of changing specific surface properties on the different levels of self-assembly (FIGURE 2). The properties include hydrophilicity/hydrophobicity, surface charge and physical properties like topography and roughness.[25] The effects describe initiation/inhibition and

acceleration/deceleration of the self-assembly, and controlling the shape of the self-assembled structures, their orientation, and their mechanical properties. For example, Angelerou *et al.*[26] have shown the effect of the surface hydrophilicity/hydrophobicity on the fiber diameter and Young's modulus of a LMWG hydrogel. The cytidine-based hydrogel on the hydrophobic surface is stiffer and consists of thicker fibers than the gel on the more hydrophilic surface. In another study, Yang *et al.*[27] demonstrated that by changing the surface charge, one peptide amphiphile can self-assemble into two different hydrogels with distinct viscoelastic properties and secondary and tertiary structures. Interestingly, both hydrogel forms were observed on the same sample in a relatively small volume (350 µl) after photopatterning of the surface. These results highlight the importance of the surface as an initiating platform for the self-assembly.

Surfaces are omnipresent during self-assembly events in the laboratory and in nature in the form of, for example, vials, flasks, flat surface samples or cell membranes. Though it is well known that the surface can affect self-assembly events in various ways, the observations are not yet fully understood. For a more in-depth elucidation, systematic studies of surface property effects on supramolecular self-assembly and their synergies are needed. Additionally, the range of the effects, i.e., the question of how far from the surface the effect persists, remains a rather open question, while the first results indicate a limited range.[26] By understanding the surface-related effects on supramolecular self-assembly, the surface can become a tool to design new materials for specific applications.

1.3   Graphene

Graphene is a two-dimensional material consisting of a single layer of carbon atoms in a hexagonal honeycomb lattice (FIGURE 3). Theoretically, the material has been studied for a long time: In 1947, P. R. Wallace predicted the electronic structure of graphene.[28] Afterwards, more theoretical and observational studies about single-layer graphene have been published.[29-32] However, the "graphene rush" started in 2004, when it was characterized for the first time by Andre Geim and Konstantin Novoselov, who received the Nobel Prize in Physics in 2010 for their groundbreaking experiments with graphene.[6,33] Since 2004, graphene has been a material of high interest to the scientific community, due to its exceptional properties. In this chapter, the structure, selected properties and characterization of graphene and graphene oxide (GO) will be reviewed, together with approaches for biological applications of and protein immobilization on the graphene-based materials (GBMs). Finally, the effects of graphene and graphene oxide on supramolecular self-assembly will be presented.
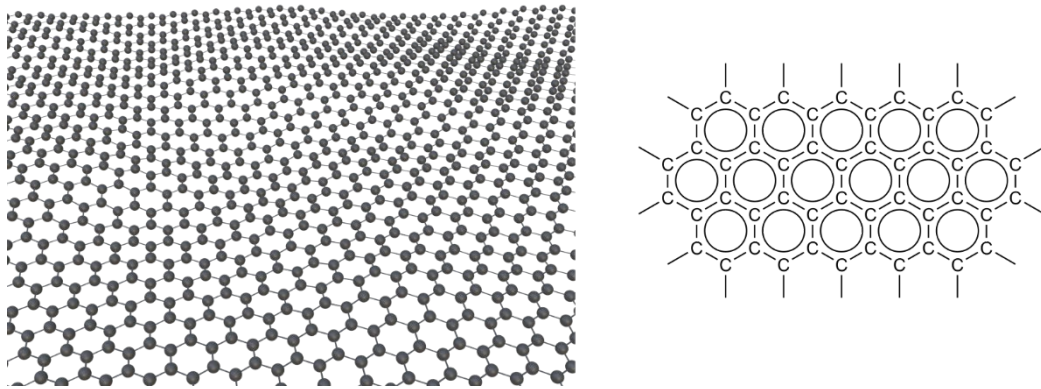
FIGURE 3   Graphene as a two-dimensional material (left) and its atomic structure (right, bond length ≈0.142 nm).

1.3.1 Structure and selected properties of graphene and graphene oxide

The outstanding electrical, mechanical and optical properties of graphene are based on its unique structure. The carbon atoms in graphene are sp^2-hybridized, with three sp^2-orbitals in one plane and one p orbital perpendicular to this plane (FIGURE 4a).[34] The three sp^2-orbitals are involved in σ-bonds to three carbon atoms, with a bond length of 0.142 nm and bond angles of 120°. The electrons in the p-orbitals of all conjugated carbon atoms form a delocalized π electron system, or π- (valence) and π*- (conduction) bands, over the whole lattice. Through this atomic structure, graphene is highly hydrophobic, and electrons can move easily over long distances in the graphene plane.
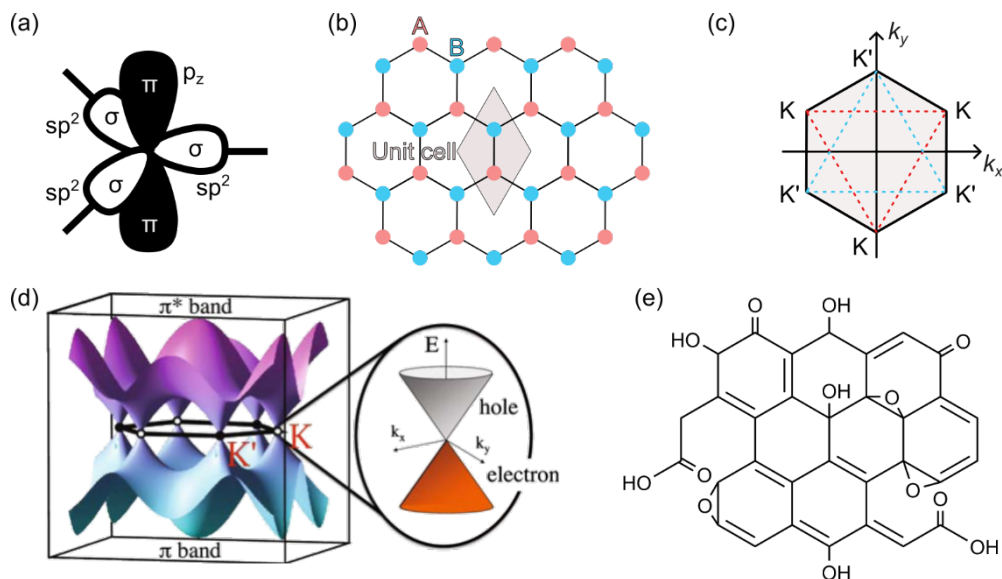
FIGURE 4   Structural features of graphene and GO: (a) Hybridization of the carbon atoms in the graphene lattice, (b) the two sublattices A and B and the unit cell consisting of two carbon atoms, (c) Brillouin zone of graphene, (d) band structure of graphene with a zoom to one Dirac cone, and (e) example structure of GO. (d) *Electronic properties and quantum transport in Graphene-based nanostructures*.[35] Copyright 2009 EDP Sciences, SIF, Springer-Verlag Berlin Heidelberg.

20

The unit cell of graphene contains the two carbon atoms, A and B (FIGURE 4b), and the material can be described as a hexagonal lattice with a two-atom basis. The Brillouin zone of graphene is a hexagon and contains the inequivalent high symmetry points K and K′ (FIGURE 4c). There are six Dirac points at the K and K′ points, with the valence band and the conduction band touching at the Fermi energy level, which makes graphene a zero-gap semimetal (FIGURE 4d). In this model, the valence band is fully occupied, while the conduction band is empty at zero temperature.

By positive or negative doping of the graphene sheet, the Fermi energy can be tuned continuously to induce electrons or holes, respectively. The charge carrier mobility is outstanding and remains high even at room temperature and high doping.[36,37] For comparison, crystalline silicon, a commonly used semiconductor in electronics, has a charge carrier mobility in the order of $10^3 \, cm^2 \cdot V^{-1} \cdot s^{-1}$ at room temperature, while graphene has one on the order of $10^5 \, cm^2 \cdot V^{-1} \cdot s^{-1}$.[38] However, for devices with a Si/SiO_2 substrate, the interactions between graphene and its support material can decrease the mobility by one order of magnitude and induce p-type doping.[39,40]

In addition to the excellent electronic properties, graphene is mechanically robust. A single-crystalline free-standing graphene layer has shown a high elasticity with a Young's modulus of approximately 900-1000 GPa.[41] These unique electronic and mechanical properties make graphene a promising material for electronic devices in general.[36] Another remarkable property of graphene is its visual transparency,[42] which makes it an interesting material for the development of transparent devices, such as organic light emitting diodes[43] and transparent conductive electrodes for organic solar cells[44].

The properties of the perfect honeycomb graphene lattice change for its derivative GO. The synthesis of GO was reported for the first time in 1859 by Benjamin Brodie,[45] 88 years before the first theoretical description of graphene itself. Brodie, however, did not describe his discovery as graphene oxide but as "graphon", a new form of carbon. In this material, a part of the carbon atoms is sp^3-hybridized and bound to oxygen atoms, introducing hydroxyl, epoxide, carbonyl, or carboxyl groups to the graphene lattice (FIGURE 4e). The carbon atoms at the edge of the graphene sheet are especially prone to functionalization because they are not surrounded by the stable sp^2 carbon lattice. Depending on the synthetic method and the extent of the oxidation, the amount and type of oxygen-containing functional groups vary.[46]

The incorporation of oxygen-containing functional groups changes the properties of graphene. The hydrophobicity of the material decreases, which opens possibilities for the use of GO in aqueous media and for further covalent and noncovalent functionalization with, for example, proteins[47–49] or drugs[50]. Herein, noncovalent immobilization is based on hydrogen bonding, van-der-Waals interactions and π-π stacking, while covalent approaches include the formation of ester or amide bonds. The change from sp^2 to sp^3 hybridization for some of the carbon atoms also affects the delocalized π electron system. As a result, a band gap opens between the valence and conduction band, which makes

highly oxidized GO an insulating material.[51] It has been shown that this band gap decreases with a decreasing number of oxygen-containing groups during the reduction of GO.[51,52] Thus, the oxidation and reduction of graphene opens the possibility to tune the band gap of the material.

1.3.2 Two-photon oxidation of graphene

The oxidation of single-layer graphene can be achieved *via* femtosecond laser-induced two-photon oxidation (2PO). This method was described for the first time in 2015 by Aumanen *et al.*[53] and presents an all-optical tool to tune the properties of graphene.

In detail, single-layer graphene – suspended or on a Si/SiO_2 substrate – is irradiated in ambient conditions with a femtosecond laser in user-defined, nanoscale patterns. The process involves two photons and oxygen and water molecules from the air, which dissociate prior to the formation of covalent bonds with the graphene carbon atoms. In this way, primarily epoxide and hydroxyl groups are introduced to the single-layer graphene surface.[54] While the hybridization of a part of the carbon atoms changes from sp^2 to sp^3 in the irradiated areas, the carbon network stays intact, and the adjacent non-irradiated pristine graphene is retained. The oxidation level can be tuned by changing the pulse energy and the irradiation time during the oxidation. At lower oxidation levels, hydroxyl and epoxide groups are present on the oxidized surface. At higher levels, carboxylic groups can also be detected, but hydroxyl and epoxide groups remain the dominating species.

2PO of graphene additionally introduces a band gap in the material, which increases with an increasing oxidation level and opens the possibility to fabricate graphene with conducting and insulating states adjacent to each other. Thus, the method allows tuning the hydrophilicity and the electronic properties of the graphene surface without the loss of the carbon network. It promises the development of user-defined, nanoscale all-graphene devices. Recently, 2PO was used as a tool to tune the sensitivity of GFETs for pH sensing[55] and to achieve area-selective atomic layer deposition of zinc oxide[56]. These results demonstrate the possibilities of 2PO for device development and surface chemistry.

1.3.3 Characterization of graphene and graphene oxide

Graphene and GO can be characterized by various spectroscopic and microscopic methods. Raman spectroscopy has become one of the most important analytic tools of graphitic materials in general, as it reveals the quality of the sample while being non-destructive. X-ray photoelectron spectroscopy shows chemical modifications and the sp^2/sp^3 ratio of the GBM. Some functionalized derivatives, such as GO, can be studied with infrared (IR) spectroscopy. To visualize graphene, atomic force (AFM), transmission electron (TEM) and scanning electron (SEM) microscopy have been used. In this chapter, the two most important methods for GBM characterization during this project, Raman

spectroscopy and AFM, will be explained regarding single-layer graphene samples, 2PO and GO.

1.3.3.1 Raman spectroscopy

Raman spectroscopy is an important and powerful tool in studying the quality of graphene and its derivatives.[57] The visible Raman spectrum of graphitic materials is dominated by the sp^2 domains of the sample because visible excitation is resonant with the π states of the material.[58] Among others, defects,[58,59] doping,[58,60] strain[61,62] and oxidation[53,63] of the graphene lattice can be detected and analyzed with this technique. The Raman spectrum of single-layer pristine and oxidized graphene (FIGURE 5a) contains several bands characteristic for the graphene lattice itself and the beforementioned effects on it. The four main bands, G, 2D, D and D′, and their fundamental processes will be explained in this chapter.

The G band at ≈1580 cm^{-1} (for pristine graphene) originates from in-plane stretching of the sp^2 C-C bonds in the graphene lattice. It is based on a first order Raman scattering process (FIGURE 5b) and is present in all poly-aromatic carbon materials.[58] However, the band shape and position of the G band varies depending on the material properties. The 2D band at ≈2700 cm^{-1} forms on a second order process involving two phonons and two inelastic scattering events between the K and the K′ points (intervalley process, FIGURE 5c). For single-layer graphene, the band shows a Lorentzian shape. An increasing lattice disorder induces a decrease in the 2D band intensity.[56] The G and 2D bands are very prominent in the Raman spectrum of pristine graphene (FIGURE 5a). Disorders in the graphene lattice, induced by, for example, edges, domain boundaries or 2PO, give rise to defect-related Raman bands.[53,64] The D band at ≈1350 cm^{-1} is based on a similar second-order process as the 2D band. However, one scattering event is inelastic by a phonon and the other one is elastic by a defect (FIGURE 5d). Similarly, the D′ band at ≈1620 cm^{-1} originates from a second-order process, which involves a phonon and a defect scattering event (FIGURE 5e). In contrast to the D band, it is an intra-valley process because it connects two points at the same K or K′ point.

By analyzing the intensities, widths, and shapes of these four main Raman bands of graphene, the quality and functionalization of the graphene sample can be obtained. To evaluate the quality of a single-layer graphene sample, the ratio of the D band and G band intensity (*I*) and the width of the 2D band are commonly used. The Raman spectrum of a high-quality pristine graphene sample has a low I_D/I_G ratio and a narrow 2D band.
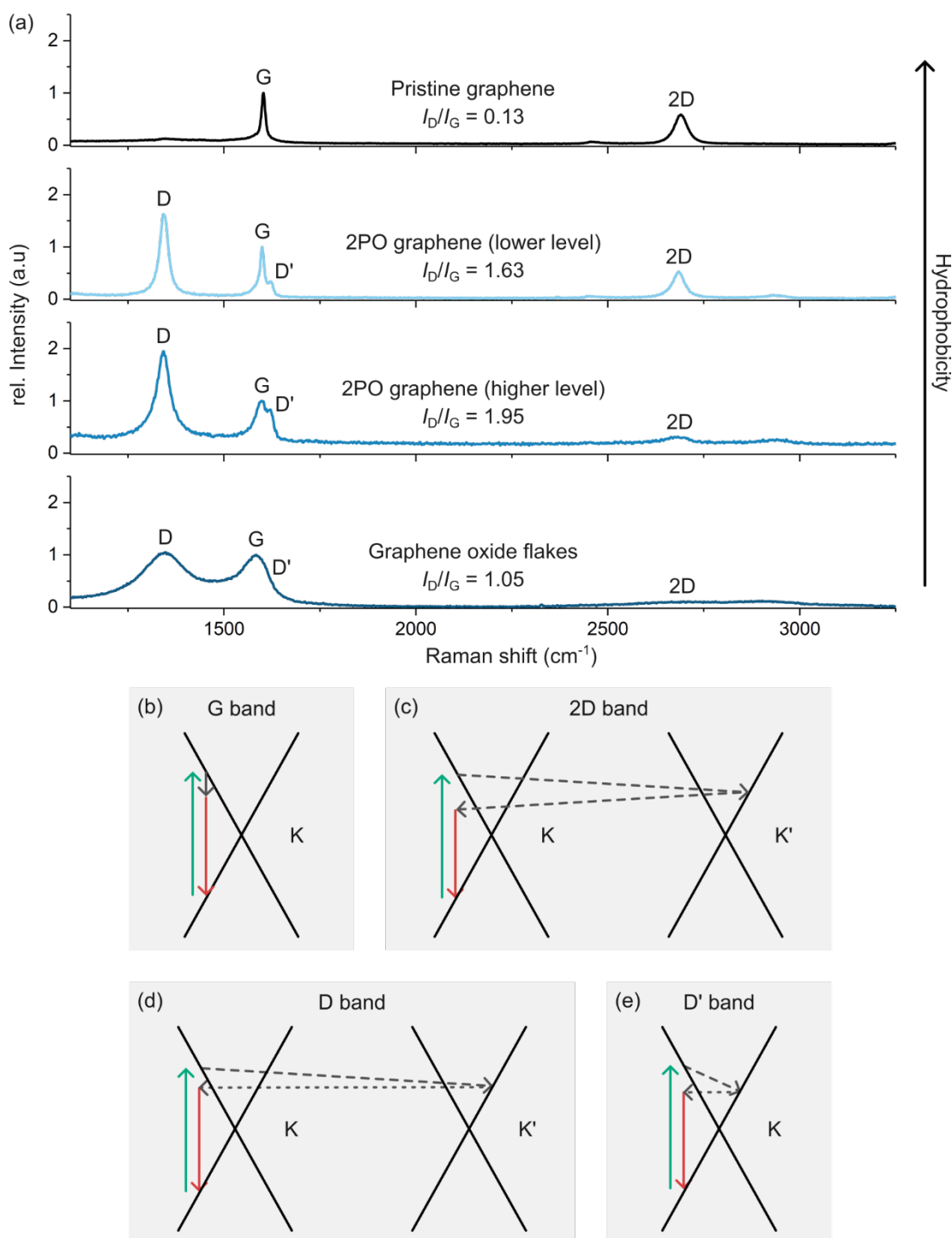
FIGURE 5   Raman characterization of graphene and oxidized derivatives: (a) Typical Raman spectra of pristine graphene, 2PO graphene with low and high oxidation levels and GO flakes with the characteristic bands. Raman scattering processes for the (b) G (c) 2D (d) D and (e) D' bands. Inelastic phonon scattering is indicated by the dashed lines and elastic defect scattering by the dotted lines.

2PO of graphene (chapter 1.3.2) introduces oxygen-containing functional groups to the graphene surface.[53,54] Consequently, the hybridization of the affected carbon atoms is converted from sp^2 to sp^3, which equals a defect introduction to the graphene lattice. Additionally, due to the higher electronegativity of oxygen

compared to carbon, 2PO induces p-type doping to the graphene lattice. These effects are directly visible in the Raman spectrum of the material (FIGURE 5a). The induced p-type doping can shift the G band to a higher Raman shift and lower the I_D/I_G ratio.[60] The increasing defect density on the surface has several effects on the Raman spectrum: (i) The intensity of the D and D' bands and the corresponding I_D/I_G ratio initially increase.[65,66] At higher defect densities, however, the I_D/I_G ratio decreases again. (ii) With increasing lattice disorder at higher oxidation levels, the intensity of the 2D band decreases.[56] (iii) The G band broadens upon increasing lattice disorder. The I_D/I_G ratio, together with the width of the G band, can be used to quantify defects and, in the case of 2PO, to estimate the oxidation level.[56,65–67]

In commercially available GO flakes, the oxidation is more extensive than for a 2PO single-layer graphene and dominated by carboxylic groups at the edge of the flakes. Caused by the functional groups and the relatively large amount of graphene edges in the GO flakes, the defect-induced bands are naturally intense (FIGURE 5a).[57]

Overall, Raman spectroscopy is sensitive to chemical and electronical changes of graphene samples and is therefore a powerful tool to study graphitic materials and their functionalization.

1.3.3.2   Atomic force microscopy

The topography of a graphene surface can be studied by AFM. In this technique, the sample is scanned by a sharp tip (nanometer range) attached to a cantilever.[68] Upon topographic changes on the sample surface, the tip and consequently the cantilever will move, which is detected by a laser reflecting from the upside of the cantilever.

There are different AFM operation modes.[68] In the contact mode, the tip is constantly in contact with the sample. While this provides a high-resolution image, it is also likely to scratch and damage the sample and blunt the tip. Another more sensitive mode is the tapping mode. Here, the tip and cantilever initially oscillate at the cantilever's resonant frequency. The contact between the tip and the sample is very short and less destructive. Upon topographic changes on the sample surface, the oscillation frequency of the cantilever changes, which is again detected by the laser reflecting from the upside of the cantilever. The vertical resolution of AFM can be as low as 0.01 nm, which makes it a suitable tool to study relatively smooth surfaces and detect even small topography changes.

On a single-layer graphene sample, AFM can reveal surface roughness and topographical defects such as grain boundaries and double layer domains. Additionally, AFM can visualize the functionalization of graphene with, for example, proteins,[47,69] peptides[69,70] or 2PO[67]. The 2PO graphene surface can be distinguished from pristine graphene in AFM images due to its elevation of typically one to two nm compared to the adjacent pristine graphene.[67,71] With its ease of use in ambient conditions and sensitive sample treatment, AFM is an

important tool for surface characterization, especially after surface functionalization with biomolecules.

1.3.4 Graphene in biological applications

Soon after the discovery of graphene's electronical properties, single-layer graphene and GO were functionalized with biomolecules towards graphene-based biosensors and biotransistors.[72,73] In 2008, Mohanty and Berry reported the functionalization of GO- and graphene-amine-Si/SiO$_2$ devices with single-stranded DNA and a gram-positive bacterium.[72] The conductivity of the graphene-based surface changed upon functionalization and was sensitive even to a single bacterial cell. Two years later, GO was used to sensitively quench the fluorescence of unbound peptides compared to protein-bound peptides and thus showed its great potential for biosensing applications.[73] Based on these early results, graphene-bio interfaces have established a research field of their own, including, for example, biosensing, cell culture, antimicrobial effects, implants and neural interfaces.[74–80]

1.3.4.1 Biocompatibility

A crucial factor towards the use of graphene and GO in any biological application is their biocompatibility. Herein, the intended use of the GBM defines the prerequisites for its biocompatibility.[81] For example, in drug delivery, the GBMs should transport the drug to the desired location, followed by excretion, directly or indirectly *via* degradation. Conversely, implants require the GBM not to degrade or delaminate from the implant while in contact with the body. Since the graphene-bio research is in its infancy, there are no studies about the long-term response of the human body to GBMs. Existing reports about the responses of rats and mice to GBMs are conflicting: Cytotoxic and inflammatory effects were reported, as well as a harmless urinary excretion.[82–84] For example, a study involving a retinal graphene implant showed no cytotoxic effects during 90 days in rats.[85] These conflicting results may originate from different material properties in the studies. Indeed, surface chemistry and reactivity, agglomeration, thickness and lateral dimensions, as well as the presence of biomolecules and chemical contamination, were reported to affect the cytotoxicity of GBMs.[81,86] The abovementioned properties are highly affected by the production of the material: A graphene layer transferred to another substrate with poly-methyl methacrylate (PMMA) could be cytotoxic or proinflammatory due to PMMA residues.[87] For GO flakes, the extent of oxidation and proportions of the oxygen-containing functional groups are not homogeneous for the most common synthesis routes.[88] Thus, when considering biological applications of graphene and GO, the biocompatibility prerequisites should be taken into account and tested at an early stage for each specific GBM. The research regarding the biocompatibility of GBMs and the effects of their properties towards safe devices for medical applications, such as neural interfaces, is ongoing.[86,89,90]

1.3.4.2   Graphene-neuron interface

The communication inside and between neurons relies on electrical and chemical signals (see section 1.1.1). Due to the high charge carrier density and mobility of graphene, it is a promising material to construct a neuronal interface, which measures and transduces the neuronal signals in order to record or stimulate brain activity. In 2017, the brain activity of rats was recorded with a solution-gated GFET array *in vivo* by placing the device on the brain tissue.[5,91] Meanwhile, this device has been tested in a sheep and the first human clinical trials are scheduled for late 2023.[92-94] This will be the first contact of a human with a graphene-based neural interface. While these results move towards whole-tissue recording with millimeter-sized devices, cell and molecular-level studies investigate the effects of graphene on a few neurons and their environment at the graphene-neuron interface. It was reported that a single-layer graphene surface can modulate the excitability of attached neurons, presumably by trapping cations at the surface.[95] Additionally, it was shown that graphene and GO-based surfaces in cell cultures enhance the differentiation of stem cells into neurons.[96,97] To obtain the differentiated neurons on graphene, the surface was functionalized noncovalently with laminin, a protein ubiquitous in the neural ECM.[96] It was found that the laminin-related receptors were significantly upregulated on the graphene surface compared to the control surface. The differentiated neurons on graphene were successfully stimulated by applying a voltage through the graphene surface and the laminin layer. These results highlight (i) the sensitivity of the neurons to their environment and (ii) the possible current transmission through the protein layer. Indeed, protein immobilization on graphene devices is beneficial for neuronal interfaces and cell cultures, and fundamental in graphene-bio interfaces in general.

1.3.5   Protein immobilization on graphene and graphene oxide

Proteins are biomolecules consisting of at least one peptide chain, which consists of many covalently bonded amino acids.[8] The amino acid sequence is specific for each protein and defines the secondary and tertiary structure of the protein, i.e., the folding and interactions between distinct amino acids or peptide chains, respectively. The most common secondary structure motifs in proteins are the α-helix and the parallel and antiparallel β-sheets (FIGURE 6). Proteins are ubiquitous in living organisms and the basis of biological processes. Upon certain chemical, optical or electronical signals, the secondary or tertiary structure of a protein can change to activate or deactivate its function. Protein functions include catalysis, which is essential for digestion and energy production in living organisms. Another protein family, the laminins, is present in the ECM and act as a bridge between the cell surface and other ECM components while simultaneously regulating several cell activities.[98] Due to their abundance in the human body, proteins are highly interesting for research towards graphene-bio interfaces.

In this chapter, approaches for protein immobilization on graphene and graphene oxide will be reviewed together with the material's effect on the biological function of the proteins. In the end, the catalytic cycle of horseradish peroxidase (HRP), the model enzyme used in this project, will be explained.
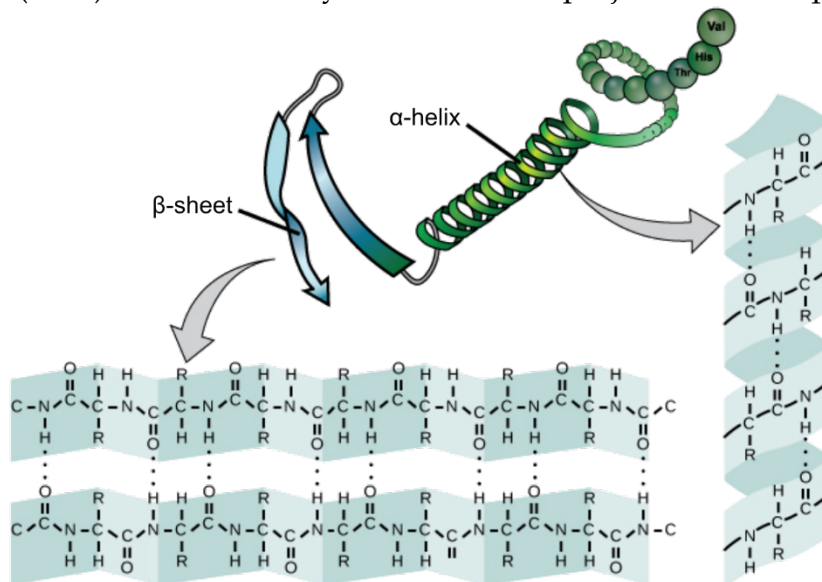

FIGURE 6   Two of the most common secondary structure motifs in proteins: the antiparallel β-sheet and the α-helix. Adapted with permission by The School of Biomedical Science Wiki.[99]

1.3.5.1   Immobilization strategies

Generally, the immobilization of proteins on GBMs can be divided into two approaches: covalent and noncovalent. Covalent approaches often include linker molecules for a controllable reaction and conservation of the natural protein structure.[48,49] Graphene oxide provides distinct functional groups that can react with the linker molecules. In contrast, pristine graphene lacks functional groups, and the covalent functionalization with linker molecules is limited. For electronic devices, the effect of covalent bonding on the electronic structure of graphene needs to be considered. By forming a covalent bond between a linker molecule and a carbon atom from the graphene lattice, the hybridization changes from sp^2 to sp^3 and the delocalized π electron system gets locally perturbated, which affects the band structure of graphene.

Noncovalent immobilization offers an alternative method that retains the intrinsic properties of graphene. The physical adsorption of biomolecules on pristine graphene is mainly based on the hydrophobic effect and π interactions.[100,101] The π interactions can occur in distinct orientations, such as face-to-face, parallel displaced and edge-to-face (FIGURE 7a).[102] Graphene offers a surface full of π orbitals, which can interact with the π orbitals and hydrogen atoms of the aromatic amino acids in proteins: phenylalanine, tyrosine and tryptophan (FIGURE 7b-d). Another commonly used approach for immobilizing proteins on graphene is semi-covalent:[103–105] Pyrene-based linker molecules (FIGURE 7e) are covalently bound to the protein. The immobilization event itself

is based on π-π stacking between the pyrene group and the graphene surface. By using these nondestructive immobilization methods, the electronic structure of graphene stays nearly intact.
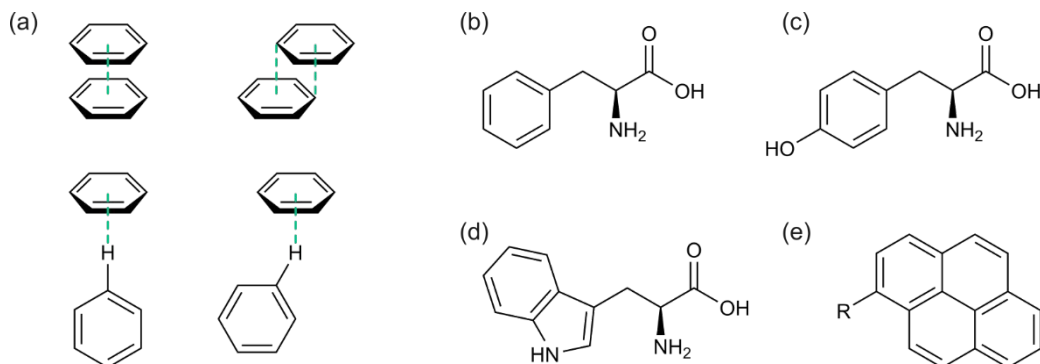

FIGURE 7   (a) π interactions: face-to-face and parallel-displaced (top) and edge-to-face configurations (bottom). Structures of the aromatic amino acids: (b) phenylalanine, (c) tyrosine and (d) tryptophan. (e) The structure of the pyrene group with "R" indicating the position for possible functionalization.

GO provides docking platforms for the π interactions with proteins through its sp^2 domains (FIGURE 4e). However, due to the various polar functional groups in the material, it additionally promotes electrostatic interactions between, for example, its negatively charged carboxylate moieties and positively charged amine groups in a protein.[106] Hydrogen bonds between the oxygen or hydrogen atoms on GO and hydrogen or oxygen/nitrogen atoms in a protein, respectively, are likely to be present as well. These interactions are also common in proteins in their natural form. Therefore, noncovalent protein immobilization is relatively easy on GO.[8] In fact, many different proteins have been successfully immobilized on GO flakes *via* simple incubation, such as HRP,[47] albumins,[107,108] and catalase[109]. As the interactions form on polar groups, the pH environment during the immobilization may affect the result due to changes in charge state of the functional groups.[107] Similar to pristine graphene, the electronic structure of GO stays nearly intact during the noncovalent immobilization of proteins.

    The noncovalent interactions between 2PO graphene and proteins are expected to be similar. Though the material is missing carboxylic acid groups almost completely[54] – and thus all interactions formed by these groups – hydrogen bonds can be obtained through interactions between proteins and hydroxyl or epoxide groups of the 2PO surface.

1.3.5.2   Effects on the protein structure and function

As explained above, the electronic structure of GBMs is retained during noncovalent immobilization of proteins. However, conformational changes might be induced to the immobilized proteins upon adhesion, as shown in several studies.[100,101,109,110] The proteins change their conformation to achieve a stable structure on the GBM surface. For example, bovine fibrinogen aligns its aromatic moieties to facilitate π-π stacking with graphene.[101] Interestingly, both

experimental and computational studies reported a partial loss of the α-helix secondary structure motif upon noncovalent immobilization on graphene.[70,100,109,110] This indicates that the α-helix is more sensitive to the graphene-protein interactions than the β-sheet motifs.

The structure of a protein is closely related to its function. Disturbances during the initial intracellular folding process of a protein can lead to a loss of the protein function.[111] A change in the protein function upon immobilization on graphene and GO is likely because of the reported structural changes induced by the GBMs.[100,101,109,110]

The easiest way to examine the function of a protein is to immobilize an enzyme and test its function. Enzymes are proteins that catalyze reactions.[8] To do so, they bind a substrate molecule and perform their specific reaction. For example, HRP can oxidize a variety of substrates by consuming hydrogen peroxide, H_2O_2, *vide infra*. If the substrate and the product of an enzymatic reaction have different properties, such as a shifting absorption maximum, the reaction can be monitored and verified easily. With this approach, the effect of GBMs on the biological function of enzymes can be investigated. HRP, when semi-covalently immobilized on a pristine graphene surface, has a lower catalytic activity than the free enzyme in the solution.[103] In contrast, glucose oxidase was more active on the graphene surface than in the solution. These opposing effects were attributed to more significant graphene-induced conformational changes in the predominantly α-helical enzyme HRP compared to the α-helix and β-sheet containing glucose oxidase. The catalytic activity of catalase immobilized on GO flakes decreases with an increasing relative GO concentration.[109] The effect was attributed to conformational changes in the α-helices during the adhesion event and to the interference of GO functional groups with the electron transfer during the catalyzed reaction.

Overall, the effects of graphene and GO on noncovalently immobilized proteins can be extensive and affect the catalytic activity of enzymes. The effects of 2PO graphene were expected to be similar but remained to be studied.

1.3.5.3   The catalytic function of horseradish peroxidase

HRP type C is a well-studied, affordable enzyme used in various biochemical methods to detect proteins and H_2O_2.[112] It is a monomeric, 44 kDa molecule that catalyzes the oxidation of various organic molecules with H_2O_2 as an oxidizing agent.[103] The often-colored products are easily detectable through absorption measurements. HRP is often used as a model enzyme for studies concerning H_2O_2 and biosensors. It has been immobilized on pristine graphene and GO flakes before, which affected its catalytic activity (see above).[103,113]

To understand the possible impact of immobilization on the catalytic activity of HRP, a thorough understanding of its structure and the catalytic cycle is necessary. The peptide chain of HRP folds into ten α-helices and one short antiparallel β-sheet, all connected by unfolded sequences of the peptide chain (FIGURE 8a). Additionally, two calcium ions and one heme molecule are located in the 4.0 nm x 4.4 nm x 6.8 nm enzyme.[112,114] The heme is the active site of HRP,

where the oxidation of the substrates happens, and consists of a porphyrin ligand that coordinates one iron atom in a square planar geometry.[115] It is located in the center of the enzyme, surrounded by several amino acid residues that contribute to coordination bonds during the catalytic mechanism. In the ground state, the Fe(III) is bound to one nitrogen atom of a histidine residue from the HRP peptide chain, which produces a pentacoordinate state.

During the first step of the catalytic cycle (FIGURE 8b), a H_2O_2 molecule reacts with the Fe(III) ground state, resulting in a change in the iron's oxidation state and radical formation.[115] The product is Compound I, where Fe(VI) is bound to an oxygen atom (ferryl oxygen) and the porphyrin is a cationic radical. This species is stabilized by hydrogen bonds between the ferryl oxygen and the nitrogen atom of an HRP arginine residue and a water molecule. The following two steps reduce the enzyme's active center back to the ground state *via* the formation of Compound II, using a reducing substrate. In Compound II, the Fe(IV) is bound to an oxygen atom similar to Compound I. However, the cationic porphyrin radical is no longer present, and a proton interacts with the ferryl oxygen. Finally, in the last step, the iron atom is reduced back to Fe(III) by another reducing substrate and a water molecule is formed with the ferryl oxygen. While the oxidation of the active site is one two-electron process, the reduction consists of two one-electron reactions. Thus, the reducing substrate is oxidized by one electron at a time, and one HRP catalytic cycle can oxidize two substrate molecules.

Several amino acid residues of the HRP peptide chain stabilize the active center throughout the catalytic cycle of HRP.[115] The enzyme is prone to structural changes upon the immobilization on pristine and 2PO graphene and GO because it consists almost only of α-helices. This property and the easily detectable activity make HRP an interesting candidate to study the effects of 2PO on the immobilized enzyme.
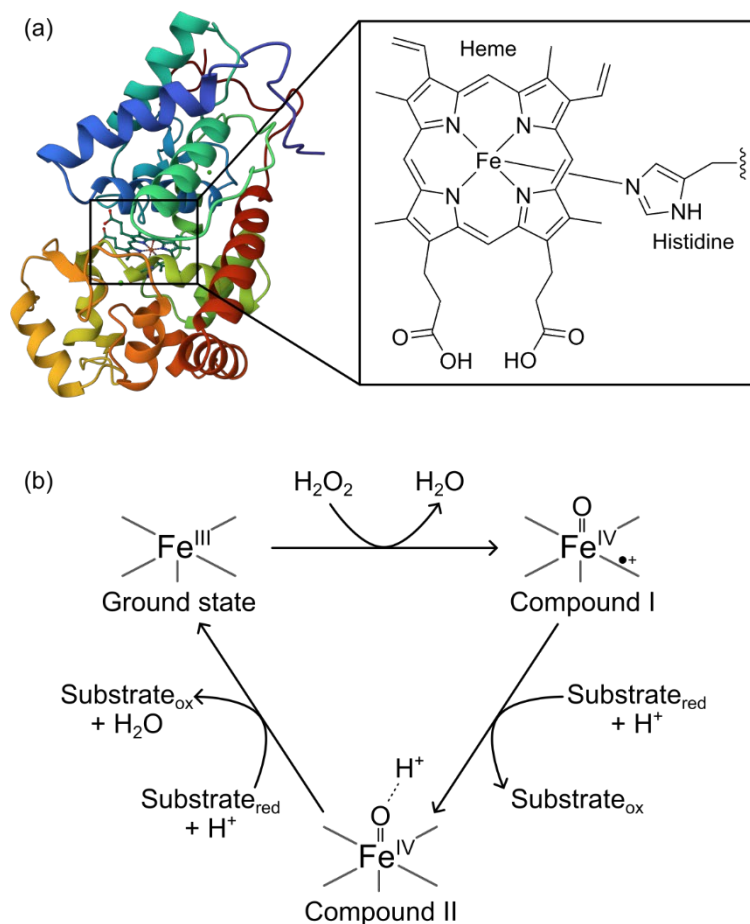
FIGURE 8   The model enzyme HRP: (a) Crystal structure of HRP[116–118] and chemical structure of the active center. (b) Catalytic cycle of HRP. For clarity, only the iron atom of the active center is shown. The grey lines indicate the coordination bonds to the nitrogen atoms of the porphyrin ligand and the histidine residue of the peptide chain.

1.3.6   The effects of graphene on self-assembled structures

The combination of graphene and LMW hydrogels is interesting because of graphene's outstanding properties and the gels' potential in biological applications. The self-assembly of organic and biological molecules can be affected by a surface (see section 1.2.2). Similar effects have been shown for graphene and GO, either in the form of a surface or as flakes inside a solution, i.e., many small surfaces. For example, a nature-inspired peptide self-assembled on a pristine graphene surface into a monolayer with specific orientations that followed the graphene lattice.[119] The protein silk fibroin selectively self-assembles into fibers on pristine graphene flakes when they are present in the solution.[120] The amyloid beta protein fibrillation, known to cause Alzheimer's and Parkinson's diseases, is inhibited on GO flakes.[121] Presumably, GO restrains the formation of specific protein secondary structures *via* noncovalent interactions with the protein.[122] Additionally, GO flakes were shown to tune the mechanical properties of a biocompatible peptide amphiphile supramolecular

hydrogel without affecting the self-assembly itself.[123] In other systems, GO flakes act as cross-linkers between LMWGs.[124,125]

The reported results demonstrate partially serious effects of GBMs on self-assembly processes. However, a direct comparison between pristine and oxidized species would be interesting to understand better the noncovalent interactions between the GBM and the self-assembling species.

1.4   Aims of this project

This research project contributes to the development of neuronal interfaces based on pristine and 2PO graphene. As explained in the previous chapters, neurons are sensitive to their environment, including proteins and viscoelastic properties. To create a growth-promoting interface, two approaches were followed:
1. Protein immobilization: A layer of protein on a surface can promote cell growth and proliferation to achieve connections between the surface and the neurons. Neuroreceptor proteins detect concentration changes of neurotransmitters and could enhance the communication between the graphene surface and the neuron.
2. ECM mimic: A material with a similar stiffness as the brain on the graphene surface could support the neuronal network until it secretes its own ECM.

The research project is focused directly on the graphene-based surface, where the molecular interactions with the biological or biomimetic components happen. As the development of devices with 2PO graphene is still in its infancy, model biological and biomimetic components were selected. They are well-studied so that the results could be easily compared with the existing literature. These model systems allow predictions for surface-related effects on other proteins and LMWGs.

The surfaces used during this work were pristine and 2PO graphene, adjacent to each other on Si/SiO_2 substrates and GO flakes (FIGURE 9). They differ in their hydrophobicity and may interact differently with the immobilized species through, for example, π-π stacking and hydrogen bonding. Two proteins and one LMWG were studied to gain a deeper understanding of the molecular interactions between GBMs and biological or biomimetic systems:
*   Horseradish peroxidase: effects of graphene and 2PO graphene surfaces on the HRP immobilization and its catalytic activity.
*   Bovine serum albumin: effects of graphene and 2PO graphene surfaces on the BSA immobilization.
*   Fmoc-phenylalanine (Fmoc-Phe): effects of graphene and 2PO graphene surfaces and GO flakes on the supramolecular self-assembly in Fmoc-Phe hydrogels.

In conclusion, the effects of pristine and 2PO graphene surfaces and GO flakes on the biological and biomimetic model systems were studied in this project.

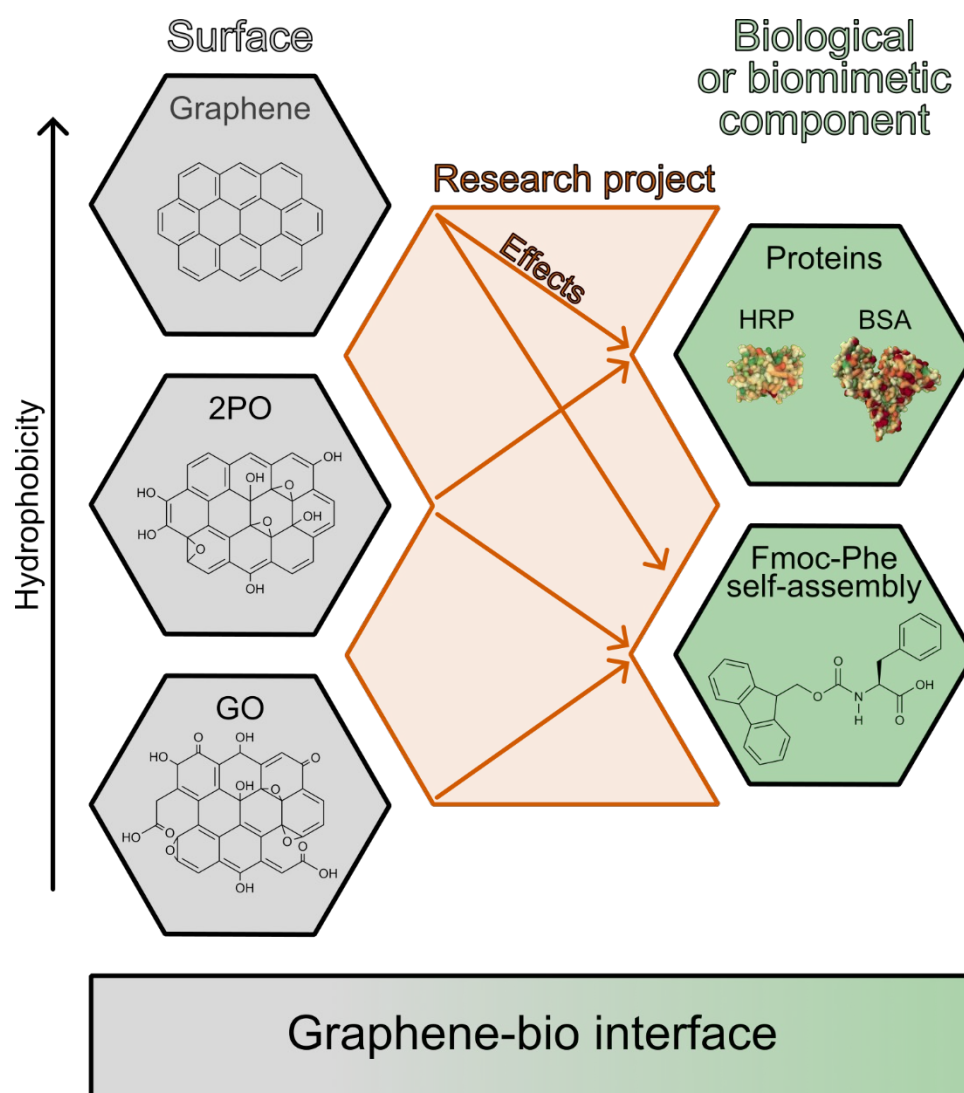Herein, 2PO graphene surfaces were studied with regard to graphene-bio interfaces for the first time.

FIGURE 9   Schematic illustration of the research project (orange) towards graphene-bio interfaces.

2 METHODS

This chapter describes the main analytical methods used during this project. At first, the use of spectroscopic techniques, namely Raman spectroscopy and absorption spectroscopy in the ultraviolet-visible (UV-vis) and infrared (IR) spectral region, will be briefly described, followed by AFM and scattering-type scanning near field optical microscopy (s-SNOM).

2.1 Spectroscopy

Generally, spectroscopy uses the interaction between electromagnetic radiation and matter to obtain information about the chemical structure, polymorphism, crystallinity and molecular interactions of a sample. By varying the excitation wavelength, different rotational, vibrational or electronic transitions can be initiated. The transmitted or scattered light is detected, providing the abovementioned information. Raman, IR and UV-vis spectroscopy were used in this work, the underlying transitions of which are presented in FIGURE 10.
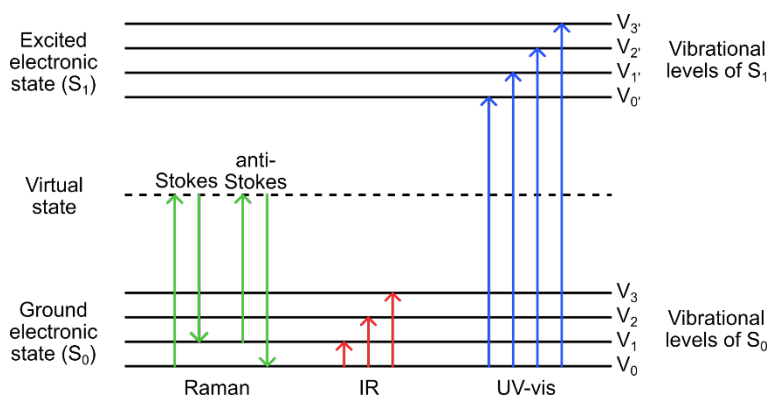

FIGURE 10   Jablonski diagram showing examples of transitions involved in Raman, IR and UV-Vis absorption spectroscopy.

2.1.1 Raman spectroscopy

During this project, Raman spectroscopy was used to study pristine and 2PO graphene surfaces before and after protein immobilization and GO flakes, either pure or incorporated in a supramolecular hydrogel. The prominent Raman bands of the graphene derivatives and the underlying processes are explained in section 1.3.3.1. A commercial (Thermo Scientific DXR Raman) and a homebuilt Raman microscope were used, both with an excitation wavelength of 532 nm. The experimental details can be found in articles **I-IV**.

2.1.2 Infrared spectroscopy

IR spectroscopy was used to characterize GO flakes, Fmoc-Phe powder, and their native and hybrid hydrogels (article **III**). The method detects molecular vibrations in the form of absorption bands, which are sensitive to hydrogen bonding. Thus, it allowed us to study the supramolecular structure of the hydrogels. Additionally, the IR spectrum of the buffer salts used in article **IV** was recorded to identify crystals on the graphene surface samples. All spectra were taken on a Fourier transform IR spectrometer in attenuated total reflectance mode (Bruker Tensor 27 FT-IR). The experimental details can be found in articles **III** and **IV**.

2.1.3 UV-vis spectroscopy

A plate reader (Tecan Spark multimode) was used to record absorption spectra in the UV-vis spectral range (wavelength 200 nm to 800 nm) to monitor the HRP-catalyzed oxidation of a substrate with absorption maxima in this wavelength range. Upon oxidation, the substrate's absorption maxima shift, allowing us to follow the reaction. One spectrum was recorded every 30 seconds from the start of the reaction. The corresponding reaction rate was calculated by plotting the absorption intensity maximum of the oxidized substrate against the reaction time and applying a linear fit to the curve. The experimental details can be found in article **II**.

2.2 Microscopy

Microscopy is a powerful and important technique to analyze surfaces. During this project, several microscopic methods were used, out of which AFM and s-SNOM will be described below.

2.2.1 Atomic force microscopy

The principles of AFM and its importance for graphene surface research are explained in section 1.3.3.2. In this project, AFM was employed to assess the

cleanliness of graphene samples, to measure the height of pristine and 2PO graphene, to characterize the 2PO areas topographically and to analyze protein immobilization and supramolecular hydrogels on the surfaces. All AFM images were recorded with a Dimension Icon AFM (Bruker) in the PeakForce Tapping® mode, using silicon nitride cantilevers (Bruker ScanAsyst-Air). The experimental details are described in articles **I-IV**.

2.2.2 Scattering-type scanning near-field optical microscopy

S-SNOM is a relatively new technique, which is based on an AFM operating in tapping mode (see section 1.3.3.2). Additionally to the AFM laser that reflects on the cantilever and is used to detect the oscillation of the cantilever, another laser, such as a mid-IR (MIR) laser (FIGURE 11a), points to the tip apex. This laser induces a plasmon mode in the tip that extends ≈ 10 nm from the apex, creating a near-field with enhanced field strength compared to the far-field, which leads to an enhanced interaction with molecules. The plasmon mode leads to a dipole in the tip apex, which again induces a mirror dipole in the sample.
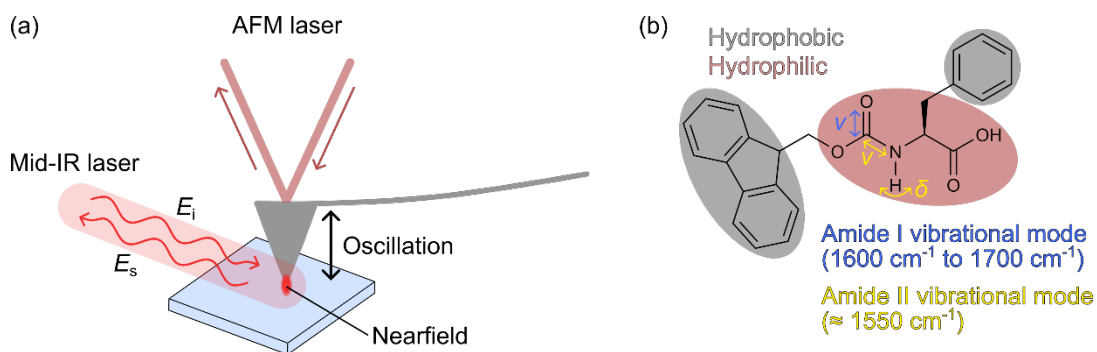

FIGURE 11 (a) Schematic representation of an s-SNOM with the energy of the incident light E_i and the energy of the scattered light E_s. (b) The structure of the LMWG Fmoc-Phe with indicated hydrophilic and hydrophobic regions and stretching (ν) and bending (δ) vibrations responsible for the amide I and II modes in IR absorption.

The wavelength of the laser pointing to the tip apex used in this work was in the MIR spectral region, with wavenumbers between 1500 cm^{-1} and 1750 cm^{-1}. The samples were supramolecular fibers constituting of Fmoc-Phe (FIGURE 11b), which contains aromatic rings, as well as an amide and a carboxylic acid group. These functional groups vibrate upon irradiation in the abovementioned frequency range, which leads to a change in their dipole moment. In the s-SNOM, the created dipole in the tip apex interacts with the dipole in the sample. Depending on how strongly the sample is excited by the laser, the nearfield between the tip and the sample changes. Then, functional groups that absorb the wavelength of the laser change the near-field signal to a larger extent. Thus, s-SNOM can detect IR absorption. However, in contrast to a standard IR spectrometer, the lateral resolution is similar to an AFM.

The MIR light is scattered back from the tip apex and contains near-field and far-field contributions. The near-field signal strongly depends on the tip oscillation, while the far-field signal is not affected. Based on this difference, the signal undergoes careful background suppression *via* demodulation techniques to extract the absorptive and reflective properties of the sample. There are two possibilities for measurements. One option is that after choosing a specific laser frequency, an image can be recorded at this resonant excitation, similar to standard tapping mode AFM. Additionally to the topography, the absorptive and reflective properties can be visualized with s-SNOM. The other option is to choose one location on the sample and irradiate it with a broadband laser to measure a nano-FTIR spectrum. This spectrum resembles a standard IR spectrum and can be interpreted accordingly. All results obtained from an s-SNOM are relative to a reference background, which is usually the sample substrate.

In this work, an s-SNOM (Neaspec neaSNOM) with integrated MIR imaging and nano-FTIR spectroscopy modules and Pt/Ir-coated silicon tips were used to characterize the supramolecular structure of the Fmoc-Phe hydrogel on pristine and 2PO graphene surfaces. The experimental details can be found in article **IV**.

3 RESULTS AND DISCUSSION

In this chapter, the results from the articles **I-IV** are presented and discussed in the broader context of the thesis. According to the project aims defined in section 1.4, the two functionalization approaches are presented: First, the protein immobilization on pristine and 2PO graphene surfaces, and subsequently, the effects of the graphene surfaces and GO flakes on the Fmoc-Phe self-assembly. Experimental and computational details can be found in the articles **I-IV** and the corresponding supplementary information.

3.1 Functionalization of graphene surfaces with proteins[I, II]

One approach to increase the interactions between graphene and neurons was immobilizing relevant proteins on the graphene surface. In articles **I** and **II**, the effects of 2PO graphene surfaces on the noncovalent immobilization of the model proteins HRP and biotinylated BSA (b-BSA) and on the catalytic activity of HRP were tested. Though these proteins are not related to neuron signal transduction, they are well-studied and provide a good basis for understanding interactions between the surface and proteins.

3.1.1 Noncovalent immobilization of selected proteins[I, II]

The noncovalent functionalization of graphene with proteins has the advantage that no defects are introduced to the sp^2 graphene lattice through covalent bonds. However, the protein binding site is not necessarily the same for each protein, and it is more difficult to control the functionalization compared to the covalent approach.

In the experiments, Si/SiO_2 microchips with a single-layer graphene surface were incubated in protein solutions with different protein concentrations and varying incubation times. These samples contained both pristine graphene and 2PO graphene with distinct levels of oxidation. After the incubation, each

microchip sample was washed with buffer to remove unbound protein and subsequently with deionized water to remove buffer salts. The samples were analyzed before the incubation and after drying at room temperature.

3.1.1.1 Selectivity

AFM was used to inspect the topography of the samples prior to the immobilization of HRP and b-BSA. The oxidized areas were visible as elevated squares (FIGURE 12a-b). The protein concentration during the incubation was $10~\mu g \cdot ml^{-1}$ for both HRP and b-BSA, and the incubation time was one hour. After the protein immobilization, the HRP samples were analyzed by AFM again, while b-BSA was labeled for confocal fluorescence microscopy.

In general, HRP and b-BSA were immobilized on pristine and 2PO graphene. HRP was detected all over the surface in the AFM topography image as higher features when compared to before the protein immobilization (FIGURE 12a,c). The green color all over the pristine and 2PO areas in FIGURE 12d verifies that b-BSA is also immobilized on both surfaces. The AFM cross sections showed an increased height difference between the pristine and 2PO areas after protein immobilization (FIGURE 12e), which demonstrated that more HRP was immobilized on the oxidized areas than on the pristine graphene, relative to the surface area. There were between one to four layers of HRP on the 2PO areas. For b-BSA, a similar conclusion could be drawn from the cross-section of the confocal microscope image (FIGURE 12f). The green signal originated from the fluorescent label of b-BSA and was stronger in the 2PO areas.

Generally, a selective immobilization of the two proteins towards the 2PO areas was observed for the abovementioned incubation conditions. The underlying noncovalent interactions presumably caused the selectivity. Both proteins contained hydrophilic and hydrophobic amino acid residues, i.e., they could interact with the hydrophobic pristine and hydrophilic 2PO surface. The observed selectivity, however, indicated that interactions with the 2PO surface – possibly *via* hydrogen bonding – led to an energetically more favorable formation compared to the pristine surface. Here, π-π stacking was assumed to be the main interaction type. Once the first protein layer was immobilized, several more HRP layers were deposited on 2PO graphene. Thus, the preferential binding site for the following layers seemed to be the first protein layer on 2PO graphene.
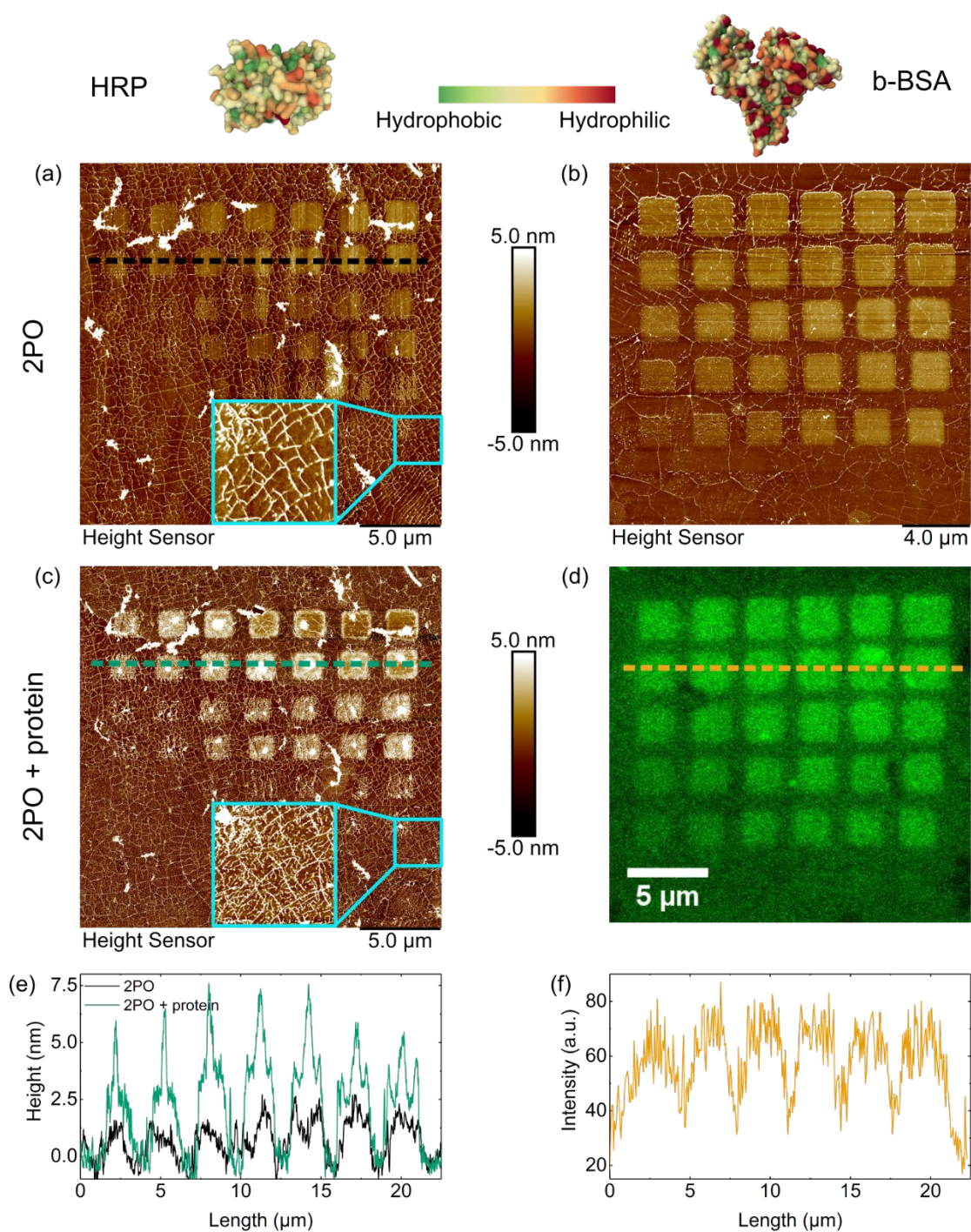
FIGURE 12   AFM and confocal microscopy results from the noncovalent immobilization of HRP (left) and b-BSA (right): AFM topography images after 2PO from sample 1 (a) and 2 (b), (c) AFM topography image of 1 after HRP immobilization, (d) confocal microscopy image of 2 after b-BSA immobilization and fluorescent labelling, (e) height cross-section from 1 before (black) and after (green) HRP immobilization as indicated in (a) and (c), (f) intensity cross-section from the confocal image of 2 as indicated in (d).

3.1.1.2   Effect of the oxidation level

By taking a closer look at FIGURE 12c, it is obvious that the HRP is immobilized in different patterns on the individual 2PO areas. Indeed, each 2PO square on this sample was prepared under distinct 2PO conditions and the oxidation level, i.e., the amount and nature of the functional groups, might have been different. The analysis in the following two paragraphs is based on data from article **I** but has been improved based on the current knowledge.

To compare the immobilization patterns of HRP between the oxidation levels, the 2PO areas were initially be sorted according to their oxidation levels, which were deduced from Raman spectra. Therefore, the Raman spectra of seven selected 2PO areas before HRP immobilization (FIGURE 13a) were analyzed. The I_D/I_G ratios, 2D band intensities and width of the G band were extracted from the spectra because they indicated the quantity of defects (= oxygen functionalization) and the lattice disorder (TABLE 1).[56,65–67] With an increasing oxidation level, the lattice disorder increased, leading to a decrease of the 2D band intensity. The 2PO areas have been arranged accordingly, with the most intense 2D band for 2PO labeled area 1 and the weakest one for the 2PO labeled area 7. By increasing the oxidation level, the I_D/I_G ratio of the 2PO areas should initially increase to a maximum, followed by a decrease to a certain level. This progression could be observed in our measurements (2PO area 1 to 7). Finally, the G band should broaden at higher oxidation levels because the lattice disorder increased, which could also be observed in our measurements. Thus, the oxidation level presumably increased from 2PO area 1 to 7.
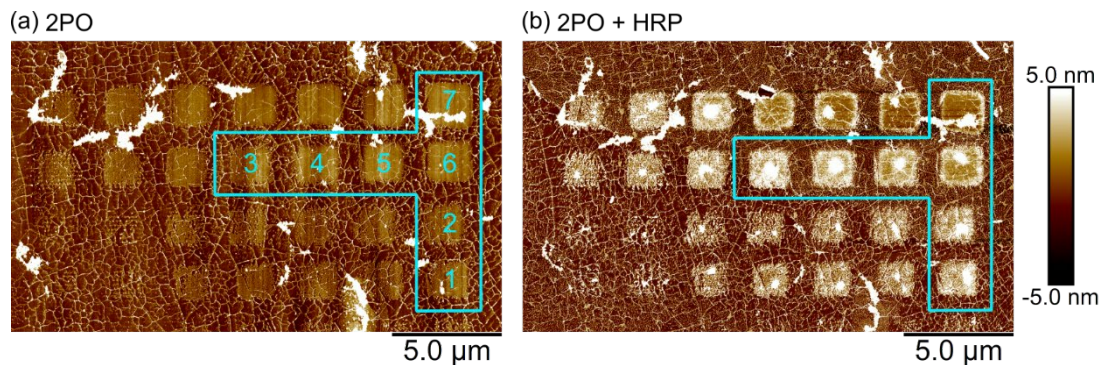

FIGURE 13   AFM images of the selected 2PO areas 1 to 7 before and after HRP immobilization for the analysis of the HRP adsorption based on the oxidation level.

TABLE 1   Comparison of HRP adsorption at different oxidation levels: Intensity (I) of the 2D band, I_D/I_G ratios and width w of the G band extracted from the Raman spectra before HRP adsorption and a description of the HRP adsorption behavior.

2PO area	I_{2D} (a.u.)	I_D/I_G	w_G (cm^{-1})	HRP adsorption
1	1.01	1.3	34.4	whole 2PO area + agglomerate in the center (1)
2	0.94	1.8	29.8	whole 2PO area + agglomerate in the center (1)
3	0.62	2.0	35.4	whole 2PO area + agglomerate in the center (1)
4	0.50	1.9	44.5	edge + agglomerate in the center (1)
5	0.35	1.7	45.6	edge + agglomerate in the center (2)
6	0.33	1.6	45.6	edge + agglomerate in the center (2)
7	0.29	1.7	63.6	edge + agglomerate in the center (2)

The HRP adsorption behavior (FIGURE 13b) could be roughly divided into two groups: group 1 showing HRP immobilization in the whole 2PO area, and group 2, where HRP immobilized mainly at the edges of the 2PO areas. For both groups, HRP agglomerates were found in the center of the 2PO area. Interestingly, the groups followed the oxidation level. HRP immobilized in a group 1 pattern for the three lowest oxidation levels (1-3). Group 2 was observed for the four 2PO areas with the higher oxidation levels (4-7). Indeed, there was no clear-cut difference between the two groups, but rather a smooth transition. For example, moving step by step from area 4 to 7, the selectivity towards the 2PO area edge became clearer.

The reason for the changing immobilization behavior could be the distinct quantities and nature of the functional groups in the 2PO areas. The lower oxidation levels were expected to contain only epoxide and hydroxyl groups. These groups also dominated the 2PO areas with higher oxidation levels, but in a greater quantity, and carboxylic groups could be present as well. At the edge of the 2PO areas, the oxidation level might have been lower than in the center because there were fewer overlapping laser spots during the 2PO. Additionally, the graphene could have started to ablate in the center of the high-oxidation-level areas. The observations indicated that HRP interacted more strongly with epoxide and hydroxyl groups and was sensitive to their concentration on the surface. These results highlighted the oxidation level as a parameter towards tuning protein immobilization on 2PO graphene.

3.1.1.3   Effect of the protein concentration and incubation time

In order to study the effect of incubation time on the immobilization of HRP on pristine and 2PO graphene, we measured samples incubated at a lower HRP concentration (2.5 µg · ml^{-1}) for zero, three, and six hours in three-hour incubation

steps. The AFM images showed that with an increasing incubation time, the amount of immobilized HRP also increased (FIGURE 14a). During the first three hours of incubation, the average height difference between pristine and 2PO graphene changed from ≈2 nm to ≈4 nm (FIGURE 14b, black and blue cross-section). The HRP adsorption at this time was not homogeneous, as could be seen from the rough profile and the topography image. The protein seems to agglomerate on the surface, comparable to FIGURE 13b (center of the 2PO squares). After the second incubation (six hours of incubation in total), the profile of the 2PO areas was relatively smooth, and the height difference increased further to ≈10 nm (FIGURE 14b, red cross-section). This was equal to approximately two additional layers of HRP on the 2PO than on the pristine surface. After the initial formation of agglomerates, longer incubation times resulted in a more homogeneous HRP covering of the 2PO areas. By adjusting the HRP concentration and the incubation time, we were able to tune the homogeneity of the immobilized protein.
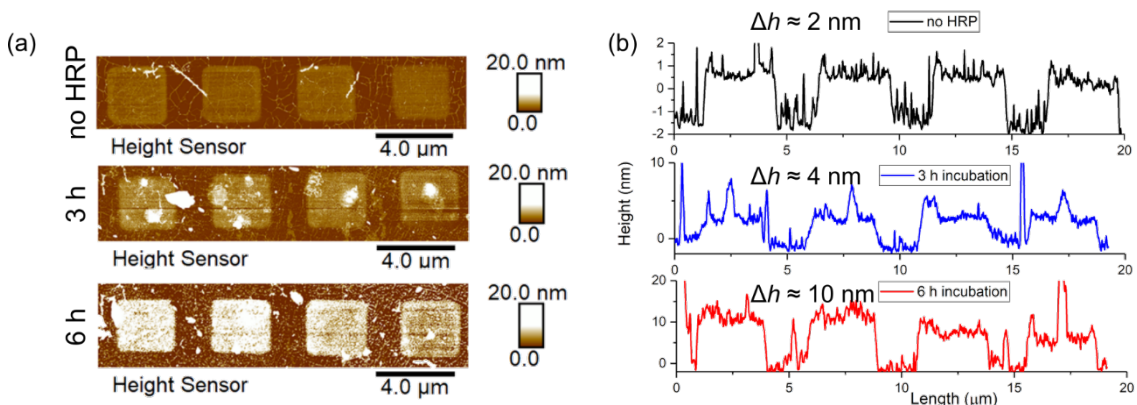

FIGURE 14   Effect of incubation time on the immobilization of HRP. (a) AFM topography images of the same 2PO areas before incubation (top) and after 3 h (middle) and 6 h (bottom) of incubation in the HRP solution. (b) Corresponding topographic profiles from the topography images in (a) with average height difference Δh between the pristine and 2PO areas. Reproduced from article **I** with permission from the Royal Society of Chemistry.

3.1.1.4   Effects on the graphene surfaces

All abovementioned effects were focused on altering the properties of the graphene and how it affected the protein immobilization. However, the reverse could happen as well: the immobilized species on the graphene lattice can affect the properties of the graphene. By comparing the Raman spectra of 2PO graphene before and after the HRP immobilization, we found that all characteristic Raman bands were shifted lower (FIGURE 15). The band at ≈1000 cm^{-1} in all spectra originated from the Si substrate and did not shift, which verified that the observed shifts of the graphene bands were not due to measurement error. All our graphene samples were initially p-type doped because the annealing during the sample cleaning procedure enhanced the graphene-SiO_2 substrate conformity, and the interaction of graphene with SiO_2 induced p-type doping.[39] The overall doping remained p-type after the

oxidization. The observed shifts after the protein immobilization could indicate a decreased p-type doping, i.e., more electrons in the graphene lattice.[60,126] For all our samples, the doping remained p-type, even after the immobilization of HRP. The results indicated that the interactions between HRP and 2PO graphene led to electron-donation from the enzyme towards the graphene surface, for example *via* hydrogen bonding.
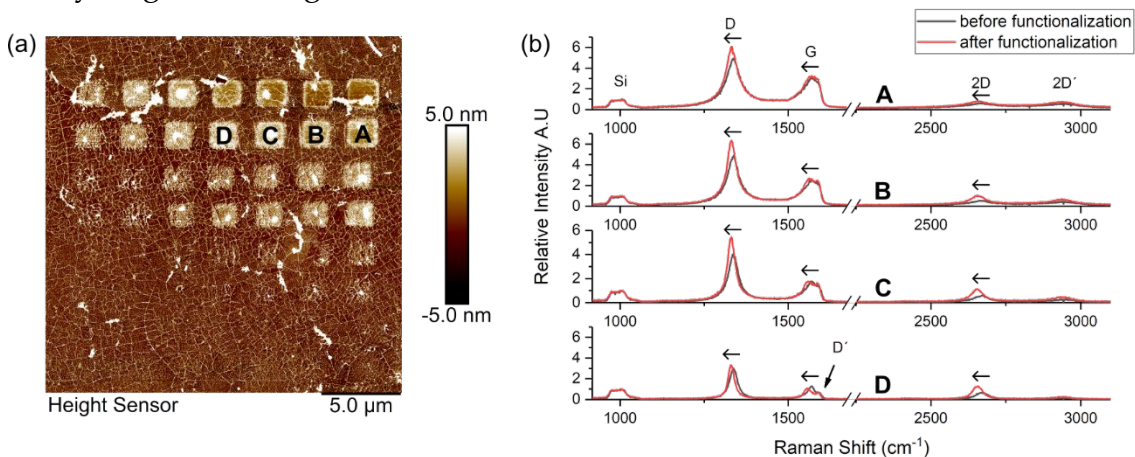

FIGURE 15 Effect of HRP immobilization on the electronic properties of 2PO graphene. (a) AFM topography image indicating the location of spectra A to D. (b) Raman spectra from positions A to D before (black) and after (red) HRP immobilization. The arrows indicate the direction of the G, D and 2D band shifts. Reproduced from article **I** with permission from the Royal Society of Chemistry.

In the presented studies, 2PO of graphene was demonstrated as a tool to tune the noncovalent immobilization of two proteins. For specific 2PO conditions, more HRP and b-BSA were immobilized on the 2PO areas compared to the pristine areas. However, there was no absolute selectivity, and both proteins adsorbed on both surfaces. By varying the oxidation level, the immobilization pattern on the individual 2PO areas could be tuned. With this noncovalent approach, initially one-to-four layers of HRP could be controllably immobilized (article **I**). In a later study (article **II**), we adjusted the HRP concentration and were able to refine the range to one-to-two layers, which suggested that at least every second HRP molecule is in direct contact with graphene. It has been shown that HRP electronically interacted with graphene by transferring electrons to the graphitic lattice. Thus, the structure and catalytic activity of HRP might be altered compared to the free enzyme in the solution.

3.1.2 Catalytic activity of immobilized HRP[II]

After demonstrating the tuning of HRP adsorption with the 2PO of graphene, the question of whether HRP retained its catalytic function after the immobilization remained open. An active HRP enzyme can catalyze the oxidation reaction of several chromophores, among which 3,3′,5,5′-tetramethylbenzidine (TMB) is a low-cost and non-dangerous option. The oxidation of TMB is a two-step process and the reduced form, as well as the intermediate charge-transfer-complex (CTC)

and the final product (TMB^{2+}) have characteristic bands in the UV-vis absorption spectrum (FIGURE 16a).[127] Here, HRP was initially immobilized on pristine (P), half-2PO (H) or full 2PO (F) graphene samples (FIGURE 16b). Afterwards, the oxidation of TMB catalyzed by HRP was monitored with a simple well-plate setup by measuring UV-vis absorption spectra (FIGURE 16c). To assess the stability of the samples, the measurements were performed on four consecutive days.
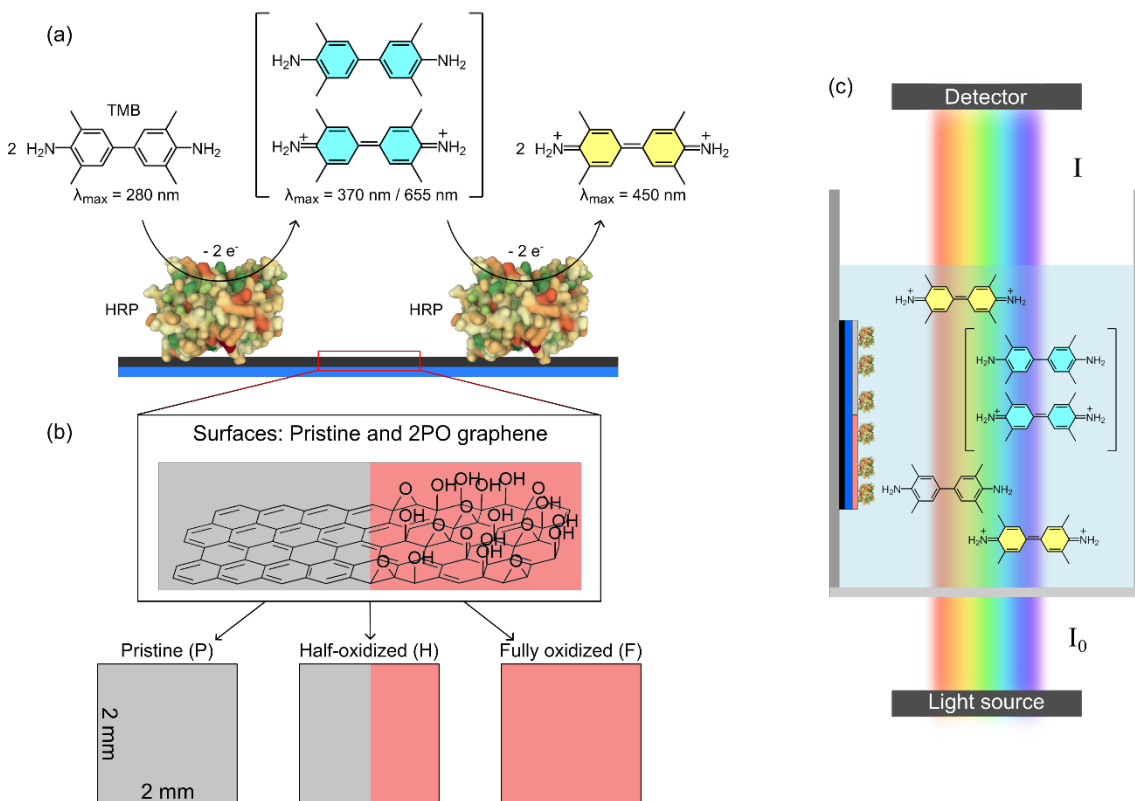

FIGURE 16   Schematic illustration of the study: (a) The oxidation of TMB catalyzed by im-mobilized HRP, including the absorption maxima of TMB, the intermediate CTC and the product TMB^{2+}. (b) Surfaces and sample geometry: Pristine sur-faces are highlighted in grey, 2PO surfaces in red. (c) Well-plate setup: the sample with immobilized HRP was mounted to the side wall of the well and the UV-Vis absorption spectra were measured from the surrounding solution. Adapted from article **II**.

Eight graphene samples were analyzed in total: three pristine (P1-P3), three half-oxidized (H1-H3) and two fully oxidized samples (F1, F2). After the addition of TMB and H_2O_2 to a well containing a sample, a UV-vis absorption spectrum was measured every 30 seconds. On the first day, immediately after the immobilization of HRP, every sample showed the characteristic bands of the TMB^{2+} and/or the CTC (FIGURE 17a-c). The reaction rate of the TMB oxidation for each sample was calculated from the increasing intensity of the 650 nm absorption band of the CTC because of its reduced overlap with the other bands. The reaction rates were the highest for the pristine samples, followed by the half-

oxidized and fully oxidized samples (FIGURE 17d). In the following days, the oxidation of TMB was detected only on the pristine samples, where it decreased over time (FIGURE 17e). On day 4, none of the samples showed catalytic activity. Three main results were concluded from this data: (i) The HRP was catalytically active directly after the immobilization on both pristine and 2PO graphene. (ii) With an increasing 2PO area, the reaction rate decreased. (iii) The reaction rates decreased over time.
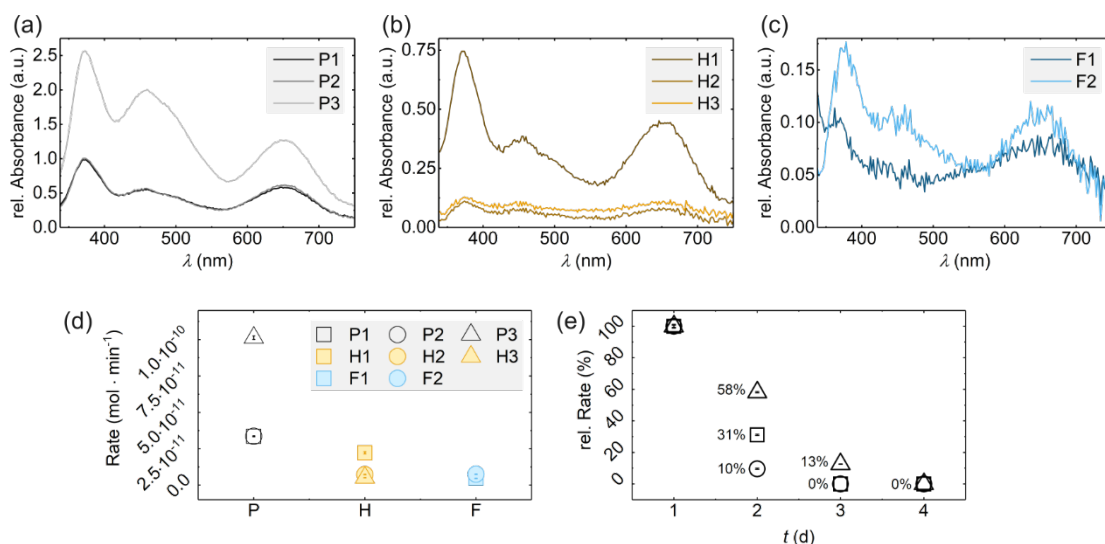

FIGURE 17   Main results for the catalytic activity of immobilized HRP: Absorption spectra from each sample 10 minutes after substrate addition for pristine (P, (a)), half-2PO (H, (b)) and full 2PO (F, (c)) samples. (d) Reaction rates for each sample on day 1 calculated from the 650 nm absorption band of the CTC. (e) Reaction rates over time for the pristine samples. The percentage indicates the rate relative to day one (=100%). The legend of (d) also applies to (e). Adapted from article **II**.

Each of the samples had distinct pristine and 2PO graphene-covered areas. To make the results of the absorption measurements more comparable, the mass of the immobilized HRP was estimated for each sample. AFM images were taken after scratching the samples to measure the height and estimate the number of protein layers. Also, the share of surface covered by HRP was considered and the resulting total masses of HRP on the samples varied between 4.41 ng and 19.94 ng (TABLE 2).

Additionally, a calibration curve was generated with free HRP in solution. The reaction rates of the free enzyme were plotted against the distinct, known masses of HRP in the solution. The calibration curve itself was generated by a linear fit through these values. By comparing the rate values of the calibration curve with the rates from the experiment on day 1, the activity of each sample was correlated with the comparable mass of the free enzyme (activity-correlated mass, TABLE 2). To further evaluate the performance of the samples compared to each other, the mass-normalized activity was calculated as the ratio of the activity-correlated mass to the total mass of HRP on each sample. The pristine samples showed up to 7.5% of the activity compared to the free enzyme. By

increasing the 2PO area, the percentage decreased to a maximum of 2.1% for half-oxidized surfaces and a maximum of 1.2% for fully oxidized surfaces.

TABLE 2   The total mass of HRP m_{HRP} on all pristine (P), half-oxidized (H) and fully oxidized (F) samples, the activity-correlated mass of HRP m_{acHRP} and the mass-normalized activity as a ratio of m_{HRP} and m_{acHRP}.

Sample	m_{HRP} (ng)	m_{acHRP} (ng)	Mass-normalized activity (%)
P1	4.41	0.33	7.5
P2	13.89	0.33	2.4
P3	19.94	0.96	4.8
H1	10.54	0.22	2.1
H2	9.99	0.09	0.90
H3	10.32	0.07	0.68
F1	16.33	0.06	0.37
F2	7.39	0.09	1.2

The results indicated an effect of the graphene surfaces on the catalytic activity of the immobilized HRP. Possible effects included the blocking of the active site by the surface or other enzymes. Blocking could have appeared on both surfaces in this noncovalent approach because the initial enzyme orientation might have been random. Thus, it could have contributed to the generally lower catalytic activity of the immobilized HRP compared to the free enzyme.

Also, surface-induced alterations of the secondary and/or tertiary structure of HRP could have occurred. These could have again led to changes of the molecular structure at the active site and could have hindered a successful catalytic cycle (see section 1.3.5.3). In fact, HRP is prone to these effects because it consists almost solely of α-helices, which have been reported to change their structure on pristine graphene.[70,100] In 2PO graphene, the carbon network is widely preserved. Hence, surface-induced structural changes could have also contributed to the lower catalytic activity of immobilized HRP on both surfaces. However, we observed a lower catalytic activity on 2PO when compared to pristine graphene. This indicated that the surface-induced structural alterations were more extensive on 2PO graphene. Obviously, pristine and 2PO graphene could have promoted different types of noncovalent interactions due to their distinct surface functional groups. Thus, we speculate that these different noncovalent interactions with HRP on the two surfaces changed the secondary and/or tertiary structure of the enzyme in different ways.

As a result, 2PO of graphene is not only a tool to tune protein adsorption but also protein function on a graphene surface. We have shown that the immobilization on pristine and 2PO graphene decreased the catalytic activity of HRP. Herein, increasing the 2PO area led to a lower reaction rate of the substrate oxidation, i.e., a lower catalytic activity. On all surfaces, the rate decreased over time. We attributed the effects to noncovalent interactions between HRP and the surfaces, which could alter the secondary and/or tertiary structure of the protein. The effect of 2PO on the protein function of the model enzyme HRP was significant. We believe that similar effects can be expected for other proteins,

including components of the extracellular matrix of neurons and neuroreceptor proteins.

In conclusion, by patterning a graphene surface with 2PO, it could be possible to selectively bind different proteins on one surface and tune their activity. Thus, the sensitivity of a GFET array to distinct neurotransmitters and the neuron-graphene communication could be tuned in a defined nanoscale pattern.

3.2 Effects of graphene surfaces and graphene oxide flakes on the self-assembly of Fmoc-Phe[III, IV]

The functionalization of graphene with a supramolecular hydrogel was the second goal of this project and aimed to provide an environment for viable and functional neurons, similar to the extracellular matrix in the human body. The model used in articles **III** and **IV** was the well-known amphiphilic LMWG Fmoc-Phe and the solvent was phosphate buffer saline (PBS), which was selected due to its biocompatibility. Two distinct systems were studied during this work: (i) the bulk gel as native and hybrid gel with GO flakes to assess the critical gelation concentration and the suitability of the gel as a mimic for the brain ECM and (ii) the effect of pristine and 2PO graphene surfaces on the Fmoc-Phe surface-mediated self-assembly to further understand the interactions between the gel and graphene surfaces.

3.2.1 Gel formation and properties

The supramolecular gels were prepared by mixing Fmoc-Phe with PBS, followed by a heating-cooling cycle (room temperature to 80 °C (30 min) to room temperature). The bulk gels were cooled down to room temperature in glass vials and for the study of the surface effects, 2 µl of the hot Fmoc-Phe solution was added on the graphene surface and cooled down in a humid chamber to prevent drying (FIGURE 18a).

Self-supporting, thermoreversible and homogeneous hydrogels were produced with an Fmoc-Phe concentration between $2 \, mg \cdot ml^{-1}$ and $6 \, mg \cdot ml^{-1}$ for the native and the Fmoc-Phe/GO hybrid hydrogel. As $2 \, mg \cdot ml^{-1}$ was the critical gelation concentration, it was used to prepare the hybrid hydrogels. The incorporation of GO flakes ($0.25 \, mg \cdot ml^{-1}$ to $1.0 \, mg \cdot ml^{-1}$) did not affect the gelation outcome and the thermoreversibility of the gel (FIGURE 18b). However, it did affect the gel formation time. While the native hydrogel took at least 12 hours to form, the hybrid analogue took only 6 hours. The GO flakes in the solution provided additional nucleation sites for the self-assembly of Fmoc-Phe, which could have accelerated the gel formation. An increase of the heating temperature and time to 95 °C and 1 h, respectively, led to the precipitation of GO. Various processes, such as an enhanced collision frequency and a reduced electrostatic repulsion between the GO flakes at higher temperatures, could have

caused the precipitation.[128] Reduced GO (rGO), with fewer hydrophilic groups compared to GO, precipitated when incorporated into the gel. Presumably, the interactions between rGO and the Fmoc-Phe supramolecular structures were weaker compared to GO. This indicated that the interactions between the oxygen-containing functional groups of GO/rGO and Fmoc-Phe were stronger than those between the hydrophobic domains and the gelator.
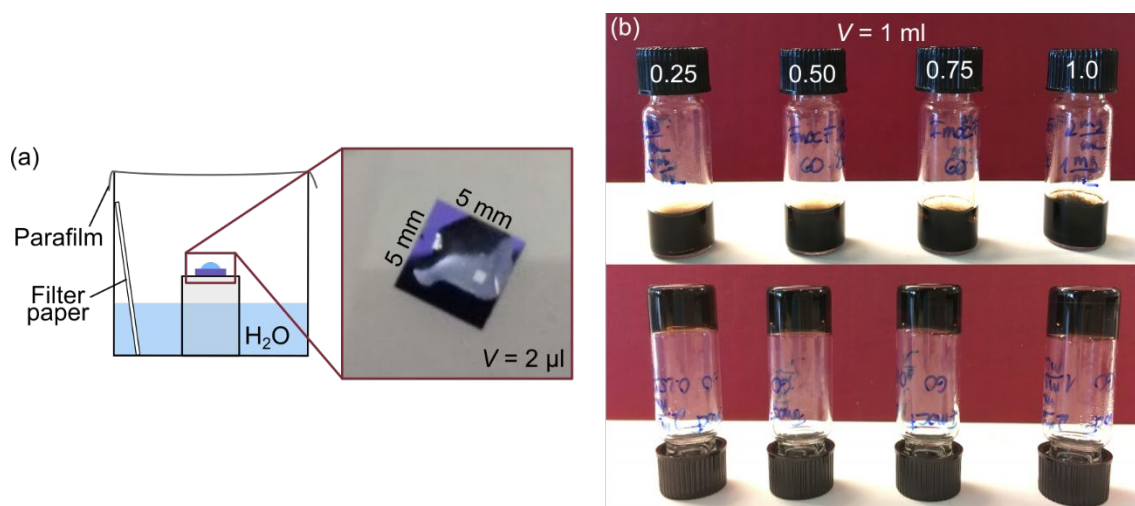

FIGURE 18 (a) Scheme of the cool-down setup for the graphene surface samples and photo of the formed gel on the sample. (b) Fmoc-Phe/GO hybrid hydrogels and vial inversion test. The Fmoc-Phe concentration was 2.0 mg·ml⁻¹ for all samples and the GO concentration in mg·ml⁻¹ is indicated in the photo. The volume of the gel V is indicated for both systems in the figure. (b) Adapted with permission by E. D. Sitsanidis, L. A. L. Dutra, J. Schirmer, R. Chevigny, M. Lahtinen, A. Johansson, C. C. Piras, D. K. Smith, M. Tiirola, M. Pettersson and M. Nissinen. Probing the Gelation Synergies and Anti-*Escherichia coli* Activity of Fmoc-Phenylalanine/Graphene Oxide Hybrid Hydrogel, *ACS Omega* **2023**, 8 (11), 10225-10234. Copyright 2022 American Chemical Society.

The viscoelastic properties of the bulk native and hybrid hydrogels were analyzed to show that the stiffness of the gel and the brain are in the same range (brain: 0.1 kPa to 1 kPa). Additionally, possible effects of the GO incorporation on the material's stiffness and elasticity were studied. The stiffness of the material was affected only by the concentration of Fmoc-Phe, not by the incorporation of GO. At higher gelator concentrations, the gel was stiffer. The native and all hybrid gels with an Fmoc-Phe concentration of 2 mg·ml⁻¹ matched the stiffness of the brain tissue. The incorporation of GO, however, led to an increase in the gel elasticity, with a higher elasticity for higher GO concentrations.

One potential application of hydrogels in general is the prevention of microbial infections.[129] In our study, the activity against Gram-negative *Escherichia coli* was tested for the native and hybrid hydrogels and GO suspensions in PBS. All the materials and solutions showed poor antibacterial activity. However, the antibacterial activity of the hybrid gel could be increased by functionalizing GO with antibacterial agents in future.

The gel formation and viscoelastic studies revealed self-supporting, homogeneous native and hybrid hydrogels that matched the stiffness of the brain,

which is beneficial for the application of the gel in this tissue. The results indicated that the GO flakes provided nucleation sites for faster gel formation and that the hydrophilic functional groups of the incorporated GBM strengthened the interactions between Fmoc-Phe and the material.

3.2.2   Gel morphology

The morphology and fiber dimensions of the bulk hybrid gel and the gel formed on the graphene surface were analyzed by AFM, SEM, TEM and HIM. In this way, the incorporation of GO flakes into the bulk hydrogel network and the surface-induced effects of pristine and 2PO graphene on the morphology of the supramolecular structures could be studied. The imaging sample of the bulk gel was prepared by dipping a carbon film into the gel and allowing it to dry overnight at room temperature. The graphene surface sample was lyophilized after gel formation and before the analysis. Different drying methods affect the morphology of the dried gel sample.[130,131] Thus, the two samples could not be directly compared.

Generally, both the bulk gel and the gel on the surfaces were supramolecular structures made of a network of fibers (FIGURE 19). The shape and dimensions of the fibers from the bulk gel were similar for the native and the hybrid hydrogels. Thus, we assumed that the fiber structure itself (primary and secondary organization level) was not affected by the GO incorporation. The hybrid gel had single, branched and entangled fibers between, on top, and around the edges of the GO flakes (FIGURE 19a). This indicated that the GO flakes interacted with the Fmoc-Phe fibers at the tertiary organization level.

On the graphene surface sample, AFM images from the center of the gel network presented similar fiber shapes and dimensions on pristine and 2PO graphene. However, when comparing fibers at the edge of the gel network, the fibers appeared straight on the pristine surface, whereas they were curved on the 2PO surface (FIGURE 19b-c, blue lines). The fibers at the edges of the gel network grew close to the surface and might have been affected by the surface to a greater extent than the fibers in the center of the network. The results indicated an effect of the distinct surface hydrophilicity between pristine and 2PO graphene on the tertiary organization level of the fibers.

To conclude, the imaging of the dried gels revealed fibers as supramolecular structures, independent of the GBM in contact with the gel. In the bulk gel, GO flakes did not affect the morphology. When studying the surface-induced self-assembly, however, the morphology was slightly different. From these results, effects on the tertiary organization level of the gel could be concluded. The primary and secondary structures, however, remained unclear.
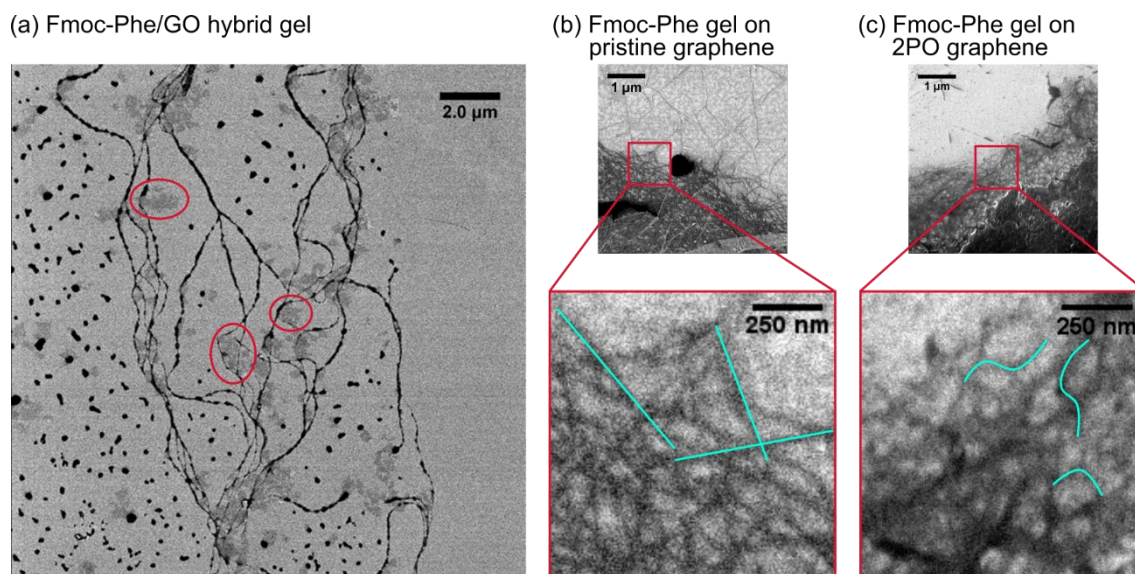
FIGURE 19 HIM images of (a) the bulk Fmoc-Phe/GO hybrid gel (GO flakes appear light grey, examples are highlighted) and the Fmoc-Phe gel on (b) the pristine and (c) the 2PO graphene surface. The blue lines follow the shape of example fibers. (a) Adapted with permission by E. D. Sitsanidis, L. A. L. Dutra, J. Schirmer, R. Chevigny, M. Lahtinen, A. Johansson, C. C. Piras, D. K. Smith, M. Tiirola, M. Pettersson and M. Nissinen. Probing the Gelation Synergies and Anti-Escherichia coli Activity of Fmoc-Phenylalanine/Graphene Oxide Hybrid Hydrogel, *ACS Omega* **2023**, 8 (11), 10225-10234. Copyright 2022 American Chemical Society. (b), (c) Reproduced from article **IV** with permission from the PCCP Owner Societies.

3.2.3 Self-assembly

The self-assembly and interactions between the Fmoc-Phe molecules themselves and with the respective GBM were studied with s-SNOM experiments and Density Functional Theory (DFT) calculations for the surface sample. The bulk gels were analyzed by powder X-ray diffraction (PXRD), FTIR and Raman spectroscopy. While the results for the bulk gel showed the average packing and interactions in the whole gel sample, the s-SNOM and DFT results of the surface sample showed interactions at specific locations on the sample and at the nanoscale.

Overall, a heterogeneous fibrous network was found for the bulk and the surface samples. This was confirmed by s-SNOM MIR imaging and PXRD patterns of the surface and bulk samples, respectively. The results confirmed previous reports about the polymorphic nature of the Fmoc-Phe gel.[132]

The interactions at the primary and secondary organization levels of the gel could be studied with IR spectroscopy. The (nano-)FTIR spectra of amides showed characteristic bands between 1500 cm^{-1} and 1750 cm^{-1}. These bands corresponded to the carbonyl C=O stretching vibration (amide I) and a combination of the N-H bending and C-N stretching vibrations (amide II, FIGURE 11b). Especially the amide I band is sensitive to hydrogen bonding and is an important parameter for the analysis of proteins and peptides. The band positions in the amide I region were assigned to the specific secondary structure

motifs of the biomolecules, such as β-sheets and helices.[133,134] These motifs are based on hydrogen bonding between the amide groups of the amino acid chain. The molecular packing of peptide amphiphiles is based on hydrogen bonding between amino acids as well. Thus, the bands in the amide I region of the gels could be interpreted similarly.

The FTIR spectrum of the Fmoc-Phe powder before gelation showed the non-hydrogen bonded carbonyl stretching at 1720 cm^{-1} and the amide I band at 1681 cm^{-1} (FIGURE 20a). For the Fmoc-Phe/GO hybrid gel, the spectrum lacked the non-hydrogen bonded carbonyl stretching band. The amide I band shifted to 1691 cm^{-1}, with a shoulder at 1672cm^{-1}. Both changes indicate the formation of sheet-like supramolecular structures during the Fmoc-Phe self-assembly based on hydrogen bonds involving the C=O groups.
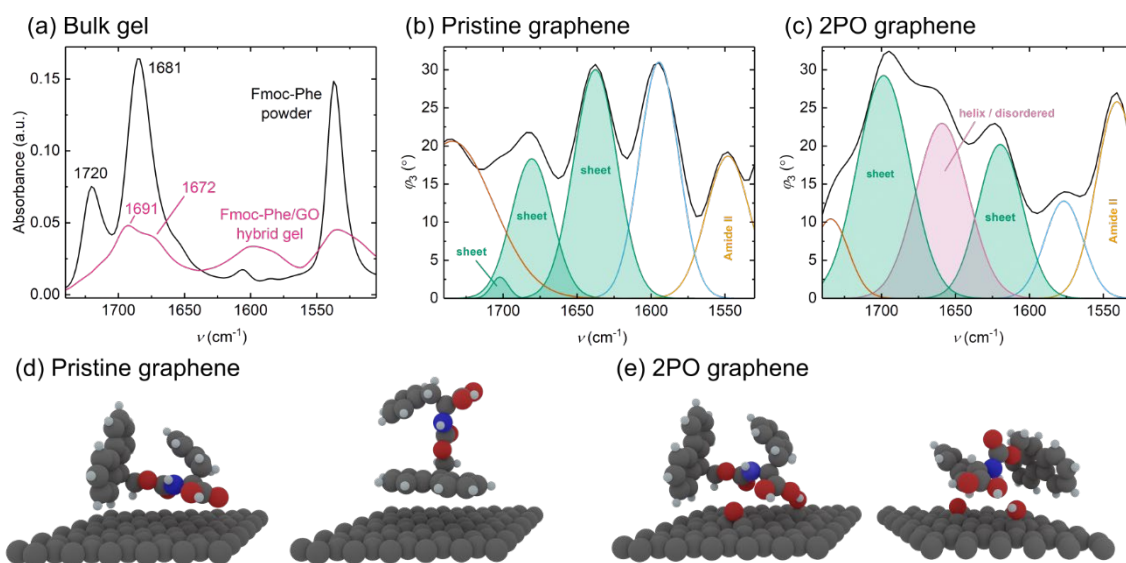

FIGURE 20   (a) FTIR spectra of the Fmoc-Phe powder and the Fmoc-Phe/GO hybrid gel; Nano-FTIR spectra of Fmoc-Phe gel on (b) pristine and (c) 2PO graphene; Two of the energetically most stable structures of Fmoc-Phe adsorbed on (d) pristine and (e) 2PO graphene. (b)-(e) Reproduced from article **IV** with permission from the PCCP Owner Societies.

The nano-FTIR spectra of the Fmoc-Phe fibers on pristine and 2PO graphene showed similar and distinct bands in the amide I region, indicating surface-related effects on the self-assembly (FIGURE 20b,c). When correlating the band positions in the nano-FTIR spectra with the secondary structure elements, there would be sheet assemblies on pristine and 2PO graphene and additionally helical or disordered structures only on 2PO graphene. On both surfaces, a band at approximately 1730 cm^{-1} could have originated from non-hydrogen bonded C=O groups.

In all studied systems, the carbonyl groups of Fmoc-Phe formed hydrogen bonds during the self-assembly process. Interestingly, the incorporation of GO into the bulk gel did not affect the bulk average hydrogen bonding. During the gelation of the bulk gels, the surfaces for nucleation sites were the glass vial and GO flakes (only for the hybrid gels). The results indicated that either the

nucleation on glass and GO led to the same molecular arrangement, or that the relative amount of different molecular packing induced by the GO flakes was too small to be detected in the average FTIR spectrum. On the other hand, the pristine and 2PO graphene surfaces led to similar and distinct hydrogen bonding in the gel fibers. Here, during the self-assembly, there was only the pristine and 2PO graphene surfaces available for nucleation. Thus, the surface-induced effect relative to the probed volume during the experiment might have been more significant and more easily detected when compared to the bulk gel.

To elucidate the interactions between the surface and the Fmoc-Phe molecules that could cause the distinct self-assembly, we performed DFT calculations. A surface-mediated self-assembly was assumed. Distinct orientations of the initially adsorbing Fmoc-Phe monomer on the surface could have affected the self-assembly process alongside the forming fiber. In our calculations, the 2PO graphene contained one hydroxyl and one epoxide group, and one Fmoc-Phe molecule was adsorbed on the surfaces. The environment of the calculations was a vacuum space. While these conditions differed from reality during the self-assembly, the calculations could reveal the driving forces of molecular adsorption. A variety of initial orientations were tested, and the energetically most stable structures were assumed to be the dominating species.

On pristine graphene, the adsorption of Fmoc-Phe was mainly based on interactions between the aromatic moieties of Fmoc-Phe and the surface. FIGURE 20d presents two of the most stable configurations, where edge-to-face and face-to-face/parallel-displaced π-π stacking was observed (FIGURE 7a). On 2PO graphene, the hydrophilic groups played a more important role in the interactions with Fmoc-Phe. The molecule oriented itself such that the carboxylic acid group was close to the epoxide or hydroxyl group (FIGURE 20e). As a result, different moieties of Fmoc-Phe interacted with each surface. In this way, hydrophilic or hydrophobic groups pointed towards the Fmoc-Phe solution on pristine or 2PO graphene, respectively. The self-assembly could have been initiated by different parts of the molecule and could have led to distinct primary and secondary structures of the fibers. The most energetically stable structures included different and similar orientations on pristine and 2PO graphene. This complements the nano-FTIR results, which showed distinct and similar bands on the two surfaces.

For the Fmoc-Phe/GO hybrid gel, molecular interactions between the gelator and GO were investigated with Raman spectroscopy. By comparing the Raman spectrum of GO flakes with the hybrid gel, two differences were observed: The I_D/I_G ratio was larger in the gel compared to the plane flakes. Additionally, the G band shifted from 1583 cm⁻¹ in the flakes to 1600 cm⁻¹ in the gel. Both observations suggested a decrease of in-plane sp² domains in the gel, which could be attributed to π-π-stacking between the GO flakes and the aromatic moieties of Fmoc-Phe.

In summary, we found polymorphic Fmoc-Phe hydrogels that matched the stiffness of brain tissue as a bulk gel. We proved that Fmoc-Phe molecules and fibers interacted with pristine and 2PO graphene surfaces and GO flakes. While

GO flakes had no detectable effect on the bulk self-assembly of Fmoc-Phe, pristine and 2PO graphene surfaces affected the self-assembly at the nanoscale near the surface. These effects might have been limited to the proximity of the surface. However, it is important to understand them towards graphene-bio interfaces, where a biological component, for example, a neuron, is near the surface.

4 CONCLUSIONS AND OUTLOOK

Since the discovery of graphene's outstanding properties, various applications of the material and its derivatives have been considered. The potential biological applications of this material generated an entire research field on their own. Due to the high charge carrier density of graphene and the communication of human neurons based on electrical signals, graphene has been successfully used to measure brain activity. Thus, graphene can become a useful material for the treatment of nervous system injuries. The properties of graphene can be tuned by laser-induced two-photon oxidation (2PO) in nanoscale patterns, which introduces mainly hydroxyl and epoxide groups to the surface and does not affect the adjacent pristine graphene. In this way, graphene-bio interfaces with user-defined nanoscale properties can be developed. However, the research is still in its infancy, and the surface-related effects of 2PO on the biosystems need to be elucidated for any biomedical applications. The analysis of these effects was started in this thesis: Biological and biomimetic model systems were studied in direct contact with pristine and 2PO graphene surfaces as well as GO flakes. Two approaches were followed: (i) the noncovalent immobilization of proteins as a coating prior to neuron attachment and (ii) the formation of an ECM mimic on the graphene-based surfaces as a support for neurons.

The model proteins were the enzyme horseradish peroxidase (HRP) and bovine serum albumin, two well-studied species. For certain incubation and 2PO parameters, both proteins immobilized selectively on the 2PO areas. Herein, the oxidation level, protein concentration and incubation time are important tuning parameters. The selectivity was attributed to distinct noncovalent interactions between the proteins and the two surfaces. HRP could be immobilized in a one-to-four-layer range, and the noncovalent interactions were assumed to lead to electron-donation from the protein to the graphene surface. These results are very promising with regard to graphene-neuron communication because former studies showed that signals can be measured through a thin protein layer. The method could also enable selective immobilization of different proteins on one GFET array. The function of HRP could be tuned by the immobilization on pristine and 2PO graphene. A higher catalytic activity was detected from HRP

on the pristine surfaces compared to the 2PO surfaces. Presumably, 2PO surfaces affect the secondary structure of HRP more significantly than the pristine graphene surfaces. These results are interesting towards graphene-bio interfaces in general, as they indicate the potential of 2PO as a tool to tune protein immobilization and function at the nanoscale, which opens possibilities for new devices.

The second part of the thesis studied the effects of pristine and 2PO graphene surfaces and GO flakes on the supramolecular self-assembly of the peptide amphiphile Fmoc-Phe. The GO flakes were successfully incorporated into the Fmoc-Phe hydrogel and did not affect the structure of the gel fibers. The stiffness of the gels matched the stiffness of the brain's ECM. This is important for a viable and functional neuronal network formation close to the artificial surface. When the supramolecular self-assembly was initiated from the pristine or 2PO graphene surface, differences in the fiber structure were observed on several organizational levels. Herein, s-SNOM, a relatively new technique, was introduced to study the secondary structure of gel fibers. While the nano-FTIR spectra of fibers on pristine graphene show sheet-like structures, additional helical/disordered structures were found on 2PO graphene. These were attributed to distinct noncovalent interactions between initially adsorbed Fmoc-Phe molecules and the two surfaces. The range of this effect, i.e., the distance from the surface at which the effect is still detectable, remains an open question. Also, it should be tested if the distinct structures lead to distinct viscoelastic properties, which have been shown for other gel systems on different surfaces. These studies highlight Fmoc-Phe as a possible gelator for brain and nerve applications and s-SNOM as a powerful technique for analyzing surface-mediated self-assembly. Additionally, 2PO was shown to affect surface-mediated supramolecular self-assembly, thus indicating its use to generate biomimetic layers with differing viscoelastic properties. This might be useful to guide neurons on a graphene surface because they are sensitive to the viscoelastic properties of their environment.

In conclusion, this thesis has contributed to advancing the knowledge of graphene-related surface-induced effects on biological and biomimetic systems. For 2PO surfaces, the studies presented were the first to explore the material for bio applications. Therefore, we started to explore well-known model systems. In this way, the observed effects could be traced back to the surface properties of graphene. The results show that 2PO could be a useful tool for developing graphene-bio and -neuron interfaces. The method might guide neurons with functional proteins and suitable stiffness of the support material to specific surface locations. This could lead to the development of more efficient devices for treating injuries to the nervous system. However, there is still a long way to go before 2PO graphene can be used clinically. The biocompatibility and safety of the material still need to be tested. Nevertheless, it is important to study interactions between the material and biological systems at the molecular level. This will deepen our knowledge and improve our ability to predict and understand possible responses of organisms at the graphene-bio interface.

REFERENCES

(1)   Brodal, P. *The Central Nervous System*, 4th ed.; Oxford University Press: New York, 2010.

(2)   Adewole, D. O.; Serruya, M. D.; Harris, J. P.; Burrell, J. C.; Petrov, D.; Chen, H. I.; Wolf, J. A.; Cullen, D. K. *The Evolution of Neuroprosthetic Interfaces*; 2016; Vol. 44. https://doi.org/10.1615/CritRevBiomedEng.2016017198.

(3)   Lorach, H.; Galvez, A.; Spagnolo, V.; Martel, F.; Karakas, S.; Intering, N.; Vat, M.; Faivre, O.; Harte, C.; Komi, S.; Ravier, J.; Collin, T.; Coquoz, L.; Sakr, I.; Baaklini, E.; Hernandez-Charpak, S. D.; Dumont, G.; Buschman, R.; Buse, N.; Denison, T.; van Nes, I.; Asboth, L.; Watrin, A.; Struber, L.; Sauter-Starace, F.; Langar, L.; Auboiroux, V.; Carda, S.; Chabardes, S.; Aksenova, T.; Demesmaeker, R.; Charvet, G.; Bloch, J.; Courtine, G. Walking Naturally after Spinal Cord Injury Using a Brain–Spine Interface. *Nature* **2023**, *618* (7963), 126–133. https://doi.org/10.1038/s41586-023-06094-5.

(4)   Ferguson, M.; Sharma, D.; Ross, D.; Zhao, F. A Critical Review of Microelectrode Arrays and Strategies for Improving Neural Interfaces. *Adv Healthc Mater* **2019**, *8* (1900558). https://doi.org/10.1002/adhm.201900558.

(5)   Blaschke, B. M.; Tort-Colet, N.; Guimera-Brunet, A.; Weinert, J.; Rousseau, L.; Heimann, A.; Drieschner, S.; Kempski, O.; Villa, R.; Sanchez-Vives, M. V; Garrido, J. A. Mapping Brain Activity with Flexible Graphene Micro-Transistors. *2d Mater* **2017**, *4*, 1–9. https://doi.org/10.1088/2053-1583/aa5eff.

(6)   Novoselov, K. S.; Geim, A. K.; Morozov, S. V; Jiang, D.; Zhang, Y.; Dubonos, S. V; Grigorieva, I. V; Firsov, A. A. Electric Field Effect in Atomically Thin Carbon Films. *Phys. Rev. Lett* **2004**, *306*, 666–669. https://doi.org/10.1126/science.1102896.

(7)   Hess, L. H.; Jansen, M.; Maybeck, V.; Hauf, M. V.; Seifert, M.; Stutzmann, M.; Sharp, I. D.; Offenhäusser, A.; Garrido, J. A. Graphene Transistor Arrays for Recording Action Potentials from Electrogenic Cells. *Advanced Materials* **2011**, *23* (43), 5045–5049. https://doi.org/10.1002/adma.201102990.

(8)   Alberts, B.; Johnson, A.; Lewis, J.; Morgan, D.; Raff, M.; Roberts, K.; Walter, P. *Molecular Biology of the Cell*, 6th ed.; Garland Science, 2015.

(9)   Georges, P. C.; Miller, W. J.; Meaney, D. F.; Sawyer, E. S.; Janmey, P. A. Matrices with Compliance Comparable to That of Brain Tissue Select Neuronal over Glial Growth in Mixed Cortical Cultures. *Biophys J* **2006**, *90* (8), 3012–3018. https://doi.org/10.1529/biophysj.105.073114.

(10)   Kayal, C.; Moeendarbary, E.; Shipley, R. J.; Phillips, J. B. Mechanical Response of Neural Cells to Physiologically Relevant Stiffness Gradients. *Adv Healthc Mater* **2020**, *9* (8). https://doi.org/10.1002/adhm.201901036.

(11) Lantoine, J.; Grevesse, T.; Villers, A.; Delhaye, G.; Mestdagh, C.; Versaevel, M.; Mohammed, D.; Bruyère, C.; Alaimo, L.; Lacour, S. P.; Ris, L.; Gabriele, S. Matrix Stiffness Modulates Formation and Activity of Neuronal Networks of Controlled Architectures. *Biomaterials* **2016**, *89*, 14–24. https://doi.org/10.1016/j.biomaterials.2016.02.041.

(12) Budday, S.; Ovaert, T. C.; Holzapfel, G. A.; Steinmann, P.; Kuhl, E. Fifty Shades of Brain: A Review on the Mechanical Testing and Modeling of Brain Tissue. *Archives of Computational Methods in Engineering* **2020**, *27* (4), 1187–1230. https://doi.org/10.1007/s11831-019-09352-w.

(13) Almdal, K.; Dyre, J.; Hvidt, S.; Kramer, O. Towards a Phenomenological Definition of the Term "Gel." *Polymer Gels and Networks* **1993**, *1*, 5–17. https://doi.org/10.1016/0966-7822(93)90020-I.

(14) Chelu, M.; Musuc, A. M. Polymer Gels: Classification and Recent Developments in Biomedical Applications. *Gels*. MDPI February 1, 2023. https://doi.org/10.3390/gels9020161.

(15) Draper, E. R.; Adams, D. J. Low-Molecular-Weight Gels: The State of the Art. *Chem* **2017**, *3* (3), 390–410. https://doi.org/10.1016/j.chempr.2017.07.012.

(16) Estroff, L. A.; Hamilton, A. D. Water Gelation by Small Organic Molecules. *Chem Rev* **2004**, *104* (3), 1201–1217. https://doi.org/10.1021/cr0302049.

(17) Hendricks, M. P.; Sato, K.; Palmer, L. C.; Stupp, S. I. Supramolecular Assembly of Peptide Amphiphiles. *Acc Chem Res* **2017**, *50* (10), 2440–2448. https://doi.org/10.1021/acs.accounts.7b00297.

(18) Jayawarna, V.; Ali, M.; Jowitt, T. A.; Miller, A. F.; Saiani, A.; Gough, J. E.; Ulijn, R. V. Nanostructured Hydrogels for Three-Dimensional Cell Culture through Self-Assembly of Fluorenylmethoxycarbonyl-Dipeptides. *Advanced Materials* **2006**, *18*, 611–614. https://doi.org/10.1002/adma.200501522.

(19) Skilling, K. J.; Citossi, F.; Bradshaw, T. D.; Ashford, M.; Kellam, B.; Marlow, M. Insights into Low Molecular Mass Organic Gelators: A Focus on Drug Delivery and Tissue Engineering Applications. *Soft Matter*. January 14, 2014, pp 237–256. https://doi.org/10.1039/c3sm52244j.

(20) Alakpa, E. V.; Jayawarna, V.; Lampel, A.; Burgess, K. V.; West, C. C.; Bakker, S. C. J.; Roy, S.; Javid, N.; Fleming, S.; Lamprou, D. A.; Yang, J.; Miller, A.; Urquhart, A. J.; Frederix, P. W. J. M.; Hunt, N. T.; Péault, B.; Ulijn, R. V.; Dalby, M. J. Tunable Supramolecular Hydrogels for Selection of Lineage-Guiding Metabolites in Stem Cell Cultures. *Chem* **2016**, *1* (2), 298–319. https://doi.org/10.1016/j.chempr.2016.07.001.

(21) Sitsanidis, E. D.; Kasapidou, P. M.; Hiscock, J. R.; Gubala, V.; Castel, H.; Popoola, P. I. A.; Hall, A. J.; Edwards, A. A. Probing the Self-Assembly and Anti-Glioblastoma Efficacy of a Cinnamoyl-Capped Dipeptide Hydrogelator. *Org Biomol Chem* **2022**, *20* (37), 7458–7466. https://doi.org/10.1039/d2ob01339h.

(22) Dastidar, P.; Roy, R.; Parveen, R.; Sarkar, K. Supramolecular Synthon Approach in Designing Molecular Gels for Advanced Therapeutics. *Adv Ther (Weinh)* **2019**, *2* (1800061). https://doi.org/10.1002/adtp.201800061.

(23) Hartgerink, J. D.; Beniash, E.; Stupp, S. I. Self-Assembly and Mineralization of Peptide-Amphiphile Nanofibers. *Science (1979)* **2001**, *294*, 1684–1688. https://doi.org/10.1126/science.1063187.

(24) Draper, E. R.; Adams, D. J. Controlling the Assembly and Properties of Low-Molecular-Weight Hydrogelators. *Langmuir* **2019**, *35*, 6506–6521. https://doi.org/10.1021/acs.langmuir.9b00716.

(25) Yang, B.; Adams, D. J.; Marlow, M.; Zelzer, M. Surface-Mediated Supramolecular Self-Assembly of Protein, Peptide, and Nucleoside Derivatives: From Surface Design to the Underlying Mechanism and Tailored Functions. *Langmuir* **2018**, *34* (50), 15109–15125. https://doi.org/10.1021/acs.langmuir.8b01165.

(26) Angelerou, M. G. F.; Sabri, A.; Creasey, R.; Angelerou, P.; Marlow, M.; Zelzer, M. Surface-Directed Modulation of Supramolecular Gel Properties. *Chemical Communications* **2016**, *52*, 4298–4230. https://doi.org/10.1039/c6cc00292g.

(27) Yang, B.; Lledos, M.; Akhtar, R.; Ciccone, G.; Jiang, L.; Russo, E.; Rajput, S.; Jin, C.; Angelereou, M. G. F.; Arnold, T.; Rawle, J.; Vassalli, M.; Marlow, M.; Adams, D. J.; Zelzer, M. Surface-Controlled Spatially Heterogeneous Physical Properties of a Supramolecular Gel with Homogeneous Chemical Composition. *Chem Sci* **2021**, *12* (42), 14260–14269. https://doi.org/10.1039/d1sc04671c.

(28) Wallace, P. R. The Band Theory of Graphite. *Physical Review* **1947**, *71* (9), 622–634. https://doi.org/10.1103/PhysRev.71.622.

(29) McClure, J. W. Diamagnetism of Graphite. *Physical Review* **1956**, *104* (3), 666–671. https://doi.org/10.1103/PhysRev.104.666.

(30) Semenoff, G. W. Condensed-Matter Simulation of a Three-Dimensional Anomaly. *Phys Rev Lett* **1984**, *53* (26), 2449–2452. https://doi.org/10.1103/PhysRevLett.53.2449.

(31) Shioyama, H. Cleavage of Graphite to Graphene. *J Mater Sci Lett* **2001**, *20*, 499–500. https://doi.org/10.1023/A:1010907928709.

(32) Viculis, L. H.; Mack, J. J.; Kaner, R. B. A Chemical Route to Carbon Nanoscrolls. *Science (1979)* **2003**, *299*, 1361. https://doi.org/10.1126/science.1078842.

(33) Nobel Prize Outreach AB 2023. *The Nobel Prize in Physics 2010.* https://www.nobelprize.org/prizes/physics/2010/summary/.

(34) Allen, M. J.; Tung, V. C.; Kaner, R. B. Honeycomb Carbon: A Review of Graphene. *Chem. Rev.* **2010**, *110*, 132–145. https://doi.org/10.1021/cr900070d.

(35) Dubois, S. M. M.; Zanolli, Z.; Declerck, X.; Charlier, J. C. Electronic Properties and Quantum Transport in Graphene-Based Nanostructures. *European Physical Journal B* **2009**, *72* (1), 1–24. https://doi.org/10.1140/epjb/e2009-00327-8.

(36) Geim, A. K.; Novoselov, K. S. The Rise of Graphene. *Nat Mater* **2007**, *6*, 183–191. https://doi.org/10.1038/nmat1849.

(37) Morozov, S. V.; Novoselov, K. S.; Katsnelson, M. I.; Schedin, F.; Elias, D. C.; Jaszczak, J. A.; Geim, A. K. Giant Intrinsic Carrier Mobilities in Graphene and Its Bilayer. *Phys Rev Lett* **2008**, *100* (016602). https://doi.org/10.1103/PhysRevLett.100.016602.

(38) Schweicher, G.; Garbay, G.; Jouclas, R.; Vibert, F.; Devaux, F.; Geerts, Y. H. Molecular Semiconductors for Logic Operations: Dead-End or Bright Future? *Advanced Materials* **2020**, *32* (1905909). https://doi.org/10.1002/adma.201905909.

(39) Kang, Y. J.; Kang, J.; Chang, K. J. Electronic Structure of Graphene and Doping Effect on SiO2. *Phys Rev B* **2008**, *78* (115404). https://doi.org/10.1103/PhysRevB.78.115404.

(40) Chen, J. H.; Jang, C.; Xiao, S.; Ishigami, M.; Fuhrer, M. S. Intrinsic and Extrinsic Performance Limits of Graphene Devices on SiO 2. *Nat Nanotechnol* **2008**, *3* (4), 206–209. https://doi.org/10.1038/nnano.2008.58.

(41) Cao, K.; Feng, S.; Han, Y.; Gao, L.; Hue Ly, T.; Xu, Z.; Lu, Y. Elastic Straining of Free-Standing Monolayer Graphene. *Nat Commun* **2020**, *11* (284). https://doi.org/10.1038/s41467-019-14130-0.

(42) Nair, R. R.; Blake, P.; Grigorenko, A. N.; Novoselov, K. S.; Booth, T. J.; Stauber, T.; Peres, N. M. R.; Geim, A. K. Fine Structure Constant Defines Visual Transparency of Graphene. *Science (1979)* **2008**, *320* (5881), 1308. https://doi.org/10.1126/science.1156965.

(43) Xu, Y.; Yu, H.; Wang, C.; Cao, J.; Chen, Y.; Ma, Z.; You, Y.; Wan, J.; Fang, X.; Chen, X. Multilayer Graphene with Chemical Modification as Transparent Conducting Electrodes in Organic Light-Emitting Diode. *Nanoscale Res Lett* **2017**, *12* (1). https://doi.org/10.1186/s11671-017-2009-9.

(44) Wang, P.; Jian, M.; Zhang, C.; Wu, M.; Ling, X.; Zhang, J.; Wei, B.; Yang, L. Highly Stable Graphene-Based Flexible Hybrid Transparent Conductive Electrodes for Organic Solar Cells. *Adv Mater Interfaces* **2022**, *9* (3). https://doi.org/10.1002/admi.202101442.

(45) Brodie, B. C. XIII. On the Atomic Weight of Graphite. *Philosophical Transactions Royal Society* **1859**, *149*, 249–259. https://doi.org/10.1098/rstl.1859.0013.

(46) Singh, R. K.; Kumar, R.; Singh, D. P. Graphene Oxide: Strategies for Synthesis, Reduction and Frontier Applications. *RSC Adv* **2016**, *6*, 64993–65011. https://doi.org/10.1039/c6ra07626b.

(47) Zhang, J.; Zhang, F.; Yang, H.; Huang, X.; Liu, H.; Zhang, J.; Guo, S. Graphene Oxide as a Matrix for Enzyme Immobilization. *Langmuir Letter* **2010**, *26* (9), 6083–6085. https://doi.org/10.1021/la904014z.

(48) De Sousa, M.; Martins, C. H. Z.; Franqui, L. S.; Fonseca, L. C.; Delite, F. S.; Lanzoni, E. M.; Martinez, D. S. T.; Alves, O. L. Covalent Functionalization of Graphene Oxide with D-Mannose: Evaluating the Hemolytic Effect and Protein Corona Formation. *J Mater Chem B* **2018**, *6* (18), 2803–2812. https://doi.org/10.1039/c7tb02997g.

(49) Yu, Q.; Zhang, B.; Li, J.; Li, M. The Design of Peptide-Grafted Graphene Oxide Targeting the Actin Cytoskeleton for Efficient Cancer Therapy. *Chemical Communications* **2017**, *53* (83), 11433–11436. https://doi.org/10.1039/c7cc06537j.

(50) Karki, N.; Tiwari, H.; Tewari, C.; Rana, A.; Pandey, N.; Basak, S.; Sahoo, N. G. Functionalized Graphene Oxide as a Vehicle for Targeted Drug Delivery and Bioimaging Applications. *Journal of Materials Chemistry B*. Royal Society of Chemistry September 28, 2020, pp 8116–8148. https://doi.org/10.1039/d0tb01149e.

(51) Jung, I.; Dikin, D. A.; Piner, R. D.; Ruoff, R. S. Tunable Electrical Conductivity of Individual Graphene Oxide Sheets Reduced at "Low" Temperatures. *Nano Lett* **2008**, *8*, 4283–4287. https://doi.org/10.1021/nl8019938.

(52) Shen, Y.; Yang, S.; Zhou, P.; Sun, Q.; Wang, P.; Wan, L.; Li, J.; Chen, L.; Wang, X.; Ding, S.; Zhang, D. W. Evolution of the Band-Gap and Optical Properties of Graphene Oxide with Controllable Reduction Level. *Carbon N Y* **2013**, *62*, 157–164. https://doi.org/10.1016/j.carbon.2013.06.007.

(53) Aumanen, J.; Johansson, A.; Koivistoinen, J.; Myllyperkiö, P.; Pettersson, M. Patterning and Tuning of Electrical and Optical Properties of Graphene by Laser Induced Two-Photon Oxidation. *Nanoscale* **2015**, *7*, 2851–2855. https://doi.org/10.1039/C4NR05207B.

(54) Johansson, A.; Tsai, H.-C.; Aumanen, J.; Koivistoinen, J.; Myllyperkiö, P.; Hung, Y.-Z.; Chuang, M.-C.; Chen, C.-H.; Woon, W. Y.; Pettersson, M. Chemical Composition of Two-Photon Oxidized Graphene Carbon. *Carbon* **2017**, *115*, 77–82. https://doi.org/10.1016/j.carbon.2016.12.091.

(55) Lampinen, A.; See, E.; Emelianov, A.; Myllyperkiö, P.; Johansson, A.; Pettersson, M. Laser-Induced Tuning of Graphene Field-Effect Transistors for PH Sensing. *Physical Chemistry Chemical Physics* **2023**, *25*, 10778–10784. https://doi.org/10.1039/D3CP00359K.

(56) Mentel, K. K.; Emelianov, A. V.; Philip, A.; Johansson, A.; Karppinen, M.; Pettersson, M. Area-Selective Atomic Layer Deposition on Functionalized Graphene Prepared by Reversible Laser Oxidation. *Adv Mater Interfaces* **2022**, *9* (29). https://doi.org/10.1002/admi.202201110.

(57) Ferrari, A. C.; Basko, D. M. Raman Spectroscopy as a Versatile Tool for Studying the Properties of Graphene. *Nature Nanotechnology*. Nature Publishing Group 2013, pp 235–246. https://doi.org/10.1038/nnano.2013.46.

(58) Ferrari, A. C. Raman Spectroscopy of Graphene and Graphite : Disorder , Electron – Phonon Coupling , Doping and Nonadiabatic Effects. *Solid State Commun* **2007**, *143*, 47–57. https://doi.org/10.1016/j.ssc.2007.03.052.

(59) Ferrari, A. C.; Meyer, J. C.; Scardaci, V.; Casiraghi, C.; Lazzeri, M.; Mauri, F.; Piscanec, S.; Jiang, D.; Novoselov, K. S.; Roth, S.; Geim, A. K. Raman Spectrum of Graphene and Graphene Layers. *Phys Rev Lett* **2006**, *97* (187401), 1–4. https://doi.org/10.1103/PhysRevLett.97.187401.

(60) Bruna, M.; Ott, A. K.; Ijäs, M.; Yoon, D.; Sassi, U.; Ferrari, A. C. Doping Dependence of the Raman Spectrum of Defected Graphene. *ACS Nano* **2014**, *8* (7), 7432–7441. https://doi.org/10.1021/nn502676g.

(61) Tsoukleri, G.; Parthenios, J.; Papagelis, K.; Jalil, R.; Ferrari, A. C.; Geim, A. K.; Novoselov, K. S.; Galiotis, C. Subjecting a Graphene Monolayer to Tension and Compression. *Small* **2009**, *5* (21), 2397–2402. https://doi.org/10.1002/smll.200900802.

(62) Ding, F.; Ji, H.; Chen, Y.; Herklotz, A.; Dörr, K.; Mei, Y.; Rastelli, A.; Schmidt, O. G. Stretchable Graphene: A Close Look at Fundamental Parameters through Biaxial Straining. *Nano Lett* **2010**, *10* (9), 3453–3458. https://doi.org/10.1021/nl101533x.

(63) Gokus, T.; Nair, R. R.; Bonetti, A.; Böhmler, M.; Lombardo, A.; Novoselov, K. S.; Geim, A. K.; Ferrari, A. C.; Hartschuh, A. Making Graphene Luminescent by Oxygen Plasma Treatment. *ACS Nano* **2009**, *3* (12), 3963–3968. https://doi.org/10.1021/nn9012753.

(64) Malard, L. M.; Pimenta, M. A.; Dresselhaus, G.; Dresselhaus, M. S. Raman Spectroscopy in Graphene. *Phys Rep* **2009**, *473*, 51–87. https://doi.org/10.1016/j.physrep.2009.02.003.

(65) Cançado, L. G.; Da Silva, M. G.; Martins Ferreira, E. H.; Hof, F.; Kampioti, K.; Huang, K.; Pénicaud, A.; Achete, C. A.; Capaz, R. B.; Jorio, A. Disentangling Contributions of Point and Line Defects in the Raman Spectra of Graphene-Related Materials. *2d Mater* **2017**, *4* (2). https://doi.org/10.1088/2053-1583/aa5e77.

(66) Lucchese, M. M.; Stavale, F.; Martins Ferreira, E. H.; Vilani, C.; Moutinho, M. V. O.; Capaz, R. B.; Achete, C. A.; Jorio, A. Quantifying Ion-Induced Defects and Raman Relaxation Length in Graphene. *Carbon N Y* **2010**, *48* (5), 1592–1597. https://doi.org/10.1016/j.carbon.2009.12.057.

(67) Koivistoinen, J.; Sládková, L.; Aumanen, J.; Koskinen, P.; Roberts, K.; Johansson, A.; Myllyperkiö, P.; Pettersson, M. From Seeds to Islands: Growth of Oxidized Graphene by Two-Photon Oxidation. *Journal of Physical Chemistry C* **2016**, *120*, 22330–22341. https://doi.org/10.1021/acs.jpcc.6b06099.

(68) Belitto, V. *Atomic Force Microscopy - Imaging, Measuring and Manipulating Surfaces at the Atomic Scale*; InTech, 2012. https://doi.org/10.5772/2673.

(69) Cha, W.; Heo, C.; Lee, S.; Yun, S. J.; Cho, B. W.; Ha, T.; Lee, Y. H. Probing Interfacial Charge Transfer between Amyloid-β and Graphene during Amyloid Fibrillization Using Raman Spectroscopy. *ACS Nano* **2022**. https://doi.org/10.1021/acsnano.2c11428.

(70) Katoch, J.; Kim, S. N.; Kuang, Z.; Farmer, B. L.; Naik, R. R.; Tatulian, S. A.; Ishigami, M. Structure of a Peptide Adsorbed on Graphene and Graphite. *Nano Lett* **2012**, *12* (5), 2342–2346. https://doi.org/10.1021/nl300286k.

(71) Sitsanidis, E. D.; Schirmer, J.; Lampinen, A.; Mentel, K. K.; Hiltunen, V. M.; Ruokolainen, V.; Johansson, A.; Myllyperkiö, P.; Nissinen, M.; Pettersson, M. Tuning Protein Adsorption on Graphene Surfaces via Laser-Induced

Oxidation. *Nanoscale Adv* **2021**, *3* (7), 2065–2074. https://doi.org/10.1039/d0na01028f.

(72) Mohanty, N.; Berry, V. Graphene-Based Single-Bacterium Resolution Biodevice and DNA Transistor: Interfacing Graphene Derivatives with Nanoscale and Microscale Biocomponents. *Nano Lett* **2008**, *8* (12), 4469–4476. https://doi.org/10.1021/nl802412n.

(73) Wang, X.; Wang, C.; Qu, K.; Song, Y.; Ren, J.; Miyoshi, D.; Sugimoto, N.; Qu, X. Ultrasensitive and Selective Detection of a Prognostic Indicator in Early-Stage Cancer Using Graphene Oxide and Carbon Nanotubes. *Adv Funct Mater* **2010**, *20* (22), 3967–3971. https://doi.org/10.1002/adfm.201001118.

(74) Priyadarsini, S.; Mohanty, S.; Mukherjee, S.; Basu, S.; Mishra, M. Graphene and Graphene Oxide as Nanomaterials for Medicine and Biology Application. *J Nanostructure Chem* **2018**, *8*, 123–137. https://doi.org/10.1007/s40097-018-0265-6.

(75) Fahmy, H. M.; Abu Serea, E. S.; Salah-Eldin, R. E.; Al-Hafiry, S. A.; Ali, M. K.; Shalan, A. E.; Lanceros-Méndez, S. Recent Progress in Graphene- and Related Carbon-Nanomaterial-Based Electrochemical Biosensors for Early Disease Detection. *ACS Biomater Sci Eng* **2022**, *8* (3), 964–1000. https://doi.org/10.1021/acsbiomaterials.1c00710.

(76) Wang, Y.; Di, S.; Yu, J.; Wang, L.; Li, Z. Recent Advances of Graphene-Biomacromolecule Nanocomposites in Medical Applications. *J Mater Chem B* **2023**, *11*, 500–518. https://doi.org/10.1039/d2tb01962k.

(77) Huang, S.; Zhong, Y.; Fu, Y.; Zheng, X.; Feng, Z.; Mo, A. Graphene and Its Derivatives: "One Stone, Three Birds" Strategy for Orthopedic Implant-Associated Infections. *Biomaterials Science*. Royal Society of Chemistry December 1, 2022, pp 380–399. https://doi.org/10.1039/d2bm01507b.

(78) Özcan, M.; Volpato, C. A. M.; Hian, L.; Karahan, B. D.; Cesar, P. F. Graphene for Zirconia and Titanium Composites in Dental Implants: Significance and Predictions. *Current Oral Health Reports*. Springer Science and Business Media B.V. September 1, 2022, pp 66–74. https://doi.org/10.1007/s40496-022-00310-3.

(79) Wang, S. X.; Lu, Y. B.; Wang, X. X.; Wang, Y.; Song, Y. J.; Wang, X.; Nyamgerelt, M. Graphene and Graphene-Based Materials in Axonal Repair of Spinal Cord Injury. *Neural Regeneration Research*. Wolters Kluwer Medknow Publications October 1, 2022, pp 2117–2125. https://doi.org/10.4103/1673-5374.335822.

(80) Hébert, C.; Masvidal-Codina, E.; Suarez-Perez, A.; Calia, A. B.; Piret, G.; Garcia-Cortadella, R.; Illa, X.; Del Corro Garcia, E.; De la Cruz Sanchez, J. M.; Casals, D. V.; Prats-Alfonso, E.; Bousquet, J.; Godignon, P.; Yvert, B.; Villa, R.; Sanchez-Vives, M. V.; Guimerà-Brunet, A.; Garrido, J. A. Flexible Graphene Solution-Gated Field-Effect Transistors: Efficient Transducers for Micro-Electrocorticography. *Adv Funct Mater* **2018**, *28* (12). https://doi.org/10.1002/adfm.201703976.

(81) Bullock, C. J.; Bussy, C. Biocompatibility Considerations in the Design of Graphene Biomedical Materials. *Adv Mater Interfaces* **2019**, *6* (11). https://doi.org/10.1002/admi.201900229.

(82) Jasim, D. A.; Ménard-Moyon, C.; Bégin, D.; Bianco, A.; Kostarelos, K. Tissue Distribution and Urinary Excretion of Intravenously Administered Chemically Functionalized Graphene Oxide Sheets. *Chem Sci* **2015**, *6* (7), 3952–3964. https://doi.org/10.1039/c5sc00114e.

(83) Jasim, D. A.; Murphy, S.; Newman, L.; Mironov, A.; Prestat, E.; McCaffrey, J.; Ménard-Moyon, C.; Rodrigues, A. F.; Bianco, A.; Haigh, S.; Lennon, R.; Kostarelos, K. The Effects of Extensive Glomerular Filtration of Thin Graphene Oxide Sheets on Kidney Physiology. *ACS Nano* **2016**, *10* (12), 10753–10767. https://doi.org/10.1021/acsnano.6b03358.

(84) Duch, M. C.; Budinger, G. R. S.; Liang, Y. T.; Soberanes, S.; Urich, D.; Chiarella, S. E.; Campochiaro, L. A.; Gonzalez, A.; Chandel, N. S.; Hersam, M. C.; Mutlu, G. M. Minimizing Oxidation and Stable Nanoscale Dispersion Improves the Biocompatibility of Graphene in the Lung. *Nano Lett* **2011**, *11* (12), 5201–5207. https://doi.org/10.1021/nl202515a.

(85) Nguyen, D.; Valet, M.; Dégardin, J.; Boucherit, L.; Illa, X.; de la Cruz, J.; del Corro, E.; Bousquet, J.; Garrido, J. A.; Hébert, C.; Picaud, S. Novel Graphene Electrode for Retinal Implants: An in Vivo Biocompatibility Study. *Front Neurosci* **2021**, *15* (615256). https://doi.org/10.3389/fnins.2021.615256.

(86) Hu, C. X.; Read, O.; Shin, Y.; Chen, Y.; Wang, J.; Boyes, M.; Zeng, N.; Panigrahi, A.; Kostarelos, K.; Larrosa, I.; Vranic, S.; Casiraghi, C. Effects of Lateral Size, Thickness, and Stabilizer Concentration on the Cytotoxicity of Defect-Free Graphene Nanosheets: Implications for Biological Applications. *ACS Appl Nano Mater* **2022**, *5* (9), 12626–12636. https://doi.org/10.1021/acsanm.2c02403.

(87) Vale, F. M.; Castro, M.; Monteiro, J.; Couto, F. S.; Pinto, R.; Giao Toscano Rico, J. M. Acrylic Bone Cement Induces the Droduction of Free Radicals by Cultured Human Fibroblasts. *Biomaterials* **1997**, *18*, 1133–1135. https://doi.org/10.1016/S0142-9612(97)00043-4.

(88) Dreyer, D. R.; Todd, A. D.; Bielawski, C. W. Harnessing the Chemistry of Graphene Oxide. *Chem Soc Rev* **2014**, *43* (15), 5288–5301. https://doi.org/10.1039/c4cs00060a.

(89) Di Mauro, G.; Amoriello, R.; Lozano, N.; Carnasciali, A.; Guasti, D.; Becucci, M.; Cellot, G.; Kostarelos, K.; Ballerini, C.; Ballerini, L. Graphene Oxide Nanosheets Reduce Astrocyte Reactivity to Inflammation and Ameliorate Experimental Autoimmune Encephalomyelitis. *ACS Nano* **2023**, *17* (3), 1965–1978. https://doi.org/10.1021/acsnano.2c06609.

(90) Girão, A. F.; Serrano, M. C.; Completo, A.; Marques, P. A. A. P. Is Graphene Shortening the Path toward Spinal Cord Regeneration? *ACS Nano*. American Chemical Society September 27, 2022, pp 13430–13467. https://doi.org/10.1021/acsnano.2c04756.

(91) Masvidal-Codina, E.; Illa, X.; Dasilva, M.; Calia, A. B.; Dragojević, T.; Vidal-Rosas, E. E.; Prats-Alfonso, E.; Martínez-Aguilar, J.; De la Cruz, J. M.; Garcia-Cortadella, R.; Godignon, P.; Rius, G.; Camassa, A.; Del Corro, E.; Bousquet, J.; Hébert, C.; Durduran, T.; Villa, R.; Sanchez-Vives, M. V.; Garrido, J. A.; Guimerà-Brunet, A. High-Resolution Mapping of Infraslow Cortical Brain Activity Enabled by Graphene Microtransistors. *Nat Mater* **2019**, *18*, 280–288. https://doi.org/10.1038/s41563-018-0249-4.

(92) Osorio, N. *Inbrain Neuroelectronics Believes Its Chips Could Outperform Elon Musk's Neuralink*. https://www.ibtimes.com/inbrain-neuroelectronics-believes-its-chips-could-outperform-elon-musks-neuralink-3243136.

(93) MINIGRAPH project. *MINIGRAPH - Minimally Invasive Neuromodulation Implant and implantation procedure based on ground-breaking GRAPHene technology for treating brain disorders*. https://minigraph-project.eu/the-project/.

(94) Moran, R. *Graphene Flagship spin-off company INBRAIN Neuroelectronics wins prestigious innovation award*. https://graphene-flagship.eu/graphene/news/graphene-flagship-spin-off-company-inbrain-neuroelectronics-wins-prestigious-innovation-award/.

(95) Pampaloni, N. P.; Lottner, M.; Giugliano, M.; Matruglio, A.; D'Amico, F.; Prato, M.; Garrido, J. A.; Ballerini, L.; Scaini, D. Single-Layer Graphene Modulates Neuronal Communication and Augments Membrane Ion Currents. *Nat Nanotechnol* **2018**, *13* (8), 755–764. https://doi.org/10.1038/s41565-018-0163-6.

(96) Park, S. Y.; Park, J.; Sim, S. H.; Sung, M. G.; Kim, K. S.; Hong, B. H.; Hong, S. Enhanced Differentiation of Human Neural Stem Cells into Neurons on Graphene. *Advanced Materials* **2011**, *23* (36), H263–H267. https://doi.org/10.1002/adma.201101503.

(97) Akhavan, O.; Ghaderi, E.; Abouei, E.; Hatamie, S.; Ghasemi, E. Accelerated Differentiation of Neural Stem Cells into Neurons on Ginseng-Reduced Graphene Oxide Sheets. *Carbon N Y* **2014**, *66* (Cvd), 395–406. https://doi.org/10.1016/j.carbon.2013.09.015.

(98) Aumailley, M. The Laminin Family. *Cell Adhesion and Migration*. 2013. https://doi.org/10.4161/cam.22826.

(99) School of Biomedical Sciences Wiki. *Secondary Protein Structure*. https://teaching.ncl.ac.uk/bms/wiki/index.php/File:Secondary.jpg.

(100) Guo, J.; Yao, X.; Ning, L.; Wang, Q.; Liu, H. The Adsorption Mechanism and Induced Conformational Changes of Three Typical Proteins with Different Secondary Structural Features on Graphene. *RSC Adv* **2014**, *4* (20), 9953–9962. https://doi.org/10.1039/c3ra45876h.

(101) Chong, Y.; Ge, C.; Yang, Z.; Garate, J. A.; Gu, Z.; Weber, J. K.; Liu, J.; Zhou, R. Reduced Cytotoxicity of Graphene Nanosheets Mediated by Blood-Protein Coating. *ACS Nano* **2015**, *9* (6), 5713–5724. https://doi.org/10.1021/nn5066606.

(102) Martinez, C. R.; Iverson, B. L. Rethinking the Term "Pi-Stacking." *Chem Sci* **2012**, *3* (7), 2191–2201. https://doi.org/10.1039/c2sc20045g.

(103) Hou, B.; Radadia, A. D. Differential Stability of Biosensing Proteins on Transferred Mono/Bilayer Graphene. *ACS Biomater Sci Eng* **2018**, *4* (2), 675–681. https://doi.org/10.1021/acsbiomaterials.7b00379.

(104) Mishyn, V.; Hugo, A.; Rodrigues, T.; Aspermair, P.; Happy, H.; Marques, L.; Hurot, C.; Othmen, R.; Bouchiat, V.; Boukherroub, R.; Knoll, W.; Szunerits, S. The Holy Grail of Pyrene-Based Surface Ligands on the Sensitivity of Graphene-Based Field Effect Transistors. *Sensors & Diagnostics* **2022**, *1* (2), 235–244. https://doi.org/10.1039/d1sd00036e.

(105) Singh, M.; Holzinger, M.; Tabrizian, M.; Winters, S.; Berner, N. C.; Cosnier, S.; Duesberg, G. S. Noncovalently Functionalized Monolayer Graphene for Sensitivity Enhancement of Surface Plasmon Resonance Immunosensors. *J Am Chem Soc* **2015**, *137* (8), 2800–2803. https://doi.org/10.1021/ja511512m.

(106) Zhang, Y.; Wu, C.; Guo, S.; Zhang, J. Interactions of Graphene and Graphene Oxide with Proteins and Peptides. *Nanotechnol Rev* **2013**, *2* (1), 27–45. https://doi.org/10.1515/ntrev-2012-0078.

(107) Šimšíková, M. Interaction of Graphene Oxide with Albumins: Effect of Size, PH, and Temperature. *Arch Biochem Biophys* **2016**, *593*, 69–79. https://doi.org/10.1016/j.abb.2016.02.015.

(108) Qi, Y.; Chen, W.; Liu, F.; Liu, J.; Zhang, T.; Chen, W. Aggregation Morphology Is a Key Factor Determining Protein Adsorption on Graphene Oxide and Reduced Graphene Oxide Nanomaterials. *Environ Sci Nano* **2019**, *6* (5), 1303–1309. https://doi.org/10.1039/c8en01408f.

(109) Wei, X. L.; Ge, Z. Q. Effect of Graphene Oxide on Conformation and Activity of Catalase. *Carbon N Y* **2013**, *60*, 401–409. https://doi.org/10.1016/j.carbon.2013.04.052.

(110) Wei, S.; Zou, X.; Tian, J.; Huang, H.; Guo, W.; Chen, Z. Control of Protein Conformation and Orientation on Graphene. *J Am Chem Soc* **2019**, *141*, 20335–20343. https://doi.org/10.1021/jacs.9b10705.

(111) Dobson, C. M. Protein Folding and Misfolding. *Nature* **2003**, *426*, 884–890. https://doi.org/10.1038/nature02261.

(112) Veitch, N. C. Horseradish Peroxidase: A Modern View of a Classic Enzyme. *Phytochemistry* **2004**, *65*, 249–259. https://doi.org/10.1016/j.phytochem.2003.10.022.

(113) Zhang, F.; Zheng, B.; Zhang, J.; Huang, X.; Liu, H.; Guo, S.; Zhang, J. Horseradish Peroxidase Immobilized on Graphene Oxide: Physical Properties and Applications in Phenolic Compound Removal. *Journal of Physical Chemistry C* **2010**, *114* (18), 8469–8473. https://doi.org/10.1021/jp101073b.

(114) Feng, D.; Liu, T. F.; Su, J.; Bosch, M.; Wei, Z.; Wan, W.; Yuan, D.; Chen, Y. P.; Wang, X.; Wang, K.; Lian, X.; Gu, Z. Y.; Park, J.; Zou, X.; Zhou, H. C. Stable Metal-Organic Frameworks Containing Single-Molecule Traps for Enzyme Encapsulation. *Nat Commun* **2015**, *6* (5979). https://doi.org/10.1038/ncomms6979.

(115) Berglund, G. I.; Carlsson, G. H.; Smith, A. T.; Szöke, H.; Henriksen, A.; Hajdu, J. The Catalytic Pathway of Horseradish Peroxidase at High Resolution. *Nature* **2002**, *417*, 463–468. https://doi.org/10.1038/417463a.

(116) Berglund, G. I. ; Carlsson, G. H. ; Hajdu, J. ; Smith, A. T. ; Szoke, H. ;; Henriksen, A. *Structure of Horseradish Peroxidase C1A Compound I*; 2002. https://doi.org/10.2210/pdb1hch/pdb.

(117) Berman, H. M.; Westbrook, J.; Feng, Z.; Gilliland, G.; Bhat, T. N.; Weissig, H.; Shindyalov, I. N.; Bourne, P. E. The Protein Data Bank. *Nucleic Acids Res* **2000**, *28* (1), 235–242. https://doi.org/10.1093/nar/28.1.235.

(118) Sehnal, D.; Bittrich, S.; Deshpande, M.; Svobodová, R.; Berka, K.; Bazgier, V.; Velankar, S.; Burley, S. K.; Koča, J.; Rose, A. S. Mol∗Viewer: Modern Web App for 3D Visualization and Analysis of Large Biomolecular Structures. *Nucleic Acids Res* **2021**, *49* (W), 431–437. https://doi.org/10.1093/nar/gkab314.

(119) No, Y. H.; Kim, N. H.; Gnapareddy, B.; Choi, B.; Kim, Y. T.; Dugasani, S. R.; Lee, O. S.; Kim, K. H.; Ko, Y. S.; Lee, S.; Lee, S. W.; Park, S. H.; Eom, K.; Kim, Y. H. Nature-Inspired Construction of Two-Dimensionally Self-Assembled Peptide on Pristine Graphene. *Journal of Physical Chemistry Letters* **2017**, *8* (16), 3734–3739. https://doi.org/10.1021/acs.jpclett.7b00996.

(120) Ling, S.; Li, C.; Adamcik, J.; Wang, S.; Shao, Z.; Chen, X.; Mezzenga, R. Directed Growth of Silk Nanofibrils on Graphene and Their Hybrid Nanocomposites. *ACS Macro Lett* **2014**, *3* (2), 146–152. https://doi.org/10.1021/mz400639y.

(121) Mahmoudi, M.; Akhavan, O.; Ghavami, M.; Rezaee, F.; Ghiasi, S. M. A. Graphene Oxide Strongly Inhibits Amyloid Beta Fibrillation. *Nanoscale* **2012**, *4* (23), 7322–7325. https://doi.org/10.1039/c2nr31657a.

(122) Jin, Y.; Sun, Y.; Chen, Y.; Lei, J.; Wei, G. Molecular Dynamics Simulations Reveal the Mechanism of Graphene Oxide Nanosheet Inhibition of Aβ1-42 Peptide Aggregation. *Physical Chemistry Chemical Physics* **2019**, *21* (21), 10981–10991. https://doi.org/10.1039/c9cp01803d.

(123) Giuri, D.; Barbalinardo, M.; Zanna, N.; Paci, P.; Montalti, M.; Cavallini, M.; Valle, F.; Calvaresi, M.; Tomasini, C. Tuning Mechanical Properties of Pseudopeptide Supramolecular Hydrogels by Graphene Doping. *Molecules* **2019**, *24* (23). https://doi.org/10.3390/molecules24234345.

(124) Han, D.; Yan, L. Supramolecular Hydrogel of Chitosan in the Presence of Graphene Oxide Nanosheets as 2D Cross-Linkers. *ACS Sustain Chem Eng* **2014**, *2* (2), 296–300. https://doi.org/10.1021/sc400352a.

(125) Tao, C. A.; Wang, J.; Qin, S.; Lv, Y.; Long, Y.; Zhu, H.; Jiang, Z. Fabrication of PH-Sensitive Graphene Oxide-Drug Supramolecular Hydrogels as Controlled Release Systems. *J Mater Chem* **2012**, *22* (47), 24856–24861. https://doi.org/10.1039/c2jm34461k.

(126) Das, A.; Pisana, S.; Chakraborty, B.; Piscanec, S.; Saha, S. K.; Waghmare, U. V.; Novoselov, K. S.; Krishnamurthy, H. R.; Geim, A. K.; Ferrari, A. C.; Sood, A. K. Monitoring Dopants by Raman Scattering in an

Electrochemically Top-Gated Graphene Transistor. *Nat Nanotechnol* **2008**, *3*, 210–215. https://doi.org/10.1038/nnano.2008.67.

(127) Palladino, P.; Torrini, F.; Scarano, S.; Minunni, M. 3,3′,5,5′-Tetramethylbenzidine as Multi-Colorimetric Indicator of Chlorine in Water in Line with Health Guideline Values. *Anal Bioanal Chem* **2020**, *412*, 7861–7869. https://doi.org/10.1007/s00216-020-02918-9.

(128) Wang, M.; Gao, B.; Tang, D.; Sun, H.; Yin, X.; Yu, C. Effects of Temperature on Aggregation Kinetics of Graphene Oxide in Aqueous Solutions. *Colloids and Surfaces A* **2018**, *538*, 63–72. https://doi.org/10.1016/j.colsurfa.2017.10.061.

(129) Li, S.; Dong, S.; Xu, W.; Tu, S.; Yan, L.; Zhao, C.; Ding, J.; Chen, X. Antibacterial Hydrogels. *Advanced Science*. John Wiley and Sons Inc. May 1, 2018. https://doi.org/10.1002/advs.201700527.

(130) Adams, D. J. Does Drying Affect Gel Networks? *Gels* **2018**, *4* (32). https://doi.org/10.3390/gels4020032.

(131) Mears, L. L. E.; Draper, E. R.; Castilla, A. M.; Su, H.; Zhuola; Dietrich, B.; Nolan, M. C.; Smith, G. N.; Doutch, J.; Rogers, S.; Akhtar, R.; Cui, H.; Adams, D. J. Drying Affects the Fiber Network in Low Molecular Weight Hydrogels. *Biomacromolecules* **2017**, *18* (11), 3531–3540. https://doi.org/10.1021/acs.biomac.7b00823.

(132) Singh, V.; Snigdha, K.; Singh, C.; Sinha, N.; Thakur, A. K. Understanding the Self-Assembly of Fmoc-Phenylalanine to Hydrogel Formation. *Soft Matter* **2015**, *11* (26), 5353–5364. https://doi.org/10.1039/c5sm00843c.

(133) Barth, A. Infrared Spectroscopy of Proteins. *Biochim Biophys Acta Bioenerg* **2007**, *1767* (9), 1073–1101. https://doi.org/10.1016/j.bbabio.2007.06.004.

(134) Barth, A.; Zscherp, C. What Vibrations Tell Us about Proteins. *Quarterly Reviews of Biophysics*. November 2002, pp 369–430. https://doi.org/10.1017/S0033583502003815.

ORIGINAL PAPERS

I

TUNING PROTEIN ADSORPTION ON GRAPHENE SURFACES *VIA* LASER-INDUCED OXIDATION

by

Efstratios D. Sitsanidis, Johanna Schirmer, Aku Lampinen, Kamila K. Mentel, Vesa-Matti Hiltunen, Visa Ruokolainen, Andreas Johansson, Pasi Myllyperkiö, Maija Nissinen & Mika Pettersson, 2021

PAPER

Check for updates

Tuning protein adsorption on graphene surfaces *via* laser-induced oxidation†

Efstratios D. Sitsanidis, [ID] [a] Johanna Schirmer, [ID] [a] Aku Lampinen, [ID] [a] Kamila K. Mentel, [ID] [a] Vesa-Matti Hiltunen, [ID] [b] Visa Ruokolainen, [ID] [c] Andreas Johansson, [ID] [ab] Pasi Myllyperkiö, [ID] [a] Maija Nissinen [ID] [a] and Mika Pettersson [ID] *[a]

An approach for controlled protein immobilization on laser-induced two-photon (2P) oxidation patterned graphene oxide (GO) surfaces is described. Selected proteins, horseradish peroxidase (HRP) and biotinylated bovine serum albumin (b-BSA) were successfully immobilized on oxidized graphene surfaces, *via* non-covalent interactions, by immersion of graphene-coated microchips in the protein solution. The effects of laser pulse energy, irradiation time, protein concentration and duration of incubation on the topography of immobilized proteins and consequent defects upon the lattice of graphene were systemically studied by atomic force microscopy (AFM) and Raman spectroscopy. AFM and fluorescence microscopy confirmed the selective aggregation of protein molecules towards the irradiated areas. In addition, the attachment of b-BSA was detected by a reaction with fluorescently labelled avidin-fluorescein isothiocyanate (Av-FITC). In contrast to chemically oxidized graphene, laser-induced oxidation introduces the capability for localization on oxidized areas and tunability of the levels of oxidation, resulting in controlled guidance of proteins by light over graphene surfaces and progressing towards graphene microchips suitable for biomedical applications.

Introduction

Graphene is a carbon allotrope, consisting of a monolayer of sp^2 hybridized carbon atoms bound together in a honeycomb lattice. Due to its mechanical, physicochemical, optical, electronic and biological properties, this two-dimensional (2D) nanomaterial has attracted much attention in the biomedical field. Indeed, functionalized graphene-based nanostructures have been already reported for tissue engineering, cancer therapy, drug delivery, regenerative medicine, imaging, cytotoxicity and biosensing applications.[1–5]

Graphene and its derivatives (graphene oxide, GO, reduced graphene oxide, rGO) can be prepared in a scalable and cost-effective manner. They demonstrate a strong antimicrobial activity and their amphiphilic nature allows conjugation with biomolecules. At the same time, a high specific surface area results in the enhancement of cell adhesion, proliferation and in certain cases, cell differentiation.[6–8] To this extent, graphene-based implantable materials have already led to advanced therapeutic approaches by fixing or replacing tissues and organs damaged by accident or disease. Such sophisticated bionic devices exploit the synergy of biology with electronics (bioelectronics) and focus on restoring vision, treating spinal cord injuries and ameliorating neurodegenerative diseases.[9] Certain devices (neural interfaces) which have been already clinically developed, consist of cortical electrodes, retina implants, spinal cord and vagal nerve stimulators, deep brain stimulation (DBS) and cochlear implants.[10]

In terms of biocompatibility, the response of the human body towards injectable or implantable graphene-based materials is not yet fully understood. As different physicochemical properties may generate different interactions with biological systems, all implantable devices need to meet specific key requirements such as minimal inflammation, an adequate signal-to-noise ratio and mechanical compliance towards the affected tissues.[10,11] Any chemical contamination during their formulation process can cause adverse biological reactions therefore, to minimize potential toxic effects, an effective sterilization and depyrogenation procedure should be followed. In addition, their stability and functionality need to be assessed over time.[12] Although the phenomenon of biocompatibility is complex and its mechanisms not fully known, for those materials exposed to the human body, it is associated with the adsorption of proteins on their surface.[13]

[a]Department of Chemistry, Nanoscience Center, University of Jyväskylä, P. O. Box 35, FI-40014 JYU, Finland. E-mail: mika.j.pettersson@jyu.fi

[b]Department of Physics, Nanoscience Center, University of Jyväskylä, P. O. Box 35, FI-40014 JYU, Finland

[c]Department of Biological and Environmental Sciences, Nanoscience Center, University of Jyväskylä, P. O. Box 35, FI-40014 JYU, Finland

† Electronic supplementary information (ESI) available: Raman spectra, Fermi level plots, compressive strain plots. See DOI: 10.1039/d0na01028f

While working towards bioinspired surfaces, our study aims at the preparation of biocompatible graphene-based microchips, to induce graphene–cell interactions, as potential implantable devices. Here, we describe the selective functionalization of laser-induced GO patterns on graphene surfaces by protein adsorption *via* non-covalent interactions.

Our protein models were HRP enzyme and b-BSA. HRP was previously immobilized on GO sheets in aqueous suspensions by Zhang *et al.*[14] Based on their findings, certain pH values favoured either electrostatic interactions or hydrogen bonding, when the pH was below or above the enzyme's isoelectric point (pI = 7.2), respectively. According to the authors, although physical adsorption resulted in conformational changes of the HRP molecule, its observed catalytic activity was mainly determined by the type of interactions with the GO sheets. In addition, loading the enzyme on GO sheets did not affect its activity, provided that the surface of the sheets was not crowded, thus allowing free diffusion of the HRP substrate and the respective product molecules.

BSA is the most abundant protein found in the blood plasma, while its adsorption over the surface of implantable materials passivates the reaction of the human body.[13] Huang *et al.* reported that incubation of GO with 10% fetal bovine serum reduced significantly its cytotoxicity.[15] Furthermore, *in silico* studies based on BSA's adsorption over graphene, showed that free adsorption occurred with little structural rearrangements.[16,17] In contrast, forced adsorption simulations led to orientations capable of preserving the structural properties of the majority of the protein's binding sites. Herein, we used the biotinylated derivative (b-BSA) due to its high affinity towards avidin to detect its immobilization by the reaction with the fluorescently labelled Av-FITC.

In our case, the immobilization of proteins is based on non-covalent interactions by immersion of the laser-patterned microchips into protein solutions. In contrast to covalent binding, supramolecular forces maintain the structure and the properties of graphene. Physical adsorption is caused by weak interactions among graphene and protein molecules, such as H-bonding, van der Waals forces, hydrophobic, electrostatic and aromatic–aromatic (π–π stacking) interactions. It is of note that such forces depend on the morphology and hydrophobicity of the GO surface. Additionally, physical adsorption is mainly hydrophobic in nature due to the sp[2] hybridization of carbon atoms within the honeycomb lattice, and it depends on both the electron density and geometry of the protein molecules. By adapting their shape, proteins orientate their aromatic residues accordingly, resulting in stronger π–π stacking with graphene.[18,19]

In this study, the focus is on the topography of the protein molecules rather than their functionality, therefore the catalytic activity of the immobilized HRP enzyme was not assessed. A range of different conditions for the irradiation process and adsorption protocols were used to introduce tunability in protein functionalization and investigate any consequently generated defects upon graphene. The methodology presented here can be used to selectively localize various proteins on graphene, which is highly beneficial for the development of bioinspired graphene devices suitable, for example, in virus detection,[20] electrochemical catalysis[21] and cell/tissue adhesion.

Results and discussion

Raman and AFM assessment of oxidized graphene and protein immobilization

We used a set of squared silicon chips (7 mm × 7 mm) consisting of a 300 nm upper layer of SiO_2 and a monolayer of graphene on top (5 mm × 5 mm). A reference metal grid was prepared on the surface of graphene, to ease exposure of the oxidation patterns by laser-induced 2P oxidation.[22–24] Details of the microchip preparation and its full characterization are described in our previous studies.[25] Graphene was irradiated using a range of laser pulse energies (5 to 30 pJ) and duration of irradiation from 0.2 up to 1.5 s per spot, to assess its effect on the level of oxidation and optimal conditions for protein adhesion. The matrices of squares with sizes ∼2 × 2 μm² were patterned by step-by-step irradiation with steps of 0.1 μm and laser spot diameter of ∼0.6 μm (Fig. 1).
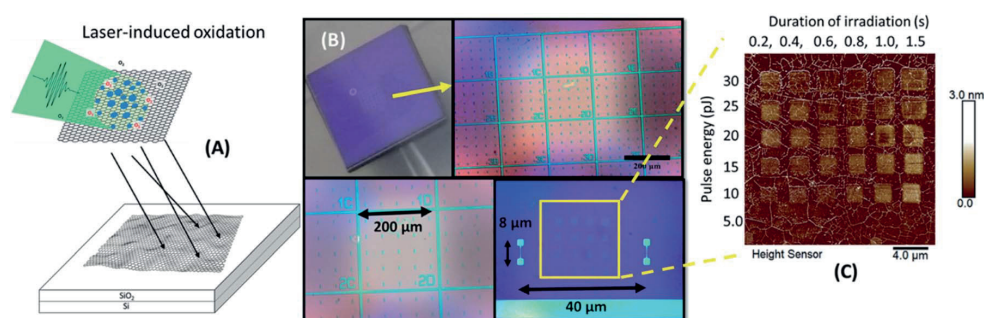
Fig. 1 Graphene microchip and depiction of the matrix of squares after irradiation. (A) Schematic representation and (B) optical images of a Si/SiO₂ microchip bearing a monolayer of graphene on top with given dimensions of the pattern grid; (C) AFM height sensor image of the irradiated area (matrix of squares), using a range of laser pulse energies and duration of irradiation; the field of view (FOV) is 22 × 22 μm².
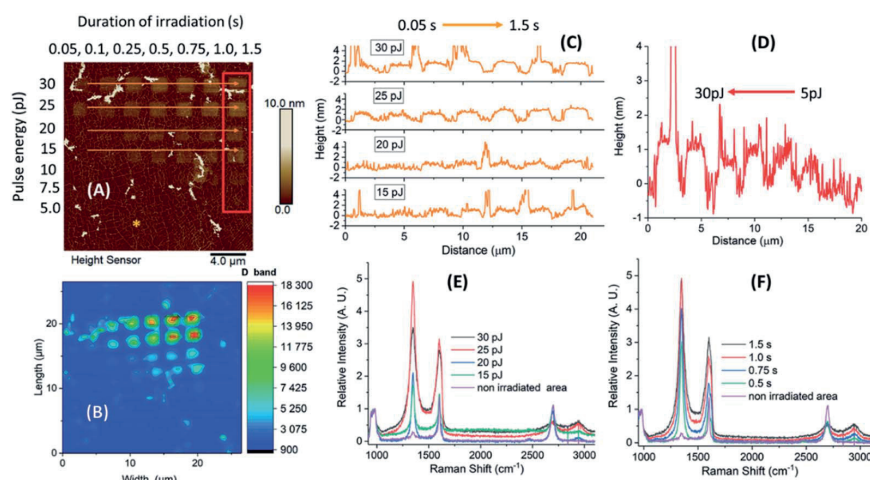
Fig. 2 Evaluation of laser induced 2P oxidation of a microchip prior to the treatment with protein solutions. (A) AFM height sensor image of the irradiated microchip with designated oxidized areas (red frame and orange arrows); (B) Raman map showing integrated intensity in the D band area at ∼1350 cm^{-1}. Height distribution profiles of the designated areas; (C) increased duration of irradiation (0.05–1.5 s, orange arrows); (D) increased laser pulse energy (5–30 pJ, red frame). Raman spectra of the designated irradiated and non-irradiated (denoted by the asterisk) spots, normalized with respect to the Si band intensities; (E) increased pulse energy at a constant irradiation of 1.5 s; (F) increased duration of irradiation at a constant pulse energy of 25 pJ.

When comparing the height distribution profiles of the irradiated graphene squares before any treatment with protein solutions, it was evident that an increase of the laser pulse energy (from 5 to 30 pJ) for the same irradiation time (1.5 s) resulted in higher height profiles for the corresponding graphene spots (Fig. 2-D; irradiated area within the red frame).

On the other hand, when increasing the irradiation time (from 0.05 to 1.5 s), no significant increase in height was noticed for higher pulse energies (30 and 25 pJ). In contrast, for lower energies (20 and 15 pJ), the difference in heights was more profound (Fig. 2-C; irradiated areas marked by the orange arrows). The observed differences in height indicate a different level of graphene oxidation achieved by laser-induced oxidation, as stated in our previous studies.[22] In addition, Raman measurements of the oxidized samples showed that the intensity of the D band and interestingly that of G were increasing by irradiation (in all times $I_D > I_G$). The G band frequency was slightly shifted towards higher wavenumbers (blue-shifted) which denotes a signature of oxidized graphene.

The effect of laser oxidation on HRP immobilization

A combination of different laser pulse energies and irradiation times allowed us to assess the effects of different levels of graphene oxidation on protein adhesion and consequently defects upon the graphitic lattice, induced by protein immobilization. A microchip sample was therefore incubated in HRP solution for one hour, and AFM images and Raman spectra were recorded prior and after incubation.

The topographic height profiles of the irradiated squares verified an increase in height from 2 nm to almost ∼7 nm after HRP adhesion (Fig. 3). A dense aggregation of enzyme

molecules was observed in the middle and over the edges of each irradiated square. For such a short incubation time (1 h) there were no significant differences among the observed height profiles for the squares irradiated by intense pulse energies (30 and 25 pJ). For moderate pulse energies (20 and 15 pJ), however, HRP adhesion was denser when irradiation time had been longer. This suggests that both the irradiation conditions and the incubation time may affect protein adhesion, *vide infra*.

In contrast to the height profiles, the Raman spectra appeared both qualitatively and quantitatively different regarding the given irradiation conditions (Fig. S1–S3 and Tables S1–S3†). As anticipated, the intensity of the G and 2D bands were prominent for all non-irradiated graphene areas. In contrast, for the oxidized areas, both D and G peaks were more intense compared to the 2D vibrational mode. It is of note that the position, intensity and full width at half maximum (FWHM) of the 2D and D + D′ peaks were changing depending on the used irradiation conditions.

Furthermore, less intense peaks of the D′ at ∼1620 cm^{-1} and G* at ∼2460 cm^{-1} were also observed. The D′ band appeared as a shoulder of the G peak in the spectra of graphene squares irradiated under moderate conditions (15 and 20 pJ/irradiation time over 0.5 s). For the regions treated with an increased laser pulse energy and irradiation time (25 and 30 pJ/irradiation over 1.5 s), both peaks merged into a broader band (Fig. S1–S3†). On the other hand, for the non-irradiated graphene regions, the G* peak was observed at a very low intensity.

The D or disorder-induced band usually ranges at ∼1250–1450 cm^{-1} and is indicative of lattice defects or appears near the edges of graphene. It originates from an intervalley process by the transverse optical phonons and associates to the breathing
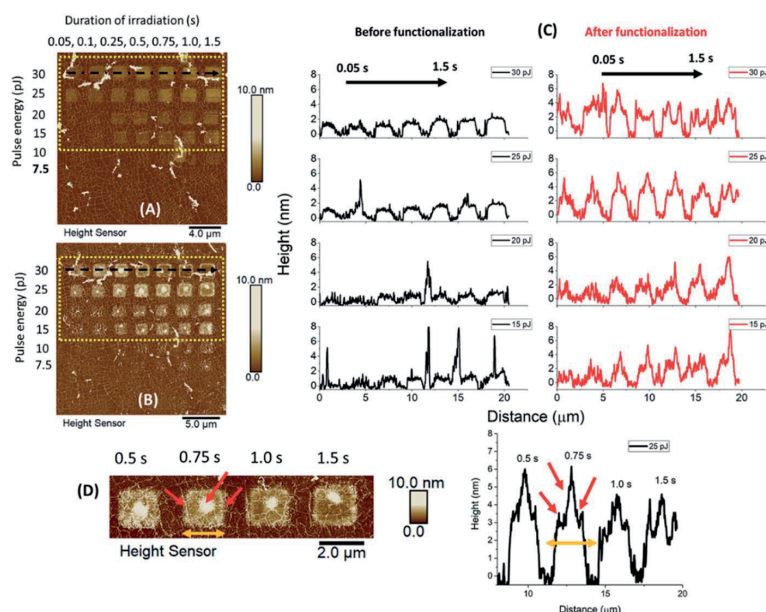
Fig. 3 Evaluation of laser pulse energy and duration of irradiation upon protein adhesion. AFM height sensor images of the microchip, before (A) and after (B) HRP adhesion; (C) topographic height profiles of a designated area (yellow frame) before and after functionalization; (D) HRP aggregation towards the middle and over the edges of the squares, irradiated by laser pulse energy of 25 pJ at different durations (red arrows and corresponding height profiles).

oscillation of the six-membered ring due to the presence of structural defects. The G or graphitic vibrational mode appears at $\sim$1580 cm^{-1} and is due to the in-plane motion of the sp^2 hybridized carbon atoms (bond stretching). The less intense D$'$ peak usually appears as a shoulder of the G band and is associated with lattice defects. The G* band can be attributed to two different time-order phonon processes, a combination of transverse optical and longitudinal acoustic phonons.[26] The 2D vibrational mode, an overtone of the D band, appears near 2700 cm^{-1} and is a second-order, two phonon, double resonance process. The D + D$'$ located near 2900 cm^{-1} is a combination of defect activated phonons related to the D and D$'$ vibrations.[27–30]

For all studied cases (irradiated and non-irradiated graphene), the Raman bands were shifted towards lower wavenumbers after HRP adhesion. The observed downshift was quantitatively different for each peak. One of our main findings is that a significant downshift was evident for areas irradiated under less intense conditions (laser pulse energy of 15 and 20 pJ for a duration of 1.5 s), especially for the G and 2D bands (Table 1 and Fig. 4). When more intense irradiation was applied, however, not any notable shift was observed for the G band in contrast to the 2D peak, which appeared notably shifted after functionalization. In addition, the shift of the D band was smaller in areas treated under intense pulse energy, following the same pattern as above (Fig. S1–S3†).

For more intense irradiation conditions (laser pulse energy of 25 and 30 pJ/irradiation time > 1.0 s), our observations

indicate that the defects on the graphitic lattice, caused by laser-induced oxidation, generated a strong Raman fingerprint. Therefore, the weak supramolecular interactions, induced by HRP adhesion, when added to the overall number of defects

Table 1 Observed downshifts of the Raman bands after HRP adhesion. Shifts were calculated based on the position of the peaks obtained by the Lorentzian function fitting procedure

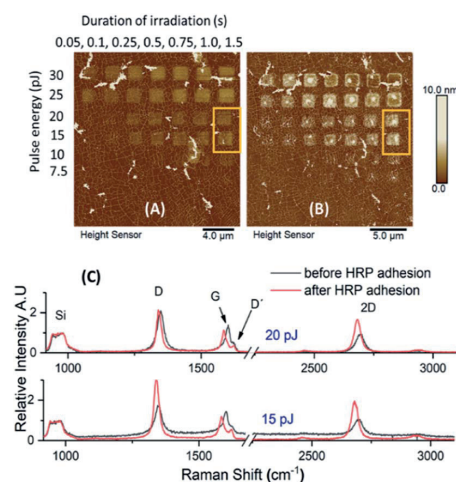| Conditions	Red shift (cm^{-1})		
	D	G	2D
Increased pulse energy (pJ)/constant irradiation time of 1.5 s			
30	4.2	0.8	8.8
25	5.3	1.0	9.7
20	6.1	13.6	11.2
15	7.4	14.0	14.4
Increased irradiation time (s)/constant pulse energy of 25 pJ			
1.5	4.7	1.1	4.3
1.0	5.2	2.3	8.3
0.75	6.5	4.9	12.8
0.5	7.4	12.8	13.5
Non-irradiated spots			
Spot 1	4.2	3.7	6.5
Spot 2	4.6	4.2	5.2
Spot 3	3.2	2.4	2.8
Spot 4	3.7	5.0	7.2
Spot 5	2.5	3.9	4.3

Fig. 4 Observed Raman shifts. AFM height sensor images of the microchip, depicting the designated areas before (A) and after (B) HRP adhesion. (C) Raman spectra recorded prior and after HRP adhesion. Moderate irradiation conditions: laser pulse energy of 15 and 20 pJ and duration of irradiation of 1.5 s; all spectra are normalized with respect to the Si band intensities.

Fig. 5 2D vs. G Raman band position plot. The green line shows the effect of pure strain without doping, and the red line the effect of doping without strain. The blue line shows a case of changing doping with constant −0.05% biaxial strain. Symbols show measurement points in different places on the sample. The blue triangle represents measurements from spots irradiated by constant 25 pJ pulse energy before HRP adhesion and green triangles after HRP adhesion. Black squares represent measurements from spots irradiated by different pulse energies (30–15 pJ) with a constant 1.5 s exposure time before functionalization and red circles after functionalization. Purple diamonds refer to non-irradiated graphene before functionalization and yellow triangles after.

were not strong enough to cause significant changes at the spectroscopic features of the densely deformed graphene areas and thus causing a smaller downshift. Furthermore, for any specific irradiated spot on the lattice, the Raman vibrational modes originate by different phonon processes and therefore respond to a different extent towards the applied supramolecular forces.

Similar shifts caused by strain on the graphitic lattice have already been reported.[31,32] In a previous case, the deposition of gold nanoparticles (GNPs) on graphene resulted in the whole Raman spectrum to downshift.[33] More specifically, the shift of the 2D peak (~6 cm^{-1}) was more significant than that of the G band (~3 cm^{-1}). In the attempt to explain the observed downshift, a model of local strain was proposed, generated by the charge transfer among GNPs and graphene. Regarding our sample, the observed downshift of the G and 2D bands could be associated to both strain and doping effects due to charge transfer from the protein to graphene. Based on Ferrari et al., a downshift for both bands would indicate a decrease of positive doping.[34,35] In general, for strained or doped graphene, both the G and 2D bands are shifted. Depending on its origin, such shifting is slightly different, which makes it possible to differentiate their contributions. We, therefore, calculated the level of strain and doping from the obtained Raman data (Fig. 5, S4 and S5†)[36–39] following a methodology described by Lee et al.[36]

Non-irradiated graphene is initially p-type doped (about 0.35 eV) because of annealing enhanced graphene/SiO$_2$ substrate conformity, which is the case for all our graphene samples on SiO$_2$ substrate. Laser-induced oxidation does not seem to change the doping substantially, and the change is in different directions at the different irradiated spots as can be seen by the
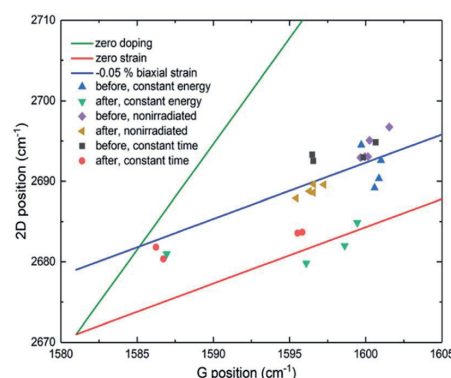
Fermi level plots (black squares, Fig. S4 and S5†). HRP adhesion (red circles, Fig. S4 and S5†) does not change the doping significantly for most of the patterns. However, in those squares where it does (15 and 20 pJ laser pulse energy; Fig. S4-A†/irradiation over 0.5 s; Fig. S5-A†), the change is large, and the doping is almost neutralized. It changes from ~0.35 eV to ~0.05 eV but still remains p-type.

According to the applied experimental conditions, the HRP molecules were positively charged as we adjusted the pH of the phosphate buffer solution slightly below the pI (7.2) of the enzyme. Our intention was to induce coulombic forces between the protein molecules and GO. Albeit a dense aggregation of HRP was observed by AFM upon the irradiated areas, the enzyme interacted with the whole graphitic surface. Indeed, the non-irradiated spot 4 (pristine graphene, Fig. S3†), although positioned far from any irradiated areas, showed a similar downshift pattern to the irradiated areas after the functionalization process. However, the magnitude of the shift was smaller. The differences in shifting among the irradiated and non-irradiated regions of graphene can only suggest differences in the type of supramolecular interactions (electrostatic forces or hydrogen bonding) between the protein molecules and the graphitic lattice.

For the non-irradiated spots and those oxidized under moderate conditions, a sharp 2D band was present before and after HRP adhesion. For regions bearing denser deformities, however, the sharp 2D band was significantly broadened. According to Ferreira et al., an increase of the lattice defects leads to an increase in the intensity of the defect activated bands. In contrast, for denser deformities, the 2D band is suppressed as the honeycomb graphene network is disturbed.[40]

This explains the increase of the FWHM of the 2D peak and other defect activated bands (D and D + D′) towards regions oxidized under more intense conditions. Therefore, for irradiation time of 1.5 s and pulse energy ranging from 15 pJ to 30 pJ, the FWHM of the D and 2D bands was increased by 56 and 170 cm^{-1} accordingly, while the D + D′ vibrational mode was visible only at regions bearing denser deformities. Similarly, by increasing the irradiation time from 0.5 s to 1.5 s under constant pulse energy of 25 pJ, the FWHM of the D, 2D and D + D′ bands increased by 18, 99 and 25 cm^{-1} respectively.

The effect of HRP immobilization on GO was further assessed by comparison of the I_D/I_G ratio before and after the functionalization of the microchip (Fig. 6). Significant changes in the ratio values were noticed only over the areas of graphene oxidized under moderate conditions. For a constant irradiation time (1.5 s), the highest difference in the I_D/I_G ratio was spotted at areas treated with the lowest laser pulse energy (15 pJ). The ratio increased from 1.29 to 2.16, whereas minor changes were observed as the pulse energy increased. For those regions treated with constant pulse energy (25 pJ) over different irradiation times, the alterations in the I_D/I_G ratio were significant at 0.5 s of irradiation.

Differences in the I_D/I_G ratio related to differences in doping have been previously reported. In their work, Ferrari *et al.*

describe how the intensity of the D band decreases as doping increases.[35] In our case, the same observation applies; the intensity of the D band is increased when doping is decreased, which explains the increase in I_D/I_G ratio. Such a result denotes that although HRP adhesion introduces defects upon the graphene monolayer, these are noticeable at a different extent, depending on the initial deformities achieved by laser-induced 2P oxidation. In other words, the weak supramolecular interactions between the enzyme and GO surface are notably visible when the deformities over the lattice of graphene are less dense.

The effect of incubation cycles on HRP immobilization

A second microchip was successively incubated in HRP solution for 1, 2 and 3 h, respectively, (totally 6 h of incubation) to investigate potential concentration and sample handling effects on protein immobilization. The enzymatic solution was diluted to a quarter of the initial concentration, AFM height sensor images were captured after each incubation cycle, and Raman spectra were recorded prior any treatment and after functionalization (Fig. 7).

For a selected area of graphene, irradiated by 15 pJ for different lengths of times, the 2P oxidation process increased the height of the irradiated squares up to 1–1.5 nm in a homogeneous manner. After two cycles of incubation (totally 3 h of treatment), the designated squares increased their heights due to protein adhesion. Based on the topographic height profiles, a denser accumulation of the enzyme molecules was observed at the centre and over the edges of each square. A third incubation cycle for 3 more hours (totally 6 h of treatment) resulted in heights up to 15 nm. It is of note that for an increased irradiation time (1.5 s) the same aggregation pattern was observed. For shorter irradiation times (0.75–1.25 s), however, HRP enzymes immobilized upon the surface of the squares almost evenly.

To ensure that the observed changes in height and the topography of HRP enzyme are not related to non-specific adsorption of the buffer solutes, we compared the height profile of a non-irradiated area of the microchip after each incubation cycle. Indeed, no changes in height were present after 6 h of treatment, indicating the absence of HRP molecules upon pristine graphene (Fig. S6†). In addition, although scanning electron microscopy (SEM) images of the microchip showed the deposition of crystals on its surface, their shape was rather distinct and could not be related to immobilized HRP (Fig. S6-D†).

Further to this, we generated histograms corresponding to the topographic height profiles of the irradiated area (Fig. 7-A) by using the depth function of Nanoscope analysis software (Fig. S7-C†). The x axis of each histogram represents the measured heights from the AFM height sensor channel *versus* the percentage of data points (y axis) related to the corresponding heights. Before treatment, two distinct peaks are visible (black histogram). By comparison to the AFM height sensor image (Fig. 7-A and B) it is evident that the peak at ∼0 nm corresponds to non-irradiated graphene while the peak at ∼0.5 nm to oxidized graphene. After each incubation cycle,
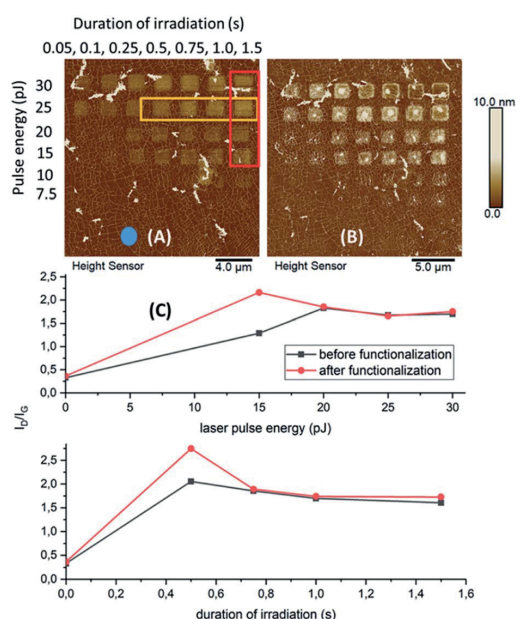

Fig. 6 I_D/I_G ratios prior and after incubation of the microchip in HRP solution. AFM height sensor image of the microchip, before (A) and after (B) HRP adhesion with designated areas. The blue spot is non-irradiated graphene. (C) Ratio values correspond to graphene squares (red frame) irradiated at a constant duration of 1.5 s over a range of pulse energies (top plot) and those squares (yellow frame) irradiated at a constant pulse energy of 25 pJ over a range of time durations (bottom plot).
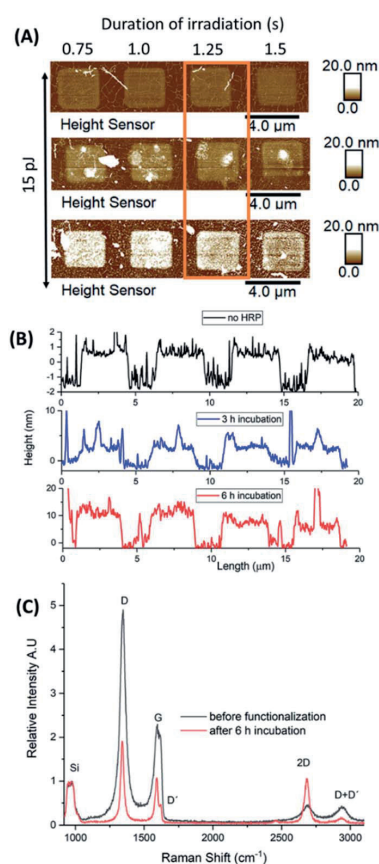
Fig. 7 Incubation studies in HRP solution. (A) AFM height sensor images of a selected area at different cycles of incubation. Graphene was irradiated by laser pulse energy of 15 pJ at different time durations; (B) topographic height profiles of the designated area after 3 and 6 h of incubation; (C) Raman spectra of a selected irradiated square (orange frame) before and after functionalization. All spectra are normalized to the Si bands intensity.

both peaks were broadened (blue and red histograms) while a notable shift was observed for those peaks related to irradiated graphene. Indeed, shifting denotes an increase of height (x axis values) by increasing the time of incubation from 3 h (4 nm) to 6 h (10 nm). Prior treatment, two distinct height levels (x axis values) are observed and almost all data points (y axis) fall within this range. The broadening of the peaks after each incubation cycle, suggests the preference of HRP molecules to immobilize upon irradiated graphene resulting in a rougher surface with variations in height. The shifting towards increased heights (x axis) supports the increased deposition of HRP molecules.

To relate the successive incubation cycles with the formation of multiple HRP layers upon irradiated graphene (measured heights, Fig. 7-B) we took into account the dimensions and hydrophobic–hydrophilic distribution of the enzyme itself

(Protein Data Bank ID, 1HCH).[41] Assuming that the GO–HRP interaction is mostly electrostatic then one could expect that regions with a higher amount of hydrophilic amino-acids will be more prone to adsorption. According to the measured height profiles (Fig. 3-C, S8-A†) the nominal height of immobilized HRP in a single layer should be around 3 nm ($\pm$0.6 nm owing to the deformation-induced upon AFM indentation). Based on our findings, after 3 h of incubation 1–2 layers of the enzyme seem to have been deposited (1 nm + 3 nm) while after 6 h, 3–4 layers (Fig. S8†).

After 6 h of incubation, the Raman spectra showed a significant decrease in the intensity of the D and G bands ($I_D > I_G$ in both cases). Also, the initial broad G band appeared rather sharp after 6 h of treatment, bearing the D′ peak as a shoulder, while the 2D signal increased its intensity almost to that of the G band (Fig. 7-C). The I_D/I_G ratio values, prior and after HRP adhesion were 2.28 and 1.85, respectively, which suggests an increase in doping after 6 h of treatment. Finally, a downshift was also observed which was qualitatively different for all peaks (D: 3.5 cm^{-1}, G: 5.7 cm^{-1}, 2D: no shift observed, D + D′: 5.6 cm^{-1}) showing the presence of strain and/or doping effects due to charge transfer over the graphitic lattice.

In contrast to shorter incubation times (1 h, first microchip), additional immersion cycles in HRP solution (second microchip) increased further the height of the irradiated squares, indicating a denser aggregation of proteins. The differences in Raman spectroscopy between the two microchips suggest that the initial incubation cycles favoured interactions among the protein molecules and graphene. Indeed, the induced supramolecular forces had an immediate structural effect on the graphitic lattice, which was reflected by the outstanding vibrational responses (*i.e.* downshifting) of the Raman peaks (first microchip). Depending on the type of interactions (*i.e.* electrostatic or hydrogen bonding), graphene is affected either by charge transfer and/or mechanical deformations, leading to different phonon processes. A denser accumulation of enzyme molecules through additional incubation cycles (second microchip), favours intermolecular interactions, causing minor effects on the graphitic lattice. This hypothesis is justified by the smaller downshifting before and after functionalization. In addition, the moderate changes in the Raman spectra can be attributed to the reduced concentration of HRP used during the treatment of the second microchip.

Detection of b-BSA/Av-FITC attachment by fluorescence microscopy

In our attempt to visualize the topography/selective aggregation of protein molecules over irradiated graphene, a third microchip was initially treated with a b-BSA solution and reacted thereafter with fluorescently labelled Av-FITC, before imaging by fluorescence confocal microscopy. Using ImageJ software, we analysed the obtained red, green, blue (RGB) colour image and generated the given grayscale plot profiles of the selected areas of the microchip (Fig. 8). The surface plot displays the intensity of light which reflects from the chosen areas, designated by the dashed lines. It defines the brightness of the pixels along the
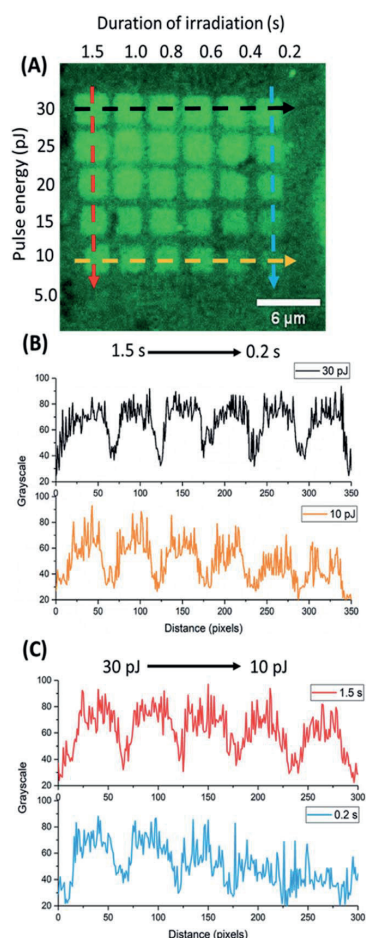
Fig. 8 Evaluation of the b-BSA/Av-FITC topographic immobilization by fluorescence microscopy. (A) Fluorescence microscopy image of the microchip after treatment with given oxidation parameters; (B) grayscale surface plot profiles corresponding to constant laser pulse energies of 30 and 10 pJ; (C) grayscale surface plot profiles corresponding to constant irradiation times of 1.5 and 0.2 s.

drawn lines and relates to the number of immobilized protein molecules. The denser the protein aggregation, the higher the grayscale value is.

The black and yellow horizontal lines correspond to graphene treated by a constant pulse energy of 30 and 10 pJ respectively, over a range of irradiation times (0.2–1.5 s). The red and blue vertical lines represent graphene irradiated for 1.5 and 0.2 s respectively, at a range of laser pulse energies (30–10 pJ). From the plot, it is evident that for intense oxidation conditions (higher pulse energy and longer irradiation time), b-BSA adhered on graphene almost evenly (black and red plots). On the other hand, for moderate oxidation conditions, the intensity varies. The intensity is reaching the highest values on the grayscale when higher pulse energies (30 and 25 pJ) are used

over short irradiation times (blue plot) and when longer irradiation is applied (1.5 to 0.8 s) at lower energies (yellow plot).

As the protein carries a net negative charge at the used pH value (7.3), it was expected to adhere less upon areas bearing a high surface density of oxygen-containing groups due to electrostatic repulsion. The experimental results, however, can be attributed to the induced coulombic forces between the negatively charged GO and the positively charged amino acids of b-BSA (lysine, histidine).[42] This also explains the poor adhesion of protein molecules over graphene areas irradiated under moderate conditions hence bearing a lower surface density of oxygen functional groups.

The functionalization of graphene surfaces by proteins expands the potential of the microchips towards applications in biomedicine, such as in biosensors, drug delivery systems and immunological assays. In comparison to the existing patterning technologies,[43,44] laser-induced oxidation introduces tunability on protein adhesion by controlling the levels of oxidation. In other words, proteins can be guided over graphene surfaces by light. Sequential irradiation of different areas followed by the immobilization of proteins can be used to functionalize chips with multiple proteins, localized in separate regions. Since the selective immobilization of proteins is based on non-covalent interactions, our approach does not require the addition of chemicals or the use of chemical masking techniques resulting in a facile and free from chemical contaminants patterning method.

Conclusions

We studied protein adhesion upon laser-induced GO patterns. Our key observations are: (i) by modification of the irradiation conditions we introduced tunability of the levels of graphene oxidation and hence induced the selective immobilization of protein molecules; (ii) the type of protein, its concentration, incubation time and pH value of the buffer solution have an immediate effect on physical adsorption; (iii) any consequent deformities upon the graphitic lattice due to protein adhesion are notably visible by Raman spectroscopy over areas oxidized under moderate conditions; (iv) we facilitated a Raman spectroscopic fingerprint of protein adhesion and observed the topography of protein immobilization by AFM and fluorescence microscopy.

Working towards bioinspired graphene surfaces, we can control the topography of protein immobilization by laser-induced oxidation in contrast to chemically oxidized graphene. Our methodology has a high potential for advancing the development of bioelectronic devices and sensors, for example, *via* the selective immobilization of antibodies on active sensor areas.

Materials and methods

Material

Horseradish peroxidase, HRP (type VI, ≥250 units per mg solid), biotinylated Bovine Serum Albumin, b-BSA (A8549) and

avidin-fluorescein isothiocyanate, Av-FITC from egg white (A2901) were purchased from Sigma Aldrich.

Preparation of protein solutions

HRP solutions were prepared in phosphate-buffered saline, PBS (0.0754 M $Na_2HPO_4 \cdot 2H_2O$, 0.0246 M $NaH_2PO_4 \cdot 2H_2O$, pH 7.1) with final concentrations of 2.5 units per mL or 10 μg mL^{-1} and 0.625 units per mL or 2.5 μg mL^{-1}. b-BSA and Av-FITC solutions were prepared in PBS (137 mmol L^{-1} NaCl, 2.7 mmol L^{-1} KCl, 10 mmol L^{-1} Na_2HPO_4, 2.0 mmol L^{-1} KH_2PO_4, pH 7.3 pH) at final concentrations of 10 μg mL^{-1} and 80 μg mL^{-1} respectively.

Immobilization of HRP enzyme

The microchip was immersed in HRP solution (2.5 units per mL) for 1 h at 0 °C. The graphene surface was then extensively washed with PBS solution (pH 7.1) and MilliQ water before dried under the stream of N_2 gas. A lower concentration of the enzyme was used (0.625 units per mL) to assess concentration and immersion timing effects on HRP adsorption. The microchip was therefore immersed into HRP solution for 1, 2 and 3 h respectively. After each immersion cycle, washings were performed using PBS solution (pH 7.1) and MilliQ water followed by drying.

Immobilization of b-BSA and binding with Av-FITC

The microchip was immersed in b-BSA solution (10 μg mL^{-1}) for 24 h at r.t. The graphene surface was washed with a PBS solution (pH 7.3) and MilliQ water to remove unbound proteins. The chip was then dried under a stream of N_2 gas before it was immersed for a second time into an Av-FITC solution (80 μg mL^{-1}) for 1 h at r.t. Excess of Av-FITC was removed by PBS solution and water washings followed by drying.

Instruments

Oxidized patterns were curved on graphene monolayer by irradiation with 515 nm focused femtosecond laser in the ambient atmosphere (pulse duration 250 fs, repetition rate: 600 kHz). A home-built Raman setup was used for mapping and spectra acquisition, as previously described.[22,45] The laser power of 0.250 mW and 532 nm of excitation was utilized, the exposure time was set at 10 s and mapping was conducted in a 25 × 25 μm area. AFM imaging was carried on a Bruker Dimension Icon atomic force microscope, using Peak Force Tapping mode. ScanAsyst-Air probes from Bruker were used during imaging with the peak force set to 2.0 nN. All AFM images were processed with NanoScope Analysis 1.9 software. Images of the height channel were smoothed with a Gaussian low-pass filter to suppress noise to generate 3D structures. Fluorescence imaging was performed on a Nikon A1R laser scanning confocal microscope. Images were acquired by using argon laser excitation at 488 nm and a 512/30 emission filter for detection. All images were processed with Fiji2 software.

AFM and Raman analysis

The height distribution profile of the functionalized surfaces was evaluated by PeakForce tapping (PFT) mode AFM.[46] The irradiated graphene surfaces were visualized by Raman mapping of the integrated intensity of the D band, while Raman spectra were recorded for all samples at selected spots (irradiated and non-irradiated). By comparison of the vibrational response of the graphene surfaces before and after protein adhesion, we attempted to facilitate a spectroscopic fingerprint of the functionalized areas. Both first (1050–1750 cm^{-1}) and second (2400–3100 cm^{-1}) order scattering spectral regions were evaluated prior and after protein functionalization to assess potential defects on the lattice of graphene. Our study focused on features such as the position, intensity and displacement of the recorded bands, the I_D/I_G ratios and the FWHM of the vibrational modes which were quantified by the Lorentzian function fitting procedure.

To calculate the level of strain and doping, the sensitivity factors we used were $(\Delta\omega_{2D}/\Delta\omega_G)_n^{hole} = 0.7$ and $(\Delta\omega_{2D}/\Delta\omega_G)_\varepsilon^{biaxial} = 2.63$. Doping was estimated simply by $n = (E_F/(\hbar\nu_F))/\pi$, where n is carrier concentration, E_F Fermi energy and ν_F Fermi velocity. The shift of the G band frequency is given by $\Delta\omega_G = E_F \times 42$ cm^{-1}/eV.[37] The effect of strain on the G band frequency was estimated with a sensitivity factor of -69.1 $cm^{-1}/\%$, which is an average value derived from previous studies.[36–39] The point of zero doping and strain we used in calculations was 1581 cm^{-1} (G band frequency) and 2671 cm^{-1} (2D band frequency) (Fig. 5, S4 and S5†).

Author contributions

E. D. S. and J. S. contributed equally to this work. E. D. S. wrote the manuscript and with J. S. functionalized the microchips, performed Raman mapping/spectroscopy measurements, conducted AFM imaging and data analysis. A. L. conceived and performed preliminary studies on HRP adhesion. K. K. M. oxidized and characterized the microchips. V. M. H. calculated the level of strain and doping. V. R. performed fluorescence imaging. A. J. evaluated the fabrication of the microchips. P. M. designed and developed the laser setups. M. N. supervised the protein adhesion work. M. P. planned the experiments, coordinated and supervised the work. All of the authors discussed the results, commented on the manuscript and have given approval to the final version of the manuscript.

Conflicts of interest

There are no conflicts to declare.

Acknowledgements

References

1 S. Y. Wu, S. S. A. An and J. Hulme, *Int. J. Nanomed.*, 2015, **10**, 9–24.

2 W. Cheng, K. Ping and C. Teck, *Biomaterials*, 2018, **155**, 236–250.

3 Z. Gu, S. Zhu, L. Yan, F. Zhao and Y. Zhao, *Adv. Mater.*, 2019, **31**, e1800662.

4 J. A. Jaleel, S. Sruthi and K. Pramod, *J Control Release*, 2017, **255**, 218–230.

5 T. A. Tabish, *Biochem. Biophys. Res. Commun.*, 2018, **504**, 686–689.

6 M. Wierzbicki, S. Jaworski, M. Kutwin, M. Grodzik, B. Strojny, N. Kurantowicz, K. Zdunek, R. Chodun, A. Chwalibog and E. Sawosz, *Int. J. Nanomed.*, 2017, **12**, 7241–7254.

7 S. Liu, T. H. Zeng, M. Hofmann, E. Burcombe, J. Wei and R. Jiang, *ACS Nano*, 2011, **9**, 6971–6980.

8 J. Vlček, L. Lapčík, M. Havrdová, K. Poláková, B. Lapčíková, T. Opletal, J. P. Froning and M. Otyepka, *Nanoscale*, 2019, **11**, 3222–3228.

9 D. Kireev and A. Offenhäusser, *2D Mater.*, 2018, **5**, 042004.

10 K. Kostarelos, M. Vincent, C. Hebert and J. A. Garrido, *Adv. Mater.*, 2017, **29**, 1700909.

11 A. E. Nel, L. Mädler, D. Velegol, T. Xia, E. M. V Hoek, P. Somasundaran, F. Klaessig, V. Castranova and M. Thompson, *Nat. Mater.*, 2009, **8**, 543–557.

12 C. J. Bullock and C. Bussy, *Adv. Mater. Interfaces*, 2019, **6**, 1900229.

13 M. Seredych, L. Mikhalovska, S. Mikhalovsky and Y. Gogotsi, *C*, 2018, **4**, 3.

14 J. Zhang, F. Zhang, H. Yang, X. Huang, H. Liu and J. Zhang, *Langmuir*, 2010, **26**, 6083–6085.

15 W. Hu, C. Peng, M. Lv, X. Li, Y. Zhang, N. Chen, C. Fan and Q. Huang, *ACS Nano*, 2011, **5**, 3693–3700.

16 J. G. Vilhena, P. Rubio-Pereda, P. Vellosillo, P. A. Serena and R. Pérez, *Langmuir*, 2016, **32**, 1742–1755.

17 P. Rubio-Pereda, J. G. Vilhena, N. Takeuchi, P. A. Serena and R. Pérez, *J. Chem. Phys.*, 2017, **146**, 214704.

18 G. Faccio, *Sensors*, 2018, **18**, 1204.

19 M. Simsikova and T. Sikola, *J. Nanomed. Res.*, 2017, **5**, 00109.

20 E. Vermisoglou, D. Panáček, K. Jayaramulu, M. Pykal, I. Frébort, M. Kolář, M. Hajdúch, R. Zbořil and M. Otyepka, *Biosens. Bioelectron.*, 2020, **166**, 112436.

21 H. Seelajaroen, A. Bakandritsos, M. Otyepka, R. Zbořil and N. S. Sariciftci, *ACS Appl. Mater. Interfaces*, 2020, **12**, 250–259.

22 J. Aumanen, A. Johansson, J. Koivistoinen, P. Myllyperkiö and M. Pettersson, *Nanoscale*, 2015, **7**, 2851–2855.

23 J. Koivistoinen, L. Sládková, J. Aumanen, P. Koskinen, K. Roberts, A. Johansson, P. Myllyperkiö and M. Pettersson, *J. Phys. Chem. C*, 2016, **120**, 22330–22341.

24 A. Johansson, H. C. Tsai, J. Aumanen, J. Koivistoinen, P. Myllyperkiö, Y. Z. Hung, M. C. Chuang, C. H. Chen, W. Y. Woon and M. Pettersson, *Carbon*, 2017, **115**, 77–82.

25 A. Johansson, P. Myllyperkiö, P. Koskinen, J. Aumanen, J. Koivistoinen, H. C. Tsai, C. H. Chen, L. Y. Chang, V. M. Hiltunen, J. J. Manninen, W. Y. Woon and M. Pettersson, *Nano Lett.*, 2017, **17**, 6469–6474.

26 J. Zhu, R. Rao, A. M. Rao and R. Podila, *Recent Pat. Mater. Sci.*, 2018, **11**, 24–32.

27 K. Tsirka, A. Katsiki, N. Chalmpes, D. Gournis and A. S. Paipetis, *Front. Mater.*, 2018, **5**, 37.

28 S. Eigler, C. Dotzer and A. Hirsch, *Carbon*, 2012, **50**, 3666–3673.

29 A. Kaniyoor and S. Ramaprabhu, *AIP Adv.*, 2012, **2**, 032183.

30 L. M. Malard, M. A. Pimenta, G. Dresselhaus and M. S. Dresselhaus, *Phys. Rep.*, 2009, **473**, 51–87.

31 E. Del Corro, M. Taravillo and V. G. Baonza, *Phys. Rev. B: Condens. Matter Mater. Phys.*, 2012, **85**, 033407.

32 F. Ding, H. Ji, Y. Chen, A. Herklotz, K. Dörr, Y. Mei, A. Rastelli and O. G. Schmidt, *Nano Lett.*, 2010, **10**, 3453–3458.

33 X. Zheng, W. Chen, G. Wang, Y. Yu, S. Qin, J. Fang, F. Wang and X. A. Zhang, *AIP Adv.*, 2015, **5**, 057133.

34 A. Das, S. Pisana, B. Chakraborty, S. Piscanec, S. K. Saha, U. V. Waghmare, K. S. Novoselov, H. R. Krishnamurthy, A. K. Geim, A. C. Ferrari and A. K. Sood, *Nat. Nanotechnol.*, 2008, **3**, 210–215.

35 M. Bruna, A. K. Ott, M. Ijäs, D. Yoon, U. Sassi and A. C. Ferrari, *ACS Nano*, 2014, **8**, 7432–7441.

36 J. E. Lee, G. Ahn, J. Shim, Y. S. Lee and S. Ryu, *Nat. Commun.*, 2012, **3**, 1024.

37 C. F. Chen, C. H. Park, B. W. Boudouris, J. Horng, B. Geng, C. Girit, A. Zettl, M. F. Crommie, R. A. Segalman, S. G. Louie and F. Wang, *Nature*, 2011, **471**, 617–620.

38 J. Zabel, R. R. Nair, A. Ott, T. Georgiou, A. K. Geim, K. S. Novoselov and C. Casiraghi, *Nano Lett.*, 2012, **12**, 617–621.

39 T. M. G. Mohiuddin, A. Lombardo, R. R. Nair, A. Bonetti, G. Savini, R. Jalil, N. Bonini, D. M. Basko, C. Galiotis, N. Marzari, K. S. Novoselov, A. K. Geim and A. C. Ferrari, *Phys. Rev. B: Condens. Matter Mater. Phys.*, 2009, **79**, 205433.

40 E. H. Martins Ferreira, M. V. O. Moutinho, F. Stavale, M. M. Lucchese, R. B. Capaz, C. A. Achete and A. Jorio, *Phys. Rev. B: Condens. Matter Mater. Phys.*, 2010, **82**, 125429.

41 G. I. Berglund, G. H. Carlsson, A. T. Smith, H. Szöke, A. Henriksen and J. Hajdu, *Nature*, 2002, **417**, 463–468.

42 A. Hasan, G. Waibhaw and L. M. Pandey, *Langmuir*, 2018, **34**, 8178–8194.

43 H. Zhao, Y. Lee, M. Han, B. K. Sharma, X. Chen, J. H. Ahn and J. A. Rogers, *Nano Today*, 2020, **30**, 100825.

44 N. Vigneswaran, F. Samsuri, B. Ranganathan and Padmapriya, *Procedia Eng.*, 2014, **97**, 1387–1398.

45 M. Pettersson, J. Rintala, O. Herranen, A. Johansson and M. Ahlskog, *J. Phys. Chem. C*, 2009, **113**, 15398–15404.

46 K. Xu, W. Sun, Y. Shao, F. Wei, X. Zhang, W. Wang and P. Li, *Nanotechnol. Rev.*, 2018, **7**, 605–621.

Tuning Protein Adsorption on Graphene Surfaces via Laser-Induced Oxidation

Efstratios D. Sitsanidis,[a] Johanna Schirmer,[a] Aku Lampinen,[a] Kamila K. Mentel,[a] Vesa-Matti Hiltunen,[b] Visa Ruokolainen,[c] Andreas Johansson,[a,b] Pasi Myllyperkiö,[a] Maija Nissinen[a] and Mika Pettersson[*a]

[a] Department of Chemistry, Nanoscience Center, University of Jyvaskyla, P.O. Box 35, FI-40014 JYU, Finland.
[b] Department of Physics, Nanoscience Center, University of Jyvaskyla, P.O. Box 35, FI-40014 JYU, Finland.
[c] Department of Biological and Environmental Sciences, Nanoscience Center, University of Jyvaskyla, P.O. Box 35, FI-40014 JYU, Finland.
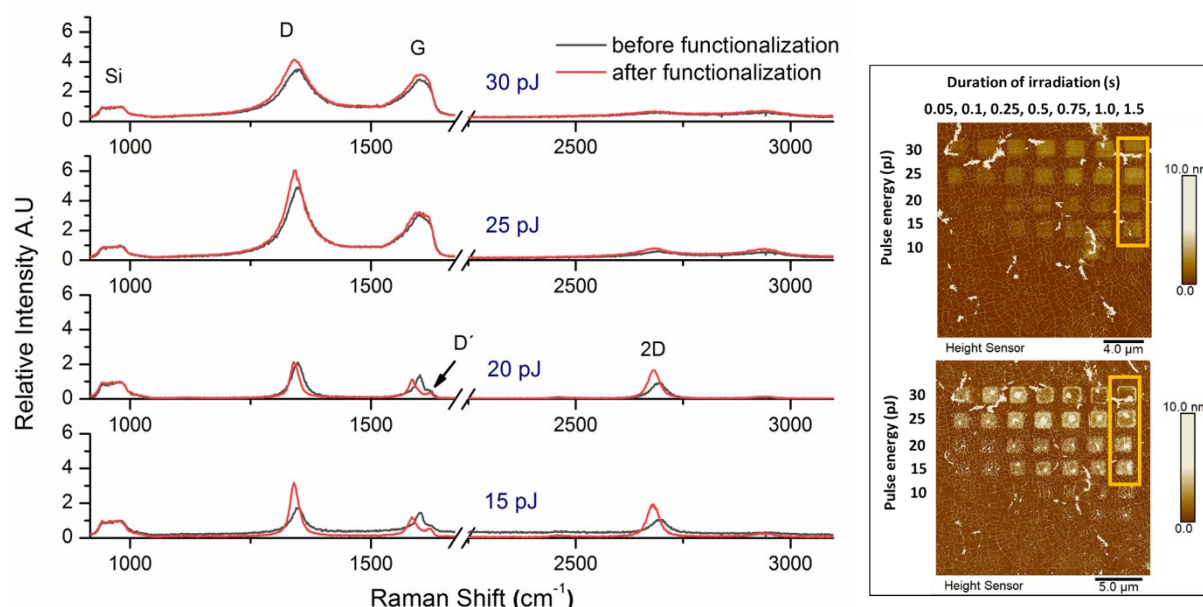
Figure S1. Raman spectra before and after HRP adhesion. Increased pulse energy (15 to 30 pJ) for a constant irradiation time of 1.5 s. Insert depicts the location of the corresponding squares, before (top) and after (bottom) HRP adhesion. All spectra are normalized with respect to the Si band intensities.

Table S1. Raman shifts (cm^{-1}), quantified by the Lorentzian function fitting procedure, corresponding to the spectra depicted in **Figure S1**. Shifts are given in black colour font (before HRP adhesion) and red colour font (after HRP adhesion).

Pulse energy (pJ)	D	G	2D	D+D´
30	1347.8	1596.6	2692.5	2933.5
	1343.6	1595.8	2683.7	2930.5
25	1348.5	1596.5	2693.3	2933.9
	1343.2	1595.5	2683.6	2931.4
20	1347.4	1599.8	2693.0	2939.8
	1341.3	1586.2	2681.8	---
15	1348.3	1600.7	2694.8	---
	1340.9	1586.7	2680.4	---
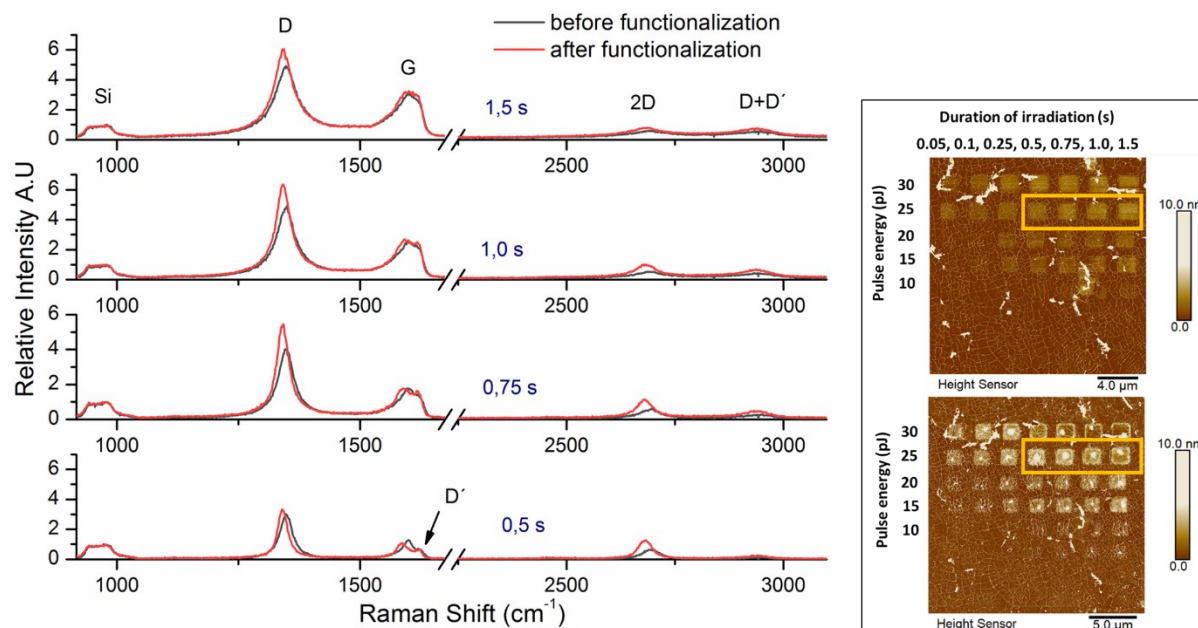
Figure S2. Raman spectra before and after HRP adhesion. Increased irradiation time at a constant pulse energy of 25 pJ. Insert depicts the location of the corresponding squares, before (top) and after (bottom) HRP adhesion. All spectra are normalized with respect to the Si band intensities.

Table S2. Raman shifts (cm^{-1}), quantified by the Lorentzian function fitting procedure, corresponding to the spectra depicted in **Figure S2**. Shifts are given in black colour font (before HRP adhesion) and red colour font (after HRP adhesion).

Duration of irradiation (s)	D	G	2D	D+D´
1.5	1347.3 / 1342.6	1600.6 / 1599.5	2689.2 / 2684.9	2938.1 / 2931.7
1.0	1347.1 / 1341.9	1600.9 / 1598.6	2690.3 / 2682.0	2941.2 / 2934.8
0.75	1347.6 / 1341.1	1601.0 / 1596.1	2692.6 / 2679.8	2943.7 / 2937.4
0.5	1348.3 / 1340.9	1599.7 / 1586.9	2694.5 / 2681.0	2949.9 / 2938.6
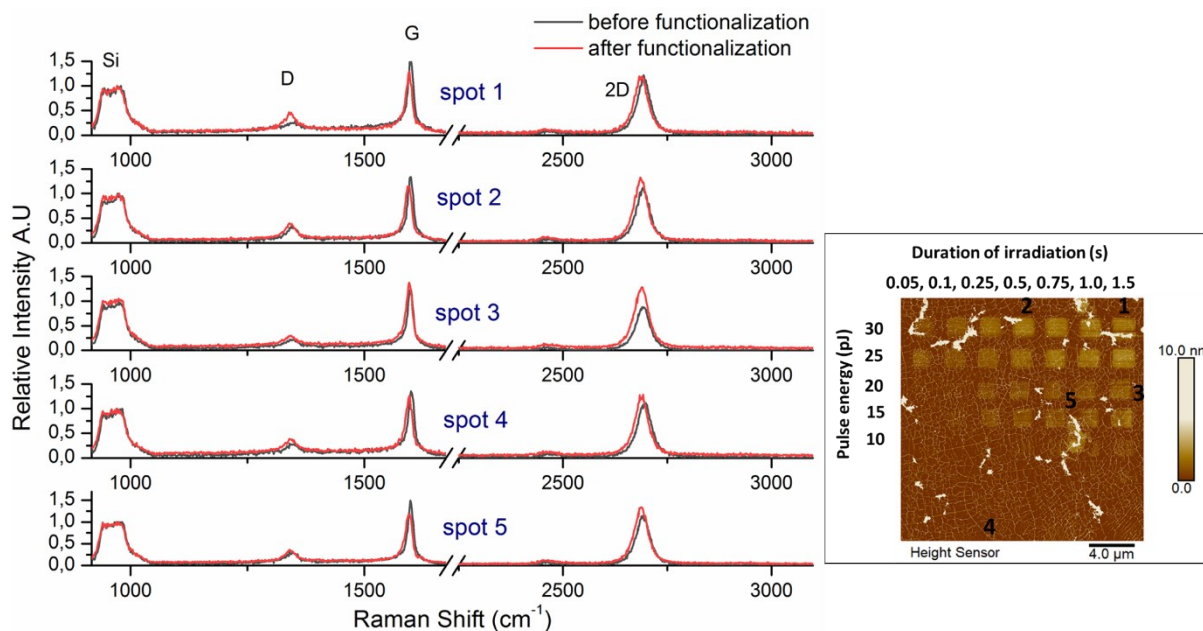
Figure S3. Raman spectra before and after HRP adhesion. Non-irradiated graphene spots. Insert depicts the location of the corresponding spots. All spectra are normalized with respect to the Si band intensities.

Table S3. Raman shifts (cm^{-1}), quantified by the Lorentzian function fitting procedure, corresponding to the spectra depicted in **Figure S3**. Shifts are given in black colour font (before HRP adhesion) and red colour font (after HRP adhesion).

Non-irradiated spots	D	G	G*	2D
spot 1	1347.4 1343.2	1600.3 1596.6	2465.7 ---	2695.1 2688.6
spot 2	1347.6 1343.0	1599.6 1595.4	2464.2 ---	2693.1 2687.9
spot 3	1345.9 1342.7	1599.7 1597.3	--- ---	2692.4 2689.6
spot 4	1347.8 1344.1	1601.6 1596.6	--- ---	2696.8 2689.6
spot 5	1345.6 1343.1	1600.2 1596.3	--- ---	2693.1 2688.8
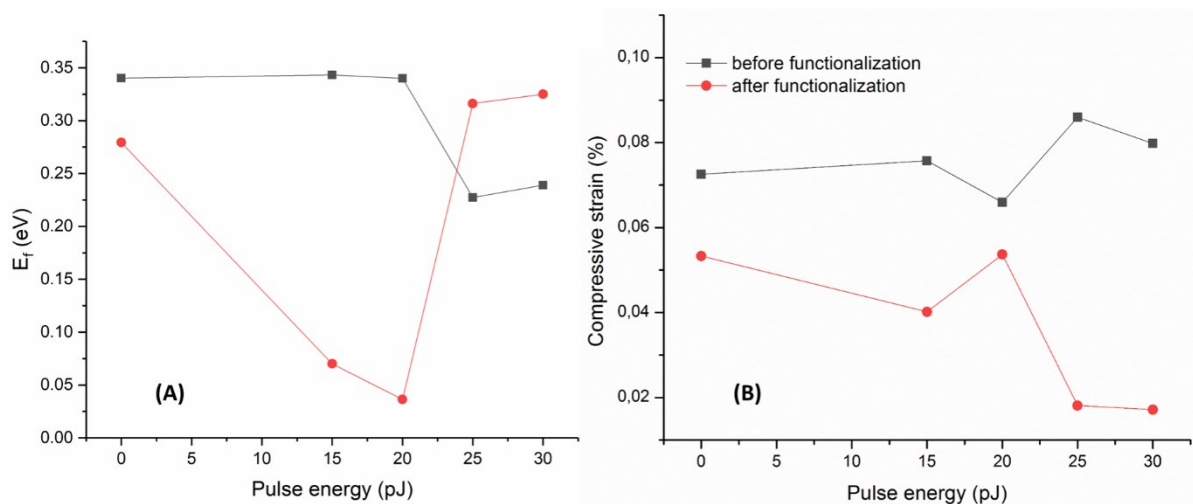
Figure S4. Fermi level (A) and compressive strain (B) plots calculated from the obtained Raman data before and after HRP adhesion. The values correspond to graphene squares irradiated at a constant duration of 1.5 s over a range of pulse energies (corresponding Raman spectra are given in **Figure S1**).
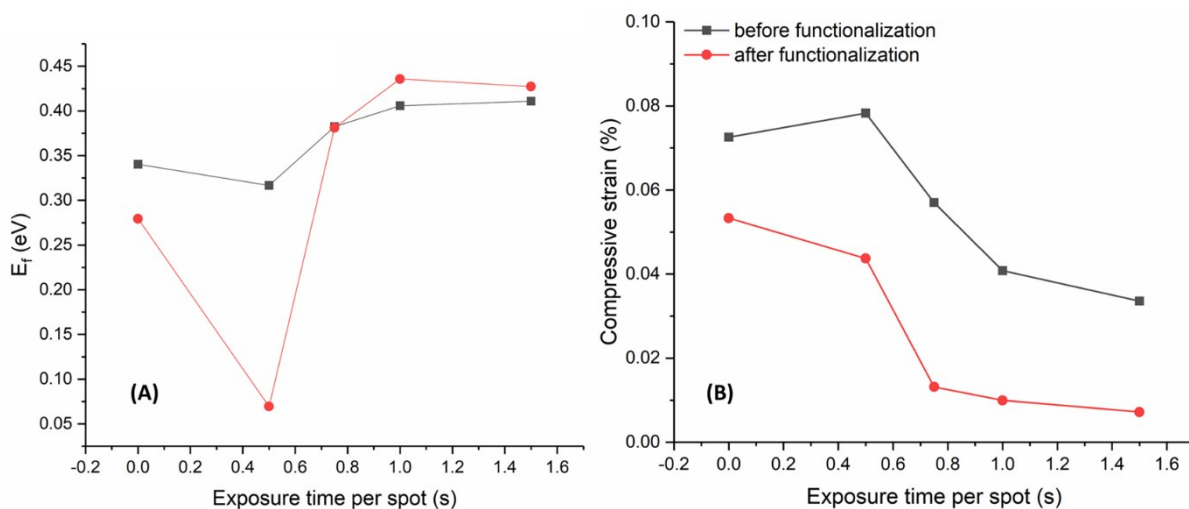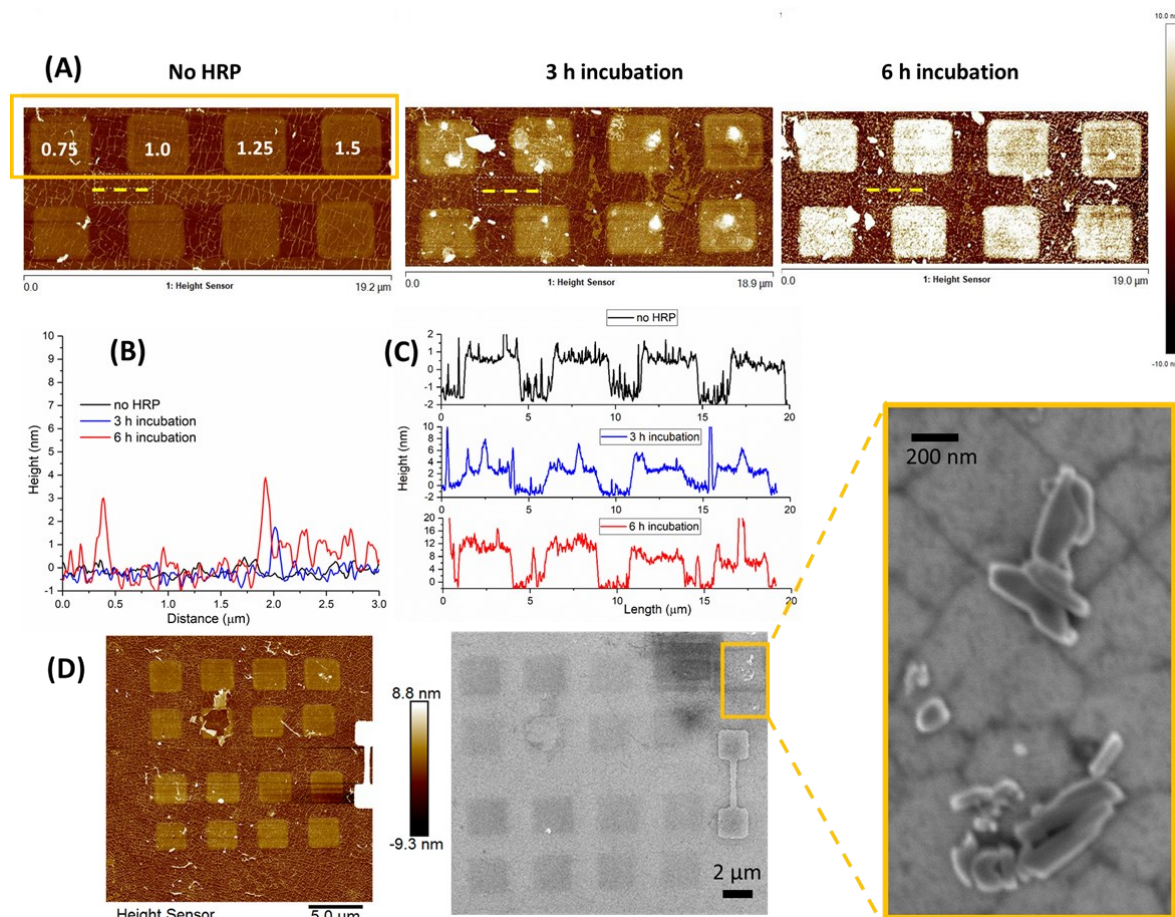

Figure S5. Fermi level (A) and compressive strain (B) plots calculated from the obtained Raman data before and after HRP adhesion. The values correspond to graphene squares irradiated at a constant pulse energy of 25 pJ over a range of time durations. (corresponding Raman spectra are given in **Figure S2**).

Figure S6. Control measurements of protein adhesion based on topographic height profiles. (A) AFM height sensor images of a selected area at different cycles of incubation. Graphene was irradiated by laser pulse energy of 15 pJ at different time durations (orange frame); (B) Topographic height profile of non-irradiated graphene (yellow dashed line) at different cycles of incubation; (C) Topographic height profile of irradiated graphene (orange frame) at different cycles of incubation; (D) Comparison of the microchip´s AFM height sensor image with the corresponding SEM image. Crystals of the PBS solutes (magnification insert) are distinct in shape compared to the immobilized HRP upon the irradiated squares. Images were captured after incubating the microchip in HRP solution for 1 h.
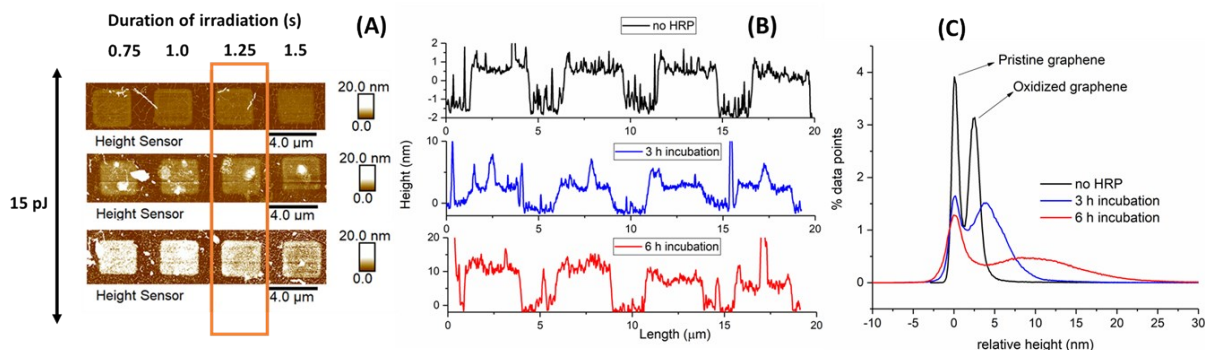
Figure S7. Incubation studies in HRP solution. (A) AFM height sensor images of a selected area at different cycles of incubation. Graphene was irradiated by laser pulse energy of 15 pJ at different time
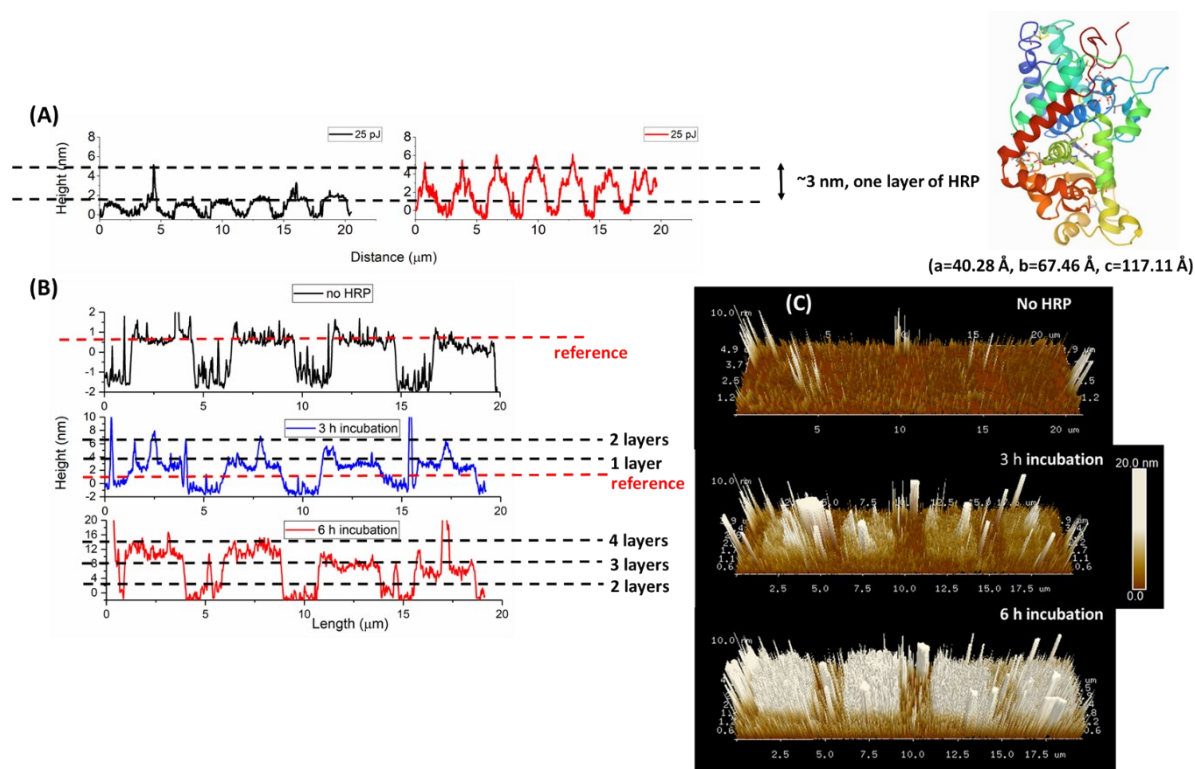
Figure S8. Layer deposition of HRP enzyme. (A) Topographic height profile of irradiated graphene (25 pJ for a range of time durations) before (black) and after (red) incubation in HRP solution for 1 h. A 3 nm increase in height suggests the deposition of a single layer of HRP. The insert depicts the structure of HRP enzyme and given dimensions (protein data bank ID: 1HCH)[1]; (B) Topographic height profile of irradiated graphene (15 pJ for a range of time durations) at different incubation cycles. After 3 h of incubation 2 layers of HRP appear to be immobilized while after 6 h almost 4 layers of HRP have been deposited; (C) Three-dimensional images of the corresponding microchip area at different incubation cycles showing the immobilization of HRP upon irradiated graphene.

References

1. G. I. Berglund, G. H. Carlsson, A. T. Smith, H. Szöke, A. Henriksen, J. Hajdu, *Nature*, 2002, **417**, 463-468.

II

CATALYTIC ACTIVITY OF HORSERADISH PEROXIDASE IMMOBILIZED ON PRISTINE AND TWO-PHOTON OXIDIZED GRAPHENE

by

Johanna Schirmer, Ester Iatta, Aleksei Emelianov, Maija Nissinen & Mika Pettersson, 2023

Accepted manuscript.

Catalytic Activity of Horseradish Peroxidase Immobilized on Pristine and Two-Photon Oxidized Graphene

Johanna Schirmer, Ester Iatta, Aleksei V. Emelianov, Maija Nissinen, and Mika Pettersson*

J. Schirmer, E. Iatta, A. V. Emelianov, M. Nissinen, M. Pettersson
Department of Chemistry, Nanoscience Center, University of Jyväskylä, P. O. Box 35, FI-40015, Finland
E-mail: mika.j.pettersson@jyu.fi

Conflict of Interest

The authors declare no conflict of interest.

Data Availability

The data that support the findings of this study are available from the corresponding author upon reasonable request.

Ethics Approval

The research and manuscript meet the ethical guidelines outlined in this journal's Author Guidelines, including adherence to the legal requirements of the study country

Abstract

Biosensors based on graphene and bio-graphene interfaces have gained momentum in recent years due to graphene's outstanding electronic and mechanical properties. By introducing the patterning of a single-layer graphene surface by two-photon oxidation (2PO), the surface hydrophobicity/hydrophilicity and doping can be varied at the nanoscale while preserving the carbon network, thus opening possibilities to design new devices. In this study, the effect of 2PO on the catalytic activity of the noncovalently immobilized enzyme horseradish peroxidase (HRP) on single-layer graphene-coated Si/SiO$_2$ chips is presented. To monitor the activity continuously, a simple well-plate setup is introduced. Upon controllable 1–2-layer immobilization, the catalytic activity decreases to a maximum value of 7.5% of the free enzyme. Interestingly, the activity decreases with increasing 2PO area on the samples. Hence, the HRP catalytic activity on the graphene surface is locally controlled. This approach could enable the development of graphene-bio interfaces with locally varying enzyme activity.

1. Introduction

The immobilization of biomolecules has a wide range of applications, including biosensing, drug delivery and industrial processes used in the production of pharmaceutical, chemical and food products.[1,2] Additionally, immobilized biomolecules can improve a surface's biocompatibility for medical applications.[3] When proteins and enzymes are immobilized on a solid support, it is crucial to preserve their functionality and, for enzymes, their catalytic activity. Therefore, investigating the interactions between the protein or enzyme and the solid support and their effects on the functionality and catalytic activity is central in the research developing biocompatible surfaces and enzyme-based biosensors.

Support materials for enzymes include polymers and two-dimensional materials, such as graphene and its derivatives.[2,4–6] Enzymes can be immobilized on the graphene materials covalently or noncovalently, with the latter being preferred as it preserves graphene's outstanding electronic and mechanical properties.[7] The noncovalent immobilization of enzymes on graphene oxide (GO) is based on dipole-dipole and ionic interactions between the enzyme and the oxygen-containing functional groups of GO as well as π-π stacking. For pristine graphene, noncovalent approaches commonly include linker molecules such as pyrene derivatives[8–10], which are covalently attached to the enzyme and interact with graphene via π-π stacking. However, a direct attachment was also demonstrated for a dihydrolipoyl acyltransferase supramolecular complex and horseradish peroxidase (HRP).[11,12]

HRP is a 44 kDa, well-studied biosensing enzyme that has shown catalytic activity both free in solution and when immobilized on different support materials, including a pristine graphene surface[10] and GO flakes[13]. It catalyzes the oxidization reaction of its substrates by consuming hydrogen peroxide (H$_2$O$_2$). The catalytic activity of HRP was preserved after noncovalent immobilization on graphene and GO, although it was lower for the immobilized than for the free enzyme in the solution.[10,13] This was attributed to structural changes of HRP upon the noncovalent immobilization. However, the thermal and storage stability improved after the immobilization of HRP on GO.[14] On pristine graphene, the stability of HRP was lower compared to the free enzyme in the solution,[10] suggesting that the two graphene derivatives might interact differently with HRP.

Two-photon oxidation (2PO)[15] of graphene is a tool that allows for the combination of the properties of oxidized and pristine graphene on one surface with a nanoscale resolution. While the carbon network remains intact, mainly hydroxyl and epoxide groups are introduced on the graphene surface.[16] This method enables the design of new sensors and bio interfaces with graphene. So far, the tuning of the graphene field effect transistor sensitivity for pH sensing[17] and the tuning of protein immobilization[12] have been demonstrated. In detail, HRP adsorption on the surface happened preferably in the 2PO compared to the pristine areas and the immobilization affected the doping level of graphene, demonstrating an electronic interaction. However, the question of whether the immobilized enzyme retains its catalytic activity remained open.

In this study, we combine the existing knowledge about HRP with 2PO of graphene to assess the catalytic activity of the enzyme. We noncovalently immobilized HRP on pristine and 2PO single-layer graphene surfaces and performed a kinetic analysis of an HRP-catalyzed reaction using UV-vis spectroscopy. The results were correlated with the surface type. In this way, we demonstrate how 2PO of graphene can control the catalytic activity of HRP.

2. Experimental Section

2.1. Materials

Horseradish peroxidase (Type VI, lyophilized, $\geq$250 units per mg), $Na_2HPO_4 \cdot 2H_2O$ and $NaH_2PO_4 \cdot 2H_2O$ were purchased from Merck. 3,3',5,5'-tetramethylbenzidine (TMB) solution containing <0.1% hydrogen peroxide was purchased from Immunochemistry Technologies. All chemicals were used as described by the manufacturer and without further purification.

2.2 Graphene samples

2.2.1 Single-layer graphene surface preparation. Graphene was synthesized on Cu (111) thin films evaporated onto single-crystal sapphire (0001) substrates. The catalyst film was annealed at 1060 °C under the gas flows of argon (470 sccm) and hydrogen (27 sccm) for 30 min to promote mono-crystallinity through secondary grain growth. After annealing, graphene growth was initiated by adding 6.8 sccm of 1% methane in argon to the furnace while keeping the temperature at 1060 °C. The growth time was 25 min. The graphene films were transferred by a standard PMMA transfer method[18] onto a silicon substrate (2 mm x 2 mm) with a 300 nm thermal oxide film. The PMMA film was removed with acetone (30 min at 50 °C). Finally, the samples were annealed at 300 °C in Ar/H2 atmosphere for two hours to remove PMMA residues.

2.2.2 Two-photon oxidation. Two-photon oxidation of graphene was performed with a 515 nm femtosecond laser (Pharos-10, Light Conversion Ltd., 600 kHz repetition rate, 250 fs pulse duration, 6 nJ pulse energy, Lithuania) in an ambient atmosphere with a relative humidity of 45%. A high-speed galvanometer scanner (Newson, Belgium) with high numerical aperture optics with a focal length of 65 mm (Sill Optics, Germany) was utilized. To pattern the graphene areas, we used the scanner speed of 4 mm/s with a beam spot of 5 μm and 0.1 μm separation between lines. The laser parameters for the 2PO of graphene used in this work were optimized (to achieve the highest ID/IG ratio) as reported previously[19,20]. The oxidation was verified by Raman spectroscopy (Figure S1, Supporting Information).

2.3 Sample characterization

2.3.1 Atomic force microscopy. AFM imaging was performed in air on a Bruker Dimension Icon AFM, operated in PeakForce Tapping mode. Scan-Asyst-AIR probes (Bruker, USA) made from silicon nitride with a spring constant of 0.4 N/m were used, and the PeakForce Setpoint

was 2 nN for all images. The images were processed and analyzed with the Nanoscope Analysis 1.9 software.

2.3.2 Raman spectroscopy. The Raman spectra of pristine and laser-oxidized graphene were recorded with a DXR Raman (Thermo Scientific), equipped with a 50x objective. The excitation wavelength was 532 nm, and the laser power was 1 mW.

2.4 HRP immobilization

Phosphate buffer saline (0.2 M) was prepared by mixing a 0.2 M solution of $Na_2HPO_4 \cdot 2\ H_2O$ in deionized water with a 0.2 M solution of $NaH_2PO_4 \cdot 2\ H_2O$ until the desired pH of 7.1 was reached. HRP (1 mg, 250 units) was dissolved in 1 mL of PBS to obtain the enzyme stock solution (250 U/mL), which was diluted with PBS to obtain an HRP concentration of 1.25 U/mL. The graphene samples were incubated in freshly prepared and diluted HRP solutions (2 mL) for 1h at room temperature (rt), protected from light, before washing with PBS (3x1 mL). Subsequently, each sample was mounted at the side wall of a well in a 96-well plate (polystyrene, Sarstaedt) using commercially available double-sided adhesive tape. PBS (300 µL) was added to each well for sample storage before the activity measurements to prevent the drying of the enzyme.

2.5 Catalytic activity measurements

All measurements were performed on a Spark multimode microplate reader (Tecan) in absorbance scan mode. The absorption spectra were measured between 200 nm and 800 nm wavelength, in the ultraviolet and visible spectral range, with a resolution of 2 nm. All spectra were baseline corrected. To exclude the interference of the tape and the sample, negative control experiments were performed (Table S1, Figure S2, Supporting Information).

2.5.1 Kinetic cycles. After immobilization of the enzyme, PBS (5 µL) was replaced by TMB solution (containing <0.1% H_2O_2) in the well containing the sample. Then, a kinetic loop absorbance scan was started, taking an absorption spectrum every 30 seconds for 30 minutes.

2.5.2 Stability over time. To assess the reusability of the immobilized HRP, the samples were stored overnight after the first kinetic cycle measurement. The next day, 5 µL of solution was replaced by TMB solution (5 µL, containing <0.1% H_2O_2) in each well. A kinetic loop was measured as described above (section 2.5.1.). The procedure was repeated on the following two days (4 days in total) until no catalytic activity was detected. After the last measurement, the liquid was removed from each well, and the samples were dried overnight at rt.

2.5.3 Calibration curve. An HRP solution ($2.5 \cdot 10^{-5}$ µg $\cdot$ µl^{-1}) was prepared from the HRP stock solution. For the calibration curve, nine wells in a 96-well plate were prepared as described in Table S2 (Supporting Information). TMB solution (5 µl, containing <0.1% H_2O_2) was added immediately before measuring absorption spectra every 30 s for 10 min.

2.5.4 Rate calculation. From each spectrum, the maximum of the 655 nm absorption band was extracted and plotted against time after TMB addition. A linear fit was applied to the data points at the beginning of each measurement (usually the first 0.5 to 5 min). The slope of the fit (unit Abs $\cdot$ min^{-1}) was defined as the reaction rate, with its standard deviation as the error of the rate. The Lamber-Beer law (1) and the volume of solution were used to convert the unit of the rate and its error to mmol $\cdot$ min^{-1}:

$$c = \frac{A}{\varepsilon \cdot l} \qquad (1)$$

4

, where A = the measured absorbance, ε = the extinction coefficient for the charge transfer complex (CTC; $\varepsilon_{CTC} = 3.9 \cdot 10^4$ L $\cdot$ mol^{-1} $\cdot$ cm^{-1} (for the absorption at 650 nm)[21]) and l = the path length in the plate reader (0.9 cm).

2.6 HRP coverage

To estimate the mass of HRP immobilized on the graphene samples, each dried sample was gently scratched with a spatula to remove both HRP and graphene from the Si/SiO$_2$ substrate. AFM images were recorded covering the protein layer and a part of a scratch (Figure S3, Supporting Information). From each sample, 2 or 3 images were recorded and compared with the AFM images before the HRP immobilization at the edge of the graphene sheet. The height differences between SiO$_2$ and graphene (h_{gr}) or HRP (h_{gr+HRP}), respectively, were measured with the Nanoscope Analysis 1.9 software step tool and used to calculate the height of the HRP layer h_{HRP}:

$$h_{HRP} = h_{gr+HRP} - h_{gr} \qquad (2)$$

The obtained heights of the protein layer were compared to the dimensions of HRP (4.0 nm x 4.4 nm x 6.8 nm)[22], and the number of layers on each sample was determined.
To assess the relative area covered by the enzymes (PC), the bearing analysis tool of Nanoscope analysis was used. The tool gives the amount of data points above a certain, user-defined level in % (Figure S 4, Supporting Information). The bearing level was set to h_{gr} to include only points above the graphene surface.
Assuming that HRP lays mainly on one of the longer sides, it would cover either 6.8 nm x 4.0 nm = 27.2 nm^2 or 6.8 nm x 4.4 nm = 29.92 nm^2. For further calculations, the mean of these two areas, 28.56 nm^2, was used as the area covered by one HRP enzyme (A_{HRP}). The mass of HRP m_{HRP} on each sample was estimated as follows:

$$m_{HRP} = \frac{\frac{A_{gr} \cdot PC}{A_{HRP}} \cdot M_{HRP}}{N_A} \qquad (3)$$

, where A_{gr} = the total area on a sample covered by graphene, M_{HRP} = the molar mass of HRP (44 kDa) and N_A = the Avogadro constant (6.022 $\cdot$ 10^{23} mol^{-1}).

3. Results and Discussion

3.1. Setup

Measuring the catalytic activity of surface-immobilized enzymes with UV-Vis spectroscopy has some practical challenges. The enzymes cannot be immobilized in the same container used to record the spectra, such as a cuvette or a well plate, since the enzymes would immobilize not only on the desired surface but also in the container itself. In an earlier approach, separate containers were used for catalytic reaction and absorption measurement.[10] However, this experiment design limits the number of possible measurements because the solution needs to be transferred for the measurement. The reaction cannot be monitored continuously, and consequently, reaction rates cannot be calculated. To monitor the reaction continuously, the sample must be mounted in the measurement container without disturbing the measurement. Here, we introduce a simple approach: We used double-sided adhesive tape to mount our 2 mm x 2 mm Si/SiO$_2$ chips coated with single-layer graphene and HRP into a 96-well plate and were able to continuously measure the progress of the HRP-catalyzed oxidation of TMB **(Figure 1)**. The possible interference of the tape and the sample were excluded with negative control experiments (Table S1, Figure S2, Supporting Information).
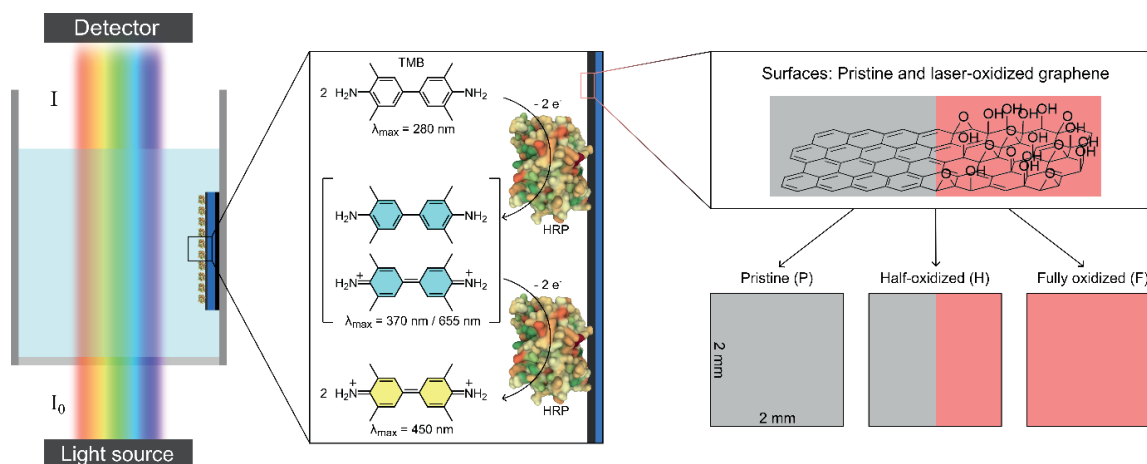
Figure 1: Schematic representation of the experiment: UV-Vis absorbance spectra were recorded from a well plate with a sample mounted on the side of the well. The sample consists of a graphene surface with noncovalently immobilized HRP enzyme, which oxidizes 3,3',5,5' tetramethylbenzidine (TMB) if it is catalytically active. The two-step reaction can be observed in the UV-Vis absorbance spectra. Three distinct graphene surfaces were studied to see the effect of laser-oxidation on the catalytic activity of HRP.

3.2. HRP loading

The noncovalent immobilization of proteins is based on physical interactions between the surface and the protein. Thus, controlling the amount of immobilized protein and its orientation is challenging. However, to sufficiently evaluate the catalytic activity of immobilized enzymes, it is crucial to know the enzyme load.

In our experiments, HRP was immobilized on three different graphene surfaces, which differ in the area of 2PO graphene: pristine (P), half-oxidized (H) and fully oxidized (F) graphene (Figure 1). Our previous study showed that under certain conditions, HRP prefers to adsorb to the 2PO areas.[12]

Here, the amount of HRP on each sample was estimated as described in section 2.6, using AFM images before and after the protein immobilization and extrapolating the whole area covered by graphene. (Figure S 3, Supporting Information, **Table 1**, **Figure 2**). The amount of HRP varies between a monolayer and 2.5 layers, demonstrating that we were able to immobilize HRP noncovalently on graphene in a controlled manner in a range of a few layers on the pristine and 2PO graphene surfaces. In contrast to our previous study[12], there was no clear preference towards one surface. This might be caused by different oxidation and immobilization conditions. Since the HRP layer does not cover the whole graphene surface for some samples, we calculated the protein coverage from the same AFM images (Figure S4, Supporting Information, Table 1), showing that HRP covered 84 - 100% of the graphene area. The graphene and 2PO areas were measured from optical microscope images and varied between the samples in the range from 2.76 mm^2 to 3.62 mm^2 (total graphene area) and from 1.63 mm^2 to 3.23 mm^2 (2PO area). The variation of the total graphene area originates from the graphene layer position on the surface after the transfer process. Considering the molar mass of HRP, the total mass of HRP on each sample was calculated (section 2.6, Table 1) and was found to vary from 4.41 ng to 19.94 ng. Thus, distinct catalytic activity differences could be expected from the samples due to a varying mass of HRP.
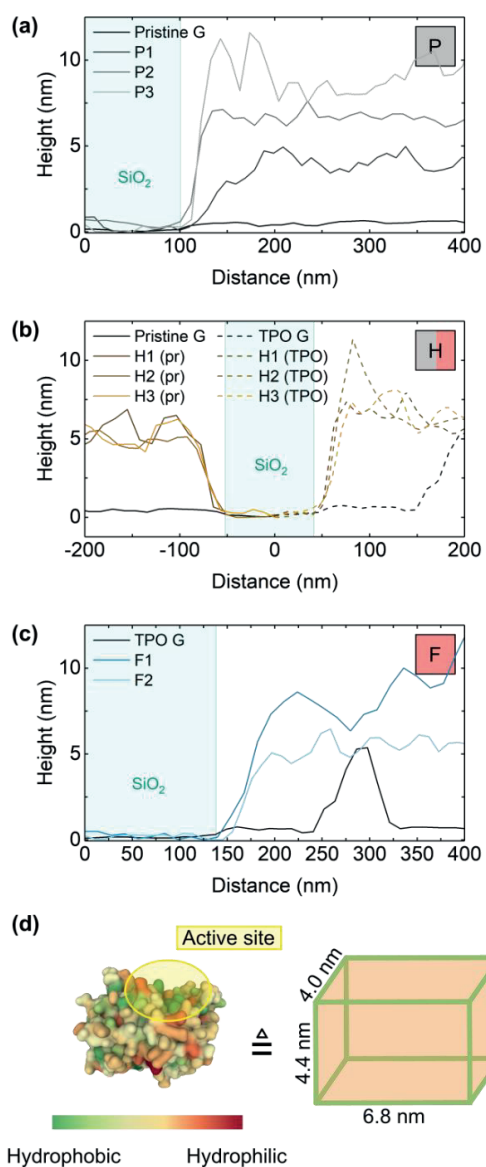
Figure 2: (a-c) Example AFM topography cross sections from all samples and pristine and 2PO graphene (G) as a base for the estimation of the HRP mass on each sample. The corresponding AFM images are shown in Figure S3, Supporting Information. (d) Crystal structure of HRP in the Gaussian surface view, showing hydrophobic and hydrophilic amino acid residues,[23–25] and the simplified cuboid model used for HRP mass calculations.

Table 1: Estimation of the total HRP mass on each sample and values used for the calculation, with the height of the HRP layer h_{HRP} and the resulting mass of HRP m_{HRP}.

	h_{HRP} [nm]	#HRP layer	Protein Covering [%]	Graphene area [mm^2]	2PO area [mm^2]	m_{HRP} [ng]
P1	3.5	1	89	2.76	0	4.41
P2	3.5 - 6.6	1.5	100	3.62	0	13.89
P3	8.4 - 10.6	2.5	100	3.12	0	19.94
H1	5.1 - 6.4 (ox), 3.9 (pr)	1.5 (ox) 1 (pr)	98 (ox) 99 (pr)	3.36	1.68	10.54
H2	5.0 - 5.4 (ox), 3.9 (pr)	1.5 (ox) 1 (pr)	98 (ox) 95 (pr)	3.13	1.78	9.99
H3	5.9 - 7.3 (ox), 4.2 - 6.4 (pr)	1.5 (ox) 1.5 (pr)	84 (ox) 100 (pr)	2.94	1.63	10.32
F1	8.5	2	99	3.23	3.23	16.33
F2	4.4 - 5.7	1	97	2.93	2.93	7.39

3.3. Surface effect on the catalytic activity of HRP

The catalytic activity and stability of HRP can be measured by following the oxidation of a substrate over time. TMB absorbs light in the UV-vis spectral region, with distinct absorbance maxima for each oxidation step (Figure 1). If HRP is active, TMB is oxidized under consumption of H_2O_2 from a diamine (TMB^0) to a diimine (TMB^{+2}) *via* the formation of a charge transfer complex (CTC). The monitoring of the arising absorption bands over time elucidates the reaction progress. On day 1, the absorption bands of the CTC (370 nm and 655 nm) were observed for all samples ten minutes after the addition of TMB and H_2O_2 (**Figure 3a-c**), demonstrating catalytically active HRP on all three surface types. The formation of TMB^{+2} was observed on all samples except for F1 (450 nm absorption band). Indeed, as expected due to the varying mass of HRP on the samples, the band intensities clearly vary between the sample type and the single samples. To quantitatively compare the catalytic activity of HRP on the samples, the oxidation reaction rate from TMB^0 to CTC was calculated using the absorption maximum at 655 nm due to its minimal overlap with other bands (**Figure 3d**, Table S1, Supporting Information). A general trend shows decreasing rates with increasing oxidized area (P to F). To eliminate the varying enzyme load of the samples from the calculated values, the rates were divided by the calculated mass of HRP for each sample (**Figure 3e**, Table 1, Table S3, Supporting Information). The trend remains for the normalized rate values. These results show that 2PO of the graphene surface reduces the catalytic activity of noncovalently bound HRP.

When binding noncovalently to a surface, certain amino acid residues interact with certain surface features. Depending on the strength of interaction and stability of the protein, the tertiary structure of a protein may be altered, and – in the case of enzymes – the function may be lost. Indeed, according to previous experimental and theoretical results α-helical structural motifs tend to change their structure on pristine graphene in contrast to β-sheets, which are less affected.[26-28] HRP consists predominantly of α-helices and is prone to these effects. In 2PO graphene, the carbon network is largely preserved despite introducing oxygen-containing groups.[15,16] Hence, similar effects could trigger structural changes and loss of function in HRP

on both pristine and 2PO graphene. However, lower reaction rates on samples with 2PO graphene indicate that the effects are more significant after 2PO of the surface, i.e. the structure of the enzyme is perturbed more on 2PO than on pristine graphene.

In addition, HRP could lose its activity due to the blocking of the active site by the support material or other enzymes.[28,29] In our noncovalent approach, the orientation of the enzymes approaching the surface is random, and a part of the immobilization might occur with the active site facing the surface. Blocking the active site by the graphene surface itself is, therefore, possible for both surfaces. Blocking HRP's active site by other enzymes is possible for samples with more than one protein layers. The upper layer could make the active sites of the lower layer inaccessible for the substrate.
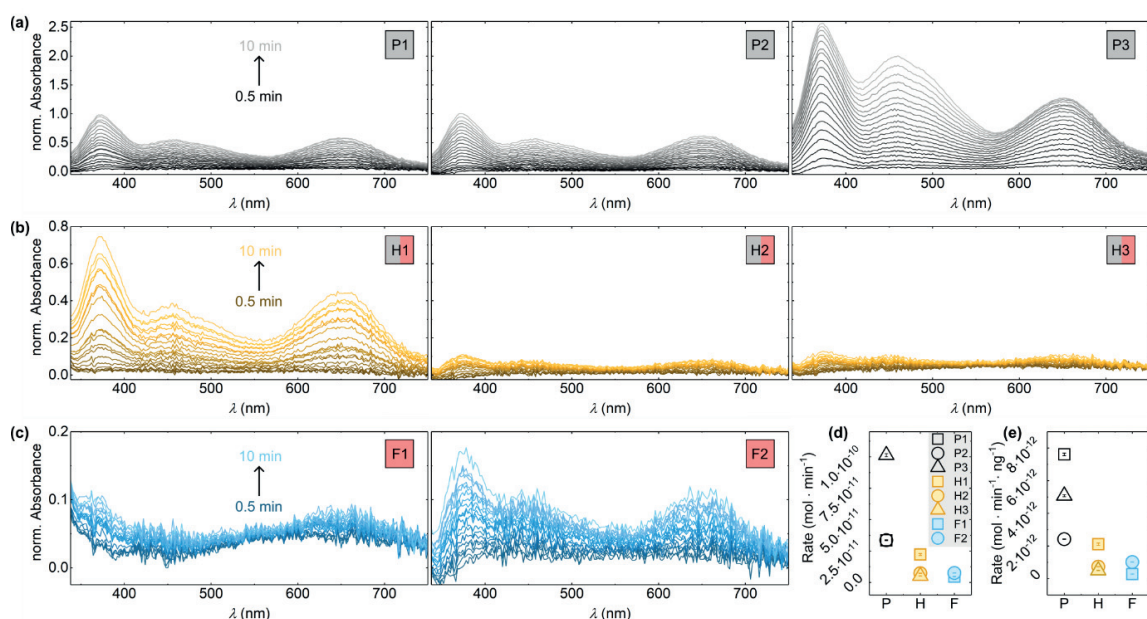
Figure 3: (a)-(c) Normalized absorbance spectra from the first 10 minutes after substrate addition on day 1 for each sample. Sample name and color gradient are indicated in the plots. (d) Reaction rates for the oxidation of TMB^0 to CTC on day 1 for each sample. Error bars indicate the standard deviation of the calculated rates.

To estimate the catalytic activity of the immobilized HRP on each sample, we compared the rates of the immobilized enzymes to the rate of free HRP. A calibration curve was generated by measuring the reaction rate from TMB^0 to CTC from 9 solutions with distinct, known masses of HRP and fitting a linear curve to the rate values (**Figure 4a**). Knowing the reaction rate, the mass of active HRP on each sample was calculated with the linear fit equation (**Figure 4b**). The estimated masses of active HRP vary between 0.06 ng (F1) and 0.96 ng (P3).
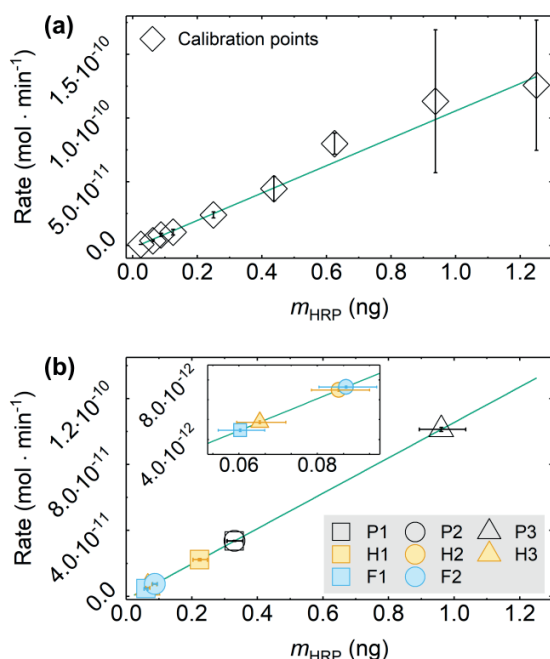
Figure 4: (a) Calibration points and resulting linear calibration fit (green). Error bars present the standard deviation of each rate. The linear fit equation was Rate = $m_{HRP} \cdot (1.1 \cdot 10^{-10} \pm 6.4 \cdot 10^{-12}) - (1.9 \cdot 10^{-12} \pm 1.6 \cdot 10^{-13})$ (b) Calibration fit from (a) and calculated position on fit for each sample. Error bars indicate the maximum and minimum mass of HRP.

To further classify the amount of active HRP on each sample, the mass of active HRP was related to the previously calculated total mass of HRP on each sample (**Table 2**). Overall, the activity of the immobilized HRP was a maximum of 7.5% of the free enzyme (P1). The activity loss might originate from the surface-induced structural changes or the blocking of the active site, as suggested above.[26-29] Looking at the samples in detail, the biggest mass-normalized activity was found on the pristine samples P1, P3 and P2, respectively. The mass-normalized activity of HRP on the half-oxidized samples is in a similar range as on the fully oxidized samples. Considering that perhaps only the top layer of HRP is accessible for the substrate, the mass-normalized activity of HRP would change to 7.5% (P1), 3.6% (P2) and 12.0% (P3) for pristine samples, 2.6% (H1), 1.2% (H2) and 1.0% (H3) for half-oxidized samples and 0.73 (F1) and 1.2% (F2) for fully oxidized samples. These values are in a similar range than before and follow the same trend. The results indicate that, compared to pristine graphene, the interactions between 2PO graphene and HRP lead to either more HRP binding to the surface with the active site inaccessible for the substrate or a more significant impact on the enzyme structure and a consequent loss of function. Whether we analyze the raw data or include the graphene area, the HRP mass or the monolayer theory into our calculations, the results are the same: HRP was less active on 2PO graphene compared to the pristine graphene. However, the activity was not lost completely, and HRP on 2PO graphene can perform its enzymatic function. Thus, with 2PO of graphene, we can control the catalytic activity of the model enzyme HRP, which suggests that there might be similar effects on other proteins as well.

Table 2: Mass-normalized activity of HRP as a ratio of the mass of active HRP $m_{HRP,active}$ and the total mass of HRP m_{HRP}.

	m_{HRP} [ng]	$m_{HRP,active}$ [ng]	Mass-normalized activity [%]
P1	4.41	0.33	7.5
P2	13.89	0.33	2.4
P3	19.94	0.96	4.8
H1	10.54	0.22	2.1
H2	9.99	0.09	0.90
H3	10.32	0.07	0.68
F1	16.33	0.06	0.37
F2	7.39	0.09	1.2

3.4. Stability of the samples

To assess the stability of the noncovalently immobilized HRP on pristine and 2PO graphene, the catalytic activity measurement was repeated on the three following days after the incubation. The samples were stored in the solution overnight to prevent drying of HRP. The absorption spectra 10 minutes after the substrate addition show activity only for the three P samples on day 2 (**Figure 5a**) and on day 3 only for sample P3 (**Figure 5b**). On day 4, no catalytic activity was detected for any sample (Figure S5, Supporting Information). The corresponding reaction rates of the P samples present a decreasing activity over time for each sample (**Figure 5c**, Table S4, Supporting Information). On day 2, the activity had decreased relative to day one to 10% (P2), 31% (P1) and 58% (P3). P3 shows 13% of its initial activity on day 3. The decrease for the oxidized samples is 100% from day 1 to day 2, which could be caused by the already small initial activity, i.e. a possible activity on day 2 would be below the detection limit of the experiment. For our samples, the desorption of HRP from the surfaces can be neglected due to extensive washing after HRP immobilization. We, therefore, attribute the catalytic activity loss over time to structural changes of the immobilized enzymes. Blocking of the active site, as described above, might not happen after the initial immobilization of the enzymes, as noncovalent interactions should hold them in place. For the free enzyme, Hou *et al.* reported a remaining activity of roughly 40% after 12 h at 20 °C,[10] which is in the same range as our pristine samples after 24 h at rt. Therefore, the stability of HRP on pristine graphene is similar or better compared to the free enzyme. Hence, our results support the hypothesis of structural changes due to interactions between surface and HRP and are consistent with previous experimental and theoretical results for HRP on pristine graphene and graphene oxide flakes.[10,14,26]
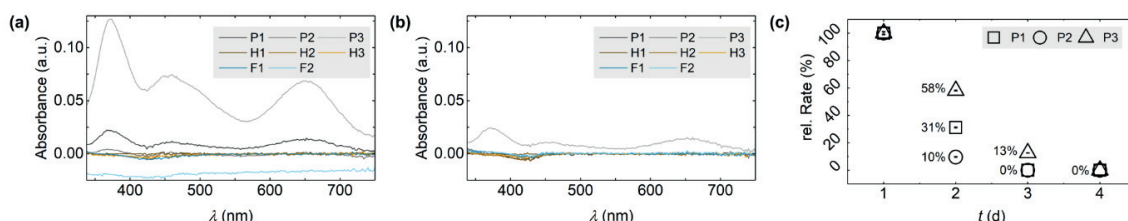

Figure 5: Catalytic activity of HRP over time: Absorbance spectra 10 minutes after substrate addition of all samples on (a) day 2 and (b) day 3. (c) Reaction rates relative to day 1 for the oxidation of TMB^0 to CTC from day 1 to 4 for each sample. Error bars indicate the standard deviation of each rate. The exact values are shown in Table S4, Supporting Information.

4. Conclusion

In this study, we controllably immobilized HRP on single-layer graphene surfaces on Si/SiO$_2$ chips and demonstrated the effect of 2PO of the graphene surface on the catalytic activity of HRP. With our noncovalent approach, we were able to controllably immobilize 1-2 layers of HRP on both pristine and 2PO graphene in the nanogram scale. The catalytic activity was measured for the HRP catalyzed oxidation of TMB and observed *via* UV-vis spectroscopy. To continuously monitor the oxidation, we introduced a simple setup where the graphene sample was mounted to the wall of the measurement container. In this way, we could calculate reaction rates that correlate with the catalytic activity of the samples. The initial activity of the immobilized enzyme showed a clear trend of decreasing activity with increasing 2PO area. We attribute this to distinct interactions between HRP and the two surfaces, which differ in functional groups and the extent of p-type doping. Over the following three days, the activity steadily decreased for all pristine samples, while the oxidized samples lost their activity entirely after day 1. These results are consistent with the previous studies, which connect the activity loss to structural changes in the enzyme upon immobilization.

We demonstrated that 2PO of graphene affects the activity of HRP. In a previous study, we showed that the adhesion of HRP and bovine serum albumin on graphene surfaces can be tuned with 2PO.[12] Though these studies demonstrate the effects for one or two proteins, respectively, we believe that similar effects could be found for other proteins as they consist of similar amino acids that can interact with the surface. Herein, distinct secondary structure elements and 2PO levels might lead to different effects on the protein adhesion, function, and stability. Hence, 2PO as an optical, locally defined nanoscale method enables the construction of surfaces with differing protein loading and functionality. Our approach was performed for graphene, GO and HRP on a Si chip configuration and opens new possibilities for the design and development of biosensors and bio-graphene interfaces on Si chips.

Supporting Information

Supporting Information is available from the Wiley Online Library or from the author.

Acknowledgements

References

[1]   H. M. Fahmy, E. S. Abu Serea, R. E. Salah-Eldin, S. A. Al-Hafiry, M. K. Ali, A. E. Shalan and S. Lanceros-Méndez, *ACS Biomater Sci Eng*, 2022, **8**, 964–1000.

[2]   A. Basso and S. Serban, *Molecular Catalysis*, 2019, **479**, DOI:10.1016/j.mcat.2019.110607.

[3]   S. Bose, S. F. Robertson and A. Bandyopadhyay, *Acta Biomater*, 2018, **66**, 6–22.

[4]   N. Rohaizad, C. C. Mayorga-Martinez, M. Fojtů, N. M. Latiff and M. Pumera, *Chem Soc Rev*, 2021, **50**, 619–657.

[5]   H. Seelajaroen, A. Bakandritsos, M. Otyepka, R. Zbořil and N. S. Sariciftci, *ACS Appl Mater Interfaces*, 2020, **12**, 250-259.

[6]   Y. Wang, S. Di, J. Yu, L. Wang and Z. Li, *J Mater Chem B*, 2023, **11**, 500–518.

[7]   A. K. Geim and K. S. Novoselov, *Nat Mater*, 2007, **6**, 183–191.

[8]   M. Singh, M. Holzinger, M. Tabrizian, S. Winters, N. C. Berner, S. Cosnier and G. S. Duesberg, *J Am Chem Soc*, 2015, **137**, 2800–2803.

[9]   K. Besteman, J. O. Lee, F. G. M. Wiertz, H. A. Heering and C. Dekker, *Nano Lett*, 2003, **3**, 727–730.

[10]   B. Hou and A. D. Radadia, *ACS Biomater Sci Eng*, 2018, **4**, 675–681.

[11]   A. Alshammari, M. G. Posner, A. Upadhyay, F. Marken, S. Bagby and A. Ilie, *ACS Appl Mater Interfaces*, 2016, **8**, 21077–21088.

[12]   E. D. Sitsanidis, J. Schirmer, A. Lampinen, K. K. Mentel, V. M. Hiltunen, V. Ruokolainen, A. Johansson, P. Myllyperkiö, M. Nissinen and M. Pettersson, *Nanoscale Adv*, 2021, **3**, 2065–2074.

[13]   J. Zhang, F. Zhang, H. Yang, X. Huang, H. Liu, J. Zhang and S. Guo, *Langmuir Letter*, 2010, **26**, 6083–6085.

[14]   F. Zhang, B. Zheng, J. Zhang, X. Huang, H. Liu, S. Guo and J. Zhang, *Journal of Physical Chemistry C*, 2010, **114**, 8469–8473.

[15]   J. Aumanen, A. Johansson, J. Koivistoinen, P. Myllyperkiö and M. Pettersson, *Nanoscale*, 2015, **7**, 2851–2855.

[16]   A. Johansson, H.-C. Tsai, J. Aumanen, J. Koivistoinen, P. Myllyperkiö, Y.-Z. Hung, M.-C. Chuang, C.-H. Chen, W. Y. Woon and M. Pettersson, *Carbon*, 2017, **115**, 77–82.

[17]   A. Lampinen, E. See, A. Emelianov, P. Myllyperkiö, A. Johansson and M. Pettersson, *Physical Chemistry Chemical Physics*, 2023, **25**, 10778-10784.

[18]   J. W. Suk, A. Kitt, C. W. Magnuson, Y. Hao, S. Ahmed, J. An, A. K. Swan, B. B. Goldberg and R. S. Ruoff, *ACS Nano*, 2011, **5**, 6916-6924.

[19]   A. V. Emelianov, D. Kireev, A. Offenhäusser, N. Otero, P. M. Romero and I. I. Bobrinetskiy, *ACS Photonics*, 2018, **5**, 3107-3115.

[20]   K. K. Mentel, A. V. Emelianov, A. Philip, A. Johansson, M. Karppinen and M. Pettersson, *Adv. Mater. Interfaces*, 2022, **9**, 2201110

[21]   P. D. Josephy, T. Eling and R. P. Mason, *Journal of Biological Chemistry*, 1982, **257**, 3669–3675.

[22] D. Feng, T. Liu, J. Su, M. Bosch, Z. Wei, W. Wan, D. Yuan, Y. Chen, X. Wang, K. Wang, X. Lian, Z. Gu, J. Park, X. Zou and H. Zhou, *Nature Communications*, 2014, **6**, 5979.

[23] G. I. Berglund, G. H. Carlsson, J. Hajdu, A. T. Smith, H. Szoke and A. Henriksen, *Structure of horseradish peroxidase C1A compound I*, 2002, DOI:10.2210/pdb1hch/pdb.

[24] H. M. Berman, J. Westbrook, Z. Feng, G. Gilliland, T. N. Bhat, H. Weissig, I. N. Shindyalov and P. E. Bourne, *Nucleic Acids Res*, 2000, **28**, 235–242.

[25] D. Sehnal, S. Bittrich, M. Deshpande, R. Svobodová, K. Berka, V. Bazgier, S. Velankar, S. K. Burley, J. Koča and A. S. Rose, *Nucleic Acids Res*, 2021, **49**, 431–437.

[26] J. Guo, X. Yao, L. Ning, Q. Wang and H. Liu, *RSC Adv*, 2014, **4**, 9953–9962.

[27] J. Katoch, S. N. Kim, Z. Kuang, B. L. Farmer, R. R. Naik, S. A. Tatulian and M. Ishigami, *Nano Lett*, 2012, **12**, 2342–2346.

[28] C. Garcia-Galan, Á. Berenguer-Murcia, R. Fernandez-Lafuente and R. C. Rodrigues, *Adv Synth Catal*, 2011, **353**, 2885-2904.

[29] L. Cao, *Carrier-bound Immobilized Enzymes*, 2005, Wiley-VCH.

Supplementary Information

Catalytic Activity of Horseradish Peroxidase Immobilized on Pristine and Two-Photon Oxidized Graphene

Johanna Schirmer, Ester Iatta, Aleksei V. Emelianov, Maija Nissinen and Mika Pettersson*

Department of Chemistry, Nanoscience Center, University of Jyväskylä, P. O. Box 35, FI-40014 JYU, Finland. E-Mail: mika.j.pettersson@jyu.fi

Table of Contents

Raman spectroscopy of pristine and oxidized graphene

The laser-induced two-photon oxidation (2PO) of graphene was verified by Raman spectroscopy. Figure S1 shows one Raman spectra each oxidized sample. There are two bands that appear in the spectra of pristine and laser-oxidized graphene. (i) The G band is assigned to sp^2 C-C stretching in the graphene lattice. (ii) The 2D band is based on a second-order double-resonant process. In addition to the G and 2D band, the spectra of 2PO graphene shows the D and the D' band. Both reveal defects in the carbon lattice of graphene. Here, they show the defects introduced by adding oxygen-containing functional groups to the graphene surface during laser-oxidization.[1]
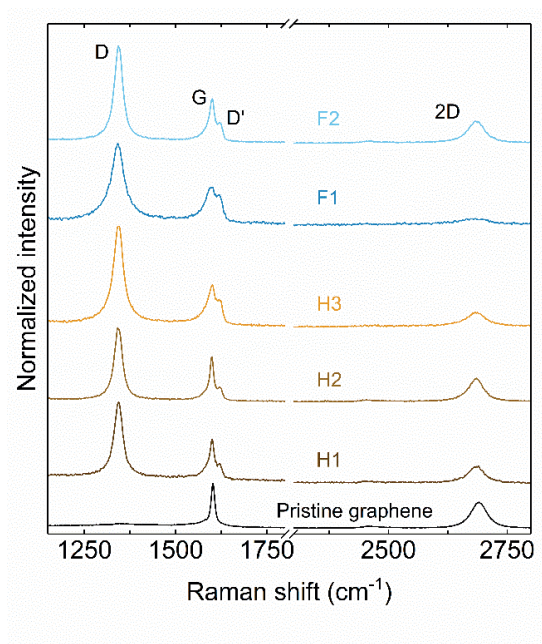
Figure S 1: Raman spectra of a typical pristine graphene samples and the oxidized samples H1, H2, H3, F1 and F2.

UV-Vis negative controls

Two negative control experiments were performed to exclude any interference of the sample and the double-sided adhesive tape to the experiment, similar to section 2.5.1 (Table S 1). A PBS spectrum was subtracted as baseline correction, and the resulting spectra did not show any absorption bands or an elevated background (Figure S 2). Thus, the tape and the sample do not interfere with the signal or catalyze the oxidation of TMB.

Table S 1: List of negative controls and the excluded effects from each control.

#Negative control	Well contained	Excluded effect
1	PBS, TMB, H_2O_2, adhesive tape	Adhesive tape interference with signal and substrate
2	PBS, TMB, H_2O_2, adhesive tape, Si/SiO_2 substrate	Sample interference with signal and substrate
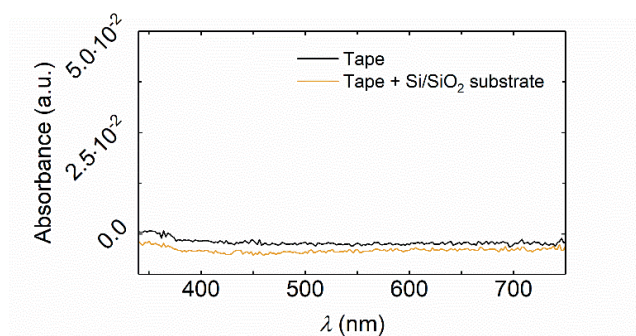
Figure S 2: Negative control spectra after subtraction of the PBS baseline spectrum.

Calibration curve

Table S 2: Calibration curve: Composition of the calibration solutions containing a certain volume of PBS (V_{PBS}) and HRP solution (V_{HRP}) and the resulting mass of HRP m_{HRP} in each solution.

Calibration point	V_{PBS} (µl)	V_{HRP} (µl)	m_{HRP} (ng)
1	294.0	1.0	$2.50 \cdot 10^{-2}$
2	292.5	2.5	$6.25 \cdot 10^{-2}$
3	291.0	3.5	$8.75 \cdot 10^{-2}$
4	290.0	5.0	$1.25 \cdot 10^{-1}$
5	285.0	10.0	$2.50 \cdot 10^{-1}$
6	277.5	17.5	$4.38 \cdot 10^{-1}$
7	270.0	25.0	$6.25 \cdot 10^{-1}$
8	257.5	37.5	$9.38 \cdot 10^{-1}$
9	245.0	50.0	$1.25 \cdot 10^{0}$

AFM imaging
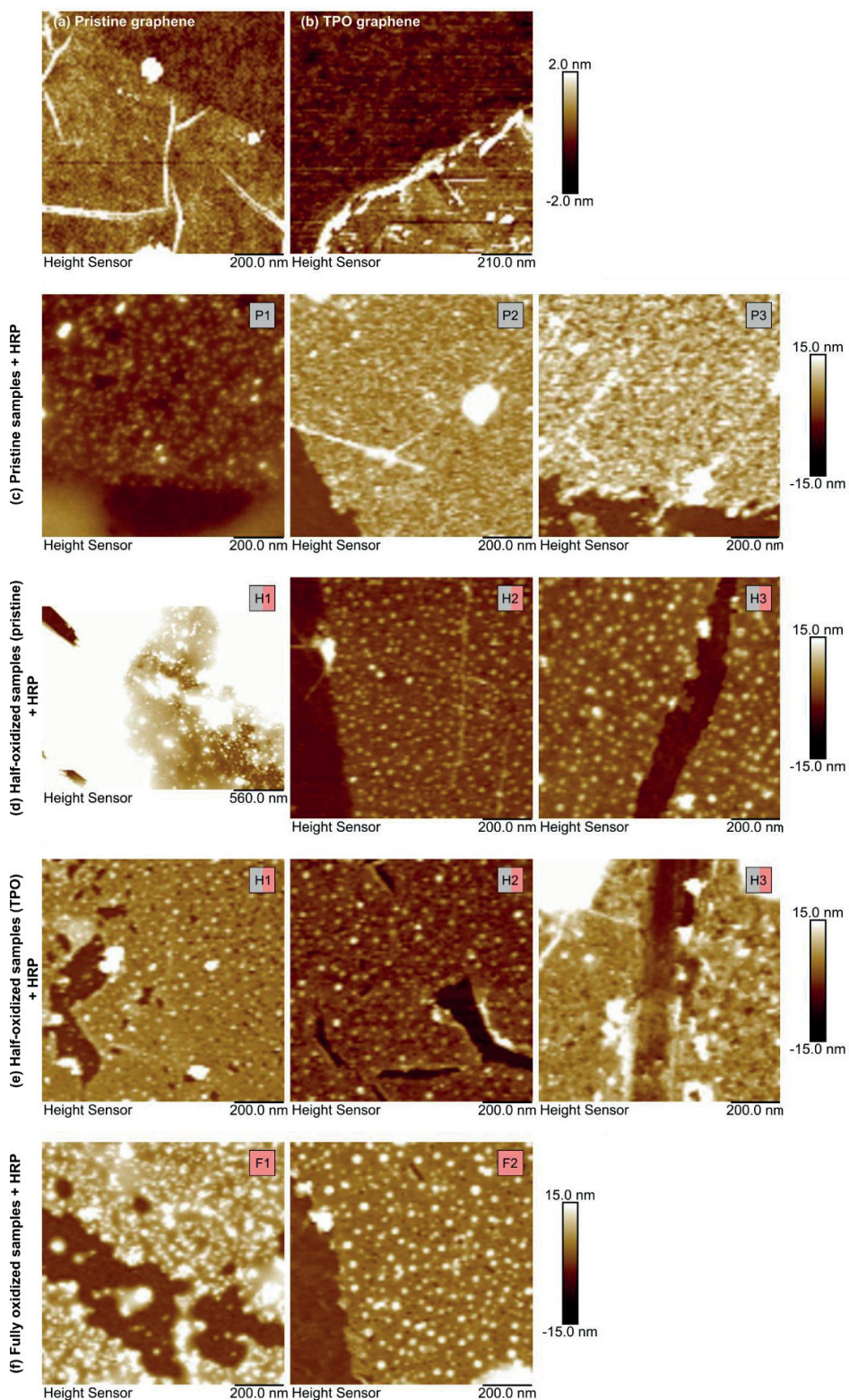
Figure S 3: AFM images of each sample after scratching. The cross-sections of the images were used to estimate the number of HRP layers on each sample.

HRP covering
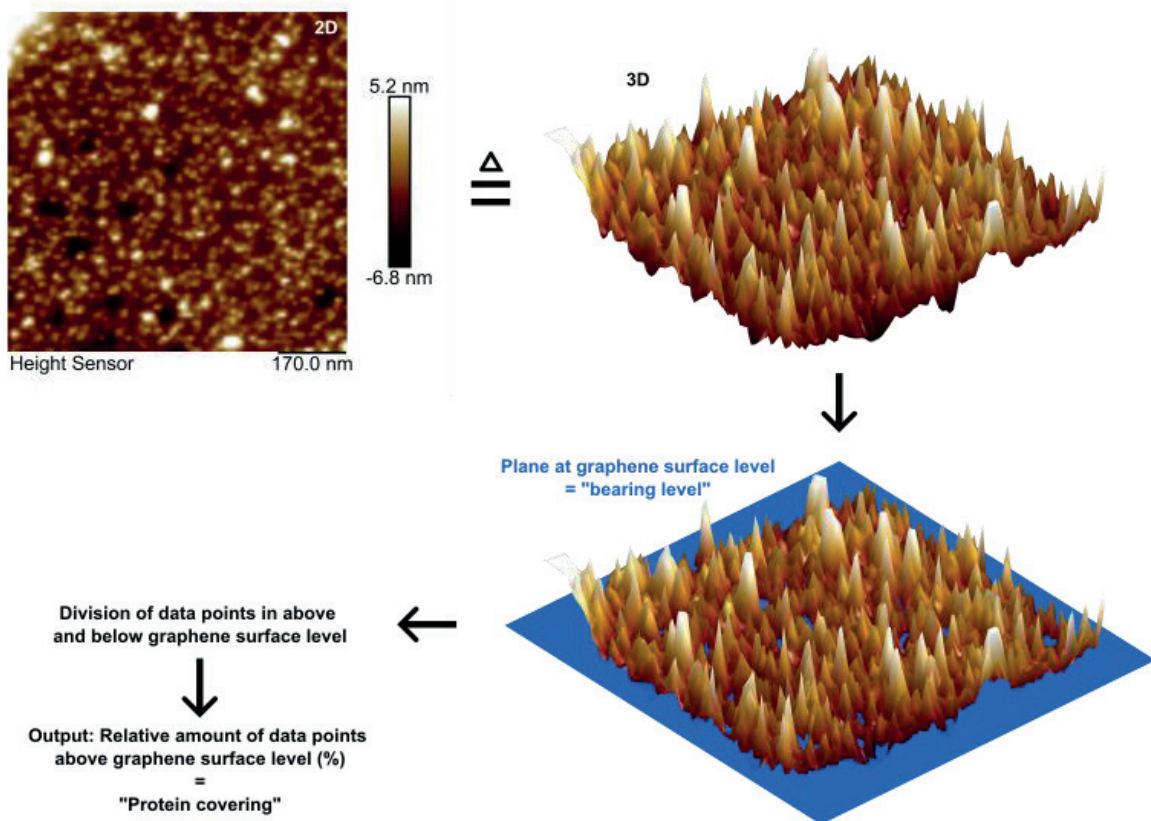
Figure S 4: Schematic illustration of the bearing analysis process: A plane is laid onto an AFM topography image at a certain height level ("bearing level"), dividing data points in "above" and "below" this level. The output is the relative amount of data points above the bearing level in %.

Catalytic activity on day 1

Table S 3: Reaction rates of all samples on day one as raw data and relative to the mass of HRP on each sample.

Sample	Rate (10^{-12} mol · min^{-1}) ± Standard deviation	Rate (10^{-12} mol · min^{-1} · ng^{-1}) ± Standard deviation
P1	33.56 ± 0.36	7.61 ± 0.082
P2	33.62 ± 0.24	2.42 ± 0.017
P3	101.32 ± 1.27	5.08 ± 0.063
H1	22.22 ± 0.77	2.11 ± 0.073
H2	7.32 ± 0.085	0.73 ± 0.0085
H3	5.16 ± 0.092	0.50 ±0.0089
F1	4.62 ± 0.088	0.28 ± 0.0054
F2	7.53 ± 0.068	1.02 ± 0.0091

Catalytic activity on day 4
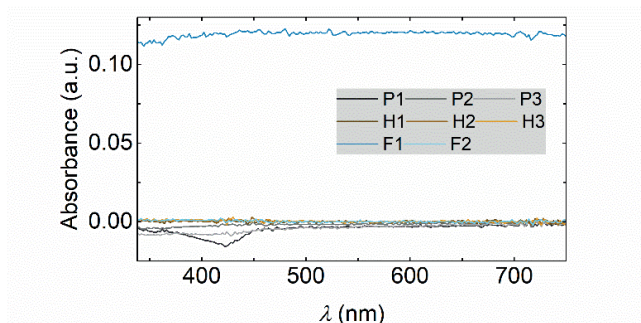
Figure S 5: UV-Vis spectra of all samples on day 4 after baseline correction. The lines are flat, indicating no catalytic activity of the immobilized HRP. The spectrum of F1 has an elevated baseline because the sample fell to the bottom of the well plate and consequently blocked part of the light beam.

Table S 4: Reaction rates of all pristine samples on days 1, 2, 3 and 4.

Sample	Rate (10^{-11} mol · min^{-1}) ± Standard deviation			
	day 1	day 2	day 3	day 4
P1	3.36 ± 0.036	1.05 ± 0.014	0	0
P2	3.36 ± 0.024	0.324 ± 0.013	0	0
P3	10.13 ± 0.13	5.90 ± 0.039	1.28 ± 0.014	0

References

[1]   L. M. Malard, M. A. Pimenta, G. Dresselhaus and M. S. Dresselhaus, Raman spectroscopy in graphene, *Phys Rep*, 2009, **473**, 51–87.

III

PROBING THE GELATION SYNERGIES AND ANTI-*ESCHERICHIA COLI* ACTIVITY OF FMOC-PHENYLALANINE/GRAPHENE OXIDE HYBRID HYDROGEL

by

Efstratios D. Sitsanidis, Lara A. L. Dutra, Johanna Schirmer, Romain Chevigny, Manu Lahtinen, Andreas Johansson, Carmen C. Piras, David K. Smith, Marja Tiirola, Mika Pettersson & Maija Nissinen, 2023

ACS Omega, vol 8, 10225-10234

DOI: 10.1021/acsomega.2c07700

Probing the Gelation Synergies and Anti-*Escherichia coli* Activity of Fmoc-Phenylalanine/Graphene Oxide Hybrid Hydrogel

Efstratios D. Sitsanidis, Lara A. L. Dutra, Johanna Schirmer, Romain Chevigny, Manu Lahtinen, Andreas Johansson, Carmen C. Piras, David K. Smith, Marja Tiirola, Mika Pettersson, and Maija Nissinen*

Read Online

ACCESS | Metrics & More | Article Recommendations | Supporting Information

ABSTRACT: The *N*-fluorenyl-9-methyloxycarbonyl (Fmoc)-protected amino acids have shown high antimicrobial application potential, among which the phenylalanine derivative (Fmoc-F) is the most well-known representative. However, the activity spectrum of Fmoc-F is restricted to Gram-positive bacteria only. The demand for efficient antimicrobial materials expanded research into graphene and its derivatives, although the reported results are somewhat controversial. Herein, we combined graphene oxide (GO) flakes with Fmoc-F amino acid to form Fmoc-F/GO hybrid hydrogel for the first time. We studied the synergistic effect of each component on gelation and assessed the material's bactericidal activity on Gram-negative *Escherichia coli* (*E. coli*). GO flakes do not affect Fmoc-F self-assembly per se but modulate the elasticity of the gel and speed up its formation. The hybrid hydrogel affects *E. coli* survival, initially causing abrupt bacterial death followed by the recovery of the surviving ones due to the inoculum effect (IE). The combination of graphene with amino acids is a step forward in developing antimicrobial gels due to their easy preparation, chemical modification, graphene functionalization, cost-effectiveness, and physicochemical/biological synergy of each component.
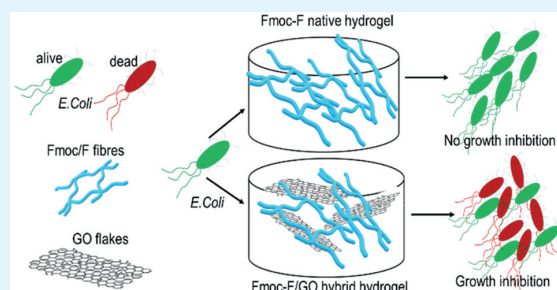
INTRODUCTION

Microbial infections pose a significant threat to human health and are one of the major concerns in public healthcare.[1] Despite the advances in drug development, limitations associated with the treatment of pathogens include antimicrobial resistance (AMR) toward existing medication and the appearance of new diseases.[2] Currently, new approaches in antimicrobial therapeutics[3] and materials are constantly introduced, such as polymers, ceramics, nanoparticles, biomacromolecules, small organic molecules, and hydrogels.[4−7]

Hydrogels have gained momentum for the treatment and prevention of microbial infections due to their physicochemical and viscoelastic properties, cost-effectiveness, ease of preparation, and manufacturing upscale. In addition, they have high water content and combine low toxicity (high biocompatibility toward mammalian cells) with antimicrobial activity. Their activity can be either inherent or, for example, caused by incorporating antimicrobial agents within the gel matrix, which can increase their spectrum of activity.[8,9] Recently, several amino acid and peptide-based supramolecular gels have been introduced, of which the *N*-fluorenylmethyloxycarbonyl (Fmoc)-protected analogues have shown high application potential.[10−13]

In particular, the phenylalanine derivative (Fmoc-F) has exhibited antibacterial activity against Gram-positive bacteria, both in the solution and gel state, via a mechanism disrupting the bacterial membrane/wall.[14,15] Additionally, Fmoc-F inhibits the formation of biofilms and eradicates the already formed ones over surfaces due to its surfactant properties.[16] Despite its efficacy over Gram-positive bacteria, its biocidal effect on Gram-negative bacteria is limited due to its inability to cross the bacterial membrane of Gram-negative microbes. Therefore, to increase the antibacterial spectrum of the amino acid, several Fmoc-F hybrid gels have been fabricated, exploiting the synergistic effect of incorporated antimicrobial agents, for example, aztreonam (AZT) antibiotic,[17] silver ions,[18] berberine chloride,[19] and salicylic acid.[20]

The research for efficient antimicrobial materials has expanded into carbon nanomaterials, such as graphite (Gt), graphite oxide (GtO), graphene oxide (GO), reduced graphene oxide (rGO), carbon nanotubes (CN), and full-

erenes.[21,22] GO forms stable colloids in water and can be easily chemically modified. Therefore, its antimicrobial activity has been extensively studied against Gram-positive/negative pathogens.[23,24] Graphene-based materials display antibacterial action as they disrupt the cell membrane and induce oxidative stress by producing reactive oxygen species (ROS). However, the reported results are somewhat controversial since their activity is influenced by several factors, such as their size, morphology, purity, concentration, and type of functionalization.[25,26]

Since GO flakes have been reported to show antibacterial activity against Gram-negative *Escherichia coli* (*E. coli*),[21] their incorporation within the Fmoc-F gel network could expand the antibacterial spectrum of the amino acid against *E. coli*.[14] In this study, we combined GO flakes with commercially available Fmoc-F amino acid for the first time to produce Fmoc-F/GO hybrid hydrogel. We investigated the synergistic effect of each component on the gelation process spectroscopically and assessed the macro-/microscopic properties of the hybrid material (Fmoc-F/GO) in relation to the native Fmoc-F hydrogel. In addition, we investigated the antimicrobial activity of the formed gel and its components against Gram-negative *E. coli*.

■ MATERIALS AND METHODS

Materials. *N*-Fluorenyl-9-methoxycarbonyl-L-phenylalanine (Fmoc-F) was purchased from Sigma-Aldrich, GO water dispersion (0.4 wt %) from Graphenea, and rGO powder (98−99%) from Wholesale Graphene. All reagents were used as supplied.

Preparation of Hydrogels. *Fmoc-F Native Hydrogel.* A suspension of Fmoc-F (2.0 mg/mL) in phosphate buffer solution (PBS, 50 mM, pH 7.4) was sonicated for 2 min and heated at 80 °C for 30 min. The obtained transparent solution was then left to cool down at room temperature for 12 h, giving a self-supporting hydrogel as verified by vial inversion.

Fmoc-F/GO Hybrid Hydrogel. GO flakes were formed by drying GO water dispersion (0.4 wt %) under a vacuum for 2 days. The obtained flakes were suspended in PBS solution (50 mM, pH 7.4) at several concentrations (0.2, 0.5, 0.75, 1.0 mg/mL) by sonication (15 min) before the addition of Fmoc-F (2.0 mg/mL). The resulting Fmoc-F/GO suspension was sonicated (2 min) and heated at 80 °C (30 min). Gelation occurred at room temperature after 12 h and was assessed by the vial inversion method. The GO flakes remained equally distributed through the final gel.

Instrumentation. *Fluorescence Spectroscopy.* Emission spectra were recorded on the Varian Cary Eclipse fluorescence spectrophotometer. Gel samples were formed *in situ* in a quartz cuvette with a path length of 1 cm. The excitation wavelength was 296 nm. Both excitation and emission slit widths were 5 nm.

Fourier Transform Infrared (FT-IR) Spectroscopy. IR spectra were measured on Bruker Tensor 27 FT-IR spectrometer in Attenuated Total Reflection (ATR) mode. (Spectral width: 400−4000 cm^{-1}; absorption mode; step: 2 cm^{-1}; the number of scans: 124). All spectra were baseline corrected.

Raman Spectroscopy. Raman spectra were recorded on Bruker Optics SENTERRA R200-785 Raman microscope (Laser 785 nm). Gels were dried under a vacuum for 2 days and placed on a microscope glass slide before measurement.

Microscopy. Helium ion microscopy (HIM) images were captured on the Zeiss Orion Nanofab microscope and transmission electron microscopy (TEM) images on the JEOL JEM-1400HC microscope. Atomic force microscopy (AFM) imaging was performed on a Bruker Dimension Icon atomic force microscope using PeakForce tapping mode. ScanAsyst-Air probes from Bruker were used during imaging with the peak force set to 2.0 nN. All AFM images were processed with NanoScope Analysis 1.9 software. To prepare xerogel samples for microscopy imaging, carbon films (400 mesh copper grids, Agar Scientific) were dipped into the gels and allowed to dry in the open air overnight.

Rheology. Oscillation rheology was performed on the Malvern Kinexus Pro+ rheometer, fitted with an 8 mm parallel plate upper geometry. All gel samples (1.0 mL volume) were prepared in homemade glass chambers and transferred onto the lower geometry of the instrument as intact gel pellets. Amplitude sweep measurements were performed at an angular frequency of 1.0 Hz, using shear strain (γ%) within the range of 0.05−100% at 25 °C. Frequency sweep measurements were performed in triplicate within the linear viscoelastic region (LVR) where the elastic (G') and loss (G'') moduli are independent of the strain amplitude. Each measurement was performed using a shear strain (γ%) of 0.25%, at a range of 0.1 to 100 rad/s at 25 °C.

Thermogravimetric Analysis (TGA). Thermogravimetric analysis was performed on PerkinElmer STA 6000 simultaneous thermogravimetric and differential scanning calorimetric analyzer (TG/DSC). Each sample was placed in an open platinum crucible and heated under air atmosphere (flow rate of 40 mL/min) with a heating rate of 10 °C/min at a temperature range of 20−600 °C. The temperature calibration of the analyzer was based on the melting points of indium (156.60 °C) and zinc (419.5 °C). The weight balance was calibrated at room temperature with a standard weight of 50.0 mg. The used sample weights were 6.0−7.0 mg.

Powder X-ray Diffraction (PXRD). Powder X-ray diffraction measurements were performed on a PANalytical X'Pert PRO MPD diffractometer in Bragg−Brentano geometry using Johansson monochromator generated Cu Kα1 radiation (λ = 1.5406 Å; 45 kV, 40 mA). Each lightly hand-ground powder sample was prepared on a silicon-made "zero-background" inducing holder using petroleum jelly as an adhesive. Diffraction patterns were recorded from a spinning sample by a position-sensitive X'Celerator detector using continuous scanning mode in a 2θ range of 4−70° with a step size of 0.017° and a counting time of 200 s/step. Diffraction data were analyzed using Malvern Panalytical HighScore Plus (v. 4.8).[27] The unit cell parameters of neat Fmoc-F powder at RT were determined by the Pawley method[28] using the corresponding single crystal structure parameters (CSD database[29] entry OGIXOT[30]) as the basis of least-squares refinement. Variable parameters were as follows: zero-offset, polynomial background, sample displacement, unit cell, and peak profile parameters. Refined unit cell parameters were used for monitoring the structural properties of Fmoc-F and Fmoc-F/GO hybrid xerogels.

Antimicrobial Screening. The antimicrobial activity of Fmoc-F/GO hybrid hydrogel against Gram-negative *E. coli* (strain DSM 882) was assessed by evaluating the bacterial growth/culture density over time (optical density-OD$_{600}$). Two-fold serial dilutions of the Fmoc-F/GO hybrid gel and its corresponding components (Fmoc-F native gel, GO suspen-

sion and PBS) were prepared in Luria−Bertani (LB) broth. Fresh *E. coli* culture, in the exponential growth phase, was used to prepare the bacterial inoculum to a final density of 1.5×10^6 CFU/mL in testing samples. The gel samples, prepared at a range of concentrations (Table 1), were pipetted in a

Table 1. Concentration of Fmoc-F/GO Hybrid Hydrogel Samples for OD$_{600}$ Screening

gel components	D1	D2	D3	D4	D5
Fmoc-F (mg/mL)[a]	1.0	0.5	0.25	0.125	0.0625
GO (μg/mL)[a]	125	62.5	31.25	15.625	7.8125

[a]Given concentrations of each component of the Fmoc-F/GO hybrid hydrogels prepared by serial dilutions (D1−D5).

honeycomb 96-well plate (200 μL/well) and incubated in a Bioscreen C spectrophotometer (37 °C, continuous shaking with low amplitude and normal speed, OD$_{600}$ readings at 10 min intervals for 24 h). The OD$_{600}$ background values were obtained by subtraction of the negative control values. The OD$_{600}$ background values of the hybrid gel and each component were obtained from samples prepared without bacterial inoculum. The control growth curve for each dilution (with growth medium) was based on the bacterial growth in the presence of the basic growth medium.

Gel samples were prepared based on the given gelation protocol and sterilized under UV light for 1 h. Fluorescence microscopy imaging of the bacteria was performed using a Leica TCS SP8 Falcon microscope. The bacterial cell viability was assessed after 5 h of incubation. *E. coli* were stained by a mixture of SYTO 9 (33.4 μM working solution) and propidium iodide (PI, 400 μM working solution) stains. The obtained images were processed by Fiji2 (ImageJ2) software.

■ RESULTS AND DISCUSSION

Gel Fabrication and Morphological Features. The gelation efficacy of the Fmoc-F/GO hybrid system was assessed by a series of concentration screening trials. The critical gelation concentration (CGC) of the protected amino acid (Fmoc-F) for both gels, native and hybrid, was found to be 2.0 mg/mL (Tables S1, S2). For the hybrid material, the gelation outcome depended only on the amino acid concentration, irrespective of the added amount of GO flakes (Table S2). The gel-to-sol phase transition temperature ($T_{gel−sol}$) was measured by controlled heating of the gels. The $T_{gel−sol}$ of the hybrid hydrogel increased only by increasing the amino acid concentration, while the incorporation of GO flakes at different concentrations showed negligible effects (Tables S3, S4). The $T_{gel−sol}$ study verified the thermoreversible nature (gel-to-sol-to-gel) of the hybrid gel system since all test samples reformed upon cooling within 12 h.

Under the given gelation conditions, the suspension of Fmoc-F/GO yielded a homogeneous self-supporting hydrogel, i.e., no phase separation or precipitation of the GO flakes was observed (Figure 1). However, heating the suspension at a higher temperature and for a longer time (95 °C, 1 h) led to the precipitation of GO (Figure S1). When rGO powder was incorporated into the amino acid solution, nonhomogeneous gels formed under the standard gelation conditions (heating at 80 °C for 30 min). Indeed, rGO precipitated in all trials at all used concentrations (0.25−1.0 mg/mL, Figure S2). The increased aggregation of GO at a higher temperature may be attributed to various processes such as enhanced collision
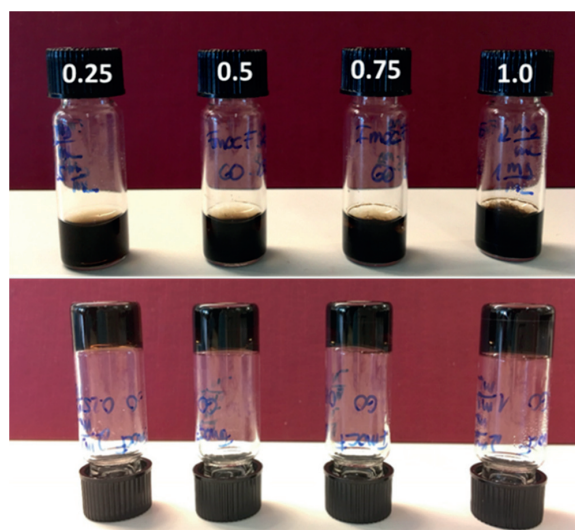

Figure 1. Gelation screening of the Fmoc-F/GO hybrid system at a range of GO concentrations (0.25−1.0 mg/mL). Homogeneous self-supporting gels were formed regardless of the amount of GO. The concentration of Fmoc-F was kept constant (2.0 mg/mL).

frequency, cation dehydration, and reduced electrostatic repulsion, as reported by Gao et al.[31] in their aggregation kinetics studies of GO in mono- and divalent aqueous solutions.

The morphology of the hybrid gel network was investigated by HIM, TEM, and AFM. The formed Fmoc-F fibers were similar in shape, width, and length among the native and hybrid materials (Figures 2, S3), suggesting that the presence of GO flakes did not affect the self-assembly of the amino acid. Therefore, the molecular packing of the Fmoc-F building blocks seems to follow a specific hierarchy, initially forming one-dimensional polymeric molecular chains, which lead to
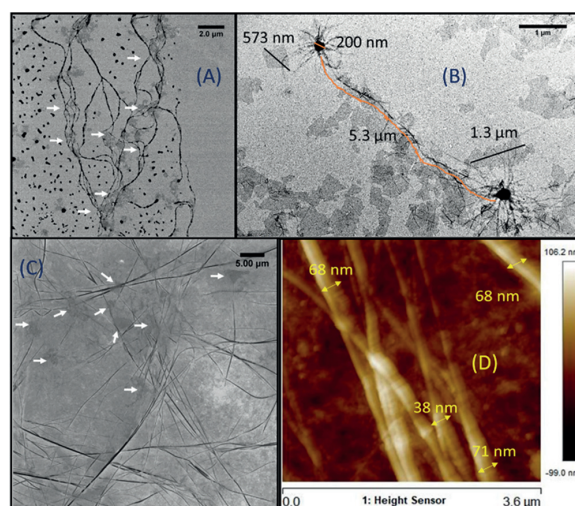

Figure 2. Microscopy images of the Fmoc-F/GO hybrid hydrogel. (A, C) HIM images; (B) TEM image; (D) AFM image with given dimensions of the fibers. The concentrations of Fmoc-F and GO were 2.0 and 0.25 mg/mL, respectively.
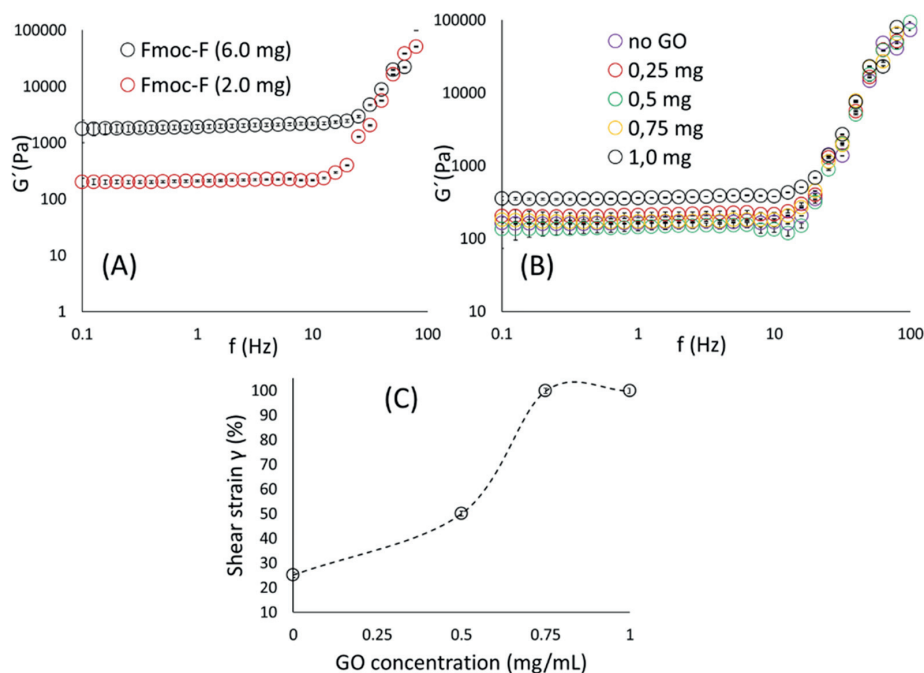
Figure 3. Rheology studies of the hybrid hydrogel. (A) The effect of Fmoc-F concentration on the stiffness (G') of the material. The concentration of GO was kept constant at 0.25 mg/mL. (B) The effect of GO concentration on the stiffness (G') of the material. The concentration of Fmoc-F was kept constant at 2.0 mg/mL. The corresponding G'' values are given in Figure S5A,B. (C) Assessing the elasticity of the hybrid gel: Comparing the G' and G'' cross points of the amplitude sweep measurements in contrast to the amount of added GO. The concentration of Fmoc-F was kept constant at 2.0 mg/mL. Error bars represent standard deviation.

higher architectures that interact with GO, *vide infra*. The three-dimensional network comprises single, branched, and entangled fibers and fine fibers in coiled-coil constructions. Their length varies up to several micrometers, and their width is within the range of ~40−70 nm (Figure 2D).

The GO flakes, seen as semitransparent sheets in the TEM and HIM micrographs, have various dimensions from nano to micrometers. The flakes are well dispersed in the gel network and encircled by Fmoc-F fibrillar loops (Figures 2A,C, white arrows). Indeed, the fibers are formed on the surface, around the edges and between the GO flakes, showcasing the development of noncovalent interactions between the already-formed fibers and GO. GO flakes do not seem to affect the self-assembly per se. However, the size of the flakes needs to be investigated further regarding the nucleation step of Fmoc-F to identify potential connection between the hydrogelation kinetics of the amino acid and the size of GO flakes.

In addition, microscopy imaging revealed spherulitic structures or nucleation points, out of which fibers grow and interpenetrate to adjacent spherulites (Figure 2B). Such structures (microcrystals) have previously been reported in Fmoc-F hydrogels at low pH values, originating from bundles of needle-shaped crystals.[30] When spin-cast, the structurally similar diphenylalanine (F−F) dipeptide also grows dendritic structures, which have been interpreted as two-dimensional spherulites.[32] For our hybrid Fmoc-F/GO material, the spherulitic pattern does not cover the entire gel network, which mostly consists of branched, entangled fibers. The hydrogel sample was allowed to dry overnight in the open air before imaging, which might have led to the crystallization of Fmoc-F and the formation of the observed spherulites.

Mechanical Properties and Thermogravimetric Analysis. The viscoelastic properties of the hybrid hydrogel were assessed by oscillatory rheology studies (Figure 3). The frequency sweep measurements were performed on self-supporting gels within the linear viscoelastic region (LVR), in which the storage (G') and loss moduli (G'') are independent of the strain amplitude. For both the native and hybrid hydrogels, the G' had a higher value than the G'', confirming the materials' viscoelastic nature (gel state) (Figures 3, S4, S5). The stiffness of the hybrid material depends only on the amino acid concentration (Figures 3A, S5A), as the incorporation of GO flakes at different concentrations had a negligible effect on the G' value (Figures 3B, S5B). However, the addition of GO flakes increased the elasticity of the material, as indicated by its resistance to shear strain, since the cross points of the G' and G'' of the amplitude sweep measurements shifted toward higher shear strain (γ%) values at higher GO concentrations (Figure 3C). It is of note that the addition of GO resulted in a faster formation of the hybrid material (within 6 h based on the vial inversion method) than the native gel, which required a longer time to fully form (at least 12 h).

The thermogravimetric (TG) data and differential scanning calorimetric (DSC) curves of the neat Fmoc-F powder and the corresponding xerogels (native and hybrid materials) are given in Figure 4 and Table S5. The neat Fmoc-F bulk powder is free of hydrated and nonbound water as the first thermal weight loss can be observed only at 194 °C, indicating the beginning of its thermal decomposition (onset value 218 °C). The primary decomposition occurs steeply between 200 and 350 °C by various degradation and cleavage processes on the
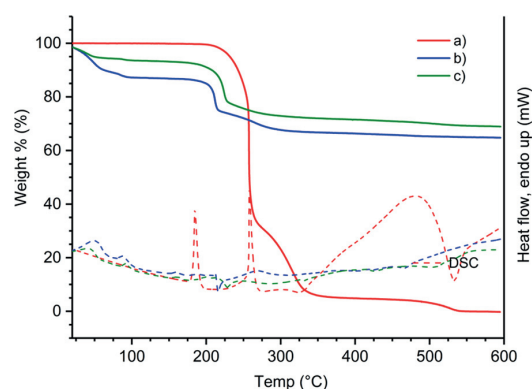
Figure 4. TG curves (solid lines) and DSC curves (dashed lines) of (a) neat Fmoc-F powder, (b) Fmoc-F native xerogel, and (c) Fmoc-F/GO hybrid xerogel, measured under an air atmosphere with a heating rate of 10 °C/min.

carboxylic acid and amide groups and finally at higher temperatures on the aromatic groups, resulting in a carbonaceous residue of ~0.5 wt % at 600 °C.

On the DSC curve, the endothermic melting transition of the neat Fmoc-F powder can be seen at 184.6 °C. The TG curves of both xerogels (native and hybrid) show their first initial weight loss from 22 °C to about 100 °C, indicating the removal of residual water remaining in the xerogels (12.5 and 4.17 wt % on the native gel and hybrid material, respectively). The thermal decomposition of both xerogels initiates at a somewhat lower temperature than that of neat Fmoc-F powder, which may be due to the more porous, less structured, and highly amorphous nature of the xerogels in contrast to the highly crystalline Fmoc-F raw material. Overall, the thermal decomposition processes follow the same path in both xerogels, showing slightly higher residue on the GO-containing xerogel. This is expected due to the thermal stability of the GO sheets.

Molecular Packing. To probe the self-assembly of Fmoc-F in the presence of GO flakes, we compared the Fourier transform infrared (FT-IR) spectra of neat amino acid powder with the native (Fmoc-F) and hybrid (Fmoc-F/GO) xerogels (dried gels) and neat GO flakes (Figure 5). Both xerogels gave identical spectra, however different from neat Fmoc-F powder. Therefore, any interactions between the formed fibers and GO flakes could not be observed. The data confirm the microscopic observations that adding GO to the system did not affect the Fmoc-F self-assembly. In addition, the obtained IR profiles of both xerogels are consistent with previously reported similar systems,[33,34] meaning that no profound changes occurred during the self-assembly of the amino acid in the hybrid system.

Both xerogels lack the 1720 cm^{-1} band of the amino acid, which corresponds to the non-hydrogen bonded carbonyl carbamate of the Fmoc group. This shows the involvement of the Fmoc moiety either in H-bond formation or other noncovalent interactions. The amide A and II bands at 3316 and 1537 cm^{-1}, respectively, are shifted in both xerogels, which corroborates the formation of amide−amide H-bonding. A blue shift is also observed for the amide I band (1681 to 1691 cm^{-1}). The C−O/C−N stretching peaks (1254, 1224 cm^{-1}) of neat Fmoc-F merged toward a broader band in both xerogels (~1255 cm^{-1}), while the C−H out of plane band (895 cm^{-1})
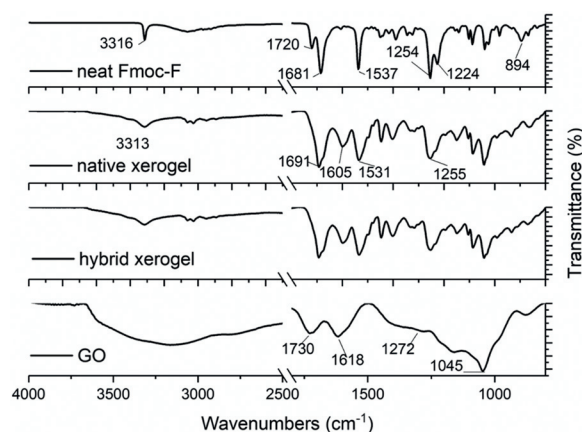

Figure 5. FT-IR spectra of neat Fmoc-F, neat GO, native, and hybrid xerogels. The amino acid concentration in both xerogels was 2.0 mg/mL. GO was added at a concentration of 0.25 mg/mL in the hybrid system. The FT-IR spectra of the phosphate salts Na$_2$HPO$_4$·2H$_2$O and NaH$_2$PO$_4$·H$_2$O used for preparing PBS solution (negative control) are given in Figure S7.

is diminished. Finally, neat GO gave the characteristic peaks of O−H stretching (broad ~3430−2940 cm^{-1}), C=O stretching (1730 cm^{-1}), aromatic C=C and O−H bending (1618 cm^{-1}), epoxy C−O stretching (1272 cm^{-1}), and alkoxy C−O stretching (1045 cm^{-1}), which are not seen in the hybrid xerogel.[35]

To further explore potential differences in the structure of the materials, we compared the powder X-ray diffraction (PXRD) patterns of the native and hybrid xerogels with the neat bulk powder of Fmoc-F and GO flakes (Figure 6). The Pawley fit (Figure S6) indicates that the crystalline bulk powder, with sharp, distinct diffraction peaks, is phase pure and
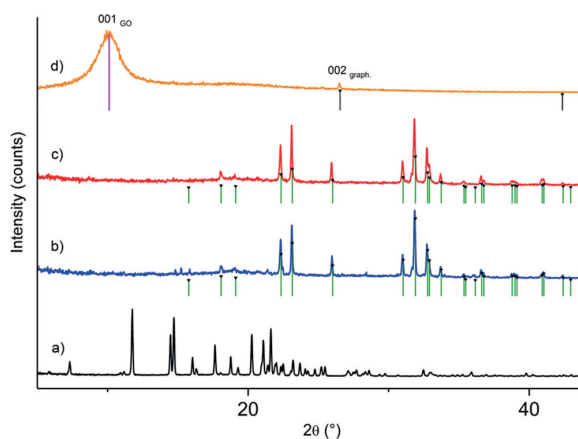

Figure 6. Powder X-ray diffraction patterns of (a) neat Fmoc-F, (b) Fmoc-F native xerogel, (c) Fmoc-F/GO hybrid xerogel, and (d) neat GO. Green vertical markers correspond to characteristic Bragg peak positions of anhydrous Na$_2$HPO$_4$, originating from the phosphate buffer solution, which crystallized in both xerogel samples. Black and magenta markers represent graphite and GO phases, respectively. The concentration of Fmoc-F was 2.0 mg/mL in both xerogel samples. GO was added at a concentration of 0.25 mg/mL in the hybrid system.
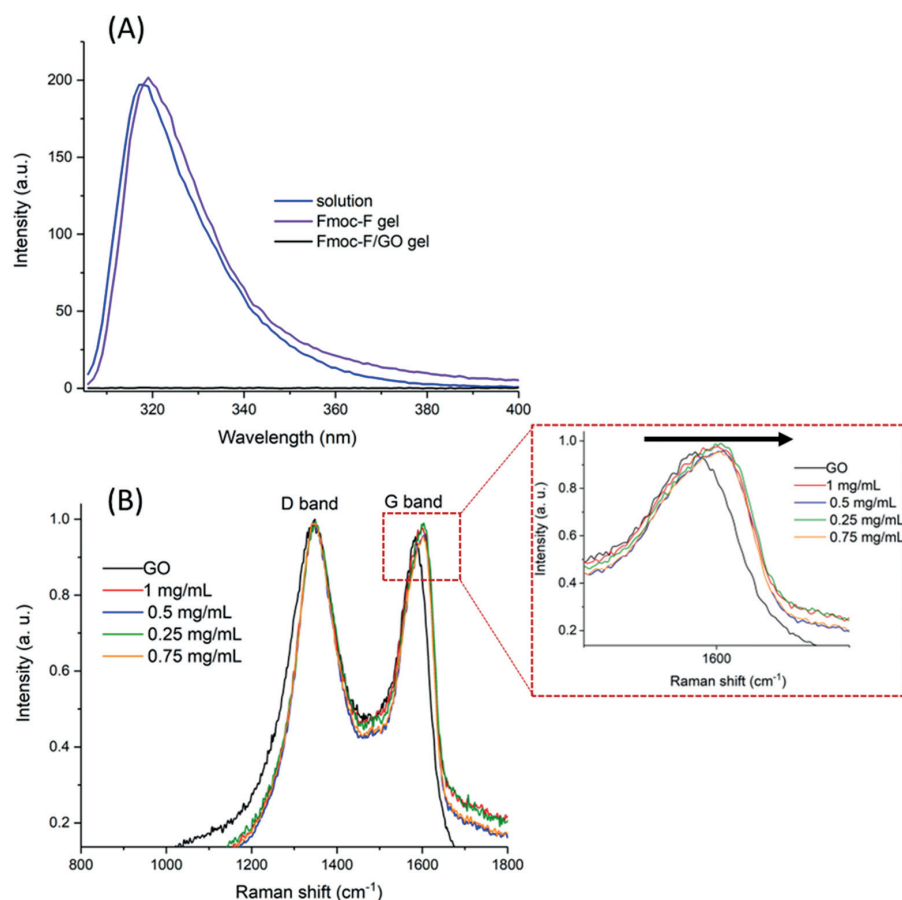
Figure 7. Spectroscopy analysis of the hydrogels. (A) Fluorescence spectra of the Fmoc-F solution in DMSO, native, and hybrid hydrogels. The concentration of Fmoc-F was 2.0 mg/mL and GO 0.25 mg/mL. The corresponding UV−vis spectra are given in Figure S8. (B) Raman spectra of neat GO and the hybrid hydrogel at a range of GO concentrations. The concentration of Fmoc-F was kept constant (2.0 mg/mL). The insert depicts a magnification of the G band plots with an arrow indicating the blue shift by addition of GO.

structurally congruent with the reported single crystal structure since no unindexed peak positions remain in the fit. The crystallographic data and the agreement indices are given in Table S6.

The native Fmoc-F xerogel shows several sharp, distinct diffraction peaks at the angular range of 15−40° 2θ. However, a search-match phase identification analysis indicated that the obtained peaks do not originate from the Fmoc-F phase. Instead, they are unambiguously characteristic of the anhydrous Na_2HPO_4 phase. The phosphate phase originates from the buffer solution, crystallized during the drying of the hydrogel. Similar peaks have also been reported previously for the Fmoc-F xerogel (gel samples prepared in PBS solution by sonication/heating).[34] Here, all gel samples were prepared in PBS solution with sonication/heating-induced gelation, as reported by Thakur et al.,[14] whose materials showed antibacterial properties against Gram-positive bacteria in the solution and gel phases. To avoid strong X-ray diffraction of phosphate salts, gels could be prepared in water, and gelation triggered by the pH switch method. However, we have intentionally followed the gelation protocol of Thakur et al.[14] to prepare materials with known antimicrobial properties. Also, changes in the gelation method and/or the solvent alter self-assembly mode resulting in materials with different properties.

In addition to the phosphate phase peaks, a few very weak peak positions remain unindexed in the pattern, for example, at 14.8°, 15.3°, 19.7°, 20.0°, and 20.7° 2θ. The peaks may correspond to a small contribution of a different Fmoc-F polymorph or a hydrated form, as suggested by Singh et al.[34] Despite the above findings, Fmoc-F in the native xerogel exists in an amorphous form.

The PXRD pattern of neat GO shows that the sample is practically amorphous, as only a few very broad diffraction peaks (humps) can be observed. The strongest broad peak at 10.08° is the characteristic carbon (001) peak for GO sheets, corresponding to a definite d spacing of 0.8−0.9 nm, as reported by Marcano et al. and Yasin et al.[36,37] The GO sample contains also traces of graphite, which is best seen by the characteristic (002) peak at 26.52° 2θ.

The diffraction pattern of the hybrid xerogel is clearly reminiscent of the native Fmoc-F xerogel pattern. In both patterns, the strongest diffraction peaks can be assigned to the anhydrous Na_2HPO_4 phase. The most significant difference between hybrid and native xerogels is the lack of additional weaker peaks, suggesting that the Fmoc-F fibers have collapsed to a fully amorphous form during the preparation of the hybrid xerogel. This differs, for example, from the previously reported structurally similar Fmoc-glutamic acid/GO gel system, in
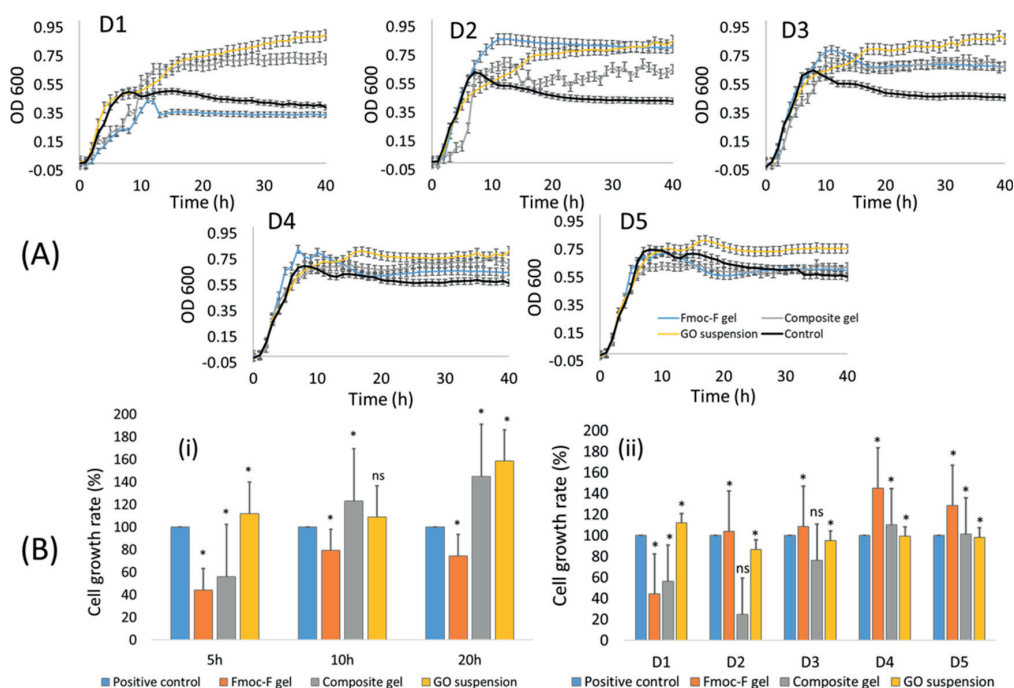
Figure 8. Antibacterial effect of GO flakes and native (Fmoc-F) and hybrid (Fmoc-F/GO) hydrogels against *E. coli*. (A) Optical density measurements of the treated bacterial cultures at five different concentrations over 40 h. (B) The cell viability at different time points of incubation at D1 concentration (i) and after 5 h of incubation at all five concentrations (D1–D5) (ii). *$p < 0.05$; ns, nonsignificant (in relation to the control); statistical analysis was performed with t-Test; $n = 3$. Error bars denote standard deviation.
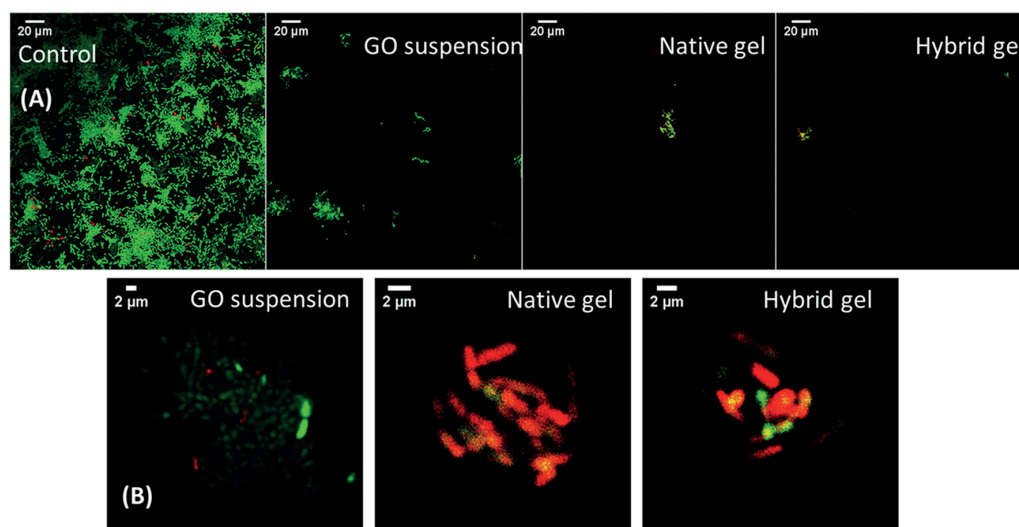
Figure 9. Live/dead staining images of the bacteria after 5 h of incubation at D1 concentration at two different magnifications (A and B). The green fluorescence indicates bacteria with both intact and damaged membrane/wall, and the red fluorescence indicates dead bacteria cells.

which a weak crystalline phase was observed.[38] It is also noted that the broad peak of GO and the weaker peak of the graphite phase are missing from the hybrid xerogel PXRD pattern. This suggests that the GO sheets most likely interact with the Fmoc-F fibrous network, which in turn partially causes some delamination of the GO sheets and, thereby, the 10.08° peak is absent.

To explore potential changes in the fluorescent properties of Fmoc-F amino acid at the gel state, we compared the emission spectra of the native and hybrid hydrogels with Fmoc-F at the solution state (Figure 7A). The amino acid shows a strong emission at the solution state, centered at 318 nm on excitation at 296 nm. No significant shifting is observed at the native hydrogel (emission, 319 nm; excitation, 296 nm). However, the fluorescence emission of the hybrid material is quenched,

suggesting either the development of supramolecular interactions between the amino acid (formed Fmoc-F fibers) and GO flakes or just their spatial proximity. To support our findings, we performed Raman spectroscopy studies of the hybrid hydrogel at a range of GO concentrations (Figure 7B). As expected, neat GO showed two fundamental vibrations at ~1345 and ~1583 cm^{-1}, corresponding to the D and G bands, respectively. The D or disorder-induced band is indicative of lattice defects or appears near the edges of graphene, while the G or graphitic vibrational mode is due to the in-plane motion of the sp^2 hybridized carbon atoms (bond stretching). For all gel samples, irrespective of the amount of added GO, the ID/IG ratio is higher than that of neat GO. In addition, the G band is blue-shifted toward higher values compared to neat GO (~1583 to ~1600 cm^{-1}). These observations suggest a decrease in the size of the GO basal plane (in-plane sp^2 domains), presumably due to the development of $\pi-\pi$ interactions between the Fmoc group of the amino acid and the basal plane of GO flakes.[38]

Antimicrobial Screening. The antimicrobial activity of neat GO (suspension in PBS) and native (Fmoc-F) and hybrid (Fmoc-F/GO) hydrogels was assessed against Gram-negative *E. coli*. The bacterial growth was evaluated over time, *in vitro*, by measuring the optical density of the treated cultures at a wavelength of 600 nm (OD$_{600}$). The results were then translated into cell growth rate (%) by considering the cell survival (OD$_{600}$) of the untreated bacteria (control) as 100%. The samples were evaluated at five different concentrations, prepared by serial dilutions (Table 1, D1–D5) over a period of 40 h (Figure 8). In addition to bacterial growth, the integrity of the bacterial membrane/wall was further assessed by a live/dead staining assay (Figure 9, intact cells are viable cells).

The Fmoc-F native hydrogel, as expected, showed poor bactericidal efficacy, especially after the second dilution (D2). The hybrid hydrogel, however, inhibited *E. coli* growth over three consecutive dilutions (D1–D3), while the GO suspension showed negligible antimicrobial effects at all five concentrations (Figure 8B,ii). Interestingly, the most profound delay in growth population was observed during the first 5 h of incubation for both gel samples, native and hybrid, at the first dilution (Figure 8A, D1). Indeed, the cell growth rate for the native gel was 44% and for the hybrid gel 56% compared to the control (Figure 8B,i).

After 10 h of incubation, at the first dilution (Figure 8A, D1), only the native hydrogel inhibited bacterial growth, which was kept below that of the control until the end of the measurement (40 h). At the same time point (10 h), the hybrid gel lost its inhibition effect as after that (from 10 to 40 h), the observed cell growth exceeded that of the control (Figure 8A, D1). Further dilutions of the Fmoc-F native gel (D2–D5) did not inhibit/delay the bacterial growth either, resulting in a cell growth increase (Figure 8B, ii). The hybrid hydrogel, instead, led to lower bacterial populations compared to the control for the first three consecutive dilutions (D1–D3). Notably, the inhibition/delay of the bacterial growth for dilutions D1–D3 occurred during the first 5 h of incubation with corresponding cell growth rates of 56%, 25%, and 76% at D1, D2, and D3 dilutions, respectively. After 10 h of incubation, the recorded OD$_{600}$ values exceeded the control values, demonstrating the lack of inhibition effects and bacterial regrowth (Figure 8A, D1, D2, D3).

The data showed that the hydrogels and the GO suspension demonstrate poor antibacterial activity against Gram-negative *E. coli*. Although the bacterial growth was delayed for the first 5 h of incubation and a large number of cells died, the remaining ones developed resistance over time and managed to increase their population density compared to the untreated cells. This could be explained by the "*inoculum effect*" (IE), in which the antimicrobial outcome of a bactericidal depends on the initial population size.[39] Several mechanisms related to the IE, such as the "*phenotypic heterogeneity*" and "*bacterial density*", may affect the cell–hydrogel interactions. Therefore, the abrupt bacterial death (in our case within the first 5 h of incubation) is followed by the regrowth of the surviving bacteria, on which the hydrogels do not have an effect due to the IE. In addition, incorporating GO flakes in the gel system may increase the surface area upon which the bacteria can grow. Finally, the extra lipopolysaccharides at the cell wall of Gram-negative *E. coli* could protect them from the Fmoc-F hydrogel, which shows bactericidal effects against Gram-positive bacteria.[10]

To further detect the antibacterial efficacy of the samples and evaluate the integrity of the bacterial membrane/wall, we performed a live/dead staining assay, after 5 h of incubation, at the first dilution D1 (Figure 9). The green fluorescent dye (Syto9) stains both live and dead cells, in contrast to the red fluorescent dye (PI), which selectively stains bacteria with destroyed cell walls and membranes. The live/dead imaging data are only qualitative and complement the OD$_{600}$ findings, meaning no statistical analysis was performed about the percentage of dead cells. The imaging data were consistent with the OD$_{600}$ findings. As expected, the untreated bacteria were intact and stained mainly green, while no changes were observed in their morphology. Similarly, those treated with GO suspension were predominantly stained green, with some negligible red fluorescence also present. However, the bacteria treated with both gel samples were mainly stained red, suggesting that most cells were dead.

CONCLUSIONS

In summary, we studied the gelation synergies of Fmoc-F amino acid and GO flakes and assessed the antimicrobial efficacy of the formed hybrid material against Gram-negative *E. coli* for the first time. GO flakes do not affect the self-assembly of Fmoc-F amino acid per se, but the formed fibers interact with the flakes, as we observed by spectroscopy analysis. The incorporation of GO flakes modulates the viscoelastic properties of the hybrid material, which also forms faster than the native gel. The hybrid hydrogel showed poor antimicrobial activity against *E. coli*, likewise the native gel, probably due to the inoculum effect. However, due to its mechanical and physicochemical properties, the Fmoc-F/GO hybrid hydrogel has a high potential for advancing the development of bactericidal soft materials, for example, via the selective immobilization of antibacterial agents on the surface area of GO flakes.

ASSOCIATED CONTENT

ⓢ Supporting Information

The Supporting Information is available free of charge at https://pubs.acs.org/doi/10.1021/acsomega.2c07700.

> Concentration screening; gelation and phase transition temperature measurements; helium ion microscopy of native gel; rheological studies; thermogravimetric and differential scanning calorimetry analysis results; powder X-ray diffraction analysis results (PDF)

■ AUTHOR INFORMATION

Corresponding Author

Maija Nissinen − *Department of Chemistry, Nanoscience Center, University of Jyväskylä, FI-40014 Jyväskylä, Finland;* ● orcid.org/0000-0001-7560-4632;
Email: maija.nissinen@jyu.fi

Authors

Efstratios D. Sitsanidis − *Department of Chemistry, Nanoscience Center, University of Jyväskylä, FI-40014 Jyväskylä, Finland;* ● orcid.org/0000-0001-5727-1336

Lara A. L. Dutra − *Department of Biological and Environmental Sciences, Nanoscience Center, University of Jyväskylä, FI-40014 Jyväskylä, Finland*

Johanna Schirmer − *Department of Chemistry, Nanoscience Center, University of Jyväskylä, FI-40014 Jyväskylä, Finland;* ● orcid.org/0000-0001-9010-3131

Romain Chevigny − *Department of Chemistry, Nanoscience Center, University of Jyväskylä, FI-40014 Jyväskylä, Finland;* ● orcid.org/0000-0002-5463-9745

Manu Lahtinen − *Department of Chemistry, Nanoscience Center, University of Jyväskylä, FI-40014 Jyväskylä, Finland;* ● orcid.org/0000-0001-5561-3259

Andreas Johansson − *Department of Chemistry, Nanoscience Center, University of Jyväskylä, FI-40014 Jyväskylä, Finland; Department of Physics, Nanoscience Center, University of Jyväskylä, FI-40014 Jyväskylä, Finland;* ● orcid.org/0000-0003-0906-6287

Carmen C. Piras − *Department of Chemistry, University of York, York YO10 5DD, United Kingdom*

David K. Smith − *Department of Chemistry, University of York, York YO10 5DD, United Kingdom*

Marja Tiirola − *Department of Biological and Environmental Sciences, Nanoscience Center, University of Jyväskylä, FI-40014 Jyväskylä, Finland*

Mika Pettersson − *Department of Chemistry, Nanoscience Center, University of Jyväskylä, FI-40014 Jyväskylä, Finland;* ● orcid.org/0000-0002-6880-2283

Complete contact information is available at:
https://pubs.acs.org/10.1021/acsomega.2c07700

Notes

The authors declare no competing financial interest.

■ REFERENCES

(1) Doron, S.; Gorbach, S. L. *Bacterial infections: Overview. In International Encyclopedia of Public Health*; Heggenhougen, H. K., Ed.; Academic Press, 2008; pp 273−282.

(2) Mancuso, G.; Midiri, A.; Gerace, E.; Biondo, C. Bacterial antibiotic resistance: The most critical pathogens. *Pathogens* **2021**, *10* (10), 1310.

(3) Tse, B. N.; Adalja, A. A.; Houchens, C.; Larsen, J.; Inglesby, T. V.; Hatchett, R. Challenges and opportunities of nontraditional approaches to treating bacterial infections. *Clin. Infect. Dis.* **2017**, *65* (3), 495−500.

(4) Zhao, X. Antibacterial Bioactive Materials. In *Bioactive Materials in Medicine*; Zhao, X., Courtney, J. M., Qian, H., Ed.; Woodhead Publishing, 2011; chapter 5, pp 97−123.

(5) Duan, S.; Wu, R.; Xiong, Y. H.; Ren, H. M.; Lei, C.; Zhao, Y. Q.; Zhang, X. Y.; Xu, F. J. Multifunctional antimicrobial materials: From rational design to biomedical applications. *Prog. Mater. Sci.* **2022**, *125*, 100887.

(6) Mahira, S.; Jain, A.; Khan, W.; Domb, A. J. Antimicrobial Materials—An Overview. In *Antimicrobial Materials for Biomedical Applications*; Domb, A. J., Kunduru, K. R., Farah, S., Ed.; The Royal Society of Chemistry: United Kingdom, 2019; chapter 1, pp 1−37.

(7) Nicolas, M.; Beito, B.; Oliveira, M.; Tudela Martins, M.; Gallas, B.; Salmain, M.; Boujday, S.; Humblot, V. Strategies for antimicrobial peptides immobilization on surfaces to prevent biofilm growth on biomedical devices. *Antibiotics* **2022**, *11* (1), 13.

(8) Yang, K.; Han, Q.; Chen, B.; Zheng, Y.; Zhang, K.; Li, Q.; Wang, J. Antimicrobial hydrogels: promising materials for medical application. *Int. J. Nanomedicine* **2018**, *13*, 2217−2263.

(9) Li, S.; Dong, S.; Xu, W.; Tu, S.; Yan, L.; Zhao, C.; Ding, J.; Chen, X. Antibacterial Hydrogels. *Adv. Sci.* **2018**, *5* (5), 1700527.

(10) Xie, Y. Y.; Zhang, Y. W.; Qin, X. T.; Liu, L. P.; Wahid, F.; Zhong, C.; Jia, S. R. Structure-dependent antibacterial activity of amino acid-Based supramolecular hydrogels. *Colloids Surf. B Biointerfaces* **2020**, *193*, 111099.

(11) Wang, H.; Niu, M.; Xue, T.; Ma, L.; Gu, X.; Wei, G.; Li, F.; Wang, C. Development of antibacterial peptides with efficient antibacterial activity, low toxicity, high membrane disruptive activity and a synergistic antibacterial effect. *J. Mater. Chem. B* **2022**, *10*, 1858−1874.

(12) McCloskey, A. P.; Draper, E. R.; Gilmore, B. F.; Laverty, G. Ultrashort self-assembling Fmoc-peptide gelators for anti-infective biomaterial applications. *J. Pept. Sci.* **2017**, *23* (2), 131−140.

(13) Rai, A.; Ferrão, R.; Palma, P.; Patricio, T.; Parreira, P.; Anes, E.; Tonda-Turo, C.; Martins, M. C. L.; Alves, N.; Ferreira, L. Antimicrobial peptide-based materials: opportunities and challenges. *J. Mater. Chem. B* **2022**, *10*, 2384−2429.

(14) Gahane, A. Y.; Ranjan, P.; Singh, V.; Sharma, R. K.; Sinha, N.; Sharma, M.; Chaudhry, R.; Thakur, A. K. Soft matter Fmoc-phenylalanine displays antibacterial activity against Gram-positive bacteria in gel and solution. *Soft Matter* **2018**, *14* (12), 2234−2244.

(15) Irwansyah, I.; Li, Y. Q.; Shi, W.; Qi, D.; Leow, W. R.; Tang, M. B.; Li, S.; Chen, X. Gram-positive antimicrobial activity of amino acid-based hydrogels. *Adv. Mater.* **2015**, *27* (4), 648−654.

(16) Singh, H.; Gahane, A.; Singh, V.; Ghosh, S.; Thakur, A. Antibiofilm activity of Fmoc-phenylalanine against Gram-positive and Gram-negative bacterial biofilms. *J. Antibiot.* **2021**, *74* (6), 407−416.

(17) Gahane, A. Y.; Singh, V.; Kumar, A.; Kumar Thakur, A. Development of mechanism-based antibacterial synergy between Fmoc-phenylalanine hydrogel and aztreonam. *Biomater. Sci.* **2020**, *8* (7), 1996−2006.

(18) Zhao, X. Q.; Wahid, F.; Zhao, X. J.; Wang, F. P.; Wang, T. F.; Xie, Y. Y.; Jia, S. R.; Zhong, C. Fabrication of amino acid-based supramolecular hydrogel with silver ions for improved antibacterial properties. *Mater. Lett.* **2021**, *300*, 130161.

(19) Xie, Y. Y.; Zhang, Y. W.; Liu, X. Z.; Ma, X. F.; Qin, X. T.; Jia, S. R.; Zhong, C. Aggregation-induced emission-active amino acid/berberine hydrogels with enhanced photodynamic antibacterial and anti-biofilm activity. *Chem. Eng. J.* **2021**, *413*, 127542.

(20) Snigdha, K.; Singh, B. K.; Mehta, A. S.; Tewari, R. P.; Dutta, P. K. Self-assembling *N*-(9-Fluorenylmethoxycarbonyl)-L-Phenylalanine hydrogel as novel drug carrier. *Int. J. Biol. Macromol.* **2016**, *93*, 1639−1646.

(21) Liu, S.; Zeng, T. H.; Hofmann, M.; Burcombe, E.; Wei, J.; Jiang, R.; Kong, J.; Chen, Y. Antibacterial activity of Graphite, Graphite Oxide, Graphene Oxide, and Reduced Graphene Oxide: membrane and oxidative stress. *ACS Nano* **2011**, *5* (9), 6971−6980.

(22) Azizi-Lalabadi, M.; Hashemi, H.; Feng, J.; Jafari, S. M. Carbon nanomaterials against pathogens; the antimicrobial activity of carbon nanotubes, graphene/graphene oxide, fullerenes, and their nano-composites. *Adv. Colloid Interface Sci.* **2020**, *284*, 102250.

(23) Seabra, A. B.; Paula, A. J.; de Lima, R.; Alves, O. L.; Durán, N. Nanotoxicity of graphene and graphene oxide. *Chem. Res. Toxicol.* **2014**, *27* (2), 159−168.

(24) Krishnamoorthy, K.; Umasuthan, N.; Mohan, R.; Lee, J.; Kim, S. J. Antibacterial activity of graphene oxide nanosheets. *Sci. Adv. Mater.* **2012**, *4* (11), 1111−1117.

(25) Radhi, A.; Mohamad, D.; Abdul Rahman, F. S.; Abdullah, A. M.; Hasan, H. Mechanism and factors influence of graphene-based nanomaterials antimicrobial activities and application in dentistry. *J. Mater. Sci. Technol.* **2021**, *11*, 1290−1307.

(26) Barbolina, I.; Woods, C. R.; Lozano, N.; Kostarelos, K.; Novoselov, K. S.; Roberts, I. S. Purity of graphene oxide determines its antibacterial activity. *2D Mater.* **2016**, *3*, 025025.

(27) Degen, T.; Sadki, M.; Bron, E.; König, U.; Nénert, G. The highScore suite. *Powder Diffr.* **2014**, *29* (S2), S13−S18.

(28) Pawley, G. S. Unit-cell refinement from powder diffraction scans. *J. Appl. Crystallogr.* **1981**, *14* (6), 357−361.

(29) Görbitz, C. H. The development and use of a crystallographic database. *Acta Crystallogr. Sect. B Struct. Sci. Cryst. Eng. Mater.* **2016**, *72*, 167−168.

(30) Draper, E. R.; Morris, K. L.; Little, M. A.; Raeburn, J.; Colquhoun, C.; Cross, E. R.; McDonald, T. O.; Serpell, L. C.; Adams, D. J. Hydrogels formed from Fmoc amino acids. *CrystEngComm* **2015**, *17*, 8047−8057.

(31) Wang, M.; Gao, B.; Tang, D.; Sun, H.; Yin, X.; Yu, C. Effects of temperature on aggregation kinetics of graphene oxide in aqueous solutions. *Colloids Surf. A: Physicochem. Eng. Asp.* **2018**, *538*, 63−72.

(32) Korolkov, V. V.; Allen, S.; Roberts, C. J.; Tendler, S. J. B. Surface mediated L-phenylalanyl-L-phenylalanine assembly into large dendritic structures. *Faraday Discuss.* **2013**, *166*, 257−267.

(33) Bairi, P.; Roy, B.; Routh, P.; Sen, K.; Nandi, A. K. Self-sustaining, fluorescent and semi-conducting co-assembled organogel of Fmoc protected phenylalanine with aromatic amines. *Soft Matter* **2012**, *8*, 7436−7445.

(34) Singh, V.; Snigdha, K.; Singh, C.; Sinha, N.; Thakur, A. K. Understanding the self-assembly of Fmoc−phenylalanine to hydrogel formation. *Soft Matter* **2015**, *11*, 5353−5364.

(35) Pham, V. H.; Cuong, T. V.; Hur, S. H.; Oh, E.; Kim, E. J.; Shin, E. W.; Chung, J. S. Chemical functionalization of graphene sheets by solvothermal reduction of a graphene oxide suspension in *N*-methyl-2-pyrrolidone. *J. Mater. Chem.* **2011**, *21*, 3371−3377.

(36) Marcano, D. C.; Kosynkin, D. V.; Berlin, J. M.; Sinitskii, A.; Sun, Z.; Slesarev, A.; Alemany, L. B.; Lu, W.; Tour, J. M. Improved Synthesis of Graphene Oxide. *ACS Nano* **2010**, *4* (8), 4806−4814.

(37) Yasin, G.; Arif, M.; Shakeel, M.; Dun, Y.; Zuo, Y.; Khan, W. Q.; Tang, Y.; Khan, A.; Nadeem, M. Exploring the Nickel-Graphene nanocomposite coatings for superior corrosion resistance: manipulating the effect of deposition current density on its morphology, mechanical properties, and erosion-corrosion performance. *Adv. Eng. Mater.* **2018**, *20*, 1701166.

(38) Xing, P.; Chu, X.; Li, S.; Ma, M.; Hao, A. Hybrid gels assembled from Fmoc-amino acid and graphene oxide with controllable properties. *Chemphyschem.* **2014**, *15* (11), 2377−2385.

(39) Frenkel, N.; Saar Dover, R.; Titon, E.; Shai, Y.; Rom-Kedar, V. Bistable bacterial growth dynamics in the presence of antimicrobial agents. *Antibiotics (Basel)* **2021**, *10* (1), 87.

Supporting information for

Probing the gelation synergies and anti-Escherichia coli activity of Fmoc-phenylalanine/graphene oxide hybrid hydrogel

Efstratios D. Sitsanidis,[a] Lara A. L. Dutra,[b] Johanna Schirmer,[a] Romain Chevigny,[a] Manu Lahtinen,[a] Andreas Johansson,[a,c] Carmen C. Piras,[d] David K. Smith,[d] Marja Tiirola,[b] Mika Pettersson[a] and Maija Nissinen[a*]

[a.]Department of Chemistry, Nanoscience Center, University of Jyväskylä, P.O. Box 35, FI-40014 JYU, Finland.
[b.]Department of Biological and Environmental Sciences, Nanoscience Center, University of Jyväskylä, P.O. Box 35, FI-40014 JYU, Finland.
[c.] Department of Physics, Nanoscience Center, University of Jyväskylä, P.O. Box 35, FI-40014 JYU, Finland.
[d.] Department of Chemistry, University of York, Heslington, York, YO10 5DD, UK.

Table of Content

1. Concentration screening

Table S1. Concentration screening trials of the Fmoc-F native hydrogel and corresponding phase transition temperature measurements

Fmoc-F (mg/mL)	Gelation outcome	$T_{gel-sol}$ (°C)
1.0	No	-
2.0*	Yes	35
3.0	Yes	50
4.0	Yes	55
5.0	Yes	60
6.0	Yes	60

*Critical gelation concentration

Table S2. Concentration screening trials of the GO flakes on the critical gelation concentration of Fmoc-F

Fmoc-F (mg/mL)	Gelation without GO	GO (mg/mL)	Gelation with GO
1.0	No	0.25	No
		0.5	No
		0.75	No
		1.0	No
2.0*	Yes	0.25	Yes
		0.5	Yes
		0.75	Yes
		1.0	Yes

*Critical gelation concentration of Fmoc-F.

2. Gelation and phase transition temperature measurements

Table S3. Gelation trials and phase transition temperature measurements of the Fmoc-F/GO hybrid hydrogels. Gelation occurred under constant Fmoc-F concertation (2.0 mg/mL)

GO (mg/mL)	Gelation	Tgel-sol (°C)
0.25	Yes	40-45
0.5	Yes	40-45
0.75	Yes	50
1.0	Yes	50

Table S4. Gelation trials and phase transition temperature measurements of the Fmoc-F/GO hybrid hydrogels. Gelation occurred under constant Fmoc-F concertation (6.0 mg/ mL)

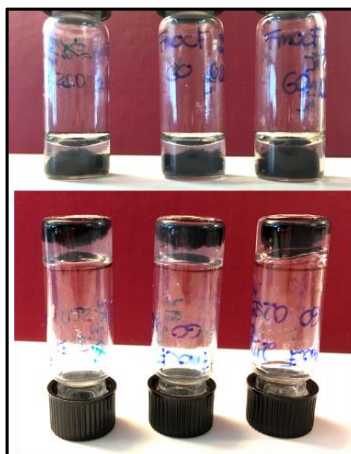| GO (mg/mL)	Gelation	Tgel-sol (°C)
0.25	Yes	60
0.5	Yes	60
0.75	Yes	60
1.0	Yes	60

Figure S1. Heating the Fmoc-F/GO suspension at 95 °C for 1 h led to the precipitation of GO (gel sample in triplicate). The concentration of Fmoc-F was 2.0 mg/mL, and that of GO flakes was 0.25 mg/mL.

Figure S2. Gelation screening of the Fmoc-F/rGO hybrid system at a range of rGO concentrations (mg/mL). The precipitation of rGO was observed irrespective of its concentration. The concentration of Fmoc-F was constant (2.0 mg/mL).
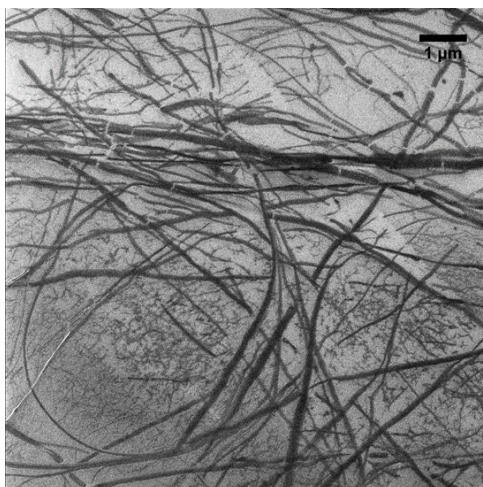
3. Helium Ion Microscopy

Figure S3. Helium ion microscopy image of the native Fmoc-F hydrogel. The formed fibres are similar to those of the hybrid Fmoc-F/GO material. The concentration of Fmoc-F was 2.0 mg/mL.
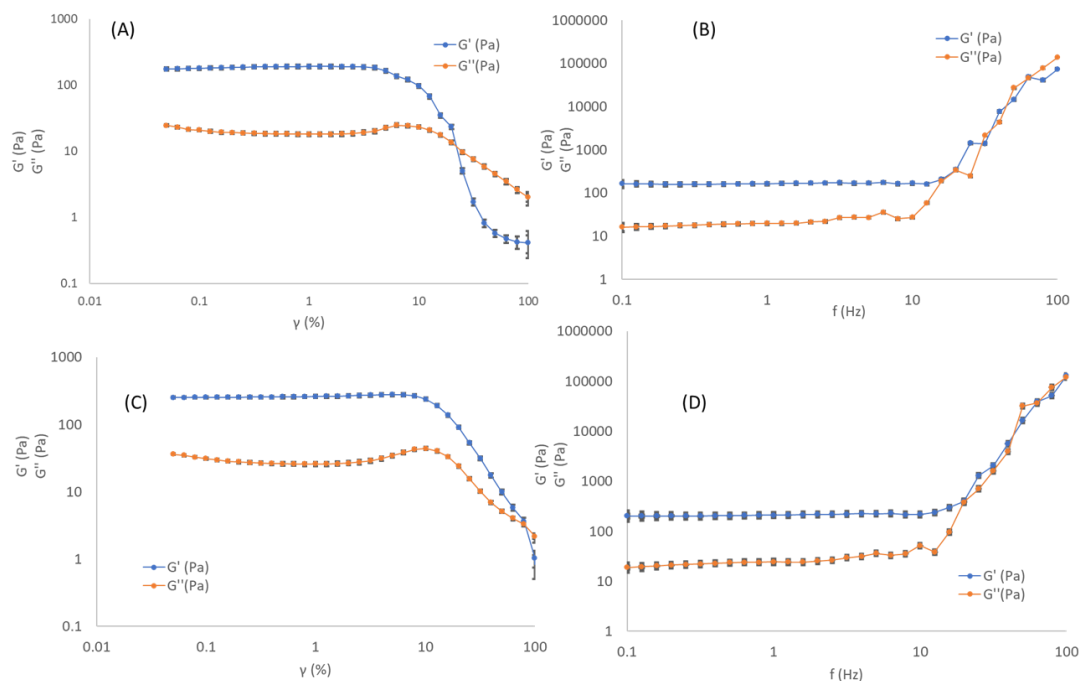
4. Rheological studies

Figure S4. Rheology studies. Amplitude (A) and frequency sweep (B) measurements of the native hydrogel. Amplitude (C) and frequency sweep (D) measurements of the hybrid gel. The concentration of Fmoc-F was 2.0 mg/mL for both samples and GO 0.25 mg/mL for the hybrid gel. Amplitude sweep measurements were performed at an angular frequency of 1.0 Hz, using shear strain (γ%) within the range of 0.05% - 100%. Frequency sweep measurements were performed in triplicates using a shear strain (γ%) of 0.25%, at a range of 0.1 to 100 rad/s. All measurements were performed at 25 °C. Error bars denote the standard deviation.
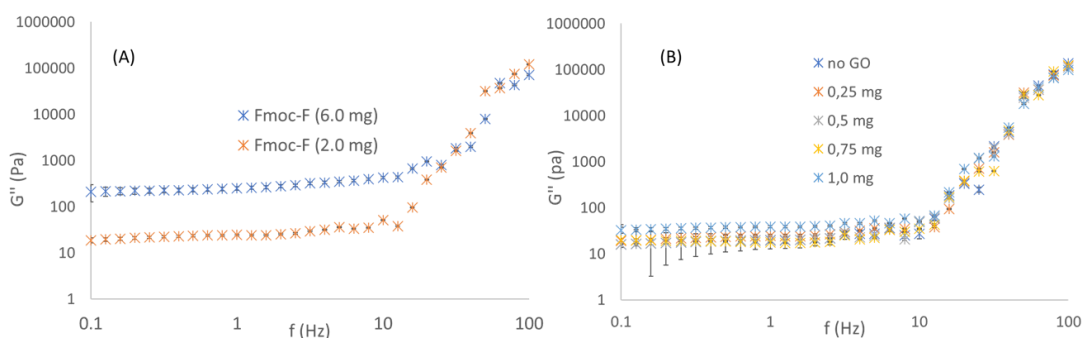

Figure S5. (A) Corresponding loss moduli (G´´) values of Figures 3A and 3B. (A) The effect of Fmoc-F concentration on G´´;(B) The effect of GO addition on G´´. Frequency sweep measurements were performed in triplicates using a shear strain (γ%) of 0.25%, at a range of 0.1 to 100 rad/s. All measurements were performed at 25 °C. Error bars denote the standard deviation.

5. Thermogravimetric and differential scanning calorimetry analysis

Table S5. The summary of TG/DSC analysis results

Sample	Weight loss per step (wt.- %), Temp. range (°C)	Residual weight (wt.- %), Temp. (°C)	T_d (°C)	Transitions by DSC (°C), (J/g)
Fmoc-F neat	67.73, (194 - 272) 26.61, (272 - 373) 5.15, (373 - 545)	 0, 545	218	184.6, (128.06)
Fmoc-F xerogel	12.50, (20 - 102) 12.79, (102 - 221) 7.10, (221 - 309) 2.59, (309 - 595)	 64.78*, 595	200	159.0, (6.68)
Fmoc-F/GO xerogel	4.17, (20 - 104) 16.84, (104 - 233) 6.14, (233 - 333) 6.14, (333 - 595)	 68.49*, 595	200	159.8, (6.02)

* mainly phosphate salts.
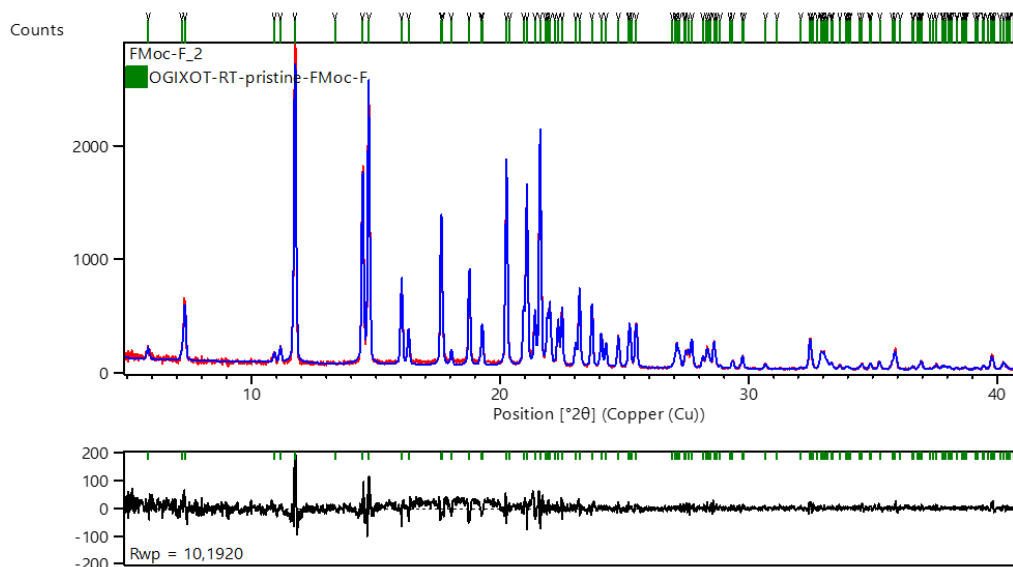
7. Powder X-ray diffraction

Figure S6. Pawley refinement plot of Fmoc-F. The experimental pattern is shown in red, the fitted profile in blue, and the green-coloured vertical markers correspond to the Bragg peak positions of the indexed unit cell. The difference plot of the experimental vs refined profile is shown below in black.

Table S6. Crystallographic data of Fmoc-F measured by powder and single-crystal diffraction[1]

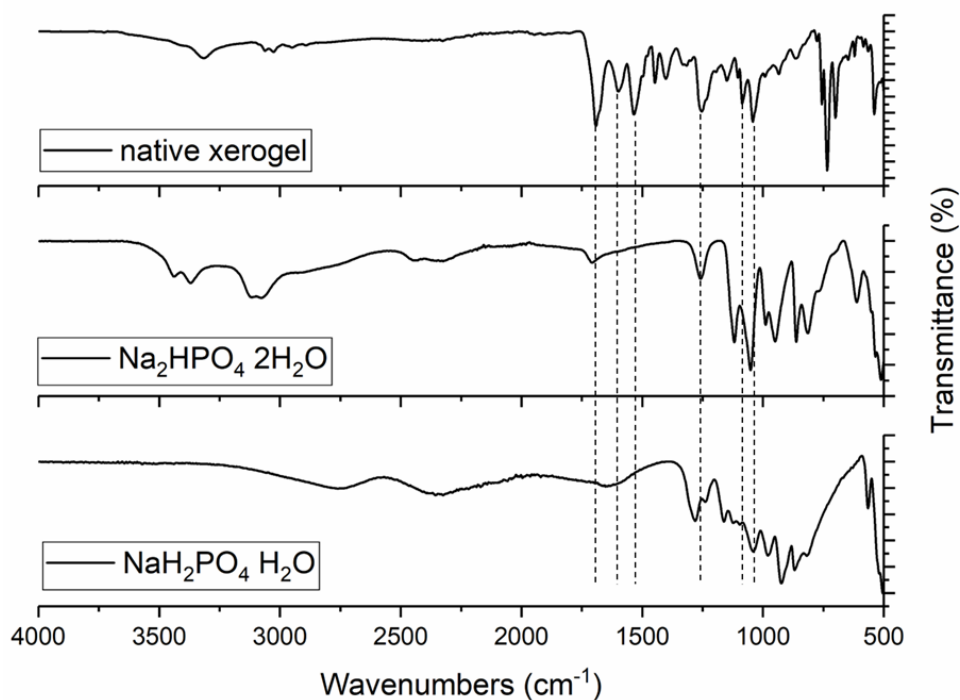| Parameters	PXRD	SC-XRD[1]
Temp [°C]	22	-173
Crystal system	monoclinic	monoclinic
Space group	$P2_1$	$P2_1$
a /Å	13.206(2)	13.1570(13)
b /Å	4.9637(8)	4.9083(4)
c /Å	16.234(2)	16.1242(16)
α /°	90	90
β /°	112,712(1)	113.135(3)
γ /°	90	90
V/Å^3	981,65(23)	957.54(16)
$R_{exp.}$	0.0891	
$R_{prof.}$	0.0740	
$R_{w\text{-prof}}$	0.1019	
R_1		0.0455
wR_2		0.1027
GOF	1.14327	0.996

Figure S7. The FT-IR spectra of the native xerogel (Fmoc-F prepared in PBS solution) and phosphate salts $Na_2HPO_4 \cdot 2\ H_2O$ and $NaH_2PO_4 \cdot H_2O$ used for the preparation of the PBS solution (50 mM, pH 7.4, negative control). The concentration of Fmoc-F was 2 mg/mL.
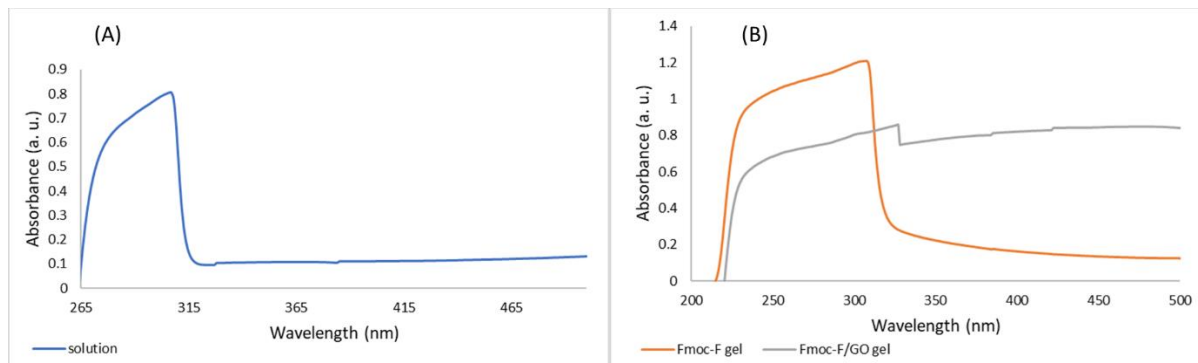

Figure S8. The UV-vis spectra of (A) the Fmoc-F solution in DMSO (spectrum cut off at 265 nm); (B) the Fmoc-F native and Fmoc-F/GO hybrid hydrogels (spectrum cut off at 200 nm). The concentration of Fmoc-F was 2.0 mg/mL and GO 0.25 mg/mL. Both gel samples were formed in situ in a quartz cuvette with a path length of 1 cm.

References

1.   Draper, E. R.; Morris, K. L.; Little, M. A.; Raeburn, J.; Colquhoun, C.; Cross, E. R.; McDonald, T. O.; Serpell, L. C.; Adams, D. J. Hydrogels formed from Fmoc amino acids. *CrystEngComm.* **2015**, 17, 8047-8057.

IV

DIVERSITY AT THE NANOSCALE: LASER-OXIDATION OF GRAPHENE AFFECTS FMOC-PHENYLALANINE SURFACE-MEDIATED SELF-ASSEMBLY

by

Johanna Schirmer, Romain Chevigny, Aleksei Emelianov, Eero Hulkko, Andreas Johansson, Pasi Myllyperkiö, Efstratios D. Sitsanidis, Maija Nissinen & Mika Pettersson, 2023

PCCP

Check for updates

Diversity at the nanoscale: laser-oxidation of single-layer graphene affects Fmoc-phenylalanine surface-mediated self-assembly†

Johanna Schirmer, [ID] [a] Romain Chevigny, [ID] [a] Aleksei Emelianov, [ID] [a] Eero Hulkko, [ab] Andreas Johansson, [ID] [ac] Pasi Myllyperkiö, [ID] [a] Efstratios D. Sitsanidis, [ID] *[a] Maija Nissinen [ID] *[a] and Mika Pettersson [ID] *[a]

We report the effects of a laser-oxidized single layer graphene (SLG) surface on the self-assembly of amphiphilic gelator *N*-fluorenylmethoxycarbonyl-L-phenylalanine (Fmoc-Phe) towards an gel–SLG interface. Laser oxidation modulates the levels of hydrophobicity/hydrophilicity on the SLG surface. Atomic force, scanning electron, helium ion and scattering scanning nearfield optical microscopies (AFM, SEM, HIM, s-SNOM) were employed to assess the effects of surface properties on the secondary and tertiary organization of the formed Fmoc-Phe fibres at the SLG–gel interface. S-SNOM shows sheet-like secondary structures on both hydrophobic/hydrophilic areas of SLG and helical or disordered structures mainly on the hydrophilic oxidized surface. The gel network heterogeneity on pristine graphene was observed at the scale of single fibres by s-SNOM, demonstrating its power as a unique tool to study supramolecular assemblies and interfaces at nanoscale. Our findings underline the sensitivity of assembled structures to surface properties, while our characterization approach is a step forward in assessing surface–gel interfaces for the development of bionic devices.

Introduction

Advances in neuron–machine connections at micro- and nanoscale have given new hope in repairing brain and nervous system damage.[1–4] A key part of such connections is the interface between the neural tissue and the bioelectronic device, as it should support neuron viability and functionality while preserving the electronic properties of the device. With its exceptional mechanical stability and electronic properties, graphene is a promising candidate for constructing neuron–machine interfaces, as it has been shown to record neural activity successfully.[5–7] In our previous studies, we employed laser-oxidation[8] to modulate the properties of single-layer graphene (SLG) towards bioinspired surfaces, functionalized with proteins.[9] The two-photon oxidation process with a femtosecond laser in ambient atmosphere

introduced patterned hydroxyl and epoxide groups on the graphene surface, while the carbon network remained intact (Fig. 1A).[8,10]

Besides the desired surface properties, the neurons must remain viable and functional, attach to the artificial device, and interact with it to achieve functional bionic devices. In living tissue, neurons build their own extracellular matrix (ECM), an extensive network of proteins such as fibrous proteins, glycoproteins, and proteoglycans,[11] which supports the cells and regulates intracellular communication. However, for constructing artificial neuron–machine interfaces, it is crucial to functionalize the surface with a biocompatible substrate material, for example, a supramolecular gel, to mimic the properties of natural ECM. This will enable and support the growth of a three-dimensional (3D) neural network, adjacent to the electronic device, forming a neuron–machine interface.[12–14]

Low molecular weight gels (LMWGs) have gained momentum in the field of biomaterials due to their biocompatibility, easy preparation, structural functionalization, tunability and mechanical properties.[15] In supramolecular gels, the gelator molecules self-assemble hierarchically towards higher order architectures. Initially, molecular recognition events promote the gelators' assembly in one or two dimensions (primary structure), followed by the formation of aggregates such as fibres, ribbons, sheets, and micelles (secondary structure), while the interaction of individual aggregates (tertiary structure)

[a] Department of Chemistry, Nanoscience Center, University of Jyväskylä, P. O. Box 35, FI-40014 JYU, Finland. E-mail: mika.j.pettersson@jyu.fi, maija.nissinen@jyu.fi, efstratios.d.sitsanidis@jyu.fi

[b] Department of Biological and Environmental Sciences, Nanoscience Center, University of Jyväskylä, P. O. Box 35, FI-40014 JYU, Finland

[c] Department of Physics, Nanoscience Center, University of Jyväskylä, P. O. Box 35, FI-40014 JYU, Finland

† Electronic supplementary information (ESI) available: Experimental and computational details, sample optimization, crystal characterization, Raman and nano-FTIR spectra, DFT results. See DOI: https://doi.org/10.1039/d3cp00117b

This journal is © the Owner Societies 2023

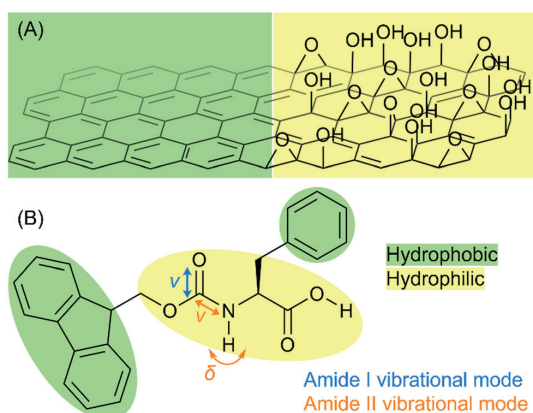*Phys. Chem. Chem. Phys.*, 2023, **25**, 8725–8733 | **8725**

Fig. 1 (A) Scheme of laser-oxidized SLG, showing pristine and oxidized areas adjacent to each other. (B) Chemical structure of Fmoc-Phe; the arrows depict vibrations that contribute to the amide I (blue) and amide II (orange) vibrational modes. Stretching vibrations are indicated as ν and bending vibrations as δ. Hydrophobic moieties are highlighted in green, hydrophilic moieties in yellow.

determines the gel's formation.[16,17] The micro- and macroscopic properties of bulk materials can be tuned by modifying the chemical structure of the gelator, the concentration and/or the solvent (i.e., buffer solutions, pH).[18–20] However, at a machine–tissue interface, the soft hydrogel is in direct contact with the tissue and the device's surface, meaning that surface-mediated self-assembly phenomena have an immediate effect on the formation and corresponding properties of supramolecular gels.[21–25] For example, interactions between the monomers and the surface can boost or decelerate the fibrillation of amyloid-β peptides.[26,27] Additionally, the hydrophobicity/hydro-philicity of the surface plays a significant role in surface-mediated self-assembly, affecting the fibre's diameter, aggrega-tion and/or Young's modulus of the formed gels.[21,22] Further to this, increased surface roughness has been found to decelerate and finally inhibit the fibrillation of an amyloid-β peptide.[28] A surface–gel system may be probed at a small volume. For example, Yang et al.[25] observed changes in the viscosity and structure of a supramolecular gel drop (350 μl) on a photo-patterned surface with different physical properties.

The analysis of a supramolecular gel–surface interface is mainly confined to microscopic and X-ray techniques: The physical properties and morphology of the gel's network have been studied by atomic force (AFM) and (cryo-)scanning electron (SEM) microscopy.[21,23,24,29] To analyse the secondary and tertiary structure of the gels, grazing-incidence wide and small angle X-ray scattering[22] and grazing-incidence X-ray diffraction[25] have been employed. A relatively new technique for surface analysis is scattering scanning near-field optical microscopy (s-SNOM), which combines AFM in tapping mode and an infrared (IR) laser that points at the AFM tip apex. When interacting with the sample, the near-field (NF) signal of the tip is altered and elucidates the absorptive properties of the sample in the spectral region of the incident laser.[30–33] With a spatial resolution down

to 6 nm for visible light and near IR absorption[34] and 1 nm for tip-enhanced Raman spectroscopy,[35] or even down to atomic resolution,[36] it is possible to obtain locally defined absorptive properties of a material in the form of nano-FTIR/Raman spectra and absorption/reflectivity images. The structure of a supra-molecular gel can be analysed at the nanoscale, and valuable information on the heterogeneity and distribution of the gel material on a surface can be received.

In this study, we assessed the surface-mediated self-assembly of model gelator N-fluorenylmethoxycarbonyl-L-phenylalanine (Fmoc-Phe) on pristine (prG) and laser-oxidized (oxG) graphene (Fig. 1). The bulk gels of Fmoc-Phe and its derivatives have been extensively studied.[19,20,37–39] Due to the anionic and amphiphilic nature of the amino acid, both electrostatic interactions and hydrophobic effects promote self-assembly. Gelation is therefore sensitive to pH changes and the presence of ions.[20] Additionally, the aromaticity, hydrophobicity and spatial flexibility of the phenyl ring affect the properties of the gel.[19,20] Fmoc-protected or Phe-based gelators tend to form β-sheet-like structures[40,41] and the crystal structure of Fmoc-Phe shows a unidirectional, sheet-like assembly of the molecules.[38] A recent study, however, demonstrates that gel fibres and crystals do not necessarily have similar structures, as the size and shape of the sample container affect the assembly event.[42] In contrast to bulk gels, the structure of Fmoc-Phe fibres on a surface is difficult to predict, as the effect of surface properties on the secondary structure remains an open question.

S-SNOM, AFM, SEM and helium ion microscopy (HIM) allowed us to study the effects of distinct surface properties on the surface-mediated self-assembly of the amino acid. We identified different secondary structures of the fibres by nano-FTIR spectroscopy and nanoscale mid-IR (MIR) imaging. At the same time, we demonstrated the modulation of the Fmoc-Phe self-assembly by laser-oxidation and hence the effects of SLG's different levels of hydrophobicity/hydrophilicity. Overall, a structurally hetero-geneous fibrous network of Fmoc-Phe is formed on both surfaces, prG and oxG.

Results and discussion

Surface effects on gel morphology and fibre dimensions

Surface-mediated self-assembly can be modulated depending on the physicochemical properties of the surface.[21,25] Here, SLG was patterned with oxidized areas via laser-irradiation, to assess the self-assembly of amphiphilic gelator Fmoc-Phe. The surface consists of hydrophobic/flat prG (R_a = 0.23 nm, where R_a is arithmetic average height[43]) adjacent to hydrophilic/rough oxG (R_a = 0.33 nm).[8] Ten parallel rectangular patterns were irradiated (40 μm × 400 μm in size) and arranged approximately 160 μm apart, creating an alternating motif of oxG and prG (Fig. 2). An Fmoc-Phe solution in phosphate buffer (PBS) was then added on the graphene surface and allowed to gel overnight, followed by freezing and lyophilization of the gel–SLG interface prior analysis. A detailed description of the experimental and sample prepara-tion procedures can be found in the ESI† (Sections S1–S4).
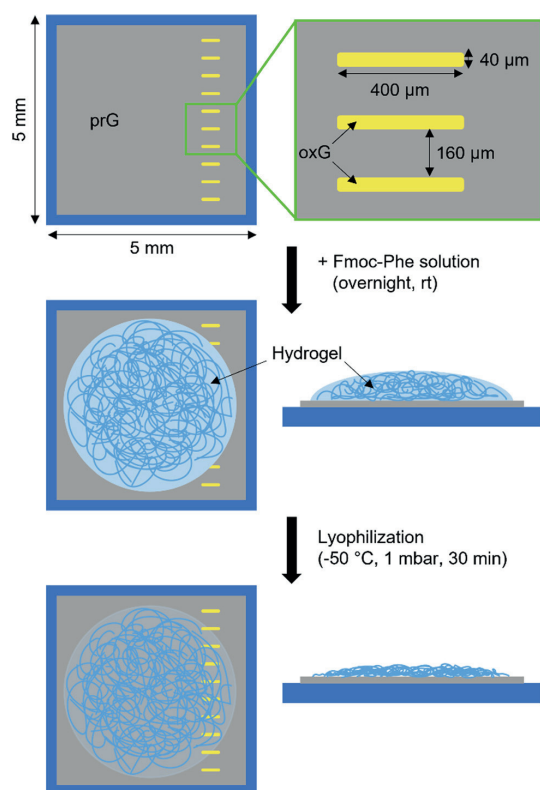
Fig. 2 Schematic depiction of the SLG sample geometry and gel–SLG interface preparation. Yellow rectangular patterns represent irradiated, laser-oxidized graphene and the Si/SiO$_2$ substrate is depicted in blue.
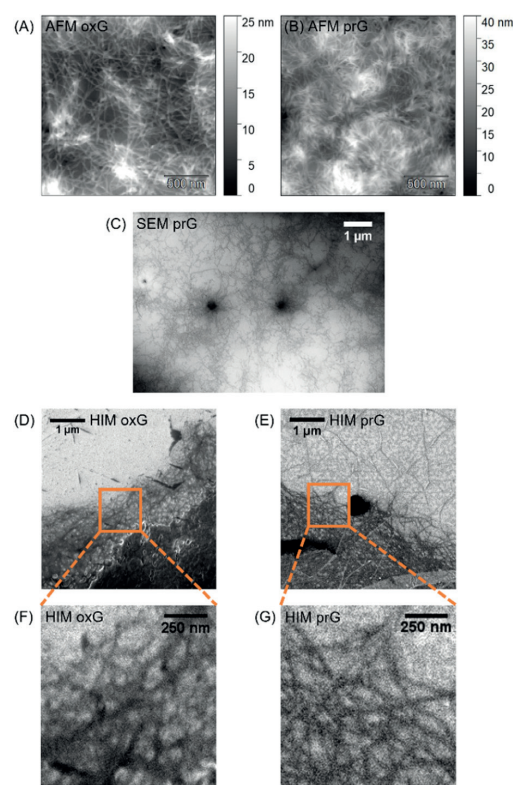

Fig. 3 Microscopic analysis of the Fmoc-Phe fibres on oxG and prG: AFM images on oxG (A) and prG (B); SEM image on prG showing two nucleation sites (C); HIM images of the Fmoc-Phe gel edge on oxG (D) and prG (E) and corresponding magnified images (F) and (G), respectively, indicated by the orange rectangles.

AFM, SEM and HIM imaging were employed to analyse the gel morphology and fibres' dimensions (Section S1, ESI†). The fibres in supramolecular gels are larger architectures formed by the organization of many fibrils. An entangled fibrous network was visible in the AFM topographic images on both prG and oxG surfaces (Fig. 3A and B). Single fibres entangle into thicker bundles, creating a dense network. The fibre thickness was measured using the AFM images, as an average of 100 single fibres on each surface. The average thickness of the fibres t on the two surfaces is almost identical (t_{prG} = 2.0 ± 1.0 nm, t_{oxG} = 2.3 ± 1.1 nm, one-way ANOVA, $p < 0.001$), which indicates no significant effect of surface properties on the size of the Fmoc-Phe fibres.

SEM imaging of the Fmoc-Phe xerogel (dried gel) on prG (Fig. 3C) showed fibres growing from spherulites (dark spots), consistent with previous observations on Phe-based gels.[24,44] HIM imaging, at the edges of the supramolecular network, on both oxG and prG (Fig. 3D–G) revealed a slightly different appearance of the fibres in contrast to the AFM images, which were taken at the center of the gel network. On oxG, the fibres appear curved in the HIM images, whereas straight on prG. During the sample preparation (Fig. 2), the fibre density was

lower at the edges of the gel. Fibres at the edges grow near the surface and may therefore be affected by the surface properties to a greater extent than fibres in the center of the gel network (AFM images).[21] The observed difference in fibre morphology suggests that the hydrophobic/hydrophilic differences upon the SLG surface affect the tertiary organization level (fibril–fibril interaction) of Fmoc-Phe in the proximity of the surface.

Surface effects on the secondary organization level

To investigate the self-assembly and molecular interactions of Fmoc-Phe on prG and oxG surfaces at the nanoscale (secondary organization level), the gel–SLG interface was studied by s-SNOM (Section S1, ESI†). Singh *et al.*[20] have reported that both hydrogen bonding and hydrophobic stacking interactions contribute to the self-assembly of Fmoc-Phe, which carries a negative net charge at pH 7.4. IR, ultraviolet-visible, circular dichroism, and nuclear magnetic resonance spectroscopy revealed a heterogeneous secondary structure, consisting of stacked molecules (different polymorphs). The fluorenyl group appears to stack with the phenyl ring while the carbamate group is involved in hydrogen bonding. However, these

observations derive from the bulk gel, meaning that the spectroscopic data of the whole bulk material were averaged. Here, we studied the absorptive properties of the fibres on the scale of single fibres and fibre bundles (nano- and microscale). We hypothesized that potential effects of the graphitic surface on the secondary structure of Fmoc-Phe could be observable in the nano-FTIR spectrum. Additionally, we suggested that the polymorphic nature of the bulk gel, as previously reported,[20] would be confirmed by MIR imaging at different frequencies.

Secondary structure analysis. Initially, nano-FTIR spectra were taken from five oxG and six prG positions on the gel–SLG interface (Section S5, ESI†). Each spectrum was normalized to the corresponding background (oxG or prG, respectively) to eliminate the contribution of the graphene surface. The optical phase spectrum (referred to as "nano-FTIR spectrum") corresponds to the absorptive properties of the fibres inside the near-field.[33] We analysed the 3rd harmonic of the cantilever oscillation as it yields detailed spectral features at an adequate signal-to-noise ratio. We focused on the frequency range between 1500 cm^{-1} and 1750 cm^{-1}, corresponding to the carbonyl and amide vibrations. The amide II band appears approximately at 1550 cm^{-1} as a combination of the N–H bending and C–N stretching vibration (Fig. 1B). The absorption band(s) between 1600 cm^{-1} and 1700 cm^{-1} (amide I region), arise from the C=O stretching vibration and are immediately related to the secondary structure of the gel sample.[45] For protein samples, it has been reported that the amide I band shifts and/or splits depending on the secondary structures[45,46] and common secondary structures like α-helices and β-sheets, forming *via* hydrogen bonding of the amide backbone, absorb at certain frequencies. According to Barth,[45] α-helices show one main absorption approximately at 1655 cm^{-1}. However, disordered structures absorb at a similar frequency, while β-sheets give rise to two absorption bands in the amide I region ($\leq 1640 \text{ cm}^{-1}$ and $\geq 1680 \text{ cm}^{-1}$), resulting from the transition dipole coupling of the carbonyl groups. In a single molecule, the carbonyl C=O vibration shows only one band. When coupled with another C=O oscillator, at a β-sheet conformation, the excitation leads to exciton splitting and splitting of the absorption band.[46] The difference between the two bands depends on the strength of the IR absorption (stronger absorption = larger splitting) and the distance and orientation of the two oscillators to each other. During the self-assembly of the amino acid-based gelators, the molecules arrange into similar secondary structures *via* hydrogen bonding of the amide group(s). Therefore, changes in the molecular arrangement due to different surface properties are expected to be observable in the amide I region of the nano-FTIR spectra. It is of note that band positions may shift a few wavenumbers when comparing transmission FTIR and nano-FTIR spectra.[47]

Fig. 4 shows the AFM images of the Fmoc-Phe fibres on oxG and prG and one nano-FTIR spectrum from each surface area. Several overlapping bands appeared in the amide I and II regions. Spectra of the same surface area showed mostly similar band positions (Table 1 and Fig. S4, ESI†). However, there were noticeable shifts among the gel–oxG and –prG interfaces. Fmoc-Phe fibres showed two absorption bands on both surfaces
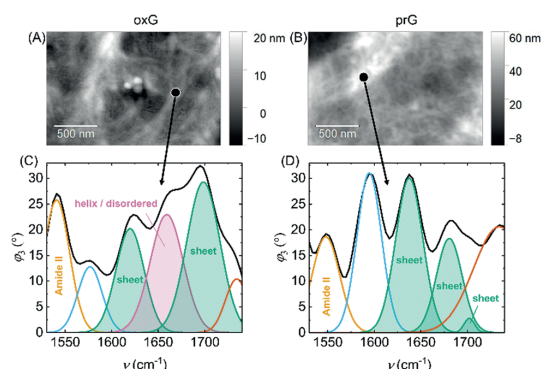

Fig. 4 Nano-FTIR study of Fmoc-Phe fibre bundles on oxG and prG: AFM topographic images of Fmoc-Phe fibres on (A) oxG and (B) prG; corresponding deconvoluted nano-FTIR spectra in the amide I and II regions (C and D). The exact position of each spectrum is highlighted with a black spot in the corresponding AFM image. The filled bands in the Amide I region show the assigned secondary structure elements.

at frequencies typical for β-sheet structures (oxG: 1618 cm^{-1} and 1699 cm^{-1}, prG: 1640 cm^{-1} and 1683 cm^{-1}). The bands' centres were further apart on oxG (distance: 81 cm^{-1}) than on prG (distance: 43 cm^{-1}). Since the strength of the IR absorption should be similar for all Fmoc-Phe molecules, our results suggest that the orientation and/or distance of C=O groups change between sheet-like assemblies on oxG or prG, leading to different couplings. On oxG, the fibres additionally gave rise to a band at 1657 cm^{-1}, suggesting the presence of α-helices or disordered structures.[46] Interestingly, this band was absent in 67% of the spectra of Fmoc-Phe on prG. Therefore, these findings indicate a connection between the secondary structure of the fibres and the surface properties (differences in hydrophobicity/hydrophilicity) of oxG and prG.

To investigate the proportion of different types of secondary structures over the oxG and prG surfaces, the areas of the bands, assigned to secondary structures (highlighted in Fig. 4C and D for the sample spectra), were compared at each spectrum. To obtain a quantitative comparison profile, the input of each secondary structure was calculated (Section S1, ESI†). The sum

Table 1 Band positions and their standard deviation derived from the second derivative of each spectrum from Fig. S4E and F, ESI. In parenthesis behind the number, the abundance of the respective band in the whole sample N is shown ($N_{oxG} = 5$, $N_{prG} = 6$). Bold numbers indicate bands that appear in at least 80% of the samples. A secondary structure was assigned to absorbance bands in the Amide I region

Peak positions oxG	Peak positions prG	Assigned secondary structure
1546 ± 5 (5/5)	**1558 ± 5 (6/6)**	
1578 ± 1 (3/5)		
1598 (1/5)	**1600 ± 4 (6/6)**	
1618 ± 3 (5/5)		Sheet
	1640 ± 4 (5/6)	Sheet
1657 ± 1 (5/5)	1656 ± 0 (2/6)	Helix/disordered
	1683 ± 6 (6/6)	Sheet
1699 ± 2 (5/5)	1707 ± 3 (4/6)	Sheet

8728 | *Phys. Chem. Chem. Phys.*, 2023, **25**, 8725–8733

This journal is © the Owner Societies 2023

Table 2 Input of sheet and helix/disordered structures for nano-FTIR spectra of Fmoc-Phe fibre bundles on oxG and prG

#Spectrum	Input sheet (%)	Input helix/disordered (%)
oxG		
1	87	13
2	74	26
3	52	48
4	62	38
5	67	33
prG		
1	100	0
2	100	0
3	87	13
4	57	43
5	100	0
6	100	0

of areas of all bands assigned to secondary structures was set to 100% in each spectrum. Although this approach is not rigorously accurate as it overlooks the differences between oscillator strengths for different vibrations, it allows to compare proportions of different structures between different areas. The inputs are presented in Table 2. As described above, all spectra on oxG showed absorption bands at both β-sheet and α-helix/disordered structure frequencies. However, the inputs varied from 52% to 87% for β-sheets and 13% to 48% for α-helix/disordered structures. This indicates a heterogeneous fibrous network, which supports the presence of different polymorphs as reported by Singh et al. in bulk gels.[20] On prG, most spectra showed a network solely consisting of β-sheets. Though, in two positions, different amounts of α-helix/disordered structures were found (13% and 43%). Possible reasons for the appearance of this band on prG are: (i) the spectra were taken at positions near the oxidized areas (Fig. S4, prG spectrum 1–3, ESI†). Since prG and oxG are adjacent (Fig. 1B) and Fmoc-Phe fibres can be several micrometres long, it is possible that some cross the boundary between the two surfaces. (ii) The dried sample transforms the 3D network to a 2D (Fig. 2). This could lead to the displacement of the fibres from their original location in the 3D network. However, the trend of solely β-sheet structures on prG is strong, and there is a clear difference between the inputs of secondary structures, depending on the surface oxidation.

Surface–monomer interactions. At the gel–SLG interface system, the differences in hydrophobicity/hydrophilicity are expected to result in secondary structure alterations of Fmoc-Phe. A previous study reported a cytidine-based gelator which formed a gel on hydrophobic/hydrophilic surfaces.[21] The material had a different Young's modulus and diameter of fibres depending on the surface's hydrophobicity. In addition, different amyloid peptides form fibrils preferably on hydrophobic surfaces,[26,29] suggesting that distinct electrostatic interactions and hydrophobic effects between the surface and the monomers are responsible for the assembly event. Such effects apply to relatively few molecules adsorbed on the surface. The monomer–surface interactions could affect the self-assembly process alongside an entire fibre if its formation starts from a nucleation point at the surface. Depending on the spatial orientation of the molecules adsorbed

on the surface, i.e. the functional groups interacting with the surface, different functional groups of the molecule point towards the monomer solution. In this way, distinct nucleation points are created. During the surface-mediated self-assembly, the subsequent molecules interact with different functional groups, depending on the spatial orientation of the monomer adsorbed on the surface. The distinct interactions could lead to distinct secondary structures. Regarding Fmoc-Phe, the self-assembly may start via π–π stacking or hydrogen bonding. The surface hydrophobicity/hydrophilicity could affect the preferred type of interaction.

To investigate the interactions between the two surfaces (oxG and prG) and the Fmoc-Phe monomer, we performed density functional theory (DFT) calculations to obtain the adsorption energies (E_{ads}) of the Fmoc-Phe monomer on oxG and prG, respectively (Section S6, ESI†). By varying the distance and orientation of Fmoc-Phe towards the two surfaces, we aimed to identify the most stable configurations. Though the model is calculated under a vacuum state, it gives insight into the driving forces of molecular adsorption onto the surfaces. On oxG, the Fmoc-Phe monomer tends to orient its polar groups towards the oxygen-containing groups of the surface (Fig. 5A–D). The distances between 2.2 Å and 3.0 Å (Table S2, ESI†) and E_{ads} between −0.63 eV and −0.77 eV indicate physisorption and the formation of hydrogen bonds. Especially, the carboxylic moiety (COOH) of Phe is involved in hydrogen bonding. The reason for the surface–COOH interaction is likely the sterically less hindered position of COOH compared to the amide group, which is sterically shielded by the Fmoc and phenyl aromatic moieties and COOH. When Fmoc-Phe adsorbs on the surface in these orientations (Fig. 5A–D), the aromatic moieties point towards the gelator solution and could generate a nucleation site for further self-assembly via π–π stacking.

On the prG surface, the adsorption of Fmoc-Phe leads partly to different orientations (Fig. 5E–H). Here, the aromatic moieties play the main role during the DFT structure optimization. With surface–monomer distances between 2.7 Å and 3.9 Å (Table S2, ESI†) and E_{ads} between −0.62 eV and −0.89 eV, non-covalent interactions such as π–π stacking may contribute to the physisorption. Indeed, parallel π–π stacking is observed between prG and Fmoc or the phenyl ring (Fig. 5G and H, respectively). By occupying the aromatic moieties of Fmoc-Phe in surface–monomer interactions, the hydrophilic amide and COOH groups could play a more significant role in initiating the self-assembly of Fmoc-Phe beyond the surface. While, for example, structures D (oxG) and G (prG) are different regarding the orientation and adsorption-involving groups, structures A and B on oxG appear similar to structures E and F on prG, respectively. The observation of similar and distinct adsorption orientations of Fmoc-Phe on both surfaces in DFT results complements the obtained nano-FTIR results: The spectra of the self-assembled structures on oxG and prG show both similar and distinct bands. Thus, it is probable that the self-assembly of Fmoc-Phe on prG and oxG is a surface-mediated process.

Heterogeneity of the fibrous network. The nano-FTIR spectra were recorded at the positions of fibre bundles and overlaying

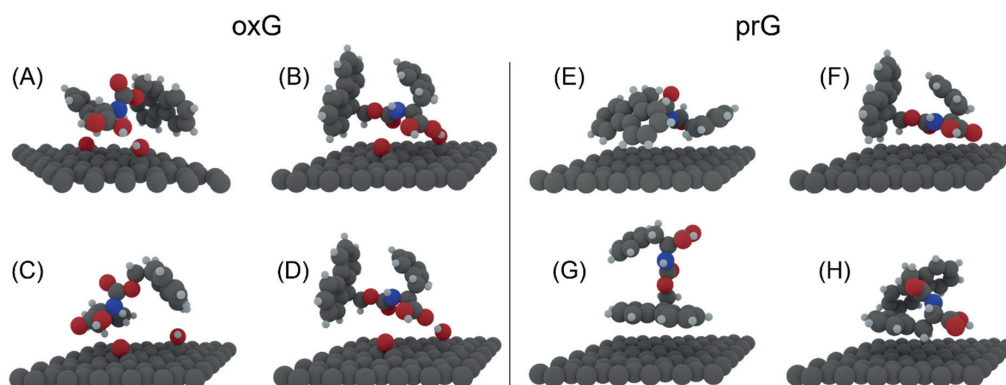oxG   prG

Fig. 5 Adsorption of Fmoc-Phe on oxG (A–D) and prG (E–H) surfaces (DFT study). Four of the energetically most stable structures are shown for each surface. The corresponding adsorption energies are (A) −0.73 eV, (B) −0.77 eV, (C) −0.63 eV, (D) −0.65 eV, (E) −0.89 eV, (F) −0.66 eV, (G) −0.63 eV and (H) −0.62 eV.

fibres to obtain an adequate NF signal. To investigate the potential polymorphic forms of the gelator in single fibres, a series of MIR phase images were obtained of the Fmoc-Phe fibres on prG. A fibrous network of low density was selected, at the edge of the gel, to achieve adequate contrast in the images. The imaging frequencies were selected to cover the amide II (1546 cm^{-1}), amide I (1600 cm^{-1}, 1645 cm^{-1}, 1672 cm^{-1} and 1699 cm^{-1}) and off-amide vibrations (1720 cm^{-1}) (Fig. 6A). The topography and corresponding optical phase images are presented in Fig. 6B–H. The three wide lines were visible in all optical phase images, while not in the topography image (Fig. 6H). These likely originate from defects or wrinkles of the graphene monolayer, which were observed in the NF signal.[48] Here, the signal overlapped with the signal of fibres deposited in this area. The highest contrast between prG surface and the fibre network was visible at frequencies of the β-sheet region (1645 cm^{-1}, 1672 cm^{-1} and 1699 cm^{-1}), underpinning the relevance of sheet-like secondary structures of Fmoc-Phe on prG. Another frequency revealing a high contrast was that of 1600 cm^{-1}. This behaviour correlates with the intense band around 1600 cm^{-1} in all the recorded spectra on prG (for example, Fig. 6A). The aromatic C–C stretching of the Fmoc and phenyl moieties could give rise to this band.[49,50]

Overall, the detected vibrational modes occurred heterogeneously throughout the fibre network, as shown by the varying intensity of the phase shift in Fig. 6C–H. To investigate if the NF phase change was caused by height variations and the accompanying varying number of molecules, a model fibre was analyzed in detail (Fig. 6I, orange dashed line). The cross-sections from the topography image and the optical phase images at 1645 cm^{-1} and 1699 cm^{-1} are shown in Fig. 6J. The phase profiles do not follow the height profile linearly or inversely throughout the cross-section. The two optical phase signals have a similar magnitude in the yellow (entangled fibres) and blue highlighted parts (single fibre) of the profile. In contrast, the height of the entangled fibres is bigger compared to the single fibre. Thus, the difference in optical phase signal intensity probably did not

originate from height variations but was due to differences, for example, in the secondary structure of the material.

To investigate trends in absorption for single and entangled fibres, all imaged frequencies were compared at specific location points on the fibres (symbols in Fig. 6I). The optical phase signals of these points were plotted against the imaging frequency (Fig. 6K), leading to an optical phase profile. For each data point in plot Fig. 6K, the optical phase values of 5 pixels were averaged. The orange and blue plots (Fig. 6K) correspond to the two single fibres, which form a coiled coil formation (represented by the black and green plots in Fig. 6K). The yellow plot shows the signal at a different entanglement point. Each plot has a different shape, meaning the signal profile is different. However, the signal profiles of the black and green plots have a similar shape except for one point (1699 cm^{-1}). The signal profiles of the two entanglement points (Fig. 6I, black and yellow squares) do not correlate. Also, the signal profiles of the two single fibres have different shapes. Indeed, these findings showcase the heterogeneity of the fibrous network and support previous findings of polymorphic forms in the Fmoc-Phe lyophilized bulk gel.[20] Moreover, our results demonstrate variations of the secondary structure of Fmoc-Phe molecules at a single fibre level.

Conclusions

In summary, we gained insight into the surface-mediated self-assembly process of amphiphilic gelator Fmoc-Phe at the interface of an SLG surface and highlighted the effect of graphene's laser-oxidation on gelation at the secondary and tertiary organization levels. Based on our findings, nano-FTIR can distinguish different secondary structures of supramolecular gels at the nanoscale. The secondary structure of Fmoc-Phe fibres is affected by the laser-oxidation of the SLG surface, which results in different hydrophobic/hydrophilic surface areas. On the hydrophobic prG, sheet-like structures dominate the network,
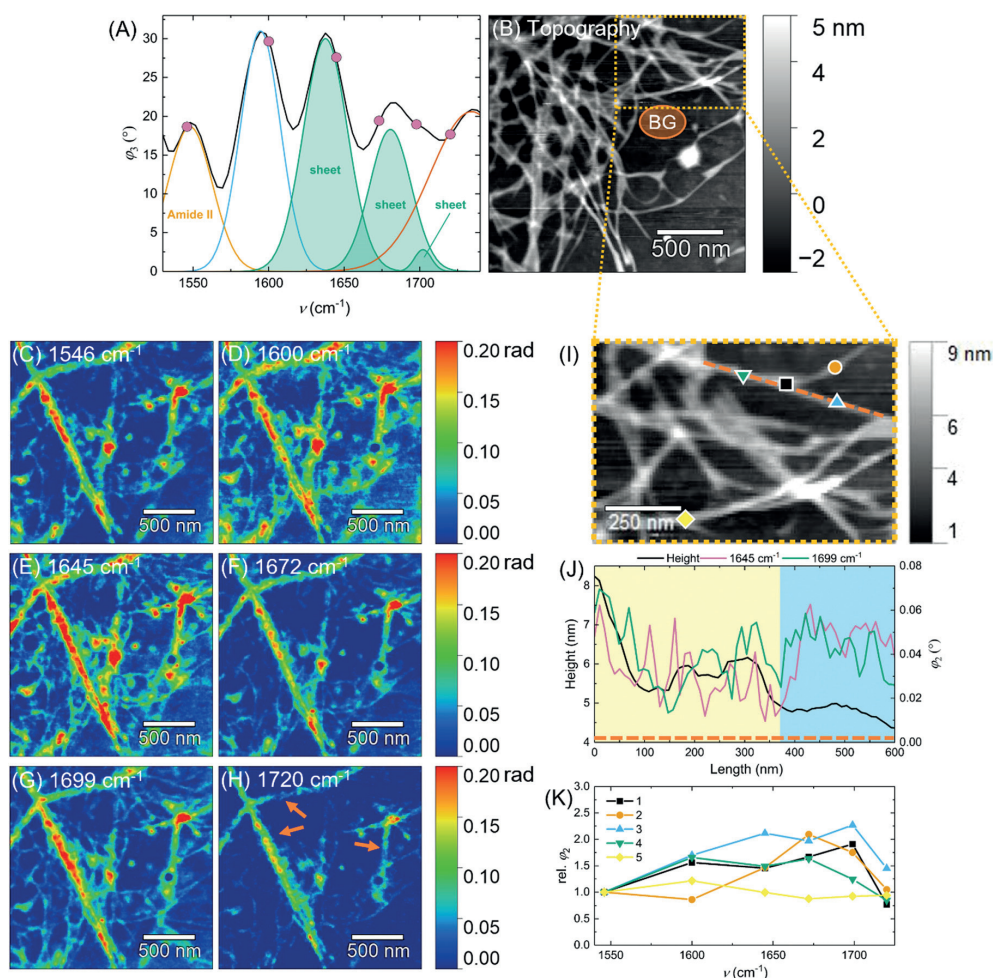
8730 | Phys. Chem. Chem. Phys., 2023, 25, 8725–8733

This journal is © the Owner Societies 2023

Fig. 6 MIR imaging study of Fmoc-Phe fibres on prG: (A) frequencies of imaging (purple dots) highlighted in a nano-FTIR spectrum of the fibres on prG; (B) AFM topographic image of the fibres on prG. The area highlighted in orange was used as a background in all images; (C–H) corresponding optical phase φ^2 images, the imaging frequency is given in each image; (I) a magnification of image (B); (J) height/intensity profiles corresponding to the orange dashed line in (I). Plots from topography (black), 1645 cm^{-1} (purple) and 1699 cm^{-1} (green); (K) relative phase from each optical phase image at certain points, marked in (I).

while additional helical or disordered structures were observed on hydrophilic oxG. Additionally, laser-oxidation can affect the tertiary organization level (fibril–fibril interactions) of Fmoc-Phe. The fibres appear rather straight on prG and curvy on oxG. Supported by DFT calculations, the self-assembly of amphiphilic Fmoc-Phe is a surface-mediated process, *i.e.*, the self-assembly process starts from the first layer of molecules adsorbed on the surface.

In addition, the Fmoc-Phe gel on prG consists of a heterogeneous network, as observed at a single fibre level. Our results are in accordance with previous findings on polymorphism in Fmoc-Phe bulk gels. However, we prove that the heterogeneity of the secondary organization level initiates at the nanoscale. It is of note that the presented observations reflect the

experimental conditions and may change under different conditions (*i.e.*, different solvents, Fmoc-Phe concentration, or sample volume).

In future, the surface effects on the physical properties of the wet gel remain to be studied. We believe that a thorough understanding of the interactions between a surface and an ECM-biomimetic gel is crucial for the engineering of bioelectronic interfaces, towards next-generation neuron–machine connections.

Author contributions

J. S.: investigation; formal analysis; validation; writing – original draft, review & editing. R. C., A. E., E. H.: investigation;

writing – review & editing. A. J.: investigation. P. M.: design and development of the oxidation laser setup. M. N., E. D. S.: conceptualization; supervision; writing – review & editing. M. P.: funding acquisition; project administration; supervision; writing – review & editing.

Conflicts of interest

There are no conflicts to declare.

Acknowledgements

References

1 M. Bramini, G. Alberini, E. Colombo, M. Chiacchiaretta, M. L. DiFrancesco, J. F. Maya-Vetencourt, L. Maragliano, F. Benfenati and F. Cesca, *Front. Syst. Neurosci.*, 2018, **12**, 12.

2 A. B. Rapeaux and T. G. Constandinou, *Curr. Opin. Biotechnol*, 2021, **72**, 102–111.

3 S. R. Shin, Y. C. Li, H. L. Jang, P. Khoshakhlagh, M. Akbari, A. Nasajpour, Y. S. Zhang, A. Tamayol and A. Khademhosseini, *Adv. Drug Delivery Rev.*, 2016, **105**, 255–274.

4 N. Wu, S. Wan, S. Su, H. Huang, G. Dou and L. Sun, *InfoMat*, 2021, **3**, 1174–1194.

5 A. K. Geim and K. S. Novoselov, *Nat. Mater.*, 2007, **6**, 183–191.

6 C. Hébert, E. Masvidal-Codina, A. Suarez-Perez, A. B. Calia, G. Piret, R. Garcia-Cortadella, X. Illa, E. del Corro Garcia, J. M. de la Cruz Sanchez, D. V. Casals, E. Prats-Alfonso, J. Bousquet, P. Godignon, B. Yvert, R. Villa, M. V. Sanchez-Vives, A. Guimerà-Brunet and J. A. Garrido, *Adv. Funct. Mater.*, 2018, **28**, 1703976.

7 C. Lee, X. Wei, J. W. Kysar and J. Hone, *Science*, 2008, **321**, 385–388.

8 J. Aumanen, A. Johansson, J. Koivistoinen, P. Myllyperkiö and M. Pettersson, *Nanoscale*, 2015, **7**, 2851–2855.

9 E. D. Sitsanidis, J. Schirmer, A. Lampinen, K. K. Mentel, V. M. Hiltunen, V. Ruokolainen, A. Johansson, P. Myllyperkiö, M. Nissinen and M. Pettersson, *Nanoscale Adv.*, 2021, **3**, 2065–2074.

10 A. Johansson, H.-C. Tsai, J. Aumanen, J. Koivistoinen, P. Myllyperkiö, Y.-Z. Hung, M.-C. Chuang, C.-H. Chen, W. Y. Woon and M. Pettersson, *Carbon*, 2017, **115**, 77–82.

11 B. Alberts, A. Johnson, J. Lewis, D. Morgan, M. Raff and K. Roberts, *Molecular Biology of the Cell*, Garland Science, 6th edn, 2015, pp. 1035–1090.

12 P. C. Georges, W. J. Miller, D. F. Meaney, E. S. Sawyer and P. A. Janmey, *Biophys. J.*, 2006, **90**, 3012–3018.

13 J. Lantoine, T. Grevesse, A. Villers, G. Delhaye, C. Mestdagh, M. Versaevel, D. Mohammed, C. Bruyère, L. Alaimo, S. P. Lacour, L. Ris and S. Gabriele, *Biomaterials*, 2016, **89**, 14–24.

14 S. Sur, C. J. Newcomb, M. J. Webber and S. I. Stupp, *Biomaterials*, 2013, **34**, 4749–4757.

15 E. R. Draper and D. J. Adams, *Chem*, 2017, **3**, 390–410.

16 L. A. Estroff and A. D. Hamilton, *Chem. Rev.*, 2004, **104**, 1201–1217.

17 B. A. Simmons, C. E. Taylor, F. A. Landis, V. T. John, G. L. McPherson, D. K. Schwartz and R. Moore, *J. Am. Chem. Soc.*, 2001, **123**, 2414–2421.

18 E. Mayans and C. Alemán, *Molecules*, 2020, **25**, 6037.

19 D. M. Murali and G. Shanmugam, *New J. Chem.*, 2019, **43**, 12396–12409.

20 V. Singh, K. Snigdha, C. Singh, N. Sinha and A. K. Thakur, *Soft Matter*, 2015, **11**, 5353–5364.

21 M. G. F. Angelerou, A. Sabri, R. Creasey, P. Angelerou, M. Marlow and M. Zelzer, *Chem. Commun.*, 2016, **52**, 4298–4300.

22 M. G. F. Angelerou, B. Yang, T. Arnold, J. Rawle, M. Marlow and M. Zelzer, *Soft Matter*, 2018, **14**, 9851–9855.

23 M. Criado-Gonzalez, M. H. Iqbal, A. Carvalho, M. Schmutz, L. Jierry, P. Schaaf and F. Boulmedais, *Front. Bioeng. Biotechnol.*, 2020, **8**, 938.

24 V. V. Korolkov, S. Allen, C. J. Roberts and S. J. B. Tendler, *Faraday Discuss.*, 2013, **166**, 257–267.

25 B. Yang, M. Lledos, R. Akhtar, G. Ciccone, L. Jiang, E. Russo, S. Rajput, C. Jin, M. G. F. Angelereou, T. Arnold, J. Rawle, M. Vassalli, M. Marlow, D. J. Adams and M. Zelzer, *Chem. Sci.*, 2021, **12**, 14260–14269.

26 A. Accardo, V. Shalabaeva, E. di Cola, M. Burghammer, R. Krahne, C. Riekel and S. Dante, *ACS Appl. Mater. Interfaces*, 2015, **7**, 20875–20884.

27 M. Mahmoudi, O. Akhavan, M. Ghavami, F. Rezaee and S. M. A. Ghiasi, *Nanoscale*, 2012, **4**, 7322–7325.

28 K. Shezad, K. Zhang, M. Hussain, H. Dong, C. He, X. Gong, X. Xie, J. Zhu and L. Shen, *Langmuir*, 2016, **32**, 8238–8244.

29 A. Keller, M. Fritzsche, Y. P. Yu, Q. Liu, Y. M. Li, M. Dong and F. Besenbacher, *ACS Nano*, 2011, **5**, 2770–2778.

30 I. Amenabar, S. Poly, W. Nuansing, E. H. Hubrich, A. A. Govyadinov, F. Huth, R. Krutokhvostov, L. Zhang, M. Knez, J. Heberle, A. M. Bittner and R. Hillenbrand, *Nat. Commun.*, 2013, **4**, 2890.

31 F. Huth, A. Govyadinov, S. Amarie, W. Nuansing, F. Keilmann and R. Hillenbrand, *Nano Lett.*, 2012, **12**, 3973–3978.

32 M. Paulite, Z. Fakhraai, I. T. S. Li, N. Gunari, A. E. Tanur and G. C. Walker, *J. Am. Chem. Soc.*, 2011, **133**, 7376–7383.

33 T. Taubner, R. Hillenbrand and F. Keilmann, *Appl. Phys. Lett.*, 2004, **85**, 5064–5066.

34 X. Ma, Q. Liu, N. Yu, D. Xu, S. Kim, Z. Liu, K. Jiang, B. M. Wong, R. Yan and M. Liu, *Nat. Commun.*, 2021, **12**, 6868.

35 S. Kim, N. Yu, X. Ma, Y. Zhu, Q. Liu, M. Liu and R. Yan, *Nat. Photon.*, 2019, **13**, 636–643.

8732 | *Phys. Chem. Chem. Phys.*, 2023, **25**, 8725–8733

This journal is © the Owner Societies 2023

36 J. Lee, K. T. Crampton, N. Tallarida and V. A. Apkarian, *Nature*, 2019, **568**, 78–82.

37 A. Y. Gahane, P. Ranjan, V. Singh, R. K. Sharma, N. Sinha, M. Sharma, R. Chaudhry and A. K. Thakur, *Soft Matter*, 2018, **14**, 2234–2244.

38 A. Rajbhandary, W. W. Brennessel and B. L. Nilsson, *Cryst. Growth Des.*, 2018, **18**, 623–632.

39 D. M. Ryan, S. B. Anderson and B. L. Nilsson, *Soft Matter*, 2010, **6**, 3220–3231.

40 B. Adhikari, G. Palui and A. Banerjee, *Soft Matter*, 2009, **5**, 3452–3460.

41 A. M. Smith, R. J. Williams, C. Tang, P. Coppo, R. F. Collins, M. L. Turner, A. Saiani and R. V. Ulijn, *Adv. Mater.*, 2008, **20**, 37–41.

42 D. Giuri, L. J. Marshall, C. Wilson, A. Seddon and D. J. Adams, *Soft Matter*, 2021, **17**, 7221–7226.

43 E. S. Gadelmawla, M. M. Koura, T. M. A. Maksoud, I. M. Elewa and H. H. Soliman, *J. Mater. Process. Technol.*, 2002, **123**, 133–145.

44 E. R. Draper, K. L. Morris, M. A. Little, J. Raeburn, C. Colquhoun, E. R. Cross, T. O. McDonald, L. C. Serpell and D. J. Adams, *CrystEngComm*, 2015, **17**, 8047–8057.

45 A. Barth, *Biochim. Biophys. Acta*, 2007, **1767**, 1073–1101.

46 A. Barth and C. Zscherp, *Q. Rev. Biophys.*, 2002, **35**, 369–430.

47 S. Mastel, A. A. Govyadinov, T. V. A. G. de Oliveira, I. Amenabar and R. Hillenbrand, *Appl. Phys. Lett.*, 2015, **106**, 023113.

48 H. Wang, L. Wang, D. S. Jakob and X. G. Xu, *AIP Adv.*, 2017, **7**, 055118.

49 A. Barth, *Prog. Biophys. Mol. Biol.*, 2000, **74**, 141–173.

50 X. Liu, *Organic Chemistry I*, Kwantlen Polytechnic University, 2021, pp. 197–200.

This journal is © the Owner Societies 2023

Phys. Chem. Chem. Phys., 2023, **25**, 8725–8733 | 8733

Supplementary Information

Diversity at the nanoscale: Laser-oxidation of single-layer graphene affects Fmoc-phenylalanine surface-mediated self-assembly

Johanna Schirmer,[a] Romain Chevigny,[a] Aleksei Emelianov,[a] Eero Hulkko,[a,b] Andreas Johansson,[a,c] Pasi Myllyperkiö,[a] Efstratios D. Sitsanidis, *[a] Maija Nissinen *[a] and Mika Pettersson *[a]

[a]*Department of Chemistry, Nanoscience Center, University of Jyväskylä, P. O. Box 35, FI-40014 JYU, Finland. E-Mail: mika.j.pettersson@jyu.fi, efstratios.d.sitsanidis@jyu.fi*
[b]*Department of Biological and Environmental Sciences, Nanoscience Center, University of Jyväskylä, P. O. Box 35, FI-40014 JYU, Finland.*
[c]*Department of Physics, Nanoscience Center, University of Jyväskylä, P. O. Box 35, FI-40014 JYU, Finland.*

Table of Contents

S1. Experimental and computational details

Materials

Fluorenylmethoxycarbonyl-Phenylalanine, Fmoc-Phe, was purchased from TCI (Japan). Phosphate Buffer Saline tablets (PBS, NaCl 137 mM, phosphate buffer 10mM, KCl 2.7 mM, pH 7.4) were purchased from Fisher Scientific (United Kingdom) and used as described by the manufacturer.

Sample Preparation

Single layer graphene (SLG) surface preparation. Graphene was synthesized on Cu (111) thin films evaporated onto single-crystal sapphire (0001) substrates. The catalyst film was annealed at 1060 °C under the gas flows of argon (470 sccm) and hydrogen (27 sccm) for 30 min to promote mono-crystallinity through secondary grain growth. After annealing, graphene growth was initiated by adding 6.8 sccm of 1% methane in argon to the furnace while keeping the temperature at 1060 °C. The growth time was 25 min. The graphene films were transferred by a standard PMMA transfer method onto a silicon substrate (5 mm x 5 mm) with a 300 nm thermal oxide film and a palladium reference grid on top. The PMMA film was removed with acetone (30 min at 50 °C). Finally, the sample was annealed at 300 °C in Ar/H2 atmosphere for two hours to remove PMMA residues.

Laser-Oxidation. Two-photon oxidation of graphene was performed with a 515 nm femtosecond laser (Pharos-10, Light Conversion Ltd., 600 kHz repetition rate, 250 fs pulse duration, Lithuania) in an ambient atmosphere with a relative humidity of 35%. To pattern ten 40 x 400 μm^2 areas, 4x objective was used with a spot diameter of approximately 6 µm. The pulse energy was set to 3 nJ, and the time of irradiation was 0.1 s/spot with a 2 µm step separation. Laser-oxidation of graphene was confirmed by Raman spectroscopy (section S4).

Gel sample preparation. Fmoc-Phe (1 mg, 2 mg or 3 mg) and PBS (1 mL, 0.1 M, pH = 7.4) were mixed and sonicated to obtain a fine suspension. Subsequently, the suspension was heated at 80 °C for 30 min to a transparent, colourless solution. 2 µL of the hot Fmoc-Phe solution were added on top of the SLG surface. The solution was let to cool down overnight at room temperature in a water-saturated environment. The remaining Fmoc-Phe solution was kept in a closed vial overnight to ensure gelation had occurred. Three different types of samples were produced, namely room temperature (rt) samples, rt-vacuumed samples, and lyophilized samples.

Next day, rt samples were transferred to a half-open petri dish and left to dry overnight at rt. The rt-vacuumed sample was transferred into a glass vial and dried under vacuum ($p < 1$ mbar) at rt. The lyophilized samples were transferred to glass vials and stored overnight at -20 °C. Next day, the lyophilized samples were dried for 30 min at -50 °C under vacuum ($p < 1$ mbar). The list of samples with the respective Fmoc-Phe concentration c and the drying method are listed in table S1.

Table S1: List of prepared samples type of surface, Fmoc-Phe concentration and drying method.

Substrate	$c_{Fmoc-Phe}$ (w%)	Drying method
Mica	0.1	rt
Mica	0.2	rt
Mica	0.3	rt
Mica	0.1	rt-Vacuum
Mica	0.1	Lyophilization
prG	0.1	rt
prG/oxG	0.1	Lyophilization

Sample Characterization

Optical microscopy. Optical images were taken with an Olympus microscope, equipped with 5x, 10x, 20x and 50x objectives and a camera. All images were processed with Fiji2 software.

Atomic force microscopy (AFM). AFM imaging was performed in air on a Bruker Dimension Icon AFM, operated in PeakForce Tapping mode. Scan-Asyst-AIR probes (Bruker, USA) made from silicon nitride with a spring constant of 0.4 N/m were employed, and the PeakForce Setpoint was 2 nN for all images.

The obtained data was processed and analysed with Nanoscope Analysis 1.9 software. The roughness of pristine and laser-oxidized graphene was calculated with the roughness analysis function, and fibre height and width were measured with the section analysis function. AFM images for figures were created with the Gwyddion software. The significancy of the difference in fibre height was determined in OriginPro 2017 software with a One-way ANOVA test ($p < 0.001$).

Scattering-type scanning near-field optical microscopy (s-SNOM). The s-SNOM experiments were performed on a neaSNOM device (attocube systems AG, Germany) equipped with a tuneable quantum cascade laser for s-SNOM imaging and a broadband laser continuum for nano-FTIR spectroscopy.

For imaging experiments, Arrow-NCPt-50 silicon probes (Nanoworld® AG, Switzerland) with a Pt/Ir coating on the tip and detector side and a resonance frequency of 285 kHz were used. Six images were taken in the same location with different MIR frequencies (1546 cm^{-1}, 1600 cm^{-1}, 1645 cm^{-1}, 1672 cm^{-1}, 1699 cm^{-1}, 1720 cm^{-1}) on a pristine graphene surface. The images were taken with a resolution of 10 nm and processed with the Gwyddion software. A plane fit was applied to remove the thermal drift of the microscope. Due to a maladjustment of the mirror amplitude, the images at 1699 cm^{-1} and 1645 cm^{-1} showed an inverse optical phase contrast. The phase values were corrected for analysis by inversion. For the analysis of the absorptive properties at specific locations, the phase values of five pixels in the respective location were averaged.

Metal-coated nanospectroscopy probes were used for nano-FTIR experiments. Initially, an AFM topographic image was taken from the area of interest. Subsequently, nano-FTIR spectra were taken from the desired spots, including background spectra from outside the region covered with gel (pristine and oxidized graphene). The used frequency range was 1500 cm^{-1} to 1800 cm^{-1}. The integration time per pixel was 80 ms and the spectral resolution ≈15 cm^{-1}. Each spectrum was divided by the corresponding background spectrum. The phase offset was manually adjusted so that each spectrum had zero points before the first and after the last band in the spectral range of interest (1500 cm^{-1} to 1800 cm^{-1}). Peak fitting was performed with OriginPro 2017 software. Firstly, the second derivative of the respective spectrum was calculated to obtain the peak maxima of the spectrum, which are located at the minima of the second derivative. Fitting was done with the "Peak Analyzer" function between 1400 cm^{-1} and 1750 cm^{-1} with fixed peak centres at the known positions. The shape of the bands was a Gaussian function.

To calculate the inputs of helical and sheet-like secondary structures, the areas of the fitted bands assigned to secondary structures were used. The inputs for helical and sheet-like structures in % were calculated with the following equations, respectively:

$$I_h = \frac{A_h}{A_h + \sum A_s} \cdot 100$$

$$I_s = \frac{\sum A_s}{A_h + \sum A_s} \cdot 100$$

with the input of helical and sheet-like structures I_h and I_s, respectiely, and the area of a fitted band assigned to helical and sheet-like structures A_h and A_s, respectively.

Scanning electron and helium ion microscopy. Scanning electron microscopy images were captured on a Raith e-LiNE microscope and helium ion microscopy (HIM) images on a Zeiss Orion Nanofab microscope. All images were processed with Fiji2 software.

Computational Details

All calculations were performed in a vacuum using the GPAW code based on the projector-augmented wave formalism. The Bayesian error estimation functional with van der Waals correlation[1] was employed together with the grid-based finite-difference basis set. A 5 x 5 graphene super cell was constructed, containing 72 carbon atoms. The dimensions of the super cell were set to 14.82 Å x 14.82 Å x 20.76 Å to exclude interactions between neighboring cells in z-direction. To obtain laser-oxidized graphene, one epoxide and one hydroxyl group were placed on top of the graphene monolayer. The resulting graphene-based surfaces were optimized in to obtain the total energy $E_{surface}$. The structure of Fmoc-Phe was obtained from PubChem (compound ID 978331) and optimized as a monomer (with the total energy $E_{Fmoc-Phe}$) before adding it to the surfaces.

Finally, Fmoc-Phe was added on the surfaces. The surface-Fmoc-Phe distance and orientation was varied and the systems were optimized to obtain the total energy E_{system} of the complex. The number of k-points was 4x4x1 to obtain an energy difference of less than 0.05 eV.

The adsorption energy E_{ads} of each system was calculated using the following equation:

$$E_{ads} = E_{system} - \left(E_{surface} + E_{Fmoc - Phe}\right)$$

with parameters described above.

S2. Sample optimization

Fmoc-Phe gelled in Phosphate Buffer Saline (PBS) solution, at a concentration of 0.2 w%, following a heating/cooling cycle. Before assessing the gel network on the graphene surfaces, we investigated gelation on mica discs (Table S1) to determine the optimal conditions for sample handling and microscopy imaging (such as Fmoc-Phe concentration, network thickness and drying methods).

For AFM imaging – and s-SNOM as an AFM-based method – a flat background with distinct structural features is a prerequisite for obtaining high-resolution images. Therefore, the desired Fmoc-Phe gel sample should provide distinct, spatially separated fibres on the flat surface. This implies that the concentration of Fmoc-Phe should be low enough to avoid the formation of a rather dense fibrous network. The minimum gelation concentration (MGC) of Fmoc-Phe is 0.2 wt.-%[2]. Below the MGC, the supramolecular network is too weak to form a self-supporting gel. However, the self-assembly process does occur, resulting in a viscous solution with a less dense network. To evaluate fibre density, we prepared Fmoc-Phe xerogel samples (gels dried overnight at rt in open air) at a range of concentrations (0.1 wt.-%, 0.2 wt.-% and 0.3 wt.-%). Optical images (Fig. S1) showed the formation of different densities (crystals) depending on concentration. At 0.1 wt.-% and 0.2 wt.-%, distinct, round-shaped, concentric crystals formed on the mica surface. Nano-FTIR analysis of the crystals showed that they consist of PBS salts (Fig. S2, section S3). Although PBS concentration is constant in all samples, the density of PBS crystals is affected by the Fmoc-Phe concentration. Indeed, the crystal density was lower at 0.1 wt.-% Fmoc-Phe samples than at 0.2 wt.-%. At 0.3 wt.-%, a thick xerogel layer was visible, lacking distinct crystalline structures. It is of note that the formation of crystals or fibres depends on the drying method (*vide infra*). Additionally, fibres could not be observed with optical microscopy. An increased gelator concentration seems to hinder the formation of distinct crystals. Therefore, since we aimed for the least dense gel network, 0.1 wt.-% was chosen as the optimal concentration for sample preparation.

SEM and HIM imaging are performed under vacuum; therefore, a dry sample (xerogel) is required. The drying method of wet gels can significantly impact the supramolecular network.[3,4] Indeed, during drying, the 3D network collapses to 2D, which appears denser. In practice, no wet and dry gels can be compared. Single fibres tend to aggregate into thicker bundles during drying, which again aggregate to higher-ordered structures than in wet gels.[4,5] To obtain the most realistic image of the supramolecular fibrous network, the drying time should be as short as possible. For example, freezing at -20 °C for 7 h and subsequent lyophilization leads to a rather realistic result.[4] For Fmoc-Phe gels, the molecular arrangement of the gelator molecules is retained after lyophilization.[2] We therefore prepared a xerogel sample on mica by freezing and subsequent lyophilization, while a reference sample was dried under vacuum at rt. The latter showed similar, round-shaped crystals as the samples dried at rt in open air (Table S1 and Fig. S1). The crystals of the freeze-dried/lyophilized sample were elongated in shape and partially aligned in a parallel manner. This observation suggests that round-shaped concentric crystals form due to the slow evaporation of the solvent, which presumably could lead to variations in the morphology and density of the Fmoc-Phe fibres. Therefore, for the analysis of Fmoc-Phe fibres, we have chosen lyophilization as a standard method for sample preparation, as it yields the most realistic image of the surface-gel interface.
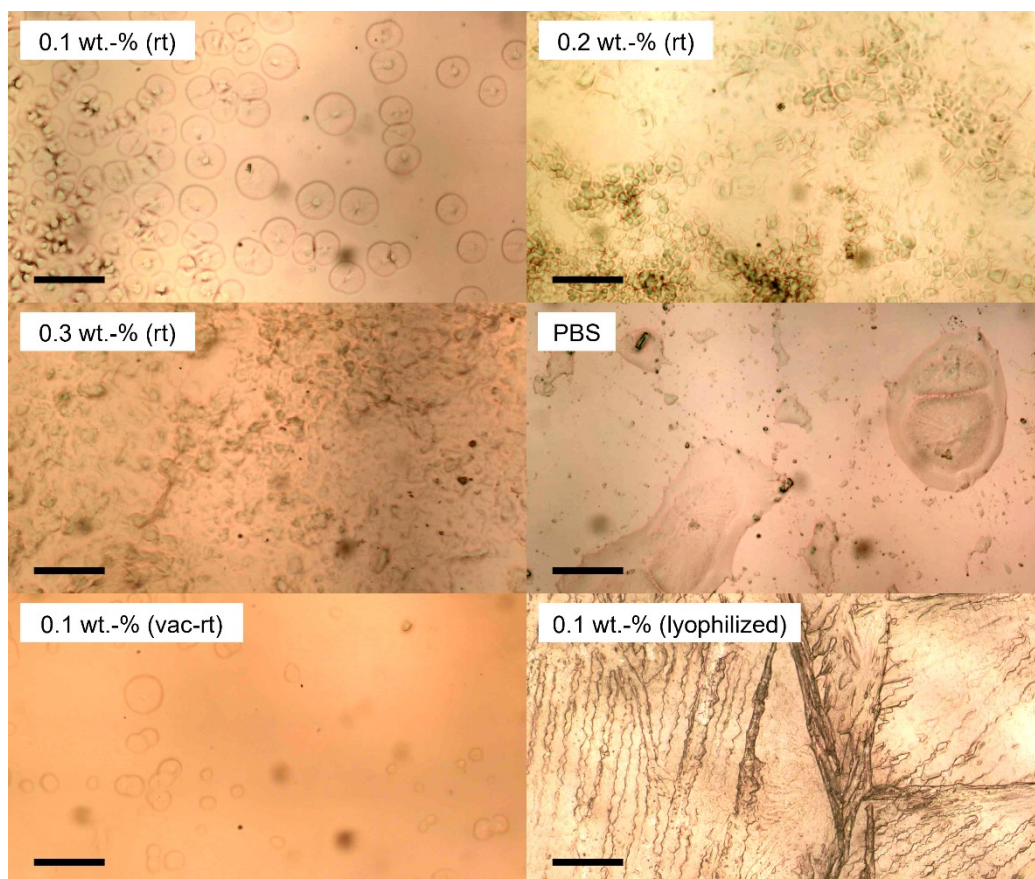
Figure S1: Optical microscopy images of Fmoc-Phe on Mica: rt-dried Fmoc-Phe gel with Fmoc-Phe concentrations of 0.1 wt.-%, 0.2 wt.-% and 0.3 wt.-%, rt-dried PBS solution, vacuumed-rt-dried and lyophilized Fmoc-Phe gel, both with an Fmoc-Phe concentration of 0.1 wt.-%. The black scalebars correspond to 50 µm in all images.

S3. Characterization of concentric crystals

The AFM image (Fig. S2A) of the concentric crystal showed a symmetric nanostructure, while HIM (Fig. S2B) and SEM (Fig. S2C) images revealed gel fibres on top of the crystal. To clarify the composition of the crystals, a control sample was prepared on mica, using a hot PBS solution without any Fmoc-Phe molecules. The sample contained various shapes of crystals. A few centred, round crystals were found, while other shapes dominate (Fig. S1). A nano-FTIR spectrum was measured from one crystal to analyse the chemical identity of the crystals. Figure S2-D shows the nano-FTIR spectrum of the crystal (red), the graphene background (black) and the ATR-FTIR spectrum of the PBS salt used to prepare the buffer (blue). The spectrum of the crystal follows the spectrum of the PBS salt with slight deviations. This indicates that the crystal consists of buffer salts. However, the symmetric shape forms when surrounded by Fmoc-Phe fibres, which indicates that the Fmoc-Phe network affects the shape of the crystals.
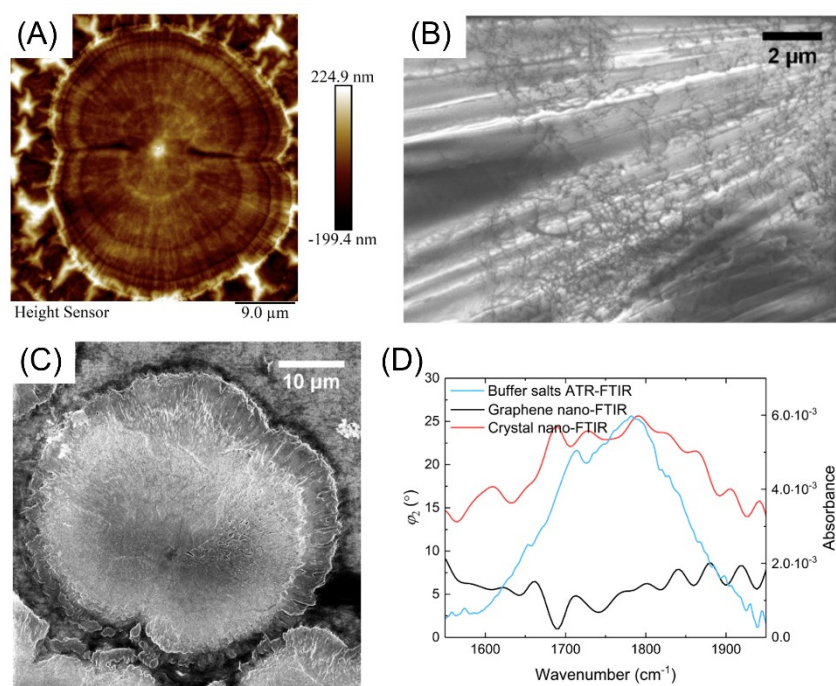
Figure S2: Concentric crystals on rt-dried Fmoc-Phe gel samples on prG: AFM (A), SEM (B), HIM (C) images and nano-FTIR spectra of prG and crystal and ATR-FTIR spectrum of the buffer salts (D).

S4. Raman spectroscopy of pristine and oxidized graphene

After the laser-oxidization of graphene, oxidization was verified by Raman spectroscopy. Figure S3 represents Raman spectra of one pristine and one oxidized area on the same sample. Two bands are observable in both pristine and laser-oxidized graphene: The G band, which is assigned to stretching in the sp2 carbon lattice of graphene and the 2D band, which is derived from a second-order double-resonant process. The spectrum of laser-oxidized graphene also shows the D and D' bands, which reveal defects in the graphene lattice. The latter is visible as a shoulder of the G band. By adding oxygen-containing functional groups to the graphene surface during laser-oxidization, defects are introduced, which give rise to the D and D' bands.

The Raman spectra were recorded with a DXR Raman (Thermo Scientific), equipped with a 50x objective. The excitation wavelength was 532 nm, and the laser power was 0.5 mW.
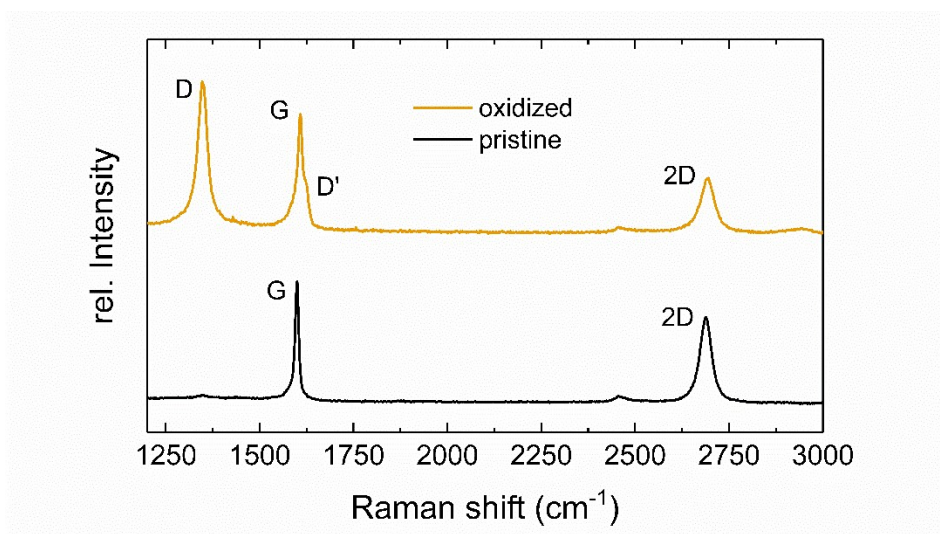
Figure S3: Raman spectra from pristine (black) and laser-oxidized (orange) graphene monolayer.

S5. Nano-FTIR spectra locations and description

The nano-FTIR spectra were taken from five and six different locations on oxidized and pristine graphene, respectively. The exact locations are shown in figure S4 A-D together with the 3rd harmonic phase spectra (Fig. S4 E-F).
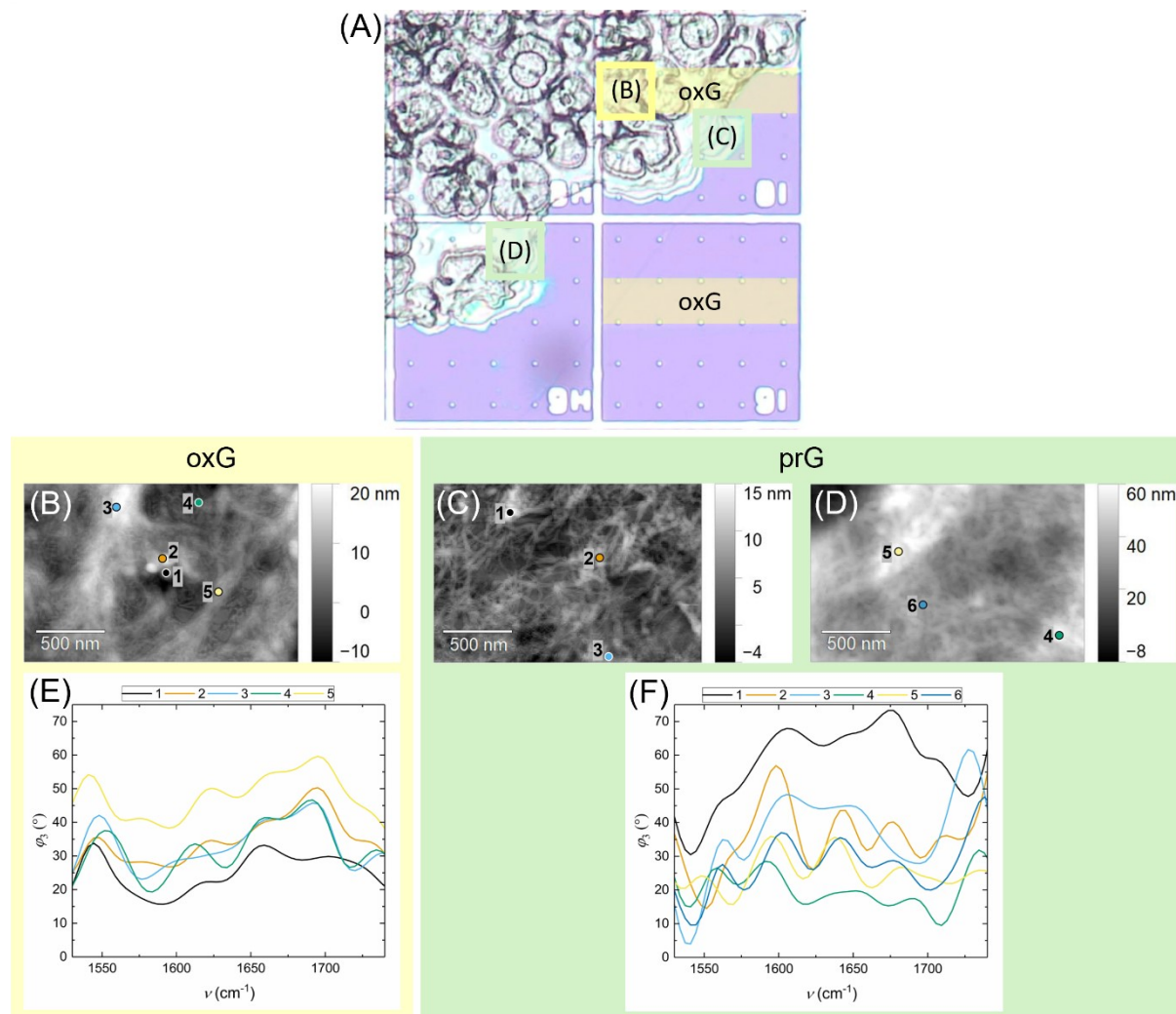
Figure S4: Locations of measured nano-FTIR spectra: (A) Optical microscopy image indicating the oxidized areas and locations of AFM images (B), (C) and (D), which again reveal the exact locations of all nano-FTIR spectra on oxG (E) and prG (F).

S6. Density Functional Theory calculations

In the first step, the pristine and oxidized graphene surfaces, as well as the Fmoc-Phe molecule were optimized in a 14.82 Å x 14.82 Å x 20.76 Å super cell. Figure S5 shows the optimized components. The Fmoc-Phe was added on top of the surfaces in distinct orientations and distances to find the energetically most preferable structures. Table S2 lists all calculated structures, including the adsorption energies of Fmoc-Phe on the surface and the surface-monomer distances.

(A) Fmoc-Phe   (B) oxG   (C) prG
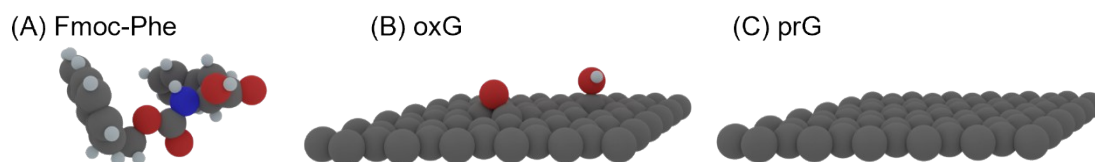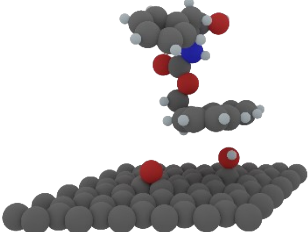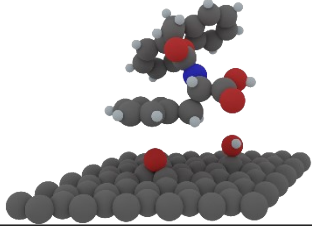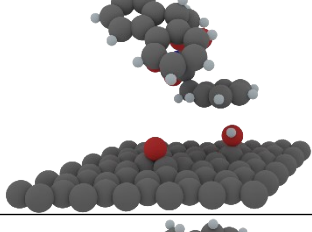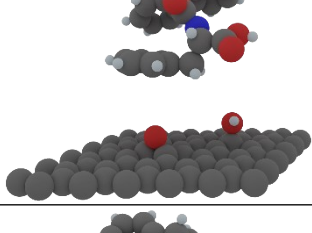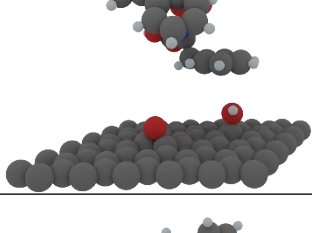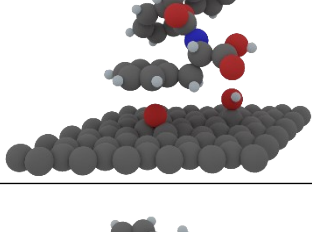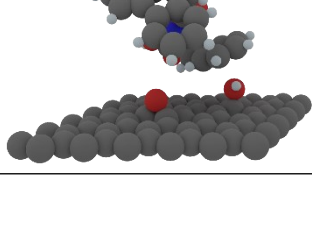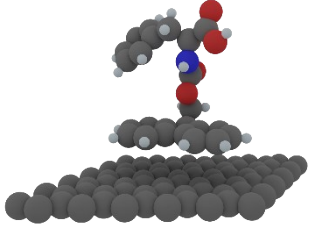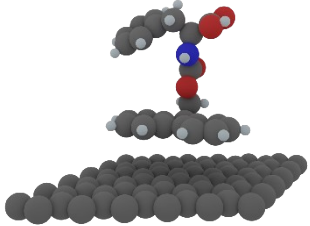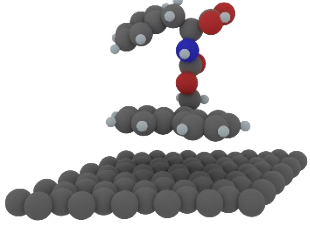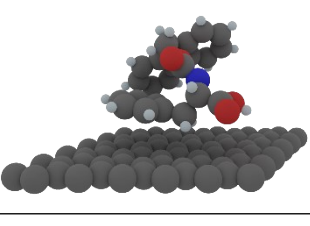
Figure S5: Structures of the optimized components before adsorption energy calculations. The calculated potential energies are (A) -585.11 eV, (B) -1260.04 eV and (C) -1223.25 eV.

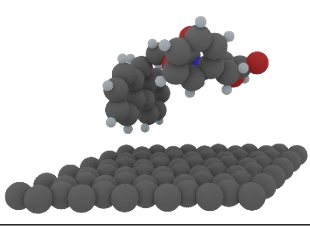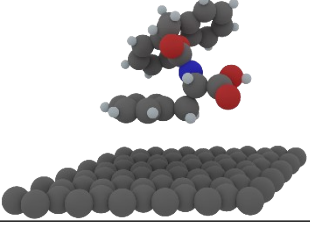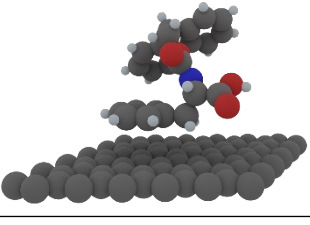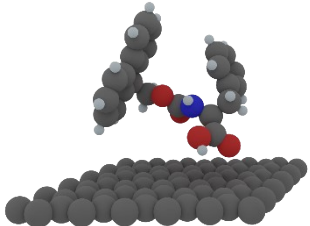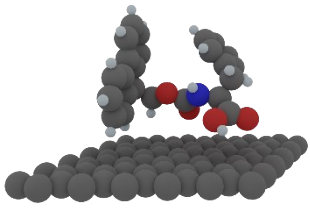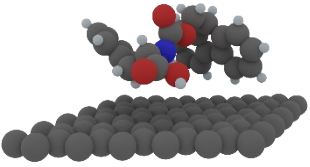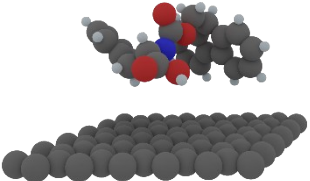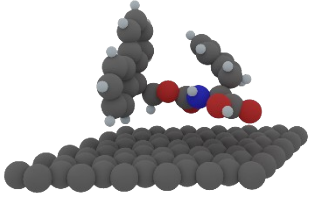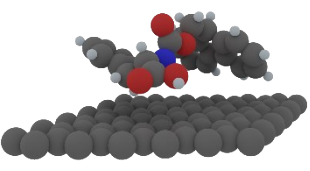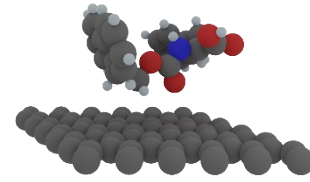Table S2: List of all optimized structures from the DFT calculations, including surface type, the Fmoc-Phe moiety closest to the surface, adsorption energy, distance between the surface and Fmoc-Phe (between the two closest atoms) and the optimized structure. Bold text indicates structures discussed in the manuscript.

Surface	Fmoc-Phe moiety pointing to the surface	Adsorption Energy (eV)	Surface-monomer distance (Å)	Structure
oxG	Fluorenyl group (F)	-0.389298	3.199	
oxG	F	-0.257192	2.788	
oxG	F	-0.400973	3.131	
oxG	F	-0.229931	2.912	

Surface	Fmoc-Phe moiety pointing to the surface	Adsorption Energy (eV)	Surface-monomer distance (Å)	Structure
oxG	F	-0.176901	2.901	
oxG	Phenyl ring (P)	-0.200131	3.387	
oxG	P	-0.231245	2.856	
oxG	P	+0.035285	4.928	
oxG	P	-0.079452	3.409	
oxG	P	-0.231245	2.943	
oxG	P	-0.401081	2.884	

Surface	Fmoc-Phe moiety pointing to the surface	Adsorption Energy (eV)	Surface-monomer distance (Å)	Structure
oxG	Carboxylic Acid (COOH)	-0.448214	2.428	
oxG	**F/COOH**	**-0.766519**	**2.708**	
oxG	COOH	-0.225065	3.117	
oxG	COOH	-0.335819	2.261	
oxG	**P/Amide N-H**	**-0.629901**	**3.028**	
oxG	**P/COOH**	**-0.733678**	**2.903**	
oxG	**COOH**	**-0.650409**	**2.152**	

Surface	Fmoc-Phe moiety pointing to the surface	Adsorption Energy (eV)	Surface-monomer distance (Å)	Structure
prG	F	-0.473977	3.649	
prG	F	-0.556214	4.217	
prG	**F**	**-0.629435**	**3.848**	
prG	F	-0.345276	4.900	
prG	P	-0.188953	4.897	
prG	P	-0.508591	3.639	
prG	**P**	**-0.622241**	**3.489**	

Surface	Fmoc-Phe moiety pointing to the surface	Adsorption Energy (eV)	Surface-monomer distance (Å)	Structure
prG	COOH	-0.296705	3.200	
prG	F/COOH	-0.622007	3.472	
prG	F/P/COOH	-0.766176	3.674	
prG	F/P/COOH	-0.248640	4.888	
prG	**F/COOH**	**-0.662321**	**2.682**	
prG	**F/P/COOH**	**-0.892036**	**3.222**	
prG	F/Amide C=O	-0.442086	3.715	

S7. References

1. J. Wellendorff, K.T. Lundgaard, A. Møgelhøj, V. Petzold, D. D. Landis, J. K. Nørskov, T. Bligaard and K. W. Jacobsen, *Phys Rev B*, 2012, **85**, 235149.
2. V. Singh, K. Snigdha, C. Singh, N. Sinha and A. K. Thakur, *Soft Matter*, 2015, **11**, 5353–5364.
3. D. J. Adams, *Gels*, 2018, **4**, 32.
4. L. L. E. Mears, E. R. Draper, A. M. Castilla, H. Su, Zhuola, B. Dietrich, M. C. Nolan, G. N. Smith, J. Doutch, S. Rogers, R. Akhtar, H. Cui and D. J. Adams, *Biomacromolecules*, 2017, **18**, 3531–3540.
5. B. Yang, M. Lledos, R. Akhtar, G. Ciccone, L. Jiang, E. Russo, S. Rajput, C. Jin, M. G. F. Angelereou, T. Arnold, J. Rawle, M. Vassalli, M. Marlow, D. J. Adams and M. Zelzer, *Chem Sci*, 2021, **12**, 14260–14269.

1. Vuolle, Mikko: Electron paramagnetic resonance and molecular orbital study of radical ions generated from (2.2)metacyclophane, pyrene and its hydrogenated compounds by alkali metal reduction and by thallium(III)trifluoroacetate oxidation. (99 pp.) 1976

2. Pasanen, Kaija: Electron paramagnetic resonance study of cation radical generated from various chlorinated biphenyls. (66 pp.) 1977

3. Carbon-13 Workshop, September 6-8, 1977. (91 pp.) 1977

4. Laihia, Katri: On the structure determination of norbornane polyols by NMR spectroscopy. (111 pp.) 1979

5. Nyrönen, Timo: On the EPR, ENDOR and visible absorption spectra of some nitrogen containing heterocyclic compounds in liquid ammonia. (76 pp.) 1978

6. Talvitie, Antti: Structure determination of some sesquiterpenoids by shift reagent NMR. (54 pp.) 1979

7. Häkli, Harri: Structure analysis and molecular dynamics of cyclic compounds by shift reagent NMR. (48 pp.) 1979

8. Pitkänen, Ilkka: Thermodynamics of complexation of 1,2,4-triazole with divalent manganese, cobalt, nickel, copper, zinc, cadmium and lead ions in aqueous sodium perchlorate solutions. (89 pp.) 1980

9. Asunta, Tuula: Preparation and characterization of new organometallic compounds synthesized by using metal vapours. (91 pp.) 1980

10. Sattar, Mohammad Abdus: Analyses of MCPA and its metabolites in soil. (57 pp.) 1980

11. Bibliography 1980. (31 pp.) 1981

12. Knuuttila, Pekka: X-Ray structural studies on some divalent 3d metal compounds of picolinic and isonicotinic acid N-oxides. (77 pp.) 1981

13. Bibliography 1981. (33 pp.) 1982

14. 6th National NMR Symposium, September 9-10, 1982, Abstracts. (49 pp.) 1982

15. Bibliography 1982. (38 pp.) 1983

16. Knuuttila, Hilkka: X-Ray structural studies on some Cu(II), Co(II) and Ni(II) complexes with nicotinic and isonicotinic acid N-oxides. (54 pp.) 1983

17. Symposium on inorganic and analytical chemistry May 18, 1984, Program and Abstracts. (100 pp.) 1984

18. Knuutinen, Juha: On the synthesis, structure verification and gas chromatographic determination of chlorinated catechols and guaiacols occuring in spent bleach liquors of kraft pulp mill. (30 pp.) 1984

19. Bibliography 1983. (47 pp.) 1984

20. Pitkänen, Maija: Addition of BrCl, B_2 and Cl_2 to methyl esters of propenoic and 2-butenoic acid derivatives and ^{13}C NMR studies on methyl esters of saturated aliphatic mono- and dichlorocarboxylic acids. (56 pp.) 1985

21. Bibliography 1984. (39 pp.) 1985

22. Salo, Esa: EPR, ENDOR and TRIPLE spectroscopy of some nitrogen heteroaromatics in liquid ammonia. (111 pp.) 1985

23. Humppi, Tarmo: Synthesis, identification and analysis of dimeric impurities of chlorophenols. (39 pp.) 1985

24. Aho, Martti: The ion exchange and adsorption properties of sphagnum peat under acid conditions. (90 pp.) 1985

25. Bibliography 1985 (61 pp.) 1986

26. Bibliography 1986. (23 pp.) 1987

27. Bibliography 1987. (26 pp.) 1988

28. Paasivirta, Jaakko (Ed.): Structures of organic environmental chemicals. (67 pp.) 1988

29. Paasivirta, Jaakko (Ed.): Chemistry and ecology of organo-element compounds. (93 pp.) 1989

30. Sinkkonen, Seija: Determination of crude oil alkylated dibenzothiophenes in environment. (35 pp.) 1989

31. Kolehmainen, Erkki (Ed.): XII National NMR Symposium Program and Abstracts. (75 pp.) 1989

32. Kuokkanen, Tauno: Chlorocymenes and Chlorocymenenes: Persistent chlorocompounds in spent bleach liquors of kraft pulp mills. (40 pp.) 1989

33. Mäkelä, Reijo: ESR, ENDOR and TRIPLE resonance study on substituted 9,10-anthraquinone radicals in solution. (35 pp.) 1990

34. Veijanen, Anja: An integrated sensory and analytical method for identification of off-flavour compounds. (70 pp.) 1990

35. Kasa, Seppo: EPR, ENDOR and TRIPLE resonance and molecular orbital studies on a substitution reaction of anthracene induced by thallium(III) in two fluorinated carboxylic acids. (114 pp.) 1990

36. Herve, Sirpa: Mussel incubation method for monitoring organochlorine compounds in freshwater recipients of pulp and paper industry. (145 pp.) 1991

37. Pohjola, Pekka: The electron paramagnetic resonance method for characterization of Finnish peat types and iron (III) complexes in the process of peat decomposition. (77 pp.) 1991

38. Paasivirta, Jaakko (Ed.): Organochlorines from pulp mills and other sources. Research methodology studies 1988-91. (120 pp.) 1992

39. Veijanen, Anja (Ed.): VI National Symposium on Mass Spectrometry, May 13-15, 1992, Abstracts. (55 pp.) 1992

40. Rissanen, Kari (Ed.): The 7. National Symposium on Inorganic and Analytical Chemistry, May 22, 1992, Abstracts and Program. (153 pp.) 1992

41. Paasivirta, Jaakko (Ed.): CEOEC'92, Second Finnish-Russian Seminar: Chemistry and Ecology of Organo-Element Compounds. (93 pp.) 1992

42. Koistinen, Jaana: Persistent polychloroaromatic compounds in the environment: structure-specific analyses. (50 pp.) 1993

43. Virkki, Liisa: Structural characterization of chlorolignins by spectroscopic and liquid chromatographic methods and a comparison with humic substances. (62 pp.) 1993

44. Helenius, Vesa: Electronic and vibrational excitations in some

biologically relevant molecules. (30 pp.) 1993

45. Leppä-aho, Jaakko: Thermal behaviour, infrared spectra and x-ray structures of some new rare earth chromates(VI). (64 pp.) 1994

46. Kotila, Sirpa: Synthesis, structure and thermal behavior of solid copper(II) complexes of 2-amino-2- hydroxymethyl-1,3-pr opanediol. (111 pp.) 1994

47. Mikkonen, Anneli: Retention of molybdenum(VI), vanadium(V) and tungsten(VI) by kaolin and three Finnish mineral soils. (90 pp.) 1995

48. Suontamo, Reijo: Molecular orbital studies of small molecules containing sulfur and selenium. (42 pp.) 1995

49. Hämäläinen, Jouni: Effect of fuel composition on the conversion of fuel-N to nitrogen oxides in the combustion of small single particles. (50 pp.) 1995

50. Nevalainen, Tapio: Polychlorinated diphenyl ethers: synthesis, NMR spectroscopy, structural properties, and estimated toxicity. (76 pp.) 1995

51. Aittola, Jussi-Pekka: Organochloro compounds in the stack emission. (35 pp.) 1995

52. Harju, Timo: Ultrafast polar molecular photophysics of (dibenzylmethine)borondifluoride and 4-aminophthalimide in solution. (61 pp.) 1995

53. Maatela, Paula: Determination of organically bound chlorine in industrial and environmental samples. (83 pp.) 1995

54. Paasivirta, Jaakko (Ed.): CEOEC'95, Third Finnish-Russian Seminar: Chemistry and Ecology of Organo-Element Compounds. (109 pp.) 1995

55. Huuskonen, Juhani: Synthesis and structural studies of some supramolecular compounds. (54 pp.) 1995

56. Palm, Helena: Fate of chlorophenols and their derivatives in sawmill soil and pulp mill recipient environments. (52 pp.) 1995

57. Rantio, Tiina: Chlorohydrocarbons in pulp mill effluents and their fate in the environment. (89 pp.) 1997

58. Ratilainen, Jari: Covalent and non-covalent interactions in molecular recognition. (37 pp.) 1997

59. Kolehmainen, Erkki (Ed.): XIX National NMR Symposium, June 4-6, 1997, Abstracts. (89 pp.) 1997

60. Matilainen, Rose: Development of methods for fertilizer analysis by inductively coupled plasma atomic emission spectrometry. (41 pp.) 1997

61. Koistinen, Jari (Ed.): Spring Meeting on the Division of Synthetic Chemistry, May 15-16, 1997, Program and Abstracts. (36 pp.) 1997

62. Lappalainen, Kari: Monomeric and cyclic bile acid derivatives: syntheses, NMR spectroscopy and molecular recognition properties. (50 pp.) 1997

63. Laitinen, Eira: Molecular dynamics of cyanine dyes and phthalimides in solution: picosecond laser studies. (62 pp.) 1997

64. Eloranta, Jussi: Experimental and theoretical studies on some

quinone and quinol radicals. (40 pp.) 1997

65. Oksanen, Jari: Spectroscopic characterization of some monomeric and aggregated chlorophylls. (43 pp.) 1998

66. Häkkänen, Heikki: Development of a method based on laser-induced plasma spectrometry for rapid spatial analysis of material distributions in paper coatings. (60 pp.) 1998

67. Virtapohja, Janne: Fate of chelating agents used in the pulp and paper industries. (58 pp.) 1998

68. Airola, Karri: X-ray structural studies of supramolecular and organic compounds. (39 pp.) 1998

69. Hyötyläinen, Juha: Transport of lignin–type compounds in the receiving waters of pulp mills. (40 pp.) 1999

70. Ristolainen, Matti: Analysis of the organic material dissolved during totally chlorine-free bleaching. (40 pp.) 1999

71. Eklin, Tero: Development of analytical procedures with industrial samples for atomic emission and atomic absorption spectrometry. (43 pp.) 1999

72. Välisaari, Jouni: Hygiene properties of resol-type phenolic resin laminates. (129 pp.) 1999

73. Hu, Jiwei: Persistent polyhalogenated diphenyl ethers: model compounds syntheses, characterization and molecular orbital studies. (59 pp.) 1999

74. Malkavaara, Petteri: Chemometric adaptations in wood processing chemistry. (56 pp.) 2000

75. Kujala Elena, Laihia Katri, Nieminen Kari (Eds.): NBC 2000, Symposium on Nuclear, Biological and Chemical Threats in the 21st Century. (299 pp.) 2000

76. Rantalainen, Anna-Lea: Semipermeable membrane devices in monitoring persistent organic pollutants in the environment. (58 pp.) 2000

77. Lahtinen, Manu: *In situ* X-ray powder diffraction studies of Pt/C, CuCl/C and Cu_2O/C catalysts at elevated temperatures in various reaction conditions. (92 pp.) 2000

78. Tamminen, Jari: Syntheses, empirical and theoretical characterization, and metal cation complexation of bile acid-based monomers and open/closed dimers. (54 pp.) 2000

79. Vatanen, Virpi: Experimental studies by EPR and theoretical studies by DFT calculations of α-amino-9,10-anthraquinone radical anions and cations in solution. (37 pp.) 2000

80. Kotilainen, Risto: Chemical changes in wood during heating at 150-260 °C. (57 pp.) 2000

81. Nissinen, Maija: X-ray structural studies on weak, non-covalent interactions in supramolecular compounds. (69 pp.) 2001

82. Wegelius, Elina: X-ray structural studies on self-assembled hydrogen-bonded networks and metallosupramolecular complexes. (84 pp.) 2001

83. Paasivirta, Jaakko (Ed.): CEOEC'2001, Fifth Finnish-Russian Seminar: Chemistry and Ecology of Organo-Element Compounds. (163 pp.) 2001

84. Kiljunen, Toni: Theoretical studies on spectroscopy and

atomic dynamics in rare gas solids. (56 pp.) 2001

85. Du, Jin: Derivatives of dextran: synthesis and applications in oncology. (48 pp.) 2001

86. Koivisto, Jari: Structural analysis of selected polychlorinated persistent organic pollutants (POPs) and related compounds. (88 pp.) 2001

87. Feng, Zhinan: Alkaline pulping of non-wood feedstocks and characterization of black liquors. (54 pp.) 2001

88. Halonen, Markku: Lahon havupuun käyttö sulfaattiprosessin raaka-aineena sekä havupuun lahontorjunta. (90 pp.) 2002

89. Falábu, Dezsö: Synthesis, conformational analysis and complexation studies of resorcarene derivatives. (212 pp.) 2001

90. Lehtovuori, Pekka: EMR spectroscopic studies on radicals of ubiquinones Q-n, vitamin K$_3$ and vitamine E in liquid solution. (40 pp.) 2002

91. Perkkalainen, Paula: Polymorphism of sugar alcohols and effect of grinding on thermal behavior on binary sugar alcohol mixtures. (53 pp.) 2002

92. Ihalainen, Janne: Spectroscopic studies on light-harvesting complexes of green plants and purple bacteria. (42 pp.) 2002

93. Kunttu, Henrik, Kiljunen, Toni (Eds.): 4th International Conference on Low Temperature Chemistry. (159 pp.) 2002

94. Väisänen, Ari: Development of methods for toxic element analysis in samples with environmental concern by ICP-AES and ETAAS. (54 pp.) 2002

95. Luostarinen, Minna: Synthesis and characterisation of novel resorcarene derivatives. (200 pp.) 2002

96. Louhelainen, Jarmo: Changes in the chemical composition and physical properties of wood and nonwood black liquors during heating. (68 pp.) 2003

97. Lahtinen, Tanja: Concave hydrocarbon cyclophane π-prismands. (65 pp.) 2003

98. Laihia, Katri (Ed.): NBC 2003, Symposium on Nuclear, Biological and Chemical Threats – A Crisis Management Challenge. (245 pp.) 2003

99. Oasmaa, Anja: Fuel oil quality properties of wood-based pyrolysis liquids. (32 pp.) 2003

100. Virtanen, Elina: Syntheses, structural characterisation, and cation/anion recognition properties of nano-sized bile acid-based host molecules and their precursors. (123 pp.) 2003

101. Nättinen, Kalle: Synthesis and X-ray structural studies of organic and metallo-organic supramolecular systems. (79 pp.) 2003

102. Lampiselkä, Jarkko: Demonstraatio lukion kemian opetuksessa. (285 pp.) 2003

103. Kallioinen, Jani: Photoinduced dynamics of Ru(dcbpy)$_2$(NCS)$_2$ – in solution and on nanocrystalline titanium dioxide thin films. (47 pp.) 2004

104. Valkonen, Arto (Ed.): VII Synthetic Chemistry Meeting and XXVI Finnish NMR Symposium. (103 pp.) 2004

105. Vaskonen, Kari: Spectroscopic studies on atoms and small molecules isolated in low temperature rare gas matrices. (65 pp.) 2004

106. Lehtovuori, Viivi: Ultrafast light induced dissociation of Ru(dcbpy)(CO)$_2$I$_2$ in solution. (49 pp.) 2004

107. Saarenketo, Pauli: Structural studies of metal complexing Schiff bases, Schiff base derived *N*-glycosides and cyclophane π-prismands. (95 pp.) 2004

108. Paasivirta, Jaakko (Ed.): CEOEC'2004, Sixth Finnish-Russian Seminar: Chemistry and Ecology of Organo-Element Compounds. (147 pp.) 2004

109. Suontamo, Tuula: Development of a test method for evaluating the cleaning efficiency of hard-surface cleaning agents. (96 pp.) 2004

110. Güneş, Minna: Studies of thiocyanates of silver for nonlinear optics. (48 pp.) 2004

111. Ropponen, Jarmo: Aliphatic polyester dendrimers and dendrons. (81 pp.) 2004

112. Vu, Mân Thi Hong: Alkaline pulping and the subsequent elemental chlorine-free bleaching of bamboo (*Bambusa procera*). (69 pp.) 2004

113. Mansikkamäki, Heidi: Self-assembly of resorcinarenes. (77 pp.) 2006

114. Tuononen, Heikki M.: EPR spectroscopic and quantum chemical studies of some inorganic main group radicals. (79 pp.) 2005

115. Kaski, Saara: Development of methods and applications of laser-induced plasma spectroscopy in vacuum ultraviolet. (44 pp.) 2005

116. Mäkinen, Riika-Mari: Synthesis, crystal structure and thermal decomposition of certain metal thiocyanates and organic thiocyanates. (119 pp.) 2006

117. Ahokas, Jussi: Spectroscopic studies of atoms and small molecules isolated in rare gas solids: photodissociation and thermal reactions. (53 pp.) 2006

118. Busi, Sara: Synthesis, characterization and thermal properties of new quaternary ammonium compounds: new materials for electrolytes, ionic liquids and complexation studies. (102 pp.) 2006

119. Mäntykoski, Keijo: PCBs in processes, products and environment of paper mills using wastepaper as their raw material. (73 pp.) 2006

120. Laamanen, Pirkko-Leena: Simultaneous determination of industrially and environmentally relevant aminopolycarboxylic and hydroxycarboxylic acids by capillary zone electrophoresis. (54 pp.) 2007

121. Salmela, Maria: Description of oxygen-alkali delignification of kraft pulp using analysis of dissolved material. (71 pp.) 2007

122. Lehtovaara, Lauri: Theoretical studies of atomic scale impurities in superfluid ^{4}He. (87 pp.) 2007

123. Rautiainen, J. Mikko: Quantum chemical calculations of structures, bonding, and spectroscopic properties of some sulphur and selenium iodine cations. (71 pp.) 2007

124. Nummelin, Sami: Synthesis, characterization, structural and

retrostructural analysis of self-assembling pore forming dendrimers. (286 pp.) 2008

125. Sopo, Harri: Uranyl(VI) ion complexes of some organic aminobisphenolate ligands: syntheses, structures and extraction studies. (57 pp.) 2008

126. Valkonen, Arto: Structural characteristics and properties of substituted cholanoates and *N*-substituted cholanamides. (80 pp.) 2008

127. Lähde, Anna: Production and surface modification of pharmaceutical nano- and microparticles with the aerosol flow reactor. (43 pp.) 2008

128. Beyeh, Ngong Kodiah: Resorcinarenes and their derivatives: synthesis, characterization and complexation in gas phase and in solution. (75 pp.) 2008

129. Välisaari, Jouni, Lundell, Jan (Eds.): Kemian opetuksen päivät 2008: uusia oppimisympäristöjä ja ongelmalähtöistä opetusta. (118 pp.) 2008

130. Myllyperkiö, Pasi: Ultrafast electron transfer from potential organic and metal containing solar cell sensitizers. (69 pp.) 2009

131. Käkölä, Jaana: Fast chromatographic methods for determining aliphatic carboxylic acids in black liquors. (82 pp.) 2009

132. Koivukorpi, Juha: Bile acid-arene conjugates: from photoswitchability to cancer cell detection. (67 pp.) 2009

133. Tuuttila, Tero: Functional dendritic polyester compounds: synthesis and characterization of

small bifunctional dendrimers and dyes. (74 pp.) 2009

134. Salorinne, Kirsi: Tetramethoxy resorcinarene based cation and anion receptors: synthesis, characterization and binding properties. (79 pp.) 2009

135. Rautiainen, Riikka: The use of first-thinning Scots pine (*Pinus sylvestris*) as fiber raw material for the kraft pulp and paper industry. (73 pp.) 2010

136. Ilander, Laura: Uranyl salophens: synthesis and use as ditopic receptors. (199 pp.) 2010

137. Kiviniemi, Tiina: Vibrational dynamics of iodine molecule and its complexes in solid krypton - Towards coherent control of bimolecular reactions? (73 pp.) 2010

138. Ikonen, Satu: Synthesis, characterization and structural properties of various covalent and non-covalent bile acid derivatives of N/O-heterocycles and their precursors. (105 pp.) 2010

139. Siitonen, Anni: Spectroscopic studies of semiconducting single-walled carbon nanotubes. (56 pp.) 2010

140. Raatikainen, Kari: Synthesis and structural studies of piperazine cyclophanes – Supramolecular systems through Halogen and Hydrogen bonding and metal ion coordination. (69 pp.) 2010

141. Leivo, Kimmo: Gelation and gel properties of two- and three-component Pyrene based low molecular weight organogelators. (116 pp.) 2011

142. Martiskainen, Jari: Electronic energy transfer in light-harvesting complexes isolated from *Spinacia oleracea* and from three

photosynthetic green bacteria *Chloroflexus aurantiacus*, *Chlorobium tepidum*, and *Prosthecochloris aestuarii*. (55 pp.) 2011

143. Wichmann, Oula: Syntheses, characterization and structural properties of [O,N,O,X´] aminobisphenolate metal complexes. (101 pp.) 2011

144. Ilander, Aki: Development of ultrasound-assisted digestion methods for the determination of toxic element concentrations in ash samples by ICP-OES. (58 pp.) 2011

145. The Combined XII Spring Meeting of the Division of Synthetic Chemistry and XXXIII Finnish NMR Symposium. Book of Abstracts. (90 pp.) 2011

146. Valto, Piia: Development of fast analysis methods for extractives in papermaking process waters. (73 pp.) 2011

147. Andersin, Jenni: Catalytic activity of palladium-based nanostructures in the conversion of simple olefinic hydro- and chlorohydrocarbons from first principles. (78 pp.) 2011

148. Aumanen, Jukka: Photophysical properties of dansylated poly(propylene amine) dendrimers. (55 pp.) 2011

149. Kärnä, Minna: Ether-functionalized quaternary ammonium ionic liquids – synthesis, characterization and physicochemical properties. (76 pp.) 2011

150. Jurček, Ondřej: Steroid conjugates for applications in pharmacology and biology. (57 pp.) 2011

151. Nauha, Elisa: Crystalline forms of selected Agrochemical actives: design and synthesis of cocrystals. (77 pp.) 2012

152. Ahkola, Heidi: Passive sampling in monitoring of nonylphenol ethoxylates and nonylphenol in aquatic environments. (92 pp.) 2012

153. Helttunen, Kaisa: Exploring the self-assembly of resorcinarenes: from molecular level interactions to mesoscopic structures. (78 pp.) 2012

154. Linnanto, Juha: Light excitation transfer in photosynthesis revealed by quantum chemical calculations and exiton theory. (179 pp.) 2012

155. Roiko-Jokela, Veikko: Digital imaging and infrared measurements of soil adhesion and cleanability of semihard and hard surfaces. (122 pp.) 2012

156. Noponen, Virpi: Amides of bile acids and biologically important small molecules: properties and applications. (85 pp.) 2012

157. Hulkko, Eero: Spectroscopic signatures as a probe of structure and dynamics in condensed-phase systems – studies of iodine and gold ranging from isolated molecules to nanoclusters. (69 pp.) 2012

158. Lappi, Hanna: Production of Hydrocarbon-rich biofuels from extractives-derived materials. (95 pp.) 2012

159. Nykänen, Lauri: Computational studies of Carbon chemistry on transition metal surfaces. (76 pp.) 2012

160. Ahonen, Kari: Solid state studies of pharmaceutically important molecules and their derivatives. (65 pp.) 2012

161. Pakkanen, Hannu: Characterization of organic material dissolved during alkaline pulping of wood and non-wood feedstocks. (76 pp.) 2012

162. Moilanen, Jani: Theoretical and experimental studies of some main group compounds: from closed shell interactions to singlet diradicals and stable radicals. (80 pp.) 2012

163. Himanen, Jatta: Stereoselective synthesis of Oligosaccharides by *De Novo* Saccharide welding. (133 pp.) 2012

164. Bunzen, Hana: Steroidal derivatives of nitrogen containing compounds as potential gelators. (76 pp.) 2013

165. Seppälä, Petri: Structural diversity of copper(II) amino alcohol complexes. Syntheses, structural and magnetic properties of bidentate amino alcohol copper(II) complexes. (67 pp.) 2013

166. Lindgren, Johan: Computational investigations on rotational and vibrational spectroscopies of some diatomics in solid environment. (77 pp.) 2013

167. Giri, Chandan: Sub-component self-assembly of linear and non-linear diamines and diacylhydrazines, formulpyridine and transition metal cations. (145 pp.) 2013

168. Riisiö, Antti: Synthesis, Characterization and Properties of Cu(II)-, Mo(VI)- and U(VI) Complexes With Diaminotetraphenolate Ligands. (51 pp.) 2013

169. Kiljunen, Toni (Ed.): Chemistry and Physics at Low Temperatures. Book of Abstracts. (103 pp.) 2013

170. Hänninen, Mikko: Experimental and Computational Studies of Transition Metal Complexes with Polydentate Amino- and Aminophenolate Ligands: Synthesis, Structure, Reactivity and Magnetic Properties. (66 pp.) 2013

171. Antila, Liisa: Spectroscopic studies of electron transfer reactions at the photoactive electrode of dye-sensitized solar cells. (53 pp.) 2013

172. Kemppainen, Eeva: Mukaiyama-Michael reactions with α-substituted acroleins – a useful tool for the synthesis of the pectenotoxins and other natural product targets. (190 pp.) 2013

173. Virtanen, Suvi: Structural Studies of Dielectric Polymer Nanocomposites. (49 pp.) 2013

174. Yliniemelä-Sipari, Sanna: Understanding The Structural Requirements for Optimal Hydrogen Bond Catalyzed Enolization – A Biomimetic Approach.(160 pp.) 2013

175. Leskinen, Mikko V: Remote β-functionalization of β'-keto esters. (105 pp.) 2014

176. 12th European Conference on Research in Chemistry Education (ECRICE2014). Book of Abstracts. (166 pp.) 2014

177. Peuronen, Anssi: N-Monoalkylated DABCO-Based N-Donors as Versatile Building Blocks in Crystal Engineering and Supramolecular Chemistry. (54 pp.) 2014

178. Perämäki, Siiri: Method development for determination and recovery of rare earth elements from industrial fly ash. (88 pp.) 2014

179. Chernyshev, Alexander, N.: Nitrogen-containing ligands and their platinum(IV) and gold(III) complexes: investigation and basicity and nucleophilicity, luminescence, and aurophilic interactions. (64 pp.) 2014

180. Lehto, Joni: Advanced Biorefinery Concepts Integrated to Chemical Pulping. (142 pp.) 2015

181. Tero, Tiia-Riikka: Tetramethoxy resorcinarenes as platforms for fluorescent and halogen bonding systems. (61 pp.) 2015

182. Löfman, Miika: Bile acid amides as components of microcrystalline organogels. (62 pp.) 2015

183. Selin, Jukka: Adsorption of softwood-derived organic material onto various fillers during papermaking. (169 pp.) 2015

184. Piisola, Antti: Challenges in the stereoselective synthesis of allylic alcohols. (210 pp.) 2015

185. Bonakdarzadeh, Pia: Supramolecular coordination polyhedra based on achiral and chiral pyridyl ligands: design, preparation, and characterization. (65 pp.) 2015

186. Vasko, Petra: Synthesis, characterization, and reactivity of heavier group 13 and 14 metallylenes and metalloid clusters: small molecule activation and more. (66 pp.) 2015

187. Topić, Filip: Structural Studies of Nano-sized Supramolecular Assemblies. (79 pp.) 2015

188. Mustalahti, Satu: Photodynamics Studies of Ligand-Protected Gold Nanoclusters by using Ultrafast Transient Infrared Spectroscopy. (58 pp.) 2015

189. Koivisto, Jaakko: Electronic and vibrational spectroscopic studies of gold-nanoclusters. (63 pp.) 2015

190. Suhonen, Aku: Solid state conformational behavior and interactions of series of aromatis oligoamide foldamers. (68 pp.) 2016

191. Soikkeli, Ville: Hydrometallurgical recovery and leaching studies for selected valuable metals from fly ash samples by ultrasound-assisted extraction followed by ICP-OES determination. (107 pp.) 2016

192. XXXVIII Finnish NMR Symposium. Book of Abstracts. (51 pp.) 2016

193. Mäkelä, Toni: Ion Pair Recognition by Ditopic Crown Ether Based bis-Urea and Uranyl Salophen Receptors. (75 pp.) 2016

194. Lindholm-Lehto, Petra: Occurrence of pharmaceuticals in municipal wastewater treatment plants and receiving surface waters in Central and Southern Finland. (98 pp.) 2016

195. Härkönen, Ville: Computational and Theoretical studies on Lattice Thermal conductivity and Thermal properties of Silicon Clathrates. (89 pp.) 2016

196. Tuokko, Sakari: Understanding selective reduction reactions with heterogeneous Pd and Pt: climbing out of the black box. (85 pp.) 2016

197. Nuora, Piia: Monitapaustutkimus LUMA-Toimintaan liittyvissä oppimisympäristöissä tapahtuvista kemian oppimiskokemuksista. (171 pp.) 2016

198. Kumar, Hemanathan: Novel Concepts on The Recovery of By-Products from Alkaline Pulping. (61 pp.) 2016

199. Arnedo-Sánchez, Leticia: Lanthanide and Transition Metal Complexes as Building Blocks for Supramolecular Functional Materials. (227 pp.) 2016

200. Gell, Lars: Theoretical Investigations of Ligand Protected Silver Nanoclusters. (134 pp.) 2016

201. Vaskuri, Juhani: Oppiennätyksistä opetussuunnitelman perusteisiin - lukion kemian kansallisen opetussuunnitelman kehittyminen Suomessa vuosina 1918-2016. (314 pp.) 2017

202. Lundell Jan, Kiljunen Toni (Eds.): 22nd Horizons in Hydrogen Bond Research. Book of Abstracts. 2017

203. Turunen, Lotta: Design and construction of halogen-bonded capsules and cages. (61 pp.) 2017

204. Hurmalainen, Juha: Experimental and computational studies of unconventional main group compounds: stable radicals and reactive intermediates. (88 pp.) 2017

205. Koivistoinen Juha: Non-linear interactions of femtosecond laser pulses with graphene: photo-oxidation, imaging and photodynamics. (68 pp.) 2017

206. Chen, Chengcong: Combustion behavior of black liquors: droplet swelling and influence of liquor composition. (39 pp.) 2017

207. Mansikkamäki, Akseli: Theoretical and Computational Studies of Magnetic Anisotropy and Exchange Coupling in Molecular Systems. (190 p. + included articles) 2018.

208. Tatikonda, Rajendhraprasad: Multivalent N-donor ligands for the construction of coordination polymers and coordination polymer gels. (62 pp.) 2018

209. Budhathoki, Roshan: Beneficiation, desilication and selective precipitation techniques for phosphorus refining from biomass derived fly ash. (64 pp.) 2018

210. Siitonen, Juha: Synthetic Studies on 1-azabicyclo[5.3.0]decane Alkaloids. (140 pp.) 2018

211. Ullah, Saleem: Advanced Biorefinery Concepts Related to Non-wood Feedstocks. (57 pp.) 2018

212. Ghalibaf, Maryam: Analytical Pyrolysis of Wood and Non-Wood Materials from Integrated Biorefinery Concepts. (106 pp.) 2018

DEPARTMENT OF CHEMISTRY, UNIVERSITY OF JYVÄSKYLÄ
DISSERTATIONS PUBLISHED IN THE JYU DISSERTATIONS RESEARCH SERIES

1. Bulatov, Evgeny: Synthetic and structural studies of covalent and non-covalent interactions of ligands and metal center in platinum(II) complexes containing 2,2′-dipyridylamine or oxime ligands. (58 pp.) 2019. JYU Dissertations 70.

2. Annala, Riia: Conformational Properties and Anion Complexes of Aromatic Oligoamide Foldamers. (80 pp.) 2019. JYU Dissertations 84.

3. Isoaho, Jukka Pekka: Dithionite Bleaching of Thermomechanical Pulp - Chemistry and Optimal Conditions. (73 pp.) 2019. JYU Dissertations 85.

4. Nygrén, Enni: Recovery of rubidium from power plant fly ash. (98 pp.) 2019. JYU Dissertations 136.

5. Kiesilä, Anniina: Supramolecular chemistry of anion-binding receptors based on concave macromolecules. (68 pp.) 2019. JYU Dissertations 137.

6. Sokolowska, Karolina: Study of water-soluble p-MBA-protected gold nanoclusters and their superstructures. (60 pp.) 2019. JYU Dissertations 167.

7. Lahtinen, Elmeri: Chemically Functional 3D Printing: Selective Laser Sintering of Customizable Metal Scavengers. (71 pp.) 2019. JYU Dissertations 175.

8. Larijani, Amir: Oxidative reactions of cellulose under alkaline conditions. (102 pp.) 2020. JYU Dissertations 217.

9. Kolari, Kalle: Metal-metal contacts in late transition metal polymers. (60 pp.) 2020. JYU Dissertations 220.

10. Kauppinen, Minttu: Multiscale computational investigation of catalytic properties of zirconia supported noble metals. (87 pp.) 2020. JYU Dissertations 231.

11. Ding, Xin: Halogen Bond in Crystal Engineering: Structural Studies on Crystals with Ruthenium Centered Complexes and 1-(4-Pyridyl)-4-thiopyridine Zwitterion as Halogen Bond Acceptors. (59 pp.) 2020. JYU Dissertations 323.

12. Neuvonen, Antti: Toward an Understanding of Hydrogen-Bonding Bifunctional Organocatalyst Conformations and Their Activity in Asymmetric Mannich Reactions. (77 pp.) 2020. JYU Dissertations 336.

13. Kortet, Sami: 2,5-Diarylpyrrolidines and Pyroglutamic-Acid-Derived 2-Diarylmethyl-5-Aryl-Pyrrolidines: Their Synthesis and Use in Asymmetric Synthesis. (221 pp.) 2020. JYU Dissertations 337.

14. Saarnio, Ville: Fluorescent probes, noble metal nanoparticles and their nanocomposites: detection of nucleic acids and other biological targets. (80 pp.) 2021. JYU Dissertations 361.

15. Chernysheva, Maria: σ-hole interactions: the effect of the donors and acceptors nature in selenoureas, thioureas, halogenated species, substituted benzenes, and their adducts. (72 pp.) 2021. JYU Dissertations 370.

16. Bulatova, Margarita: Noncovalent interactions as a tool for supramolecular self-assembly of metallopolymers. (62 pp.) 2021. JYU Dissertations 377.

DEPARTMENT OF CHEMISTRY, UNIVERSITY OF JYVÄSKYLÄ
DISSERTATIONS PUBLISHED IN THE JYU DISSERTATIONS RESEARCH SERIES

17. Romppanen, Sari: Laser-spectroscopic studies of rare earth element- and lithium-bearing minerals and rocks. (66 pp.) 2021. JYU Dissertations 393.

18. Kukkonen, Esa: Nonlinear optical materials through weak interactions and their application in 3D printing. (58 pp.) 2021. JYU Dissertations 441.

19. Kuosmanen, Riikka: The Effect of Structure on the Gel Formation Ability and the Properties of Bile Acid Based Supramolecular Organogels. (68 pp.) 2021. JYU Dissertations 465.

20. Reuna, Sini: Development of a Method for Phosphorus Recovery from Wastewaters. (67 pp.) 2022. JYU Dissertations 486.

21. Taipale, Essi: Synthetic and Structural Studies on the Effect of Non-Covalent Interactions on N(*sp2*)-Heterocyclic Molecules. (67 pp.) 2022. JYU Dissertations 496.

22. Järvinen, Teemu: Molecular Dynamics View on Matrix Isolation. (143 pp.) 2022. JYU Dissertations 544.

23. Kumar, Parveen: Synthesis and Structural Studies on Halogen(I) Complexes. (160 pp.) 2022. JYU Dissertations 549.

24. Forsblom, Samu: Design and Construction of Metal-Organic Polyhedra. (212 pp.) 2022. JYU Dissertations 569.

25. Korpelin, Ville: Computational Studies of Catalytic Active Site Properties and Reactions at the Metal–Oxide Interface. (78 pp.) 2022. JYU Dissertations 578.

26. Vuori, Hannu: Extending Benson Group Increment Theory to Compounds of Phosphorus, Silicon, and Boron with Computational Chemistry. (59 pp.) 2022. JYU Dissertations 581.

27. Pallerla, Rajanish: Studies Towards Synthesis of Favipiravir & Humilisin E. (139 pp.) 2023. JYU Dissertations 611.

28. Taponen, Anni: Radical-Ion Salts based on Thiazyls and Tetracyanoquinodimethane: Hysteretic Magnetic Bistability in a Multicomponent System. (66 pp.) 2023. JYU Dissertations 613.

29. Aho, Noora: Molecular Dynamics Simulations of Acids and Bases in Biomolecular Environments. (78 pp.) 2023. JYU Dissertations 614.

30. Sabooni Asre Hazer, Maryam: Electronic and Optical Properties of Gold Clusters with Carbene Ligands using Density Functional Theory Calculations. (68 pp.) 2023. JYU Dissertations 650.

31. Kinnunen, Virva-Tuuli: Improving the Accuracy of Single Particle ICP-MS Analyses of Au and Ag Nanoparticles. (67 pp.) 2023. JYU Dissertations 689.